Dynamics, Solvent, and Reactions: Ultrafast Infrared Spectroscopy of Vaska's Complex
and its Adducts

A DISSERTATION
SUBMITTED TO THE FACULTY OF THE GRADUATE SCHOOL
OF THE UNIVERSITY OF MINNESOTA
BY

Brynna Halley Jones

IN PARTIAL FULFILLMENT OF THE REQUIREMENTS
FOR THE DEGREE OF
DOCTOR OF PHILOSOPHY

Professor Aaron M. Massari, Advisor

February 2015

Acknowledgements

To Aaron, for emailing me when I visited, for accepting me as a member of your group, for giving me good advice and letting me go off on a tangent for a little while that turned into my thesis

To the Massariites: to my undergrads, Nagilthes Muthu, Ying Hang, RiAnna Butler, and Anthony Tabet for their questions, their hands, their work, and their companionship; to Dr. Audrey Eigner, Chris Huber, and Ivan Spector, who all taught me and let me teach them and took data for me (you're the best minions-I mean colleagues that anyone could ask for), and Dr. Tim Anglin, Dr. Dan O'Brien, Zahra Sohrabpour, Patrick Kearns, and Courtney Olson for commiseration, for all the incredible discussions, for the times you fixed the oscillator so I didn't have to, for putting up with my singing and for helping to keep me sane; and also for not laughing hysterically when your safety officer was the one that shot the laser in her eye

To the members of the Blank, K. Leopold, D. Leopold, Johns, and Frontiera groups for positively scintillating discussions every other week, for great questions and brilliant suggestions

To Ian Tonks, for a helpful discussion about catalysis when I knew practically nothing

To Mike Fayer and his group, especially Dr. Emily Fenn, for answering questions and giving me copies of your MatLab code; hopefully our group will be just as generous as you have been

To Dorothy Sayers, C. S. Lewis, J. R. R. Tolkien, Jane Austen, Garth Nix, Neil Gaiman, Ellen Raskin, Mark Haddon, John D. Fitzgerald, Madeleine L'Engle, Rick Riordan, J. K. Rowling, Bill Watterson, Bill Amend, Scott Adams, Richard Thompson, Paul Gazdikowski, John Allison, Christopher Hastings, Minna Sundberg, Tom Siddell, Randall Munroe, Evan Dahm, Kate Beaton, Ursula Vernon, Tom Dell'Aringa, Kate Ashwin,, Megan Lavey-Heaton, Isabelle Melançon, Michelle Czajkowski, Aaron Diaz, Gigi D. G., Phil and Kaja Foglio, Rich Burlew, Robin McKinley, Brian Jacques, Louis L'Amour, and especially P. G. Wodehouse for taking me away when I needed to go

To my undergrad family (the Fourth-Row Fellowship) who gave unceasing encouragement and steadfast friendship even from afar when it was sorely needed

To my GCF family for all that you have taught me about being a grad student and being human, for your prayers, and for letting me make you all sing "Watchman Tell Us of the Night" every Christmas

To Dan and Siri for being my anime buddies, for letting me eat at your house a lot, for all the trips to the airport, for talking music with me, but mostly for letting me be part of your family

To my Church of the Cross/Church of the Redeemer family for allowing me the privilege of leading you in worship, for holding to the truth while extending grace, for challenging me spiritually and intellectually and for speaking God's word into my life; also to the women of my (fluctuating) small group: Ruth Pszwaro, Anne Calvin, Dani Nicholson, Krista Mahoney, Colleen Kniffen, Annemarie Pickens, and Haley Scharf, all

of whom listened every time I complained about the laser breaking yet again, for their love, their food, and their prayers; also to the youth, who have taken from and given to me energy that I did not know I had and whose acting out of 2D-IR will remain with me forever

To my extended family for all that you have taught me about discipline, humor, and balance and for always making sure that I could explain why anyone would ever want to look at solvation dynamics

To my father, whose math and Matlab help have been of inestimable value to the work that follows, but whose love and support are worth even more

To my mother, for reminding me to take care of myself and for understanding the sentiment of what I said, if not the words

To Bethany, who has always been and is still the coolest person I know, for telling me your stories and listening to mine

To Ryan, for going on before me, for setting the bar high, and for always answering your phone

To Eli and Anastasia, for being born and being awesome

Ευχαριστω

Dedication

Soli Deo Gloria

Abstract

This thesis describes and interprets experiments using two-dimensional infrared spectroscopy (2D-IR) and infrared pump-probe spectroscopy (IPP) as applied to the organometallic catalyst Vaska's complex (VC) and its I_2 and O_2 adducts (VC-I_2 and VC-O_2 respectively) in a variety of solvation environments. The IPP observations yield information about the speed of vibrational relaxation and how it changes as the solvent is altered, giving suggestions as to the mechanism of the relaxation of vibrational energy. The 2D-IR experiments give information about the dynamics occurring in the solvation shell of the solute molecules and specifics about the molecular origins of the lineshapes found in linear infrared spectroscopy (FTIR). These studies are presented in light of possible connections between solvent dynamics and chemical reaction rates occurring in those solvents.

The solvation dynamics of VC and VC-O_2 are characterized by 2D-IR first in 3 neat solvents. 2D-IR spectra were analyzed using the inverse center line slope (CLS) as a representative of the frequency-frequency correlation function (FFCF). The dynamics are compared to previously determined oxidative addition rate constants.

Next, an IPP and linear infrared spectroscopic study was performed on VC-I_2 and VC-O_2 in two different sets of binary solvent mixtures. The vibrational lifetime changes linearly with solvent composition. Evidence that relaxation proceeds directly into the solvent modes is shown.

In the third study presented, 2D-IR was performed on the VC-I_2 vibrational mode to dissect the linear lineshape into its homogeneous and inhomogeneous contributions in

binary solvent mixtures of either chloroform or benzyl alcohol in d_6-benzene. The full FFCF was determined. Inhomogeneous dynamics are implicated as the dominant broadening mechanism.

Finally, an IPP, 2D-IR, and kinetics study on VC and VC-O$_2$ in binary solvent mixtures of d_6-benzene with chloroform and benzyl alcohol is presented. The vibrational lifetimes for VC, in contrast to VC-O$_2$ and VC-I$_2$, show a decrease with increasing mole fraction of the more polar solvent in both sets of mixtures. There is evidence of correlation between the rate constants and the homogeneous linewidth of VC-O$_2$, as well as its inhomogeneous amplitude.

Table of Contents

List of Tables

List of Figures

List of Abbreviations

2D-IR	Two-dimensional infrared spectroscopy
AN	Acceptor number
BA	Benzyl alcohol
BBO	β-barium oxide optic
CLS	Center line slope
DBP	dibutylphthalate
DFT	Density functional theory
DMF	Dimethylformamide
FFCF	Frequency-frequency correlation function
FID	Free induction decay
FTIR	Fourier transform (linear) infrared spectroscopy
FWHM	Full width at half maximum
IPP	Infrared pump-probe spectroscopy
IR	Infrared
IVR	Intramolecular vibrational redistribution
LO	Local oscillator
MCT	Mercury cadmium telluride
MD	Molecular dynamics simulation
NMR	Nuclear magnetic resonance spectroscopy
NOESY	Nuclear Overhauser effect spectroscopy
OAP	Off-axis parabolic mirror

OKE   Optical Kerr effect spectroscopy

OPA   Optical parametric amplifier

RaPTORS   Resonant pump third-order Raman probe spectroscopy

RIKES   Raman-induced Kerr effect spectroscopy

TRSS   Time-resolved Stokes shift spectroscopy

UV   Ultraviolet

VC   Vaska's complex

VC-I_2 Vaska's complex diiodide adduct

VC-O_2 Vaska's complex peroxide adduct

VER   Vibrational energy relaxation

Chapter 1: Introduction

Solvent and its Effects

With the possible exception of the mole, there is no concept more familiar to the chemist than that of solvent and solute. The literature abounds with theories and studies that have explained and explored the enormous influence the one can have on the other. In a continuation of this ongoing discussion, this work examines the effects that not merely the static properties, but also the dynamic motions of the solvent have on a number of different solute measurements for a specific system of organometallic compounds. Since molecules are continuously in motion, vibrating, rotating, and translating in a seemingly endless dance of energy, force, and probability, dynamics can play a crucial role in the multiplicity of processes that occur in the solution phase. It is this interplay of static and dynamic, or time-averaged and time-dependent, properties that is the focus of this thesis, with an end goal of investigating the influence of solvent dynamics on a particular solvent-sensitive oxidative addition reaction: the addition of O_2 to Vaska's complex. The remaining sections of this chapter are intended to place this work in its appropriate context within the literature by first discussing the use and properties of solvent mixtures and subsequently some ways solvent can affect reactions and spectra.

1.1. Solvent Mixtures

1.1.1. Solvent Mixtures: Preferential Solvation

The primary experimental method for smoothly varying solvent properties is through the use of mixed solvents. By changing the ratios of the component solvents, the overall nature of the mixture (dielectric constant, viscosity, etc.) can be altered in some way. It is important to recognize that these properties do not necessarily vary linearly

with overall solvent composition. A textbook example of this is the water/ethanol azeotropic deviation from Raoult's law. When a solute is present, the same can be true for solute characteristics that respond to solvent influence, such as solubility. Even if all purely solvent-based properties do respond linearly to solvent composition, the composition of the local solvation shell surrounding the solute can be different from the bulk solvent when the solute is preferentially solvated.

The different types of preferential solvation (also called selective solvation[1] or dielectric enrichment)[2] are as follows. The solute can have a nonspecific (and thus symmetric) tendency to be encapsulated by one solvent versus the other. This could be caused by dipole/dipole interactions as well as general dispersion interactions, or simply by size differences.[1, 3-6] Alternatively, certain regions of the solute can be attractive to one solvent, while other areas are attractive to the other. An extreme example of this might be the case of a binary salt in a heteroselective solvent mixture, where one solvent surrounds the anion and the other the cation. This second type would also include site-specific interactions such as hydrogen bonding, electron pair donation/acceptance or regional hydrophobic interactions. Thirdly, the solvent composition is constantly fluctuating on a microscopic scale. Combined with the difference between solvent A-solvent A interactions and solvent A-solvent B interactions, this can give rise to microheterogeneities, regions of self-associated solvent where the solute interacts with a concentrated proportion of the dominant solvent.[7-8] It has been shown that these microheterogeneities are dependent on solvent composition and solvent type and can have a strong influence on any solute present.[8] Of course, any or all of these may be at

play in a particular preferentially solvated system. There are different views on which of these types is the most influential, depending on the situation and the quantity being measured.[9-12] Measurements for aqueous mixtures with partially hydrophobic solutes by Bagno and coworkers suggest that hydrogen bonding is considerably less important than dispersion or microheterogeneity.[7, 9]

There are a number of methods used in measuring the degree of preferential solvation. One of the most common is the use of solvatochromic solutes (see Section 1.2.2 for a more in-depth discussion of solvatochromism) or some particular solvent-sensitive solute parameter.[1, 13-16] A variety of models are used particularly for the $E_T(30)$ parameter (a property related to the absorbance maximum of the $E_T(30)$ dye) since it is frequently used as a measure of polarity. One of the simplest, in that it involves only a single fitting parameter, is described by Rosés and coworkers as follows:[14]

$$E_{Tmix} = E_{T1} + \frac{x_2^0 f_{2/1} (E_{T2} - E_{T1})}{1 + (f_{2/1} - 1) x_2^0} \tag{1.1}$$

where x_2^0 is the bulk mole fraction of solvent 2, and E_{T1}, E_{T2}, and E_{Tmix} are the $E_T(30)$ values for solvent 1, solvent 2 and the mixture respectively. Here $f_{2/1}$ is a preferential solvation parameter modeled as $f_{2/1} = \frac{x_2^s/x_1^s}{x_2^0/x_1^0}$ with x_i^s being the mole fraction of solvent i in the solvation shell. It is thus a measure of the preference for solvent 2. There are more complex models that take into account solvent-solvent interactions, which have been shown to be important in appropriately quantifying preferential solvation.[14, 17-18] Systems with either a maximum or a minimum value in a mixture (of which there are quite a few) cannot be well modeled without solvent-solvent interactions.

Using simply the $E_T(30)$ parameter can, however, be misleading. First, the solvent shell composition found in this manner is specific to the probe being used and cannot easily be generalized to other solutes. Secondly, for luminescence solvatochromic studies the emission frequency is related to a dielectric parameter $f(D) = 2(D\text{-}1)/(2D\text{+}1)$ (D being the static dielectric constant) in a linear fashion, but this parameter is not always linear in composition.[19-20] A more direct method was used by Shin and Wakisaka demonstrating an elegant use of mass spectrometry to investigate the microheterogeneity of bulk solvent mixtures of water and DMSO as well as the solvation shells of a number of solutes.[8] They found a remarkable degree of correlation between the clustering abilities of DMSO in water-rich mixtures and the amount of DMSO surrounding the solute. NMR-NOESY experiments have also been used to measure preferential solvation, via the coupling between atoms on neighboring molecules, for a variety of solutes in a number of solvent mixtures.[4, 9] It can also be useful to calculate the preferential solvation via moledular dynamics (MD) simulation.[10, 21]

1.1.2. Solvent Mixtures: Solvent Dynamics

Studies of preferential solvation generally treat the solvent shell composition as a static parameter. In reality, however, the solvation shell, like everything in the liquid phase, is constantly in motion and its composition is certainly in flux. Many studies of solvation and solvent dynamics in mixed solvents have been carried out by various methods including time-resolved Stokes shift fluorescence measurements,[2, 12, 19, 22-23] transient hole-burning spectroscopy,[24] two-dimensional infrared spectroscopy (2D-IR),[25-29] Raman echo measurements,[30] and optical Kerr effect spectroscopy[31-34] as well as a

variety of simulations and theoretical studies.[11, 26, 35-37]   With such a multiplicity of techniques, it is important to examine how the various observables are connected.

These techniques generally fall into one of two categories: retrieving either the solvation function (a measure of the solvent response to some change in the solute), or a time correlation function of an observable related to solvent motions (either in the solvation shell or in the bulk) under equilibrium conditions. The time-resolved Stokes shift (TRSS) technique is an example of the former, where a solute dye molecule is electronically excited, causing a change in the molecular dipole moment. The frequency of the emitted fluorescence is then monitored as a function of time. The characteristic time constants of the frequency shift quantify the solvent shell's relaxation. 2D-IR measures the latter kind of motion by monitoring the electric field fluctuations that influence the frequency of a particular solute or solvent vibration (see Chapter 2 for further discussion of 2D-IR).   Though the measurements take place under different conditions, it has been shown[38-39] within the assumptions of linear response theory, that the time correlation function of the equilibrium solvent fluctuations is equal to the nonequilibrium solvation function! In addition to assuming a linear response to the solute's perturbation of the solvent, this equation also assumes that the correlation function is not substantially different between the initial and final solute states.[40] But within these assumptions, the characteristic motions that respond to solute changes and those that cause fluctuations in spectroscopic observables may be considered to be the same.

The results of solvation (nonequilibrium) dynamics studies of mixtures also generally fall into one of two categories. The relaxation of the solvent shell in mixtures is either intermediate between the two pure solvents or slower than either of them. Usually, though not always, the latter occurs when the mixture involves a polar/nonpolar solvent pair.[12, 19, 24, 36] This is generally considered to result from the requisite exchange of solvent types in the solvation shell, requiring as it does slow, diffusive, translational motion. In pure solvents, relaxation is thought to occur mostly via solvent reorientational motions, sometimes (especially, in the case of ionization) followed by compression of the solvent shell.[35-36] Both of these processes are much faster than the solvent exchange process. In a simple MD simulation involving atomic solutes and solvents, Nguyen and Stratt demonstrated the presence of both compression and solvent-switching regimes.[36] The redistribution of solvent molecules was much slower than the immediate change in the number of molecules in the solvation shell, indicating that the slower speed is due simply to the fact that it is an inherently collective process and not to any particular solvent-solvent interactions. A number of studies have found linearity of the solvation times when plotted against viscosity parameters.[2, 23] Gardecki and Maroncelli's cleverly designed acetonitrile/propylene carbonate solvent system carefully avoids preferential solvation while varying solvation time constants, rotational time constants and viscosity, all of which are linear in mole fraction.[2]

There have been fewer studies of solvent (equilibrium) dynamics in the context of a solute dissolved in a binary mixture and fewer still that study a range of compositions; this is one area where the present work contributes to the field. Kwak and coworkers

found a slowing of the solvent motions around ground state phenol and a phenol-mesitylene complex in mixtures of mesitylene and carbon tetrachloride, similar to the changes in solvation motion discussed above.[25] In a similar 2D-IR and MD study of phenol in mixtures of benzene and carbon tetrachloride, it was found that statistically the likelihood of finding a solvation shell that was primarily one solvent or the other was quite high relative to expectation.[26] There was also a relationship between the FFCF (see Chapter 2 for further discussion of this quantity) and the correlation function of the number of benzene molecules in the solvation shell. OKE measurements by Elola and coworkers in mixtures of benzene and hexafluorobenzene revealed that the collective orientational correlation time for benzene was linear in mole fraction, whereas that for hexafluorobenzene showed a maximum.[34] King and coworkers also found a correlation of the time constants of the FFCF with the viscosity of the solvent in pure solvents and in mixtures with identical linear spectra.[27]

1.2. Solvent Effects

Now that some of the static and dynamic properties of solvent mixtures have been examined, let's look at some of the ways the solvent can change things for the solute. Particular emphasis will be put on effects that will be referenced later; the following discussion should not be considered to be exhaustive. Some discussion will narrow quickly to chemical systems relevant to the work discussed later. The first section will outline some general theoretical frameworks for solvent effects on reactions, with some specifics on the reactions relevant to the rest of the work. The second will discuss the influence of solvent and solvation on various spectroscopic observables both general and

specific to the system under later discussion. Solvent effects are also common for many other chemical phenomena. The position and nature of chemical equilibria are some of the most well-documented and discussed.[1, 41] For further and more general information, consult Reichardt's work "Solvents and Solvent Effects in Organic Chemistry," (reference 1).

1.2.1. Solvent Effects: Reactions

The influence of solvent on chemical reactions has been a major driving force in the study of solvent effects.[1, 25] Solvent has been shown to influence the rate,[42-44] order,[1] mechanism,[1, 45] and even products[45-46] of reactions, but here the focus will be on the solvent effect on the rate. There are generally two ways that the solvent is thought to cause these effects. First, the static solvation properties can change barrier heights and thermodynamic driving forces of these reactions. This is the usual way solvent effects are understood within the structure of transition state theory. Second, the dynamic, sometimes called frictional, properties can change or even control reaction rates with its rearrangement during the course of the reaction.[1, 47] This area is less understood and usually applies most strongly in situations where transition state theory breaks down.

Transition state theory is the typical framework used to understand reactions and what influences them.[1, 38, 48-50] A reaction is considered in terms of the free energy of the molecules at each of its steps. By assuming 1) that the reactants and activated complex are in a pseudo-equilibrium that is unaffected by the formation of products and 2) that the net rate is determined by the reactant-to-product flux of the activated complex across the boundary, the rate for the reaction is:

$$k = \frac{k_B T}{h} e^{-\Delta G^{\ddagger}/R T} \qquad (1.2)$$

where k is the rate, T is the temperature, and $\Delta G^{\ddagger}$ is the difference in the standard Gibbs free energy between reactants and transition state (the free energy of activation). Within these assumptions, solvent effects are measured by how the presence of or change in solvation changes the Gibbs energies of the reactants and activated complex. This requires that the reactants and activated complex be in thermal equilibrium with the solvent, something that may or may not be the case. It also does not take into account recrossing of the barrier before proceeding to products, but movement across a barrier is not always unidirectional.[1, 38]

Since the rate depends on the free energy difference between the reactants and the transition state, the trends in static solvent effects can be estimated by examining the solvation (or changes in solvation, if two solvents are being compared) for both of these substances. Before the full development of transition state theory, some anti-correlation was seen between the rate constant and solubility.[1, 51] Later efforts showed some relationship between the rate constant and the Hildebrand solubility parameter,[1] generally in the context of nonpolar reactants. Trends for polar reactants were noted and codified by Hughes and Ingold[1, 52] into a set of rules for expected qualitative solvent effects considering electrostatic interactions only; thus they discuss exclusively the solvent polarity. These rules were developed originally for nucleophilic/electrophilic substitution reactions, but have been applied elsewhere.[1, 43] The rules are as follows:

1. The rate of a reaction with a more charge-dense activated complex (as compared to the reactants) will increase with increasing solvent polarity.

2. The rate of a reaction with a less charge-dense activated complex will decrease with increasing solvent polarity.

3. The rate of a reaction with little or no change in the charge density as it proceeds to the transition state will be essentially unchanged with any change in solvent polarity.

The relative strength of these effects is strongly dependent on whether the components of the reaction are charged (positively or negatively) or neutral. If a reaction mechanism is known, the solvent effect can be predicted based on these rules. Of course, the reverse is also true; by examining the solvent effect on a particular reaction, aspects of the mechanism can be investigated. A clear example of a reaction that follows the first of these rules is the Menshutkin reaction,[1, 48, 53] where amines react to form ammonium salts:

$$Et_3N + MeI \rightarrow [Et_3N^{\delta+}\cdots Me\cdots I^{\delta-}]^{\ddagger} \rightarrow Et_3MeN^+ + I^-$$
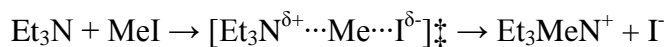
For the specific Menshutkin reaction above, the ratio of the rate constants in hexane and dimethyl sulfoxide is 1:50,000.[48, 53]

Of course, there are a number of factors that these rules do not account for. One of the most important is that entropy is not considered, assuming that greater solvation of a molecule means a lower free energy. With a more strongly solvated solute, however, the solvent will be more ordered, countering the enthalpy and working contrary to the rules stated above. Most reactions are enthalpy-driven, but exceptions certainly exist.[1]

The Hughes-Ingold rules also do not take specific solute-solvent or solvent-solvent interactions into account. Site-specific interactions between reactants and

solvent, especially if it blocks the reaction coordinate, generally work to slow reactions down.[1, 45, 48] Unsurprisingly, interactions that either stabilize the transition state/products or lead the reactants towards a configuration similar to the products (electron shift) will speed up reactions.[1, 45] Solvent-solvent interactions can also be important as the reaction will likely interrupt any structure present in the pure solvent.[1, 54-55] These can be particularly important in the case of reactions taking place in a mixture of solvents, where the different solvents interact with one another differently.[18]

These rules also have no mechanism for understanding solvent effects on reactions where there is no change in charge density. Though these effects are usually smaller, they certainly exist and usually occur because of differences in ease of cavity formation between solvents.[1] This is the area where close connections have been noticed between solubility and reaction rate.

Finally, the dynamic influence of the solvent is ignored by Hughes and Ingold. This is hardly shocking, since their rules are strongly rooted in transition state theory, which in its original structure also has no mechanism for the incorporation of the effects of solvent dynamics.

The effect of solvent dynamics on reactions was put on a firm theoretical foundation with Kramers theory.[47, 56-57] This theory recognized two different ways that solvent dynamics could change the rate predicted by transition state theory. First, collisions between the solvent and the activated complex can cause recrossing of the barrier (high friction, strong system-bath coupling). Second, the equilibrium assumption in transition state theory can break down if solvent relaxation around the activated

complex is slow (low friction, weak system-bath coupling). The former has the strongest effect in systems where the solvent and solute are strongly coupled, hindering passage across the barrier. The latter is most important in systems with low friction: reactions at low pressure or with a low, broad reaction barrier.[1, 38, 47] Using this theory, the rate falls into three different regimes: low friction, where the rate is limited by the energy transfer between solute and solvent and increases linearly with increasing frictional coefficient; high friction, where the rate is limited by the friction itself and the rate decreases with increasing frictional coefficient (rate $\propto$ 1/friction coefficient); and the region in between, where the rate is well-modeled by transition state theory.[47, 49, 56-57] Not all of these regimes will be accessible for liquids at ambient temperature and pressure, however; the earliest experimental studies of this "Kramers turnover" involved the isomerization of stilbene in supercritical ethane.[58-59] The high friction regime is generally more accessible; Caldin and Hasinoff saw a change from the central to high friction regime changing the solvent from an ethylene glycol/water mixture to glycerol.[60] Anna and coworkers used Kramers theory in the high friction limit to deduce the forward and reverse barriers for the isomerization of dicobalt octacarbonyl.[61-62]

One of the main weaknesses of Kramers theory is the assumption (via the Langevin equation) that solvent frictional forces respond instantaneously to movement along the reaction coordinate. Kramers himself related the solvent frictional constant to the shear viscosity of the solvent under consideration, a somewhat static property.[57] However, on the timescales of most chemical reactions, the solvent actions are better modeled as being time-dependent. This is one of the innovations of Grote-Hynes theory,

where the time-dependent frictional parameter is proportional to the correlation function of the solvent forces exerted in the direction of the reaction coordinate at the apex of the barrier. Although there is some question as to the applicability of this theory to certain reactive systems since it assumes a linear solvent response to movement along the reaction coordinate, it has been used recently in the modeling of kinetic isotope effects.[63] There are also examples of dynamic effects not well-described by existing theory. Horng and coworkers found a power-law relationship between solvation time and electron-transfer rates in a bound donor-acceptor dye molecule.[64] Orr-Ewing in a recent paper concerning the reactions of the CN radical showed evidence of another kind of frictional effect, not on the rate directly, but rather on the vibrational excitation of the products.[65]
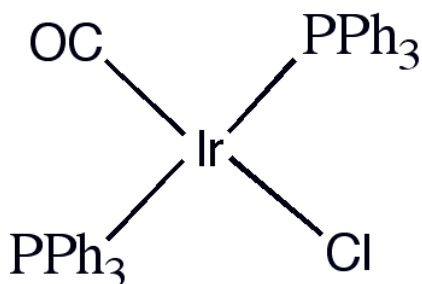
Figure 1.1: Bis(triphenylphosphine) iridium(I) carbonyl chloride, more commonly known as Vaska's complex (VC).

The primary reaction that will be discussed in the following work is the oxidative addition of O_2 to Vaska's complex. Vaska's complex (VC, see Figure 1.1) is a square planar organometallic catalyst that has been frequently studied due to its simplicity and remarkable ability to bind small molecules. The reactions of VC with O_2, H_2, and CH_3I have all been shown to have solvent-sensitive rates that increase significantly with an

increase in solvent polarity.[42-43, 66] According to the Hughes-Ingold rules, this would suggest that the activated complex has a higher charge density than the reactants. With neutral molecules this could be indicative of a polar transition state, as indeed has been articulated in the past regarding this particular reaction.[43] Considering that the formal oxidation state of the iridium increases during this reaction, this is not an unreasonable suggestion. However, as Wilson and coworkers have shown, this may not be correct, as electrostatic ligand effects can mask or cause such distinctions.[67] A recent DFT study of the mechanism of this reaction for a number of inorganic complexes examined the trimethylphosphine analogue to VC.[68] In these calculations, the structure at the transition state was very similar to the product, with elongated Ir-O bonds and a larger C-Ir-Cl bond angle. Additionally, recent work on the addition reaction of methyl iodide to VC in ionic liquids found that the reaction rate was slower than in polar organic solvents.[69]

The vast majority of studies relating nonlinear IR spectroscopies to reaction rates have done so via studies of chemical exchange in the context of reactions in the low-friction limit, such as isomerization, hydrogen bond exchange, or ion pairing.[25-26, 70-75] Chapter 6 is an investigation into the relationship between the dynamical solvent information available from such spectroscopies and the rate constants for an oxidative addition reaction in those solvents. Though reactions in the low-friction limit are certainly important, the majority of catalytically important reactions fall into the central region of Kramers theory, where transition state theory is most useful. The present work provides the first insights, to our knowledge, into this most common situation.

Other reactions involving VC primarily use it either as a precursor to make another catalytically active molecule[76-78] or as a catalyst itself.[79-80] It was originally studied because it is a simple and effective but relatively slow catalyst, allowing for more accurate speculation as to the catalytic mechanism.[81-82] Very few studies have probed the role of solvent in these reactions, so at this point it is not known if they are as sensitive to solvent as oxidative addition reactions.

1.2.2. Solvent Effects: Spectra

The impact of solvent choice on spectroscopic observables has been well-documented and is often how solvent properties are measured.[1, 13-14, 83-84] In fact, the cover of the second edition of Reichardt's "Solvents and Solvent Effects in Organic Chemistry" shows the structure of a solvatochromic molecule! For any spectroscopy, there are three parameters that can be influenced by the solvent: peak position, peak width/shape, and peak intensity. In this section, we will examine the various forms that solvent effects can take in two major sets of analytical spectroscopies: electronic absorption/fluorescence and infrared (IR) absorption. Heavy emphasis will be put on IR spectroscopy and some mention will be made of nonlinear vibrational techniques. A more detailed discussion of these methods will take place in Chapter 2. Since Vaska's complex is a neutral solute, no mention will be made of the many effects that occur with ionic solutes; for investigation into this topic, the reader is referred to references 1 and 48.

In the ultraviolet/visible region of the spectrum, solvatochromism (the shift of the absorption frequency with a change in solvent) has been extensively observed. This

occurs primarily for molecules that have a strong transition dipole moment, i.e. their ground and excited states have notably different distributions of electron density. Under these conditions, the absorption frequency is affected primarily by the solvent's polarity rather than any other parameter. This has led to the frequent use of solvatochromic compounds to measure polarity. A variety of molecules have been used for this purpose and an equal variety of scales exist to relate polarity to wavelength.[13, 84] The direction of the shift, either red (bathochromic) or blue (hypsochromic), is dependent on whether the ground state or the excited state has a greater dipole moment.[1] The solvatochromic frequency shift has also been correlated to other solvent parameters,[84] such as the acceptor number,[85-86] as well as acid dissociation constants.[83]

Under these same conditions ($\mu_{ground} \neq \mu_{excited}$), the intensity of the absorption can also change significantly due to dispersion interactions.[87] Intensities in ultraviolet (UV)/visible absorption are also sensitive to neighboring solvent modes; if a solvent absorption is nearby, the intensity of the solute mode can "borrow" from that mode and the overall intensity is increased.[87] The peak width and shape are influenced largely through electronic-vibrational coupling, which can also be influenced by solvent.[1, 88]

In fluorescence much depends on the relative timescales of emission and solvent rearrangement. If the emission lifetime is longer than the time constants for solvent rearrangement, as is usually the case, the Stokes shift can be solvent-influenced, generally through a bathochromic shift with increasing solvent polarity. The width of the emission peak can be influenced by the solvent in a different way than the absorption peak as observed for Coumarin-153.[22, 88] There is also a time-dependent component to

the emission frequency that reveals the relaxation of the Franck-Condon state, which in the solution phase generally involves movement of the solvent shell. This is how the time-resolved Stokes shift experiment has become a powerful tool for elucidating solvation dynamics (see section 1.1). The time constants for this process have also been shown by some to be connected to the time-dependent friction coefficient that influences charge-transfer reactions (see section 1.2.1).[22, 64]

In IR spectroscopy, solvent effects on peak intensity are usually relatively small.[1, 87] There are exceptions, however, particularly in the case where specific interactions are involved. The intensity of a stretch involved in a hydrogen bond usually increases significantly compared to its intensity without the interaction.[89-91]

In the absence of inhomogeneous broadening, the width (Γ) of a spectral absorption is related to three processes: energy relaxation, phase relaxation, and orientational relaxation, according to the following equation.[92-93]

$$\Gamma = \frac{1}{\pi T_2} = \frac{1}{2\pi T_1} + \frac{1}{\pi T_2^*} + \frac{1}{3\pi T_{or}} \qquad (1.3)$$

The characteristic times of these processes are the vibrational lifetime (T_1), the pure dephasing time (T_2^*) and the reorientation time (T_{or}), respectively (see Section 2.1 for discussion of the dephasing time, T_2). Each of these has their own opportunities for solvent effects and different processes dominate depending on the system.

The vibrational lifetime is a measure of how long it takes for an excited vibration to return to its ground state or, put another way, how long it takes the energy of the excitation to relax into the surroundings (including other portions of the same molecule). This energy most commonly moves to other modes on the same molecule through

intramolecular vibrational redistribution (IVR).[38]   Depending on how close the other modes are in energy, though, the energy can be back-transferred to the original mode, in which case IVR behaves more as a "pure dephasing" contribution.[30, 94]   The solvent can influence this by changing the relative positions of the solute vibrational energy levels. Usually the solvent speeds up IVR by providing additional pathways for relaxation, but King and colleagues showed that the IVR of dimanganese decacarbonyl is hindered by the formation of hydrogen bonds, though the relaxation time was unchanged.[94] If there are no other intramolecular vibrations close in energy but solvent modes are available, then the energy can be transferred to these solvent modes either through strong intermolecular interactions or through solvent-solute collisions.[65-66]   This is almost always significantly slower than an IVR-type mechanism and usually takes tens or even hundreds of picoseconds.[65]   Chapter 4 will show direct evidence for this mechanism of energy transfer for the adducts of Vaska's complex.

The reorientation time can be strongly affected by the solvent depending on the relative size of the solute and solvent. A solute that is small relative to the surrounding solvent molecules will have a faster reorientation time since it can tumble relatively freely in the space between them.[87]   A larger molecule, however, has a much slower reorientation time, so slow even that it adds very little to the absorption linewidth.[94-95] Viscosity of course can play a strong role in this as well via the Stokes-Einstein relation, where a higher viscosity leads to slower orientational relaxation.[32-33, 96]   Wang and Schwartz measured the rotational diffusion of tungsten hexacarbonyl in a number of different solvents and the augmentation of both Raman and IR linewidths.[95]   Though the

contributions did change with solvent, decreasing with increasing viscosity, the reorientation was slow enough that in most cases the added width to the IR lineshape was negligible, contributing less than 10% of the overall width.

Pure dephasing is the loss of phase without loss of excitation; namely, the phase of the coherence excited by the light changes, but the population does not. This arises from interactions that cause random fast fluctuations in the vibrational frequency of the mode of interest, usually involving energy exchange.[97] These interactions are generally with low-frequency modes of either intramolecular (for polyatomic molecules) or intermolecular (with the solvent) nature. In liquids, the pure dephasing timescale is usually the fastest, so it dominates Γ.[98] If the solvent is involved in dephasing, then there can be strong solvent effects. If the primary method of relaxation is intramolecular, then the solvent may not cause a large change, though it can modulate the intramolecular couplings as well.[99] The strength of these exchanges to dephase a particular vibration has been related to the anharmonicity of the vibrational potential, so stronger effects are expected for systems that are not well-described by a harmonic oscillator.[97, 100]

Frequency fluctuations can occur on a variety of timescales, not just very quickly. If they become so slow that they could be considered to be static, then the phenomenon of static inhomogeneous broadening appears, where the different frequencies indicate different chemical environments. The overall width (Γ_{inh}) becomes a convolution of the homogeneous widths (Γ) described by equation 1.3 with their environmental distribution. In this situation, the shape of the peak takes on a Gaussian or Voigt profile. If there is no

inhomogeneous broadening (a homogeneous linewidth), then the peak shape is generally a Lorentzian lineshape.[93, 101]

The inhomogeneous width can be very solvent-sensitive, since this width involves variation in the number and type of vibrational environments. The rule of thumb for an inhomogeneous linewidth is that the stronger the solute-solvent interactions involving that mode, the wider the peak.[1, 102] Polar and nonpolar solvents both have a wide variety of possible configurations, but polar solvents will exert a stronger perturbation on the vibration. The expectation would be that polar solvents would lead to wider IR absorbances than nonpolar solvents. The trend can also hold for specific interactions; the stretching vibration for a hydrogen bond-donating entity broadens significantly as well as shifting to lower frequencies.[1, 89-91]

To complicate matters further, the fluctuations in frequency can also occur at intermediate timescales between the fast contributions of the homogeneous linewidth and the slow contributions of an inhomogeneous linewidth. These are often called spectral diffusion, because when they occur in an inhomogeneous situation, they can be considered to be the timescales of the diffusion of the homogeneous lines between different frequencies.[93] Spectral diffusion is very solvent-sensitive; it has been related to solvent viscosity in some systems.[27, 71] For a more in-depth discussion of spectral diffusion, see Section 2.2.1.

Static solvent effects on the IR frequency of a vibration (vibrational solvatochromism) depend strongly on the mode of interest. Generally, the solvent changes either the magnitude or the direction of the transition dipole moment or both.

Jauquet and Laszlo[87] showed that for a single normal mode, assuming a time independent local electric field applied by the solvent to the solute and assuming that the perturbing force is small compared to that of the bond, the frequency shift is proportional to

$$\Delta\omega \propto -\left[(\delta\theta/\delta q)^2 - \frac{1}{\mu}\frac{\delta^2\mu}{\delta q^2}\right]V \qquad (1.4)$$

where V is the potential for a specific vibration from the solvent, μ is the magnitude of its transition dipole, θ is the angle between the solvent electric field and its transition dipole, and q is its normal internal coordinate. If the solvating energy lowers the potential, then V in the equation above is negative and the sign of the shift is dictated by the terms in brackets. Under these conditions, for a vibration where the magnitude of the dipole changes but the direction does not, such as a stretching vibration, an increase in solvation will give a red shift. Alternatively, if the direction changes but the magnitude stays roughly the same, as for a bending motion, then an increase in solvation will give a blue shift.[87] Specific interactions can play a part here also. As mentioned previously, hydrogen bonding tends to impart a red shift to stretching vibrations involved in the bond.[87, 89-91] Reichardt has published a nice list of the peak positions for three stretching motions in a variety of solvents, illustrating both a consistent red shift with increasing polarity and the substantial deviations from expectation when hydrogen bonding is involved.[1]

The situation for metal-bound carbonyls such as Vaska's complex and its adducts is somewhat different, primarily because of metal-carbonyl backbonding. The *d*-orbitals of the metal with the appropriate symmetry convey electron density into the antibonding orbitals of the CO, thus weakening the bond and lowering its frequency. If, however,

anything occurs to change the electron density at the metal, then the backbonding will change as will the CO frequency. This makes ν_{CO} markedly sensitive to the oxidation state of the metal; in fact it has been used as a way to measure the oxidation state.[103] Huber and coworkers carried out an FTIR study of Vaska's complex and a number of its adducts in a variety of solvents.[104] They found that for the majority of the adducts as well as for VC itself the frequency did not change very significantly. For the dioxygen adduct VC-O_2, however, there was a strong correlation between ν_{CO} and the solvent's acceptor number, a measure of solvent electrophilicity. They concluded that the solvent was pulling electron density from the dioxygen ligand, which, because of the particular metal *d*-orbital that the dioxygen π-bond affects, caused a through-metal interaction with a CO antibonding orbital.

Vaska's complex and its I_2 and O_2 adducts feature prominently in the work that follows. In a number of ways, this system is ideal for investigating the interplay of static and time-dependent solvent-solute interactions. The metal carbonyl is a strong IR absorber, giving excellent signal-to-noise ratios for both linear and nonlinear IR spectroscopies. Its simplicity has made it an archetypical organometallic catalyst, thus it has been frequently studied from a number of other experimental perspectives. Most organic solvents will dissolve it readily while showing an influence on the IR spectra. Its tendency of taking up small molecules in solution (which has been extensively studied) also gives a chance to investigate the relationship between dynamics and kinetics.

In spite of the large VC literature, very little has been done to study its dynamics. Apart from a single measurement of its vibrational lifetime,[66] to my knowledge, no

ultrafast measurements have been carried out on this system prior to the following work. It is a shame that a system so well-characterized in static parameters should be so neglected in the study of time-dependent properties. The two adducts with I_2 and O_2 provide additional insight into the effects of geometry and carbonyl stretching frequency on such properties. Also, as mentioned previously, few studies of equilibrium ultrafast solvent dynamics in solvent mixtures exist, and even fewer examine the ties between reactions and solvent dynamics in the transition state theory regime.

The remainder of this thesis is organized as follows. Chapter 2 discusses the theory of 2D-IR and IPP. It also explains the data treatment and extraction of the FFCF from the spectra. In Chapter 3, the first 2D-IR studies of VC and VC-O_2 in three different solvents are presented. Chapter 4 contains a IPP study of VC-O_2 and VC-I_2 in two sets of binary solvent mixtures, examining how their vibrational lifetimes are affected by solvent. Chapter 5 is a 2D-IR study of VC-I_2 in the same two sets of solvent mixtures and reveals the origins of some unexpected differences in linewidth. Chapter 6 presents the 2D-IR study of VC and VC-O_2 in these mixtures along with the kinetics of the oxygenation reaction; relationships between the solvent dynamics and the reaction are explored.

Chapter 2: Spectroscopy Theory and Practice

2.1. Linear Infrared (IR) Spectroscopy

Every kind of spectroscopy has its origin in a macroscopic polarization of the chemicals under examination. The polarization response is often fit to a Taylor series expansion

$$P = P^{(1)}(E) + P^{(2)}(E^2) + P^{(3)}(E^3)...$$
(2.1)

where $P^{(n)}$ is the nth order polarization: an $n+1$ level tensor connected to the system's response and a function of E (the electric field of the incident light) raised to the nth power. The incident light places those molecules with which it interacts into a coherent state: a superposition of (in the case of infrared radiation, which will be to focus of this discussion) the ground state (0) and the first excited state (1). This is depicted in the Figure 2.1, the double-sided Feynman diagram for a linear spectroscopic process. Such diagrams are useful for understanding the nonlinear processes that follow so it behooves us to describe them. Time begins at the bottom and progresses upwards. The solid vertical lines on the left and right represent the ket and bra sides of the density matrix, respectively. Solid arrows represent wave vectors of incident light (positive if the arrow points up and right, negative if it points up and left). The dashed arrow represents the emitted signal. To keep track of the changes in the state of the system, the appropriate density matrix element at a given point in time is placed in the center. Note that the complex conjugate of this process (proceeding through a $|0\rangle\langle 1|$ coherent state) is also an appropriate representation of the production of a linear lineshape. For simplicity, and the saving of trees, only the diagrams with the emitted signal proceeding from the ket will be shown.
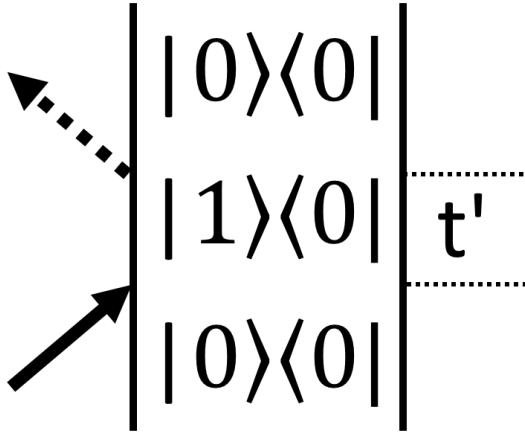
Figure 2.1: Double-sided Feynman diagram for a first order process. See text for further description.

It is the ensemble of transition dipole moments of this coherent state that creates the macroscopic polarization. For linear spectroscopy only the first term of the expansion above (Eq. 2.1) is needed to describe the response of the system to the electric field.

An emitted electric field arising from a macroscopic polarization inherently has a 90° phase shift from that polarization.[93] The linear macroscopic polarization $P^{(1)}$ is a convolution of the incident electric field $E(t)$ with the linear molecular response function $R^{(1)}$, which has been shown[93] to be (in the approximation of second order in the cumulant expansion)

$$R^{(1)}(t) = i\mu_{01}^2 e^{-i\omega_{01}t} e^{-g(t)} \tag{2.2}$$

where μ_{01} is the transition dipole moment, ω_{01} is the frequency of the transition $((E_1 - E_0)/\hbar)$, and $g(t)$ is the lineshape function (see Eq. 2.4 and below). The electric field of the signal ($E_s^{(1)}$), being shifted in phase, is related to

$$E_s^{(1)} \propto i \int_0^\infty R^{(1)}(t')E(t\text{-}t')e^{-i\omega(t\text{-}t')+i\vec{k}\cdot\vec{r}+i\varphi}\mathrm{d}t' \tag{2.3}$$

where ω is the frequency of the incident light, φ is its phase, $\vec{k}$ its wavevector and $E(t\text{-}t')$ the pulse envelope. This is often called the free induction decay (FID). As long as the incident pulse is short enough, $E_s^{(1)}$ will contain information about the molecular response. In a spectrometer, this signal is usually reflected from a grating (Fourier-transformed) and detected at the intensity level, (multiplying by its conjugate). Since the incident pulse has imparted its own direction onto the signal (note the $\vec{k}$) both will reach the detector (heterodyne detection). Due to the phase shift and the shift present in the response function itself, the signal will interfere destructively, causing less light to hit the detector than was initially present. It should also be noted that only the real part of the response function is detected, the absorptive portion; to examine the dispersive (imaginary) part would require adjustment of the phase of the heterodyning field. This decrease in the light appears as an absorbance lineshape. Note in Figure 2.1 that the emitted wavepacket has the opposite sign as the incoming wavepacket.

To go a little deeper into the connections between the response function and the molecular system, let us examine the lineshape function. It is this function that contains the dynamic information about the chemical system under study. To second order in $\delta\omega_{01}(t)$, this function is

$$g(t) = \int_0^t \int_0^{t'} \langle \delta\omega_{01}(t'')\delta\omega_{01}(0)\rangle \mathrm{d}t''\mathrm{d}t' = \int_0^t \int_0^{t'} C_{FFCF}(t'')\mathrm{d}t''\mathrm{d}t' \tag{2.4}$$

where $\delta\omega_{01}(t)$ is the frequency fluctuation in time of the transition of interest, and $C_{FFCF}(t)$ is called the frequency-frequency correlation function.

To understand $C_{FFCF}(t)$ and its possible uses, consider a vibrational mode in the solution phase. It is surrounded by solvent that is continuously in motion, on many different timescales. These motions will of course alter the electric field felt by the vibration. This change in environment can thus cause a corresponding change in the vibrational frequency. Thus the decorrelation rate of the frequency of an oscillator can give information about the speed of these motions. It will also be sensitive to the coupling of those motions to the oscillator, which is taken into account with the amplitude of particular changes.

Given the naturally decaying nature of a correlation function, it is not unreasonable that Kubo[93, 105] first proposed using an exponential decay to model this function as follows:

$$C_{FFCF}(t) = \Delta_c^2 e^{-|t|/\tau_c} \tag{2.5}$$

where Δ_c represents the amplitude of the frequency fluctuations and τ_c is the time constant for the decorrelating process. This form for the correlation function leads to the following form of the lineshape function:

$$g(t) = \Delta_c^2 \tau_c^2 (e^{-t/\tau_c} + t/\tau_c - 1) \tag{2.6}$$

If the motions occurring near the vibration are very fast or are very small in amplitude ($\Delta_c \tau_c \ll 1$), then the lineshape function can be approximated by $g(t) = \Delta_c^2 \tau_c t$ and $C_{FFCF}(t)$ will be a delta function: $\delta(t)\Delta_c^2 \tau_c \equiv \delta(t)/T_2$. This condition is called the homogeneous limit, and an aborbance arising from it is said to be homogeneously broadened. The frequency will be essentially instantaneously unrelated to the frequency at a subsequent

time (importantly, under these circumstances, Eq. 2.2 for the linear response function is an exact solution and no longer an approximation). The FID will decay with a time constant of T_2, leading to a Lorentzian absorbance lineshape with a width of $1/(\pi T_2)$ (assuming a rapid instrument response;[93] see Section 1.2.2). T_2 has units of time and is often called the dephasing time, because it represents the time for the phase relationship between different oscillators in the ensemble to be lost. In a physical sense, the T_2 term arises from the various processes that give an absorbance a finite linewidth. In the condensed phase the relaxation of vibrational energy from the mode, fast dephasing, changes in orientation, and intramolecular vibrational redistribution[30] can all influence the apparent width of a particular mode. In a sense, the homogeneous broadening of a mode in the condensed phase arises from the fact that it exists in an environment with which it can interact (different effects cause homogeneous broadening in the gas phase).

Most systems in the condensed phase, however, are not merely homogeneously broadened but also inhomogeneously broadened. That is, there are multiple possible environments in which the mode can exist. If the solvent motions are too slow for the vibration to respond to, then it will be impossible for the frequency to ever be fully de-correlated, and the FFCF will be a time-insensitive static offset ($C_{FFCF}(t)=\Delta_c^2$). The lineshape function will be proportional to the square of the time. The FID will decay as a Gaussian and a Gaussian absorbance spectrum is the result.[93] This situation represents the inhomogeneous limit, or static inhomogeneity, and is most likely to be found in the solid state. If there is a combination of homogeneous and inhomogeneous broadening (Bloch dynamics), the absorbance lineshape should show as a Voigt profile; in practice,

the homogeneous broadening is often a very small contribution and thus the spectrum is well-fit to a Gaussian.

In the liquid phase, however, it is very likely that spectral diffusion will exist in a given sample. Spectral diffusion occurs when the surroundings of a particular mode change in such a way that the entire homogeneous lineshape shifts to a different frequency. It can also be thought of as one type of environment changing to another. In this case, we return to the original Kubo equation for the FFCF, modeling it as a sum of exponential decays. This process can also yield a Voigt- or Gaussian-like profile in the linear spectrum (though the cumulant expansion is only strictly correct for a Gaussian lineshape).[93, 101]

Notice that these last two situations could possibly yield the same spectrum, to the linear "eye" so to speak. To put it another way, in any inhomogeneously-broadened system, the absorbance is a sum of all the homogeneously-broadened absorptions of the subensembles sampled. Generally the measurement of a linear spectrum is done over a large enough spot and/or over a long enough time that all possible environments available at equilibrium contribute to the lineshape, giving an inhomogeneously broadened (Gaussian) peak. It is impossible, simply from the linear spectrum, to distinguish between a system with a broad homogeneous linewidth and a small amount of inhomogeneity and that where the homogeneous linewidth is narrow and the inhomogeneity is large. Much less is it possible to distinguish between different kinds of spectral diffusion, or a spectrally diffuse sample and one containing static inhomogeneity.

In order to obtain this sort of information, to dig down into the lineshape and pry it apart, we require lasers.

2.2. Two-Dimensional Infrared (2D-IR) Spectroscopy

2.2.1. 2D-IR Theory

Looking back at Eq. 2.1, there are additional terms to the Taylor expansion of the polarization. These become important only with very large incident fields, such as pulsed lasers. The vibrational echo signal, on which 2D-IR is based, comes from the third-order polarization $P^{(3)}$, thus it involves the incidence of three laser pulses. The vibrational echo is also often described as a four-wave mixing process, the four waves including the emitted signal wavepacket as well as the three laser pulses. Since there are three pulses, there are also three times involved: τ: the time between the first and second pulse, T_w: the time between the second and third pulses (also called the waiting time), and t': the time between the third pulse and the emission of the echo signal.

There are a number of ways that these three pulses can interact to give a third-order signal. These pathways are described by the Feynman diagrams shown in Figure 2.2[93, 106] (as above, complex conjugates are omitted). The diagrams are organized by the sequence of positive and negative incident wave vectors: R_1, R_2, and R_3 all use the ordering of - + +; : R_4, R_5, and R_6 all use the ordering of + - +; : R_7 and R_8 use the ordering of + + -. The sign of a response function associated with a particular path is dictated by the evenness (positive) or oddness (negative) of the number of interactions on the bra side of the density matrix. Since (as will be seen below) the echo signal is

emitted in the phase-matched direction according to these signs on the incoming wave vectors, by controlling the temporal and spatial positions of these laser pulses, it is possible to separate these three sets of responses.
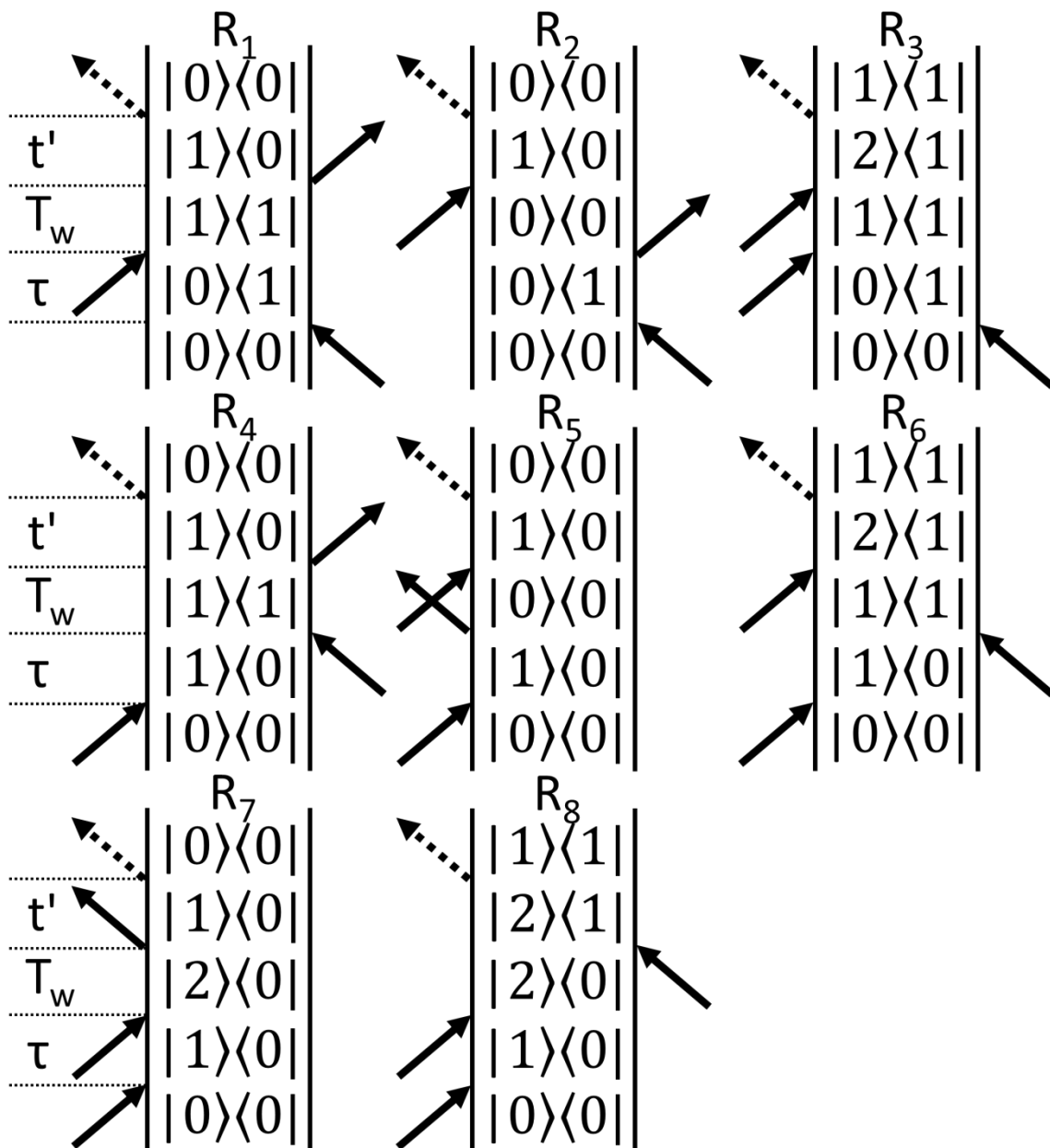
Figure 2.2: Double sided Feynman diagrams for third-order processes. See text for further description.

In examining the double-sided Feynman diagrams, it is clear that for the first six response functions, the first three interactions place the system in a coherent state, a population state, and another coherent state respectively. During the first coherent state (τ), the ensemble of oscillators will behave in the same fashion as in the coherent state discussed above; that is, the electric field due to the macroscopic polarization will decay according to the FID. They are put into an initially coherent set of coherent states! In a situation where inhomogeneous broadening is present, rapid dephasing of the coherence (of the coherent states) will occur due to the multiplicity of frequencies present.

Upon the arrival of the second pulse (T_w), the system exists in a population state and not a coherent state any longer. During this time, the phase relationships of the coherent states may be considered as frozen, unless one of two things changes during this time: the frequency of the oscillator (spectral diffusion) or the population state itself (population relaxation). In both of these cases, the phase relationship of that particular oscillator to the rest of the ensemble is lost.

During the second coherence time (t'), what happens depends on the relationship of this coherent state with that occurring during τ. If the coherent states are the same (R_4, R_5, and R_6) then the FID resumes where it left off, continuing its dephasing with only a slightly reduced number of oscillators. If, however, the coherent states are phase conjugates of one another (R_1, R_2, and R_3) something far more interesting happens. The dephasing that played out in the first coherent state is reversed. The various coherent states will rephase and emit a stronger macroscopic polarization than is present in the

other responses. Thus these pathways (R_1, R_2, and R_3) are called rephasing diagrams, and those discussed previously (R_4, R_5, and R_6) are called nonrephasing diagrams. The diagrams labeled as R_3 and R_6 include a second coherent state between the first and second excited states, rather than the ground and first. Since these diagrams have an odd number of interactions on the bra side, their response functions will be the opposite sign. Notice that only those oscillators which have retained their phase information (by retaining their frequency and also remaining in the same population state) will contribute to the rephasing process. Thus by examining the polarizations coming from both rephasing and nonrephasing separately, it becomes possible to distinguish between those molecules that have kept their frequency consistent throughout the experiment, and those that have not. Population relaxation, influencing both rephasing and nonrephasing pathways in the same manner, changes only the overall amount of signal and not its shape (though, as mentioned previously, it does contribute to the homogeneous linewidth). Diagrams R_7 and R_8 produce third-order signal, but in a different direction than the vibrational echo used by 2D-IR. Due to the sign ordering of the incident wave vectors, they will contribute in the phase-matched direction (see Figure 2.3 and discussion) only when $T_w < 0$, which is never the case in a 2D-IR experiment.
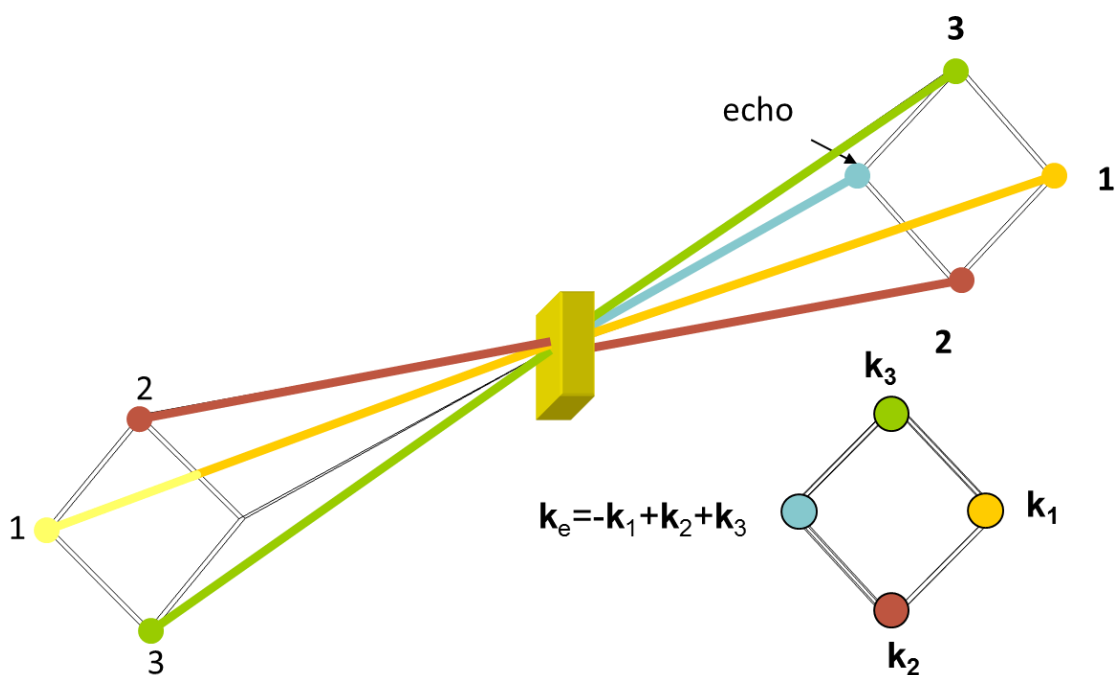
Figure 2.3: Illustration of the box-CARS geometry. Beams are labeled by time ordering for rephasing spectra.

Early vibrational echo experiments had only two beams, essentially fixing T_w at 0. This allowed motions faster than the FID, which give rise to homogeneous broadening, and those slower than the FID, which produce inhomogeneous broadening, to be differentiated from one another. By varying T_w, as has been done with later experiments, the window of what is "homogeneous" and what is "inhomogeneous" becomes changeable. Generally in the condensed phase (and certainly in the experiments discussed in this work) population relaxation is considerably longer than the FID, ensuring that signal will still be present as the experimental time increases. By altering the time of the experiment, the different timescales of those motions which influence the frequency can be discerned and differentiated.

The response functions for each of the pathways discussed can be determined from these diagrams. Since the vibrational lifetime does not change depending on whether the system is in the ground or the first excited state, R_1 and R_2 are identical, as are R_4 and R_5.

For a system with only homogeneous broadening, R_1 is

$$R_1 = R_2 = i\mu_{01}^4 e^{-i\omega_{01}\tau} e^{-\tau/T_2} e^{-T_w/T_1} e^{-i\omega_{01}t'} e^{-t'/T_2} \tag{2.7}$$

Including the possibility of inhomogeneous broadening complicates matters, but again within the cumulant expansion to second order (which is exact for Gaussian statistics), the response functions are:

$$R_1 = R_2 = i\mu_{01}^4 \exp\left(-g(\tau)+g(T_w)-g(t')-g(\tau+T_w)-g(T_w+t')+g(\tau+T_w+t')\right)$$

$$\cdot \exp(-i\omega_{01}(t'-\tau)) \cdot \exp(-T_w/T_1^{(01)}) \tag{2.8}$$

$$R_4 = R_5 = i\mu_{01}^4 \exp(-g(\tau)-g(T_w)-g(t') + g(\tau+T_w)+g(T_w+t')-g(\tau+T_w+t'))$$

$$\cdot \exp(-i\omega_{01}(t'+\tau)) \cdot \exp(-T_w/T_1^{(01)}) \tag{2.9}$$

$$R_3 = -i\mu_{01}^2\mu_{12}^2 \exp\left(-g(\tau) + g_c(T_w) - g_{12}(t') - g_c(\tau + T_w) - g_c(T_w + t')\right.$$

$$\left. + g_c(\tau + T_w + t')\right) \cdot \exp(-i((\omega_{01} - \Delta)t' - \omega_{01}\tau)) \cdot \exp($$

$$- T_w/T_1^{(12)}) \tag{2.10}$$

$$R_6 = -i\mu_{01}^2\mu_{12}^2\exp(-g(\tau) - g_c(T_w) - g_{12}(t') + g_c(\tau + T_w) + g_c(T_w + t')$$

$$- g_c(\tau + T_w + t')) \cdot \exp(-i((\omega_{01} - \Delta)t' - \omega_{01}\tau))$$

$$\cdot \exp(-T_w/T_1^{(12)})$$

(2.11)

where the population relaxation times from the different states are distinguished and μ_{12} is the transition dipole moment for the vibrational 1-2 transition, Δ is the anharmonicity of the system, such that $\omega_{12} = \omega_{01} - \Delta$, and $g_c(t)$ and $g_{12}(t)$ are the cross-correlation and 1-2 transition lineshape functions as follows.

$$g_c(t) = \int_0^t \int_0^{t'} \langle \delta\omega_{12}(t'')\delta\omega_{01}(0)\rangle dt'' dt'$$

(2.12)

$$g_{12}(t) = \int_0^t \int_0^{t'} \langle \delta\omega_{12}(t'')\delta\omega_{12}(0)\rangle dt'' dt'$$

(2.13)

This assumes that the frequency fluctuations do not influence the anharmonicity. If we assume further that the excitation of the vibrational mode does not perturb its surroundings, and thus that $g(t)$ for the transition from the ground to the first excited state and that for the transition between the first and second excited states are identical (usually a reasonable assumption, see reference [93]), then the above response functions simplify to Equations 2.14 and 2.15. It is also often assumed that $\mu_{12} = \sqrt{2}\mu_{01}$.

$$R_3 = -2i\mu_{01}^4\exp(-g(\tau) + g(T_w) - g(t') - g(\tau + T_w) - g(T_w + t')$$

$$+ g(\tau + T_w + t')) \cdot \exp(-i((\omega_{01} - \Delta)t' - \omega_{01}\tau)) \cdot \exp($$

(2.14)

$$- T_w/T_1^{(12)})$$

$$R_6 = -2i\mu_{01}^4 \exp(-g(\tau) - g(T_w) - g(t') + g(\tau + T_w) + g(T_w + t')$$

$$- g(\tau + T_w + t')) \cdot \exp(-i((\omega_{01} - \varDelta)t' - \omega_{01}\tau)) \cdot \exp($$

$$- T_w / T_1^{(12)})$$

(2.15)

From these response functions, we can proceed to calculate the third order polarization for these processes (Eq. 2.16) which consists of a convolution of the three pulses with the sum of the response functions.

$$P^{(3)}(t) = e^{i(\mp \vec{k}_1 \pm \vec{k}_2 + \vec{k}_3)\cdot\vec{r}} e^{i(\mp \varphi_1 \pm \varphi_2 + \varphi_3)} \int_0^\infty \int_0^\infty \int_0^\infty \sum_p R_p(\tau, T_w, t') \cdot E_3(t - t')e^{-i\omega(t - t')}$$

$$\cdot E_2(t - t' - T_w)e^{-i\omega(t - t' - T_w)}$$

2.16)

$$\cdot E_1(t - t' - T_w - \tau)e^{-i\omega(t - t' - T_w - \tau)} d\tau \, dT_w \, dt'$$

Note that this signal will be emitted in the $\mp \vec{k}_1 \pm \vec{k}_2 + \vec{k}_3$ direction. For $R_{1\text{-}3}$ the direction is $-\vec{k}_1 + \vec{k}_2 + \vec{k}_3$, whereas for $R_{4\text{-}6}$ the direction is $+\vec{k}_1 - \vec{k}_2 + \vec{k}_3$, in keeping with the double-sided diagrams. This is what is called the phase-matched direction for each set of response functions.
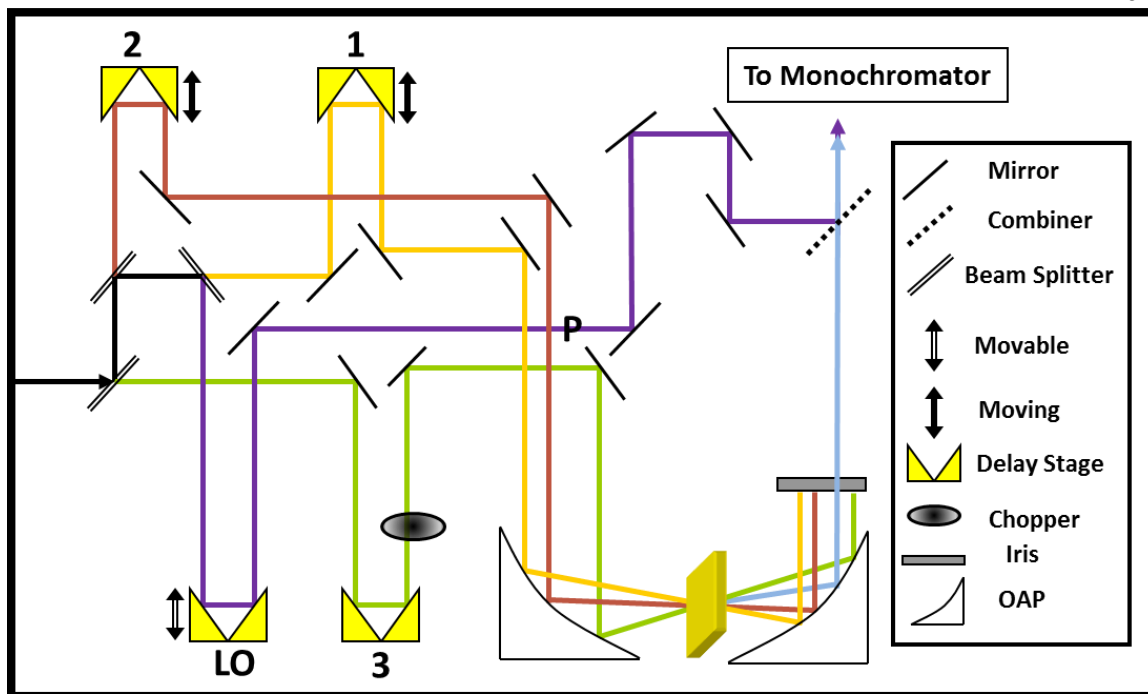
Figure 2.4: 2D-IR spectroscopic setup showing the beam paths as labeled on the delay stages. The sample is located between the two off-axis parabolic mirrors (OAPs). Position **P** is where the CaF$_2$ wedge is inserted to switch to a IPP setup.

2.2.2. 2D-IR Practice

It is important to recognize that the series of interactions described above as leading to the emission of the vibrational echo is far from being the only process occurring in the sample upon irradiation. The pump-probe interactions described in section 2.3, the absorption from section 2.1, as well as many others, all occur at the same time with the interactions leading to the echo. By appropriately configuring the beam placement, thus fixing a particular phase-matched direction to examine, the vibrational echo can be in effect isolated from the signals produced by these other processes, making

it a zero-background technique. Signals from higher-order processes can be emitted in that direction also, however, so a power study is generally recommended.

In the specific laser setup used for the following work, the beams were in what is called a box-CARS geometry,[107] with the three beams impinging on the sample at the corners of a square, as seen in Fig. 2.3. It is obvious here that the signal emerges in the $-\vec{k}_1 + \vec{k}_2 + \vec{k}_3$ direction. But both rephasing and nonrephasing scans can be taken in this geometry simply by changing the time ordering of the pulses. By setting τ to be negative beam 1 arrives after beam 2, giving the nonrephasing echo in the same physical direction. There are several other methods of isolating the desired signal (pump-probe geometry, phase cycling, etc) which will not be further discussed. Readers wishing to learn more about these methods are referred to Chapter 9 in reference 93.

Figure 2.4 shows the optical setup around the sample. The incoming light is pulsed mid IR (~90 fs FWHM time width, 1kHz rep rate, ~200 cm^{-1} FWHM bandwidth, ~3 µJ/pulse). As shown, the echo signal is combined with a small portion (~1%) of the incoming beam, called a local oscillator (LO) in tribute to the origin of heterodyne detection in radio systems, to produce a signal of the combined intensity. These two beams add as electric fields but their combination is detected as intensity, which is related to the square of the electric field. This squaring of the sum produces the three terms in Equation 2.17 below: the square of the echo signal, the square of the local oscillator and a cross term that is proportional to each individual electric field.

$$I \propto \left| E_s^{(3)} + E_{LO} \right|^2 = E_s^{(3)^2} + E_{LO}^2 + 2\text{Re}[E_s^{(3)} \cdot E_{LO}] \tag{2.17}$$

When there is good temporal and spatial overlap of the local oscillator and echo signal, the first term is very small compared to the other two. The second term is eliminated because the signal is chopped: every other pulse of beam 3 is blocked. When data are collected, the signal is recorded as:

$$S_{data} = \frac{S_{unblocked} - S_{blocked}}{S_{blocked}} \qquad (2.18)$$

The subtraction process clearly gives the signal that is only present when all the beams are reaching the sample. Division by the blocked signal is done to account for fluctuations and the shape of the laser spectrum across the wavelengths of interest. It is therefore the third term in Eq. 2.17 that dominates the signal as recorded. Since this term is linear in the two electric fields, the information regarding the phase of the echo is not lost, though it can only be seen in the interference with the local oscillator. For this reason, only phase information relative to the local oscillator can be determined. The signal and LO are combined at the detector after passing through a monochromator, which performs an optical Fourier transform of the t' time variable to ω_m in frequency.

In a typical 2D-IR experiment, the time variable τ is scanned from negative to positive values to obtain both rephasing and nonrephasing decays while the value of T_w is kept constant. This process is repeated for a number of values of T_w. The resulting interferograms are separated into rephasing and nonrephasing scans and then Fourier-transformed along the τ axis to give ω_τ.

Figure 2.5: Imaginary (a, b) and real (c, d) parts of the rephasing (b, d) and nonrephasing (a, c) 2D-IR spectra and the purely absorptive spectrum (e) for VC-I$_2$ in d_6-benzene at $T_w = 0.1$ ps. Note the relative magnitudes of the color bars

This transform also would filter out the first term in Eq. 2.17 even if it were not

small compared to the third term. This gives the advantage of doing what could not be

done spatially: separating in frequency those pathways that involve the coherent state between the first and second excited states. Again examining the double-sided Feynman diagrams in Fig. 2.2, it can be seen that the average value on the ω_τ axis for $R_{1\text{-}6}$ will be $\langle\omega_{01}\rangle$. On the ω_m axis the value for $R_{1,2,4,5}$ will be, again, $\langle\omega_{01}\rangle$, but for $R_{3,6}$ will be $\langle\omega_{12}\rangle$, shifted from $\langle\omega_{01}\rangle$ by the anharmonicity. Also recall that the sign of $R_{3,6}$ is the opposite of that of the other response functions. In looking at the spectra, therefore, we should expect to see two peaks of opposite signs shifted along the ω_m axis but in the same place on the ω_τ axis. Though conventions differ throughout the field, causing much good-natured bickering, throughout the remainder of this work the peaks arising from $R_{1,2,4,5}$ (the 0-1 transition peak) will be designated as positive in sign (thus that from $R_{3,6}$, called the 1-2 transition peak, will be negative); additionally the ω_τ axis will be set as the abscissa and the ω_m as the ordinate.

Figure 2.5 shows the real (c, d) and imaginary (a, b) parts of the rephasing (b, d) and nonrephasing (a,c) spectra for a value of $T_w = 0.1\text{ps}$ from a sample that is mostly homogeneously broadened, with some spectral diffusion (VC-I_2 in d_6-benzene, see Chapter 5). The two peaks of opposite signs can be seen in all the spectra. Notice particularly how the real rephasing spectrum peaks are elongated in the diagonal direction, while those of the nonrephasing spectrum stretch in the antidiagonal direction. Unlike linear spectra, simply taking the real part of a 2D-IR spectrum does not yield absorptive peakshapes; the wide side wings of dispersive lineshapes can be seen in each spectrum. Adding the complex rephasing and nonrephasing spectra together, however, has been shown[93, 108] to cancel dispersive aspects of the lineshapes, leaving behind what

is called the purely absorptive spectrum. This spectrum can be seen in Figure 2.5e. Notice that the peaks are much smaller and more compact in the purely absorptive spectrum, yielding much greater resolution than is present in the separated spectra.

Practically speaking, however, arriving at the correct rephasing and nonrephasing spectra (and thus the purely absorptive spectrum) is less simple than has been thus far implied. With the optical setup as shown in Figure 2.4 (operating in the time domain without a pulse-shaper), it is necessary to correct the spectra for various errors. This process is done after data collection and Fourier transformation and is called phasing or phase processing, since it corrects errors in the relative phases of the pulses. Though there are a variety of specific equations that are and have been used for the phasing procedure, all have the common form of:

$$S_{PA}(\omega_m, \omega_\tau) = S_{NR}\, e^{i\phi_{NR}} + S_R\, e^{i\phi_R} \tag{2.19}$$

where S_{PA} is the purely absorptive spectrum, S_{NR} and S_R are the nonrephasing and rephasing spectra, respectively, and ϕ_{NR} and ϕ_R are the nonrephasing and rephasing correction factors, respectively. The form that these factors take varies[93, 108-110] but only the two equations used in the following work will be discussed here.
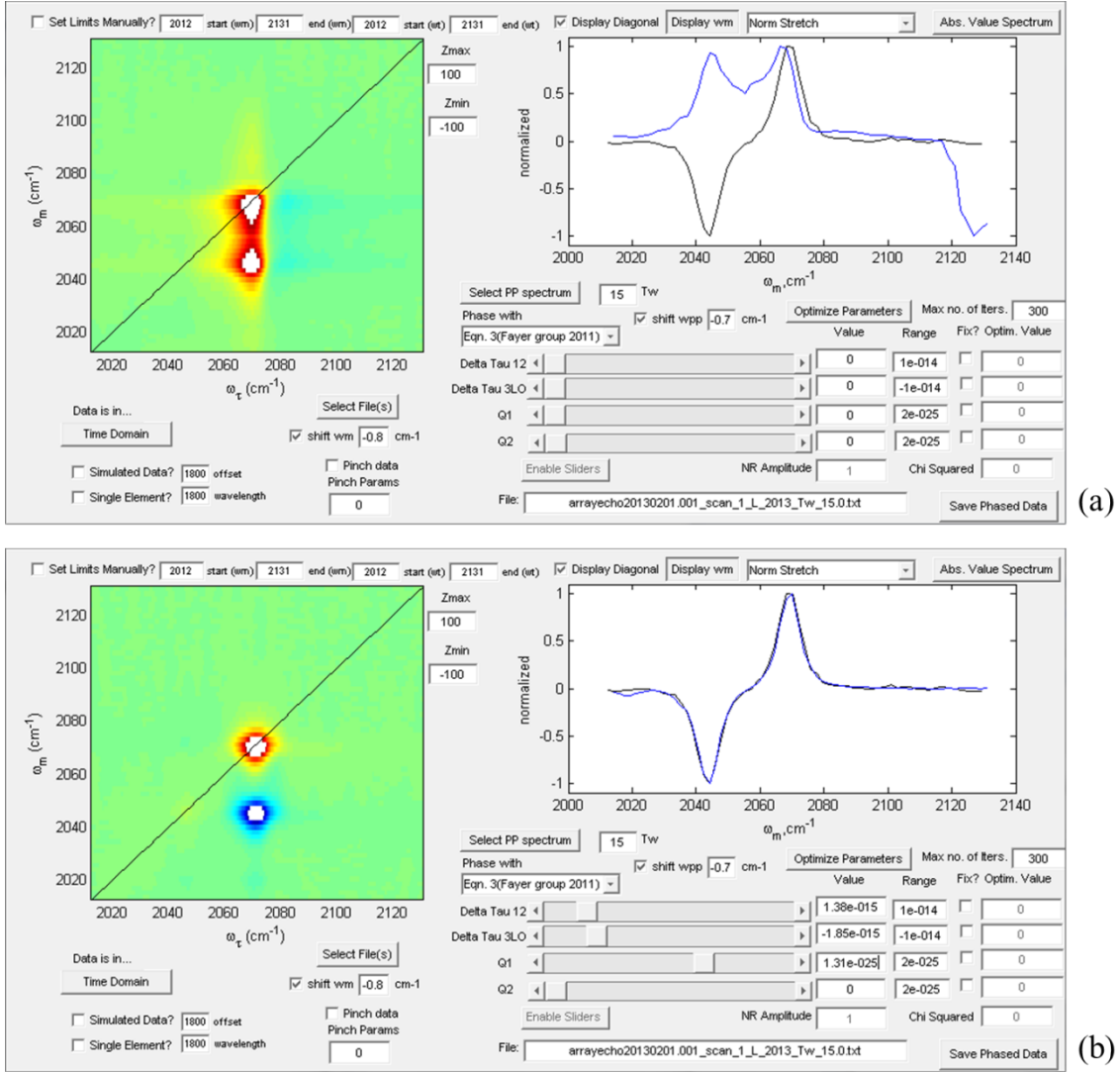
Figure 2.6: Phase correction program built by the author showing the purely absorptive 2D-IR spectrum for VC-I$_2$ in d_6-benzene at $T_w = 15$ ps before (a) and after (b) phase corrections have been applied. The pump-probe spectrum at the relevant time point is shown in the right axes plotted in black. The projection of the 2D-IR spectrum onto the ω_m axis is plotted in the same axes.

In chapter 3, the equations below[109] were used:

$$\phi_R = \omega_\tau \cdot \Delta\tau_{12} + \omega_m \cdot \Delta\tau_{3LO} + \omega_m^2 \cdot Q_1 + \omega_\tau\omega_m \cdot Q_2 \tag{2.20}$$

$$\phi_{NR} = -\omega_\tau \cdot \Delta\tau_{12} + \omega_m \cdot \Delta\tau_{3LO} + \omega_m^2 \cdot Q_1 + \omega_\tau\omega_m \cdot Q_2 \tag{2.21}$$

where $\Delta\tau_{12}$ is the correction for errors in the relative timing of beams 1 and 2 (thus negative in ϕ_{NR}), $\Delta\tau_{3LO}$ is the correction for errors in the relative timing of beam 3 and the LO, Q_1 is a correction for chirp due to propagation of the echo through the back window of the sample cell, and Q_2 is a correction for chirp due to the propagation of the echo through the sample itself. In chapters 5 and 6, the following more phenomenological equations were used:

$$\phi_R = \omega_\tau \cdot \Delta\tau_{12} + \omega_m \cdot \Delta\tau_{3LO} + \omega_m\delta\omega_m \cdot Q_1 + \omega_\tau\delta\omega_m \cdot Q_2 \qquad (2.22)$$

$$\phi_{NR} = -\omega_\tau \cdot \Delta\tau_{12} + \omega_m \cdot \Delta\tau_{3LO} + \omega_m\delta\omega_m \cdot Q_1 - \omega_\tau\delta\omega_m \cdot Q_2 \qquad (2.23)$$

where $\delta\omega_m = (\omega_m - \langle\omega_m\rangle)/(\omega_{max} - \omega_{min})$ where ω_{max} and ω_{min} are the maximum and minimum values for ω_m. In addition to chirp, the final terms here are thought to correct for errors in the actual vs. expected dispersion of the monochromator. For the samples studied in the remainder of this work, the value of Q_2 was very small and generally zero. These equations give fine control over the final shape of the spectrum, allowing for excellent phase correction.

There are two major constraints on the phasing process. The first and most useful is called variously the pump-probe projection theorem or the projection slice theorem.[111] As will be discussed further in section 2.3, the same four-wave mixing processes that give rise to the vibrational echo also produce the pump-probe signal. This signal, however, has a constant value of $\tau = t' = 0$ and thus is insensitive to phase errors during the coherence times (which are the only ones that matter for 2D-IR[93, 101]). The pump-probe spectrum, therefore, should be the same shape as the projection of the correctly phased 2D-IR spectrum onto the ω_m axis. By changing the various phasing parameters

until the projection lines up with the pump-probe, in principle one can retrieve the correct 2D-IR spectrum. Unfortunately, but not unexpectedly, the projection on the ω_m axis is not as sensitive to $\Delta\tau_{12}$, the parameter that has the least connection with that axis. As a constraint along the ω_τ axis, the absolute value spectrum was used.[112] The absolute value spectrum, being simply the sum of the magnitudes of the rephasing and nonrephasing spectra, also has no dependence on the phase errors. The peak values of the absolute value spectrum for each value of ω_m are found and compared with the peak values of the absolute value of the purely absorptive spectrum. The difference between them is then minimized. This method was developed for use with the O-H stretch of water, an enormous peak,[112] but has proved useful for the systems studied here.

Figure 2.6 shows the phasing process at the start (a) and end (b) for the same sample shown earlier (VC-I$_2$ in d_6-benzene, see Chapter 5) at $T_w = 15$ ps. The agreement between the pump-probe and the projection is typical of the quality of fitting achieved throughout the following work.
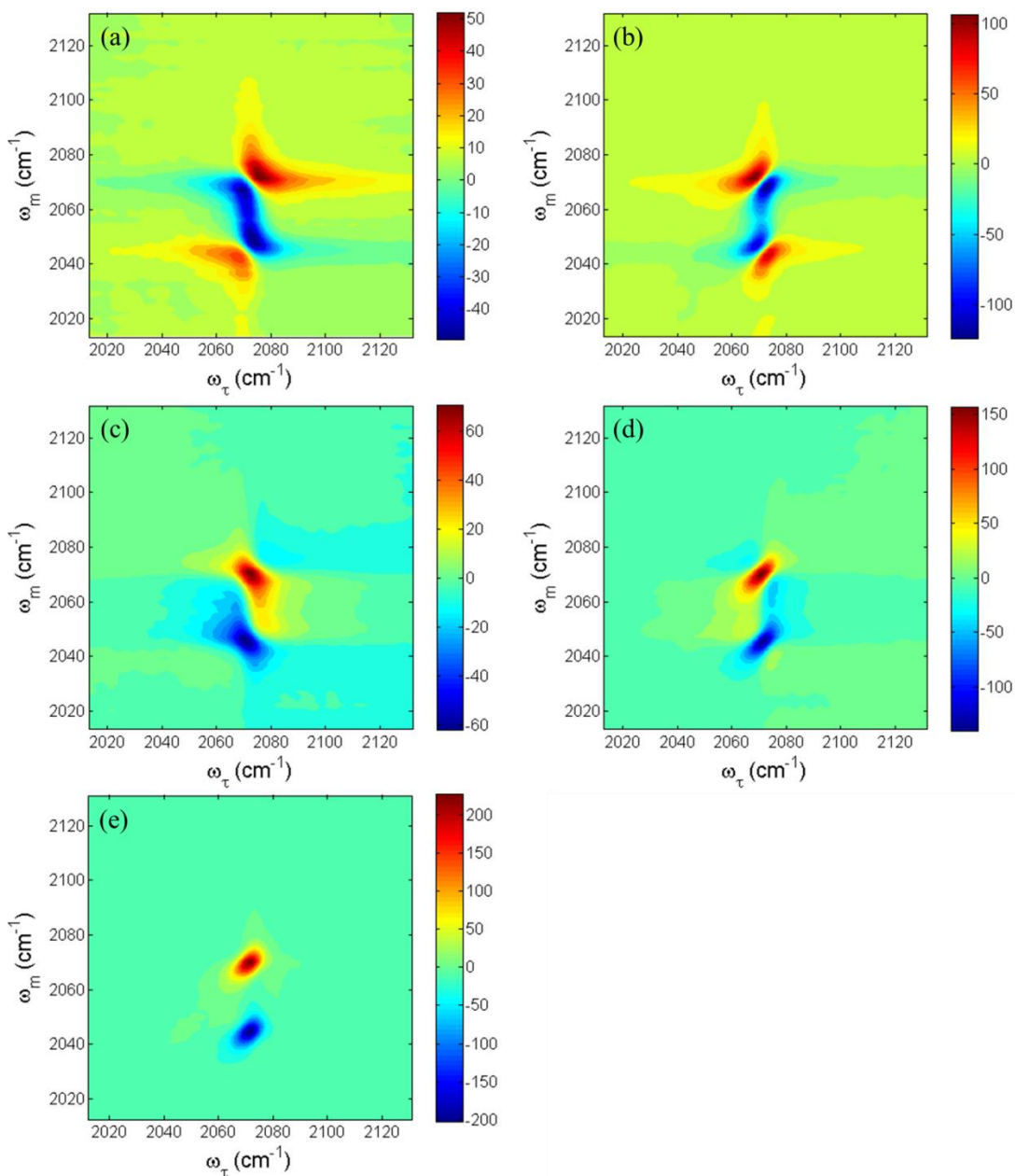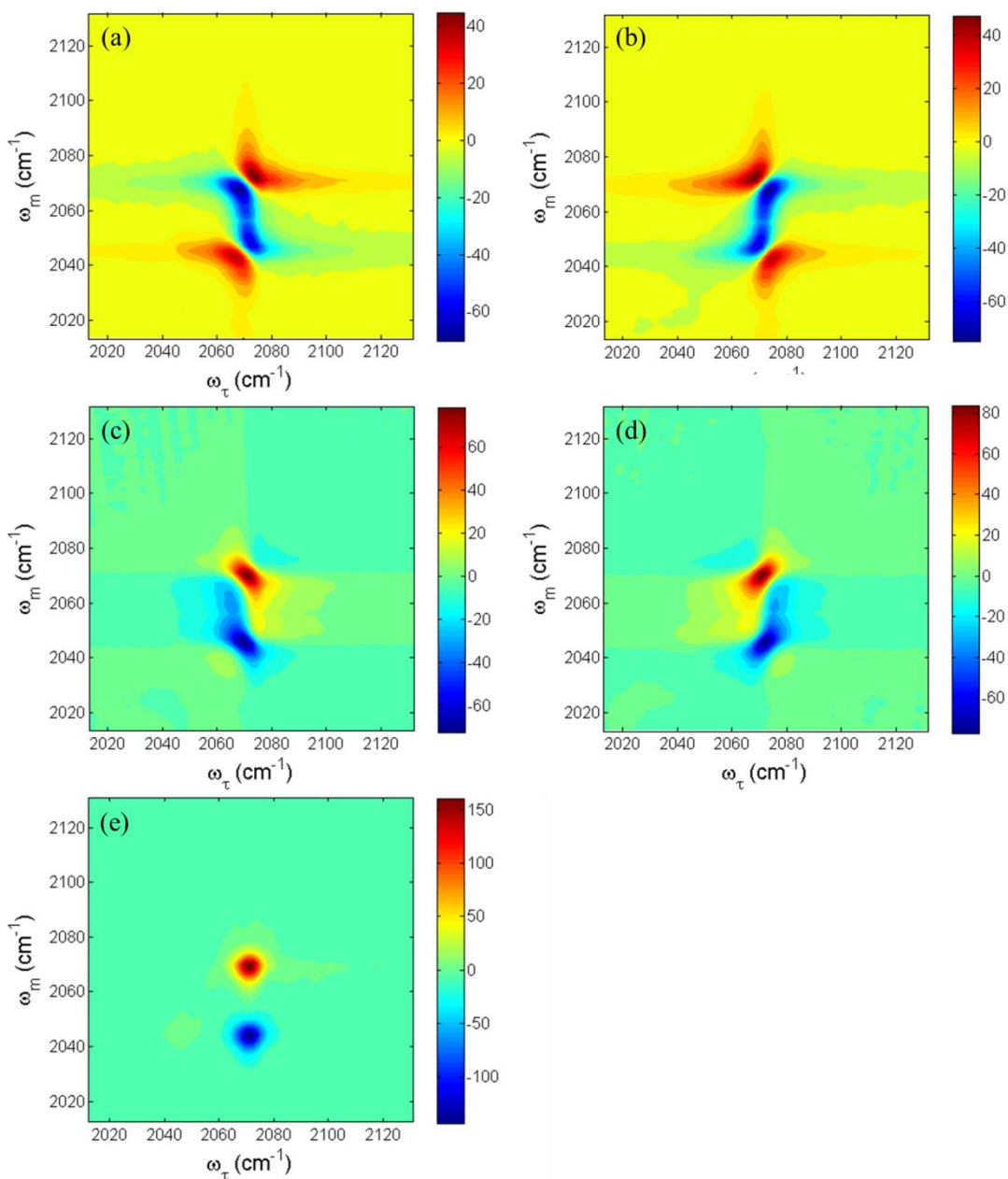
Figure 2.7: Imaginary (a, b) and real (c, d) parts of the rephasing (b, d) and nonrephasing (a, c) 2D-IR spectra and the purely absorptive spectrum (e) for VC-I$_2$ in d_6-benzene at $T_w = 15$ ps. Note the relative magnitudes of the color bars, especially as compared with Figure 2.5.

The specific laser setup used for the remainder of this work (see Figure 2.4) can be easily modified to perform IPP spectroscopy by simply replacing the first and second

beam splitters with mirrors and placing a CaF_2 wedge in position **P**. The path for beam 1 then becomes the pump path and the small amount of LO that reflects from the wedge is diverted into the formerly echo path and used as the probe beam (polarizers are also inserted just before and after the sample, as discussed in section 2.3). This works well, but gives rise to irregularities when the pump-probe projection theorem is employed due to the fact that the probe passes through the sample and the LO does not. The absorption of the sample as well as any solvent peaks in the area causes distortion of the pump-probe relative to the 2D-IR due to the division by the blocked signal (Equation 2.18). Since the spectrum of the probe is a better approximation of the light that is actually reaching the sample, the 2D-IR spectra were corrected rather than the pump-probe spectra. Since it is the denominator in the signal that needs to be changed, the correction was applied by multiplying the raw 2D-IR data by the FTIR transmission spectrum. This correction was developed and used for the work in Chapter 6, where the multiplicity of solvent peaks surrounding the mode of interest made it necessary.

Figure 2.7, (in analogy to Figure 2.5) shows the real and imaginary parts of the rephasing and nonrephasing (as well as the purely absorptive) spectra for the same sample at $T_w = 15$ps. Again, the rephasing spectra show elongation along the diagonal, while the nonrephasing ones show it along the antidiagonal. This is characteristic of rephasing and nonrephasing spectra. It is this fact that allows for a clear and visible distinction between the homogeneous and inhomogeneous dynamics. Recall that those oscillators that contribute to the rephasing spectrum are all those that have maintained their energy and frequency throughout the entire experimental time frame. Along the

diagonal of the purely absorptive spectrum, therefore, is the signal arising from these sources. Along the antidiagonal, however, is the nonrephasing contribution, which comes from only those oscillators that have maintained their phase relationship throughout the entire experimental time frame. It is no surprise, therefore, that in Figure 2.5 (the shorter T_w) the colorbar shows that the rephasing has about twice the signal of the nonrephasing in both the positive and negative directions. This produces a purely absorptive spectrum that is elongated along the diagonal; the rephasing spectrum dominates. Comparing this with Figure 2.7 (the longer T_w) it is clear that the shapes of the rephasing and nonrephasing spectra have not changed very much. Examining the relative amounts of signal in this instance, however, they are approximately equal. This yields a round shape in the purely absorptive spectrum. In interpreting 2D-IR spectra, then, to retrieve the response function, it is the shape of the peak that is the variable of interest.

Many specific methods exist for pulling the FFCF (which is usually the dynamic function desired) from a series of 2D-IR spectra. One is simply to relate the amplitude of the rephasing and nonrephasing spectra to one another.[27, 108] For laser systems that require phasing this method is not generally used, since the phase correction process is done with the purely absorptive spectrum. Since this spectrum has greater resolution, it is usually advantageous to use one of the following quantifying techniques that use the purely absorptive spectrum. Often the best method depends upon the size of the anharmonicity, since the 1-2 peak can interfere with the shape of the 0-1 peak. In instances where the anharmonicity is small, the angle of the node between the two peaks

is a frequently used method.[93, 113-114] At early T_ws the angle will be steep, decaying as the peaks grow more round. If the two peaks are well-separated, then the ellipticity can be calculated, the ratio of the difference between to the sum of the diagonal and antidiagonal width.[93, 113, 115] In the work that follows, there is neither a continuous overlap of 0-1 and 1-2 peaks, nor are they consistently isolated from one another. Thus a third method, called the center line slope (CLS) method, was used.

The concept behind the CLS is simple, yet more easily shown graphically, as in Figure 2.8 for simulated 2D-IR spectra. For a given 2D-IR spectrum, slices are taken parallel to the ω_m axis and the maximum at each slice is marked. These maxima are then fit to a line, the slope of which is the CLS. As the shape of the spectra change from elongated (Figure 2.8a) to round (Figure 2.8b), the CLS changes from ~1 to 0. It has been shown mathematically[116] that the CLS is proportional to the normalized FFCF (that is, $CLS(T_w) = C_{FFCF}(T_w)/C_{FFCF}(0)$) under the previous simplifying assumption that $g(t) = g_c(t) = g_{12}(t)$ and under the assumption of Gaussian dynamics invoked by the cumulant expansion. It has also been shown, however, that even in a situation where this is not true, the CLS method retrieves values for the FFCF parameters that are remarkably similar to the true FFCF.[116] Additionally under these circumstances, the cross-correlation function $\langle \delta\omega_{12}(t'')\delta\omega_{01}(0) \rangle$ can be found by application of the CLS method to the peak arising from the 1-2 transition.

The CLS method gives only the normalized FFCF. To obtain the full FFCF, including the true amplitudes and the dephasing time, the (normalized) linear lineshape is calculated according to Equation 2.3 and fit to the FTIR.[117] Initial guesses as to the

values of T_2 and the amplitude(s) of the FFCF are made using the full-width-at-half-maximum (FWHM) of the linear lineshape.[117] Since the homogeneous FWHM cannot be larger than the overall FWHM, these initial guesses are also lower limits.

When the CLS method was originally developed, the slices were taken parallel to the ω_τ axis (CLS:ω_τ) which also yields the normalized FFCF when the 0-1 peak and the 1-2 peak are well-separated,[117] but the interference of the 1-2 peak can cause distortion in situations where this is not the case. For the analysis in Chapter 3, the CLS:ω_τ method was used, while in Chapters 5 and 6 the CLS:ω_m method was used, followed by fitting of FTIR to obtain the full FFCF.
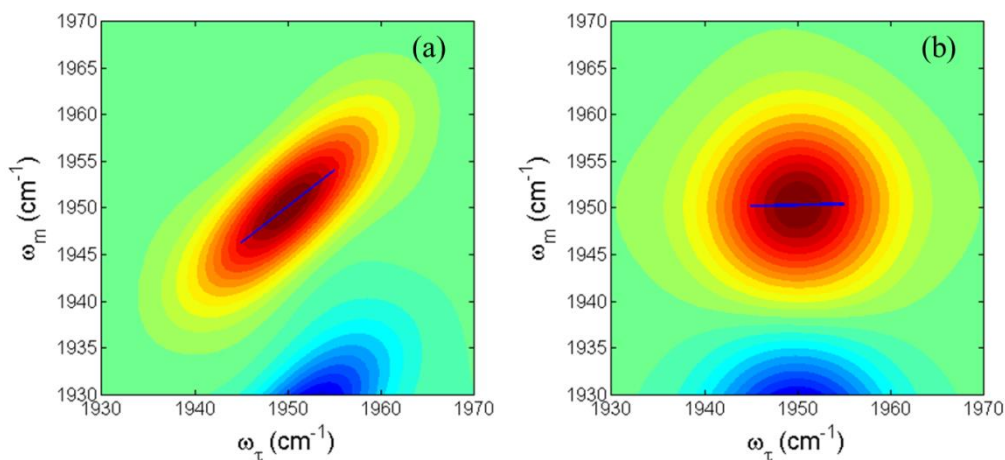
Figure 2.8: Simulated purely absorptive 2D-IR spectra at short (a) and long (b) values of T_w. The center line for slices taken parallel to ω_m is plotted above the positive peak.

2.3. Infrared Pump-Probe Spectroscopy (IPP)

Infrared, or vibrational, pump-probe spectroscopy can be thought of as a precursor to 2D-IR spectroscopy. All of the information obtained in IPP is contained in 2D-IR, but IPP is a considerably simpler experiment and (as discussed above) is not sensitive to the phase errors present in the more complex method.

Like all pump-probe spectroscopies, IPP involves two beams, a strong pump beam and a weak probe beam, separated by a time delay (called here T_w for reasons that will become obvious). The signal comes from four-wave mixing processes, as mentioned previously. The double-sided Feynman diagrams in Figure 2.2, therefore, also apply to the pump-probe signal. Unlike 2D-IR, however, the first two interactions both come from the pump beam. Since the signal is again emitted in the $\mp \vec{k}_1 \pm \vec{k}_2 + \vec{k}_3$ direction, and $\vec{k}_1 = \vec{k}_2$, the signal's phase-matched direction is the same direction as the probe. The IPP signal is thus self-heterodyning. (Signal in this direction can also come from three interactions with the probe;[101] by placing a chopper on the pump beam and using the same detection scheme as for 2D-IR, as was done for all the IPP experiments in this work, any signal arising from such processes is subtracted away.)

The first two interactions occur at the same time, $\tau = 0$, so for IPP $R_1 = R_4$, $R_2 = R_5$, and $R_3 = R_6$. R_7 and R_8 are once again neglected because they only give signal in the relevant direction when $T_w < 0$; they contribute primarily to the coherent artifact that occurs close to $T_w = 0$.[93] Though IPP spectra are taken at negative time delays, only time points not containing the artifact are used (to establish the experimental baseline) and the signal in these spectra is not analyzed.

The three remaining response pathways each belong to one of the familiar processes of light-matter interaction: R_1 illustrates the stimulated emission path, R_2 the ground state bleach, and R_3 the excited state absorption. Since $\tau = 0$ and $t' = 0$,

$$R_1 = R_4 \propto i\mu_{01}^4 \exp(-T_w/T_1^{(01)}) \tag{2.24}$$

$$R_2 = R_5 \propto i\mu_{01}^4 \exp(-T_w/T_1^{(01)}) \tag{2.25}$$

$$R_3 = R_6 \propto -2i\mu_{01}^4 \exp(-T_w/T_1^{(12)}) \tag{2.26}$$

where again the population relaxation times for the different transitions are distinguished. Note that the signal arising from the excited state absorption is opposite in sign. In many pump-probe spectroscopies, the bleach and stimulated emission are negative by convention. In this work, however, the excited state absorption will be taken to be negative, to remain consistent with the previous conventions of 2D-IR spectra.

The signal here is expected to decay with a time constant of the relevant vibrational lifetime. Figure 2.9 shows the full spectrum of a pump-probe decay (the same sample as previously: VC-I$_2$ in d_6-benzene) as a function of delay time. The negative signal occurs at a lower energy as expected: a manifestation of the anharmonic shift. In this sample (as in the others examined in this work) $T_1^{(12)}$ was found to have a value very similar to $T_1^{(01)}$.
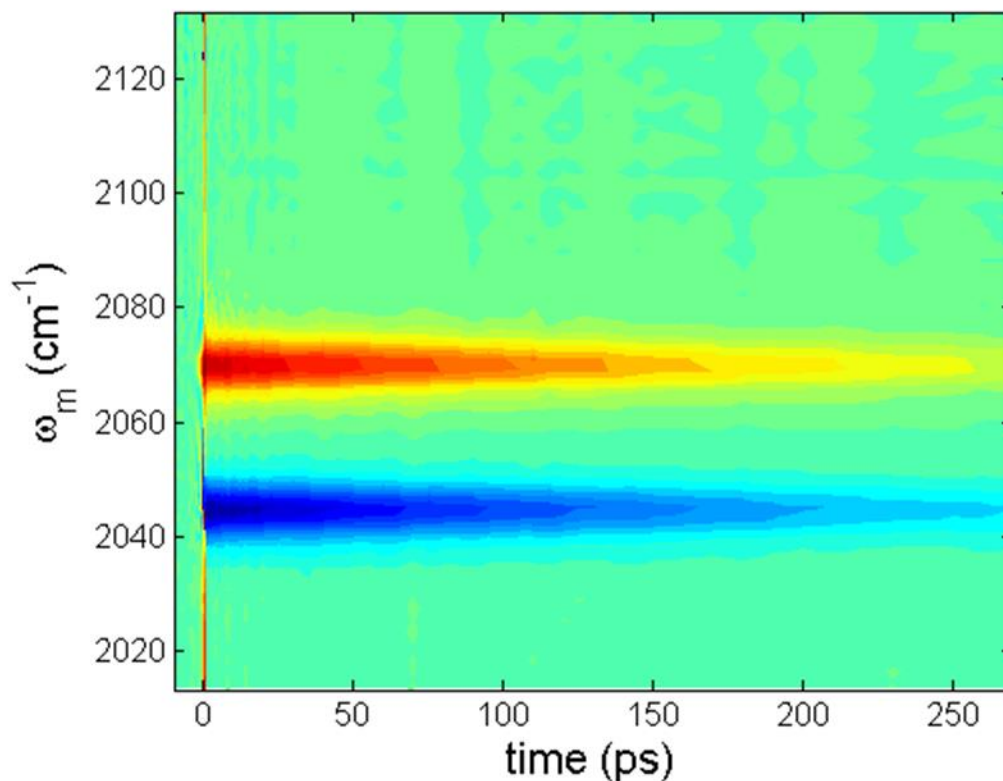
Figure 2.9: Vibrational pump-probe spectra plotted as a function of delay time T_w for VC-I$_2$ in d_6-benzene. The higher frequency peak (~2070) is positive and shows the contribution from stimulated emission and the ground state bleach; the lower frequency (~2045) peak is negative and shows the contribution from excited state absorption. The decay of each peak gives the vibrational lifetime T_1 for that transition.

In order to calculate T_1, the pump-probe spectrum is generally fit to a single exponential function. However, it is important to recognize that, in the solution phase, orientational relaxation may also contribute to this decay unless measures are taken to suppress it. One of the most common methods for doing this is magic angle polarization.[118] By setting the polarization of the pump and probe beams to be 54.7° relative to one another, the orientational changes (molecules rotating in and out of being

aligned usefully with the relevant electric field) cancel one another and only the population relaxation process remains.

The practical implementation of this procedure is less simple, however, than might appear. Though polarizers are relatively easy to come by, any other optics in the light path can have a deleterious effect on the polarization. Mirrors, for example, can induce slight phase shifts between the components (usually designated $S(\perp)$ and $P(\parallel)$) of a polarized beam. The grating and mirrors of a monochromator can also cause considerable difficulty, since the S and P components have different diffraction efficiencies from one another. It has been shown that by placing the two polarizers (at the correct angle) on the pump and probe beams immediately before the sample, and by placing an analyzing polarizer on the probe after the sample, the resulting signal has no orientational dependence, even when passed through a monochromator.[118]

Chapter 3: Solvation Dynamics of Vaska's Complex by 2D-IR Spectroscopy

Reproduced in part with permission from:

Brynna H. Jones, Christopher J. Huber, and Aaron M. Massari "Solvation Dynamics of Vaska's Complex by 2D-IR Spectroscopy," B. H. Jones, C. J. Huber, A. M. Massari; Journal of Physical Chemistry *C* **2011**, *115,* 24813

3.1. Chapter Summary

The solvation dynamics for Vaska's complex and its oxygenated adduct (VC and VC-O_2) were characterized using two-dimensional infrared (2D-IR) spectroscopy in d_6-benzene, chloroform, and DMF. The iridium-bound carbonyl was used as a probe of the static and dynamic chemical environments in each solvent system. The linear IR spectra of the complexes were consistent with CO frequency modulation though d-π^* backbonding interactions. The VC center frequencies were insensitive to the solvent type, but those of VC-O_2 were sensitive to the surrounding solvent, presumably due to the indirect influence of the dioxygen ligand on the carbonyl vibrational frequency. The vibrational lifetimes of both carbonyls were consistent with intramolecular relaxation though the metal-carbon linkage, and showed faster relaxation in the presence of solvent accepting modes. 2D-IR spectra were analyzed using the inverse centerline slope (CLS) as a representative of the frequency-frequency correlation function. Multiexponential fits to the CLS decays revealed solvation dynamics on several time scales, with the faster fluctuations being correlated with pure solvent properties and the slower dynamics (tens of ps) tentatively assigned to solvent-solute interactions. The measured dynamics were compared to previously determined oxidative addition rate constants in order to hypothesize the potential role of solvent shell fluctuations in the overall reaction rate.

3.2. Introduction

The mechanistic details of condensed-phase chemical reactions are not limited to the reactants and products, but must also include the surrounding solvent molecules.[119-122] These participants lower the average energies of the initial and final solute structures and stabilize (or destabilize) the transition state configurations during reaction events. Perhaps most importantly, the collective motions of the molecules in the proximal solvent shells allow the reactants to sample the energetic landscape that spans the reaction coordinate through random, thermally-driven fluctuations in their relative positions around the solute species. The time scales of these dynamics depend on the nature and strength of the solvent-solute and solvent-solvent interactions, and the time evolution of this solvation environment has been shown to be integral to some of the most important chemical processes, such as proton transport, electron transfer, and catalysis.[119, 121-125]

Scheme 3.1. Oxidative addition reaction of Vaska's complex (VC)
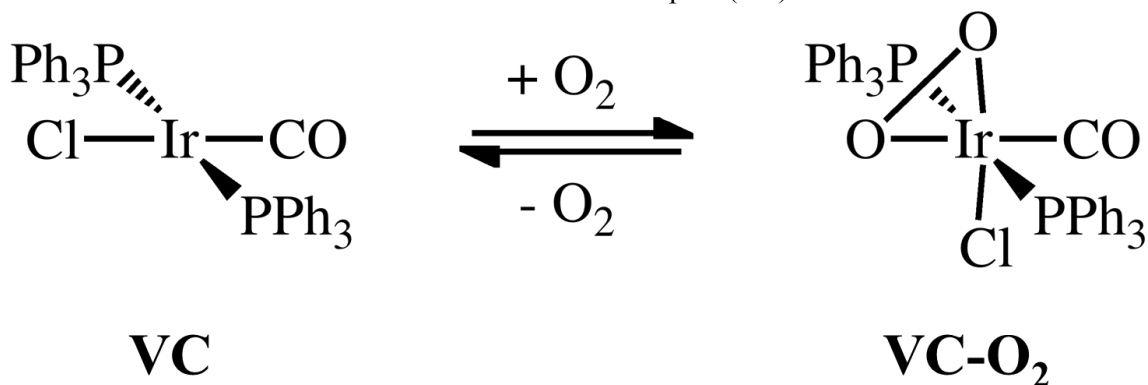
Despite their relevance to reaction dynamics, the fast restructuring events that occur in the solvent are often poorly characterized due, in large part, to the challenges associated with the measurements and the interpretation of the resulting data. Important insight into the microscopic processes in neat solvents has been gleaned from molecular dynamics (MD) simulations.[126-129] In turn, these simulations have been validated and refined by experimental observables from higher order spectroscopies such as optical Kerr effect,[130-136] fluorescence Stokes shift,[133, 137] RaPTORS,[138] and photon echo spectroscopies.[39, 122, 139-141] Two-dimensional IR (2D-IR) spectroscopy has emerged as a powerful experimental approach to characterizing the solvation dynamics in the vicinity of a solute molecule.[142-150] In a 2D-IR experiment, an IR-active chromophore or functional group is viewed as a reporter of the local solvation environment through the vibrational Stark effect, whereby the time dependent electrostatics of the surrounding molecules induce frequency shifts with the characteristic time scales of the solvation dynamics.[72, 151-152] By preparing a coherent collection of vibrations in the sample and allowing those ensembles to experience their surrounding environments for varying lengths of time before recovering the surviving oscillators in the form of a rephased vibrational echo signal, the associated molecular dynamics are obtained as vibrational dephasing and spectral diffusion from amidst the heavily inhomogeneously broadened environments that are common in the condensed phase. The result is a frequency-frequency correlation function (FFCF) that characterizes the time scales of solvation dynamics over the range of a few vibrational relaxation lifetimes. It must be recognized that the experimental observables that are obtained through 2D-IR spectroscopy (as well

as all other approaches) are seen through the lens of that technique and are inherently biased to report the dynamics to which the observable is most tightly coupled. As a cautionary note, it has been shown that the time correlation functions obtained for the same chemical systems are not always the same when observed by different techniques.[119] Nonetheless, the FFCFs obtained through 2D-IR methods have been shown to be representative of the dynamics that are predicted by MD simulations.[153-155]

In the interest of understanding of the role of solvation dynamics in the area of catalytic reactions, the current study applies 2D-IR spectroscopy to bis(triphenylphosphene) iridium(I) carbonyl chloride ($Ir(PPh_3)_2COCl$), also known as Vaska's complex (VC).[81-82, 156] Interest in this organometallic compound was piqued by its ability to reversibly add molecular oxygen, converting the square planar reactant to an octahedral adduct (see Scheme 3.1), in a manner reminiscent of oxygen transporting proteins in biological systems.[156] In fact, owing to the stability of the oxygenated complex, VC was one of the first systems that allowed detailed studies of the binding motifs for dioxygen to metal complexes.[157-158] The kinetics of this reaction were measured by several groups to be dependent on the solvent polarity, which led to the hypothesis of a polar transition state.[42-43, 69] It was later recognized that other substrates, such as hydrogen and methyliodide, could also form adducts with VC, which could in some cases be reductively eliminated through a photochemical mechanism.[42-43, 69, 159-162] Catalytic transformations of a number of important chemical reactions have been demonstrated by VC over the past four decades since its first report, and it has come to serve as a model system for studying catalytic reactions.[43, 69, 157, 163-168] Yet, aside from

one investigation of the vibrational lifetime of the iridium-bound CO ligand in a single solvent, to our knowledge no reports exist that delve into the ultrafast dynamics of VC.[66]

Here we present the linear IR and 2D-IR spectroscopic characterization of Vaska's complex and its oxygen adduct in three pure solvents with varying polarities and reaction rates for the oxidative addition of molecular oxygen. These experiments will be further augmented in Chapter 6 with studies in binary mixtures. IPP spectroscopy was used to determine the rates of vibrational energy relaxation in each solvent environment to aid in the interpretation of the 2D-IR results. The time scales of spectral diffusion are obtained from the 2D-IR data and are discussed in the context of previously reported reaction rate constants for oxygenation in order to postulate the potential role of solvation dynamics in this chemical reaction.

3.3. Experimental Materials and Methods

Bis(triphenylphosphene)iridium(I) carbonyl chloride (Vaska's complex, VC), was used as received from Sigma Aldrich (99.99% purity). Chloroform and N,N-dimethylformamide (DMF) were used as received from Mallinckrodt Chemicals and deuterated benzene (d_6-benzene) was used as received from Cambridge Isotope Laboratories. The deoxygenated samples were prepared and sealed in a nitrogen-purged glove bag using solvent that was nitrogen purged by sparging for $\geq$ 30 minutes. The oxygenated samples were allowed to equilibrate with air in the dark for 2-3 days. Linear and nonlinear IR spectroscopies were performed on VC samples that were almost exclusively in the deoxygenated (VC) or oxygenated (VC-O$_2$) forms. The IR

spectroscopic cell was prepared for most samples by sandwiching a small amount of VC

solution between two 3 mm thick CaF_2 windows with a 50 micron Teflon o-ring spacer.

For some $VC-O_2$ samples in DMF a 100 micron spacer was used due to the low solubility

of the complex in this solvent that required a longer pathlength.   The additional

pathlength had no noticeable effect on the extracted CLS values.   Typical sample

absorbances were between 0.07 and 0.14 at the peak of the CO symmetric stretching

vibrational mode, depending on the solubility of the complex in each solvent. Linear IR

absorbance spectra were collected on a Nicolet 6700 FTIR spectrometer (Thermo

Scientific) as an average of 16 scans with a resolution of 2 cm^{-1}.

3.3.1. 2D-IR Spectroscopy

The fundamentals of 2D-IR spectroscopy were discussed in Chapter 2. For the

particular experiments in this chapter, the laser system consisted of a regeneratively

amplified Ti:Sapph laser (Spectra-Physics, 800 nm, 40 fs pulse duration FWHM, 30 nm

bandwidth FWHM, 600 mW) pumping an optical parametric amplifier (OPA) (Spectra-

Physics) at a repetition rate of 1 kHz. The near IR signal and idler beams generated by a

β-barium borate (BBO, 3 mm thick) crystal in the OPA were difference frequency mixed

in a silver gallium sulfide crystal ($AgGaS_2$, 0.5 mm thick) to generate 3-4 μJ mid-IR

pulses. The mid-IR spectrum of the final output pulses was centered at the iridium-bound

CO symmetric stretching frequency in VC with approximately 200 cm^{-1} of bandwidth

(full width at half maximum, FWHM) and the pulses had a temporal duration of 90 fs

FWHM (~1.2 times the transform limit).

The mid-IR beam was split into three roughly equal intensity beams for use in the 2D-IR excitation sequence. Each of the pump beams transmitted through 7 mm of ZnSe on the path to the sample (5 mm beam splitters at 45°) and all other steering optics were reflective. An off-axis parabolic reflector crossed and focused the three p-polarized excitation pulses in the sample in the boxCARS geometry[107] with the third order signal (vibrational echo) generated in the phase-matched direction. The three pulses were temporally overlapped and their durations were characterized by optimizing the non-resonant third-order signal from a 50 μm thick carbon tetrachloride sample. After exiting the sample cell, the vibrational echo signals were spatially coaligned with a local oscillator reference pulse using an uncoated ZnSe window as a combining optic through which the echo was transmitted and the LO was partially reflected. After three partial reflections from the uncoated surfaces of ZnSe windows (assuming 7% reflectance), the LO power was approximately 0.3-0.5 nJ per pulse. The coaligned LO and signal beams were spectrally resolved in a 0.32 meter monochromator with a 75 line/mm grating and detected with a liquid N_2 cooled 64-element mercury cadmium telluride (MCT) linear array detector (Infrared Associates, Inc). The spectral resolution of the detection system was ~4 cm^{-1}. On a single detector pixel at the maximum of the vibrational echo spectrum, the LO was approximately 100 times larger than the signal. The vibrational echo and LO pulses were temporally aligned by offsetting the LO by a few ps and measuring the spectral interferogram with the signal pulse. The interferogram was inverse Fourier transformed to determine the precise time difference and the LO was moved to time zero with a delay stage with 2 fs (0.6 micron) accuracy (Newport XM-50). The entire optical

system was purged with dry air (-100 ºF dewpoint) during data collection. Over the range of powers tested, no power dependence was observed for the samples in this work.

In the 2D-IR technique, the third order signal (vibrational echo) is heterodyne detected with the spatially and temporally overlapped LO signal at the detector after being spectrally dispersed by a monochromator grating. The first frequency dimension was achieved by the Fourier transform performed optically by the diffraction grating.[70, 106, 169-170] For the second dimension, the time delay between pulses 1 and 2, τ, was scanned in increments of 5 fs as the time delay between pulses 2 and 3, T_w, was maintained at a fixed value. Beam 3 was chopped at 500 Hz and the chopped signal was divided by the laser spectrum to account for the laser power differences across the range of frequencies examined. This resulted in a temporal interferogram at each of the spectrally resolved detector pixels. The temporal interferograms were separated into two datasets with the pulse orderings such that pulse 1 arrived at the sample before pulse 2 (rephasing echo diagrams) and pulse 2 arrived before pulse 1 (nonrephasing echo diagrams). The Fourier transform of these datasets produced the rephasing and nonrephasing 2D-IR spectra that were added to produce the purely absorptive 2D-IR spectrum.[144] In order to account for systematic and random errors in the instrumentation, the data were then phase processed, as has been described in detail by others.[109, 116] The pump-probe projection theorem was used as a constraint during this procedure.[144] The resulting data plots were then analyzed using the centerline slope procedure developed by Kwak and coworkers in order to extract the FFCF from the 2D-IR data directly, as described in more detail below and in Chapter 2.[117]

3.3.2. IPP Spectroscopy

Using the laser system described above, approximately 0.1% of the full IR laser power was split from the parent beam and used as the weak probe beam while the remaining strong beam was used as the pump. The pump beam was temporally delayed from the probe and chopped at half of the repetition rate of the pulse train, allowing every other pump pulse to be blocked from the sample. The pump and probe beams were both p-polarized. The pump and probe beams were spatially overlapped in the sample volume (same sample cell as described above), and the transmitted probe beam was aligned through a 0.32 m monochromator. The probe was detected using the same 64-element MCT array as described above for the 2D-IR studies. The pump-probe signal was obtained as the difference between the probe transmission with and without the pump beam present, normalized by the laser spectrum of the probe, and recorded as a function of the time delay between the pump and probe pulses. With the utilized beam polarizations, the collected signals decayed as the result of orientational and population relaxation. Orientational relaxation in solution is typically completed within a few ps, while population relaxation of metal carbonyls in the solvents studied occurs on the tens of ps time scale. The data were fit from 1-2 ps to 100 ps to determine the population relaxation times reported in Table 3.1.

3.4. Results and Discussion

The linear spectra for the carbonyl stretch of VC (solid lines) and VC-O_2 (dashed lines) in d_6-benzene (black), chloroform (red), and DMF (blue) are shown in Figure 3.1.

The spectra have been baselined and normalized and the solvent spectra subtracted where solvent peaks would inhibit clarity of presentation. The peak centers (v_{CO}) and linewidths for each of the six samples are compiled in Table 3.1 for comparison. For VC, center frequencies of the CO mode are approximately 1964 cm^{-1} and are nearly unchanged by the nature of the solvent. The insensitivity of the mean CO frequencies demonstrates similar average solvation environments of VC despite significant changes in the solvent polarity. This is somewhat surprising since VC is square planar and has the potential to accept solvent ligands above and below the molecular plane. It must therefore be true that either there is minimal coordination of these solvents to the iridium or that these interactions are not reflected in the v_{CO}.

The carbonyl vibrations on the VC-O$_2$ exhibit a blue-shift upon binding of molecular oxygen and the conversion from a square planar to an octahedral configuration (see Scheme 3.1). The oxidative addition of O$_2$ decreases back-bonding of metal d-orbital electrons into the CO π^* orbital.[171-172] This weakens the iridium-carbon bond to the CO ligand resulting in a higher frequency CO vibration. In contrast to VC, the v_{CO} values for VC-O$_2$ are noticeably sensitive to the solvent identity, experiencing a shift of more than 10 cm^{-1} over the three solvents studied here. The frequency shifts are not well correlated with the solvent polarity indices (Table 3.1). Vibrational solvatochromism is the result of changes in the local electrostatic environment around the vibrational oscillator that induce shifts in the vibrational transition energies.[173-175] The interactions can be parameterized by describing the nucleophilicity and electrophilicity of the solvent species, and are not always well correlated with empirical polarity indices such as those

developed by Reichardt for solvatochromic dyes.[13, 84] Pensack and coworkers showed that organic carbonyl vibrational frequencies were more accurately described by the acceptor number (AN) or Lewis acidity metrics of Gutmann and Mayer.[174-175] We find that the frequency shifts of the VC-O_2 carbonyl mode track well with the Lewis acidity for benzene, chloroform, and DMF (shown in Table 3.1).[174, 176]

There are two peculiar observations surrounding the vibrational solvatochromism of VC. The first is that, contrary to previous organic carbonyl reports,[175, 177-178] the VC-O_2 carbonyl actually blue-shifts with increasing solvent Lewis acidity. The second is that the v_{CO} for VC-O_2 is solvent dependent while on VC it is not. These can both be rationalized by the indirect effect of the surrounding solvent on the triphenylphosphine, chloride, and dioxygen ligands and their influence on the ability of the metal to back-bond into the CO π^* orbital. As a starting point, electron withdrawal from the iridium by the O_2 ligand is reflected in the > 40 cm^{-1} blue-shift due to the decrease in back-bonding. The solvent insensitivity of the CO frequency in VC, which has the chloride and triphenylphosphine ligands but not O_2, further suggests that the extent of interaction of the dioxygen ligand with the solvent is the key factor in modifying the CO frequency. As the solvent Lewis acidity increases from d_6-benzene to DMF to chloroform, electron density is progressively shifted onto the O_2 from iridium, thereby decreasing the ability of the metal to back-bond to the CO and increasing its vibrational frequency.

Table 3.1: Vibrational parameters for VC, solvent properties, and oxidative addition of O_2 reaction rate constants.

parameters	d_6-benzene		chloroform		DMF	
	VC	VC-O_2	VC	VC-O_2	VC	VC-O_2
FTIR center (cm^{-1})	1964.7	2003.5	1964.7	2013.9	1963.5	2006.9
FTIR width (FWHM, cm^{-1})	16.7	17.2	24.9	21.4	18.9	22.5
vibrational lifetime, T_1 (ps)	40 ± 1	65 ± 3	41 ± 1	93 ± 5	28.2 ± 0.5	42 ± 1
polarity index[179-180]	2.7[a]		4.1		6.4	
acceptor number[176]	8.2[a]		23.1		16.0	
viscosity (cP at 25°C)[181]	0.604[a]		0.537		0.794	
rate constants (M^{-1} min^{-1})[42]	2.05[a]		3.00		7.85	

a. Values for benzene, not d_6-benzene.

The lineshapes in Figure 3.1 reflect changes in the distributions of vibrational frequencies in each of the solvents. In solution, these linewidths are influenced by the static spread of chemical environments (inhomogeneous broadening) as well as the time-dependent fluctuations of the vibrational frequencies and spectral diffusion that are driven by solvent dynamics. The spectra of the VC and VC-O_2 complexes in d_6-benzene are narrower than either complex in either of the other solvents (see Table 3.1). It is conceivable that the range of solvent-solute configurations in the nonpolar d_6-benzene is more homogeneous than chloroform or DMF in which there are more diverse palettes of nonbonding interactions. However, without prior knowledge of the dynamic and static contributions to the linewidths, it is not possible to determine whether the increased linewidths are the result of increases in solvation inhomogeneity or changes in the time scales of spectral diffusion. It is worth noting that the ~20 cm^{-1} FWHM Gaussian lineshapes imply that these ensembles are at least partially inhomogeneously broadened,

and it would be valuable to know the extent to which the solvation environments are statically or dynamically defined. Reviewing Table 3.1 shows that the trends in linewidths are not consistently correlated with either the solvent polarity indices or the Lewis acidities, which indicates that the relative contributions of these factors may not be the same in different solvents.
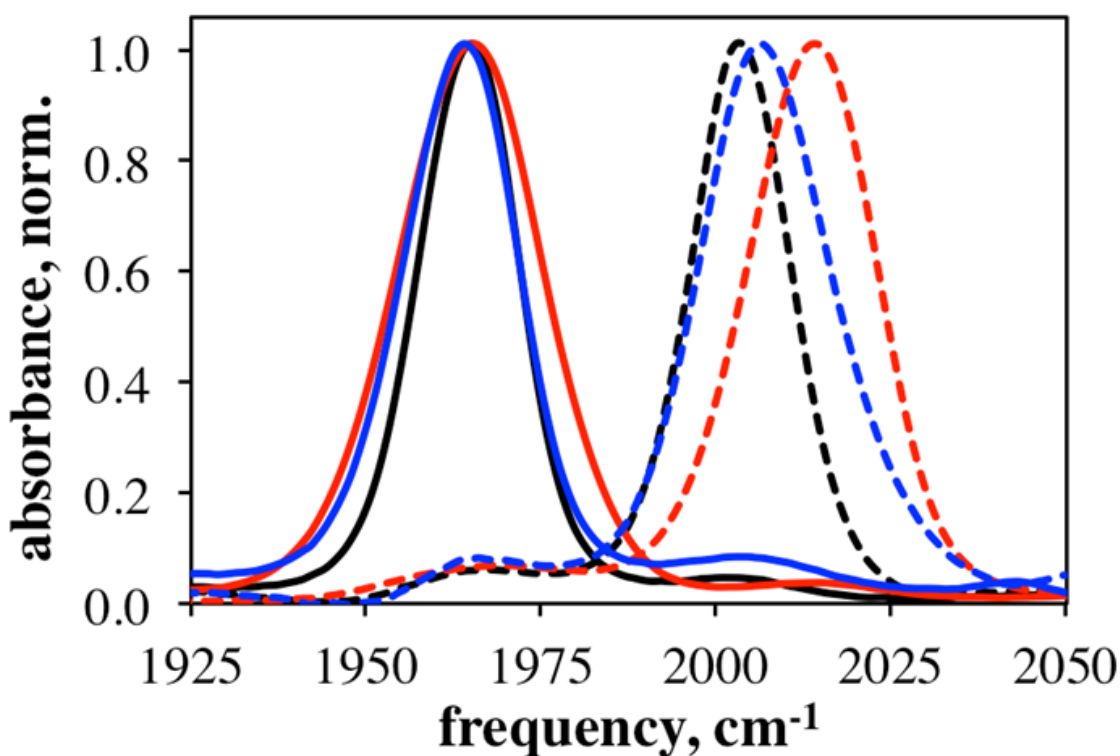
Figure 3.1: Baselined and normalized FTIR spectra of VC (solid lines) and VC-O$_2$ (dashed lines) dissolved in d_6-benzene (black), chloroform (red), and DMF (blue).

Also shown in Table 3.1 are the values for T_1, the vibrational relaxation time. These were calculated from a single exponential fit to the pump-probe decays at the maximum of the iridium-bound CO absorbance. To our knowledge, this is the first report

of the vibrational relaxation time of the oxygenated form of VC and of the complex in multiple solvents. Heilweil and coworkers examined VC in only chloroform along with several other metal carbonyl complexes in various solvents (including chloroform and benzene), and observed an increase in the T_1 with increasing v_{CO}.[66] This trend was confirmed and extended to a large library of metal carbonyl compounds by Dlott and coworkers.[182] The large increase in T_1 and corresponding blue-shifting of the v_{CO} upon oxygenation for VC agrees well with these previous observations.[66, 183] The increased relaxation time is explained by the fact that the lengthening of the iridium-carbon bond with addition of O_2 (due to changes in backbonding) causes a decrease in the vibrational frequency (v_{Ir-C}) of this mode (as well as the M-C-O bending mode), along with the observed increase in the v_{CO}. The increased separation of these modes, already well separated since typical values for metal-carbon vibrations are in the hundreds of wavenumbers,[66] increases the number of these lower frequency modes that must be excited for the relaxation of the carbonyl stretch.

While VC versus VC-O_2 T_1 trends are consistent with the mechanisms of relaxation described above, a comparison of v_{CO} to T_1 in Table 3.1 for either VC or VC-O_2 shows that the frequencies and relaxation times across the studied solvents are not. For example, VC in all three solvents has a very similar v_{CO}, but while the values for T_1 are identical within error in chloroform and d_6-benzene, the T_1 is faster by more than 10 ps in DMF. Additionally, VC-O_2 has a large range of values for T_1, with the fastest relaxation occurring again in DMF, the slowest in chloroform, and d_6-benzene as an intermediate. These trends are due to solvent vibrations in the same spectral region as the

carbonyl stretch that serve as energy accepting vibrational modes to decrease T_1 for the CO. In d_6-benzene, there is a weak absorbance at ~1995 cm^{-1}, likely due to residual non-deuterated benzene, which would clearly have a more marked effect on VC-O$_2$ than VC. In DMF, the entire region of interest from ~1950-2000 cm^{-1} is populated by weak solvent peaks, which have a large effect on the relaxation times of both VC and VC-O$_2$.[184] Thus the solute intramolecular relaxation pathways are modified by solvent-solute mechanisms that vary with solvent type.

In addition to their influence on the vibrational relaxation dynamics, the motions of the solvent also lead to time dependent fluctuations of the vibrational frequencies that result in the dephasing of a coherently driven collection of oscillators. These dephasing dynamics are also reflected in the linear lineshape, but cannot be directly extracted without prior knowledge of the extent of inhomogeneous broadening. 2D-IR spectroscopy has the ability to separate the homogeneous and inhomogeneous contributions to the FTIR lineshapes and to characterize the time scales of the solvation dynamics that are obscured beneath the linear lineshape. The full 2D-IR datasets for VC are collected in Figures 3.6, 3.8 and 3.10. Figure 3.2 shows representative 2D-IR spectra collected for VC in d_6-benzene (Figs 3.2a-c), chloroform (Figs 3.2d-f), and DMF (Figs. 3.2g-i), respectively. Three T_ws (0.5 ps, 10 ps, and 50 ps) are shown for each solvent, and the spectra at all measured T_ws are available in Figures 3.6-3.11. In each spectrum, the optical transform performed by the monochromator is displayed as the vertical axis and is called ω_m. The horizontal axis arises from the Fourier transform of the τ axis of the interferogram and is called ω_τ (see Sections 2.2 and 3.3.1 for further description). Each

spectrum contains a positive-going peak (red) and a negative-going peak (blue) at similar ω_τ values but shifted along the ω_m axis. Recall from Chapter 2 that the positive peaks result from vibrational oscillators that were coherently driven by the first pulse in the 2D-IR sequence at the $v = 0$ to $v = 1$ transition frequency (0-1), and then rephased by the third pulse at the 0-1 frequency. Likewise, the negative peaks arise from coherences that were initiated at the 0-1 transition but rephased at the $v = 1$ to $v = 2$ frequency (1-2). Hence, the 1-2 peaks are shifted along ω_m by the vibrational anharmonicity.

Within a given vibrational manifold (0-1 or 1-2), the motions of the surrounding solvation environment induce time dependent frequency shifts that accumulate phase errors among the vibrational modes during the coherence periods (between pulses 1 and 2 and after pulse 3). In other words, the vibrational oscillator frequencies become progressively decorrelated with their starting frequencies due to solvation dynamics. This leads to a finite width along the antidiagonal slice across the 2D-IR plot; a large antidiagonal width at small values of T_w is characteristic of fast homogeneous dynamics that allow the oscillators to sample many frequencies beneath the IR lineshape. At short T_ws, 2D-IR plots are generally elongated along the diagonal with their antidiagonal slices approaching the homogeneous linewidth. Increasing T_w affords additional opportunities for solvent and solute motions to decorrelate the frequencies of the vibrational oscillators, thereby sampling the solvation dynamics that occur on longer time scales. This can lead to spectral diffusion that is manifest in the 2D-IR spectrum as a broadening along the antidiagonal direction. The solvation dynamics that affect the 1-2 peak are typically similar to those influencing the 0-1 transitions, though there are examples in which this is

not the case.[108] In the discussion that follows, only the dynamics of the 0-1 peak were analyzed.
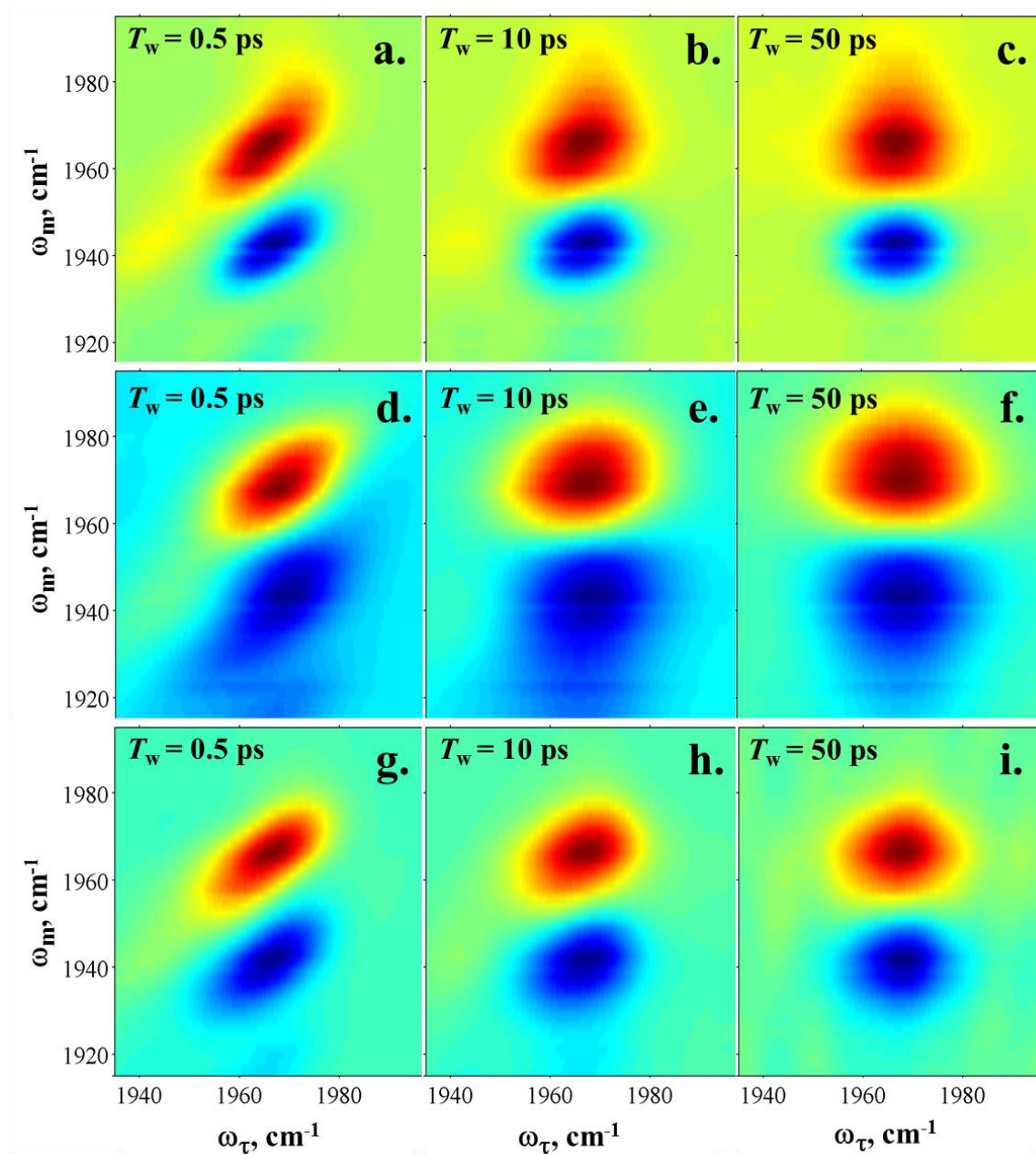
Figure 3.2: 2D-IR spectra of VC in d_6-benzene (a-c), chloroform (d-f), and DMF (g-i) collected at T_w = 0.5, 10, and 50 ps (first, second, and third columns, respectively).
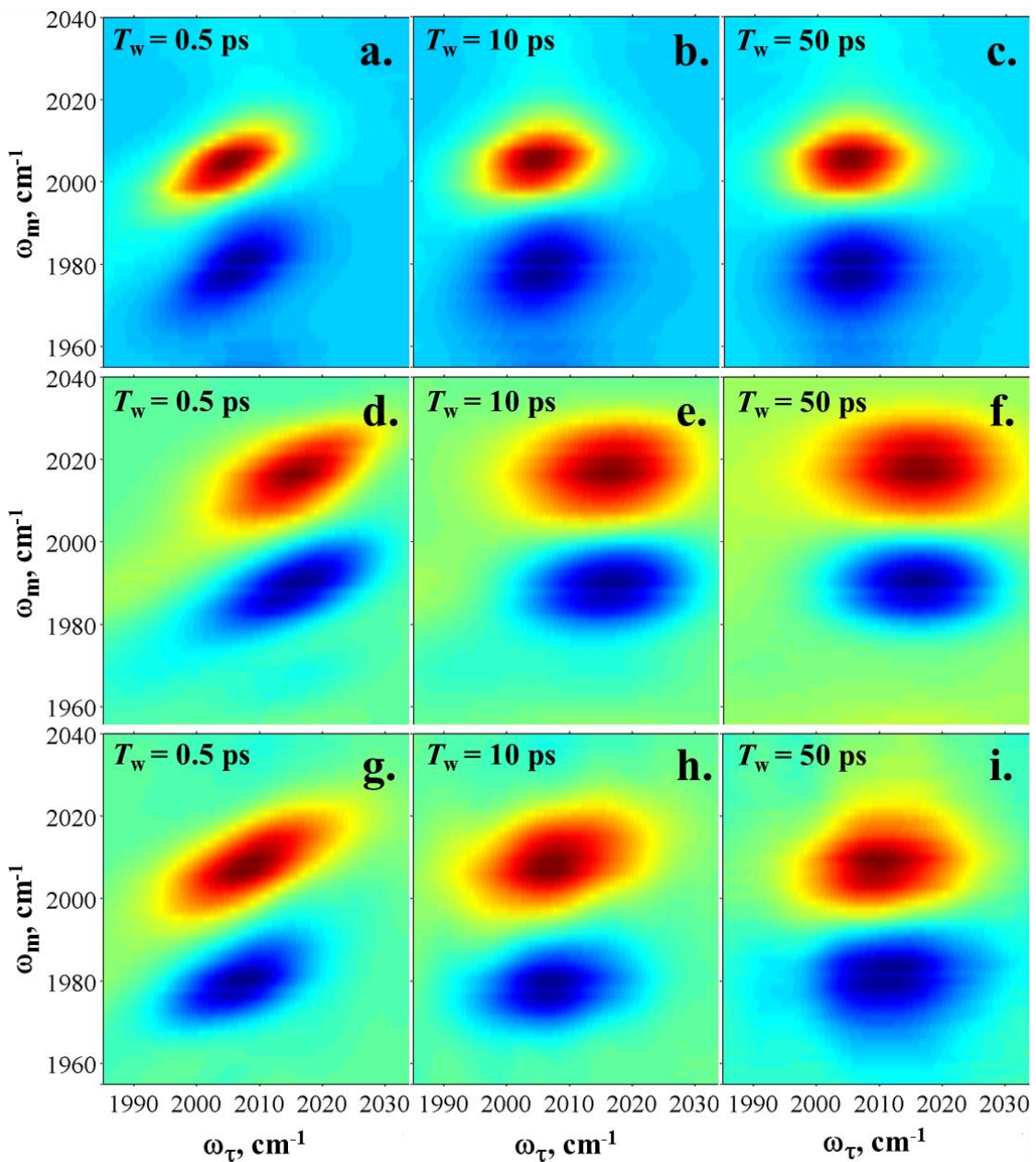
Figure 3.3: 2D-IR spectra of VC-O$_2$ in d_6-benzene (top row), chloroform (middle row), and DMF (bottom row) collected at $T_w = 0.5$, 10, and 50 ps (first, second, and third columns, respectively).

Figures 3.2a, 3.2d, and 3.2g demonstrate that the VC carbonyl peak exhibits significant elongation along the diagonal in all solvents at short T_ws, indicative of strong correlation between the frequencies. The antidiagonal slices, characteristic of the homogeneous lineshapes, are generally no more than 10 cm^{-1} wide (FWHM), which confirms the earlier assertion that the FTIR lineshapes were inhomogeneously broadened. It can also be said that the antidiagonal slice across the 0-1 peak center at the shortest T_ws has the widest lineshape in chloroform, similar to the FTIR linewidths, demonstrating that the increased linear linewidth in this solvent is at least partly a dynamical effect rather than an increase in the inhomogeneity. As T_w is increased to 10 ps (Figs. 3.2b, 3.2e, and 3.2h) and then to 50 ps (Figs. 3.2c, 3.2f, and 3.2i), more time is allowed for the solvent motions to influence the frequencies of the carbonyl vibrations and the 2D-IR peak shapes become round. Regardless of their starting excitation frequencies, the solvation dynamics enable the CO oscillators to sample nearly the entire FTIR lineshapes within 50-100 ps. Visual inspection of the spectra in Figure 3.2 shows that the dynamics vary with the solvent. In particular, at 50 ps there is still evidence of elongation along the diagonal for the carbonyl 0-1 transition in DMF (Fig. 3.2i), while in d_6-benzene and chloroform (Figs. 3.2c and 3.2f) the peaks appear entirely round. This indicates that in DMF there are solvation dynamics affecting the carbonyl frequencies that are slower than those present in either d_6-benzene or chloroform.
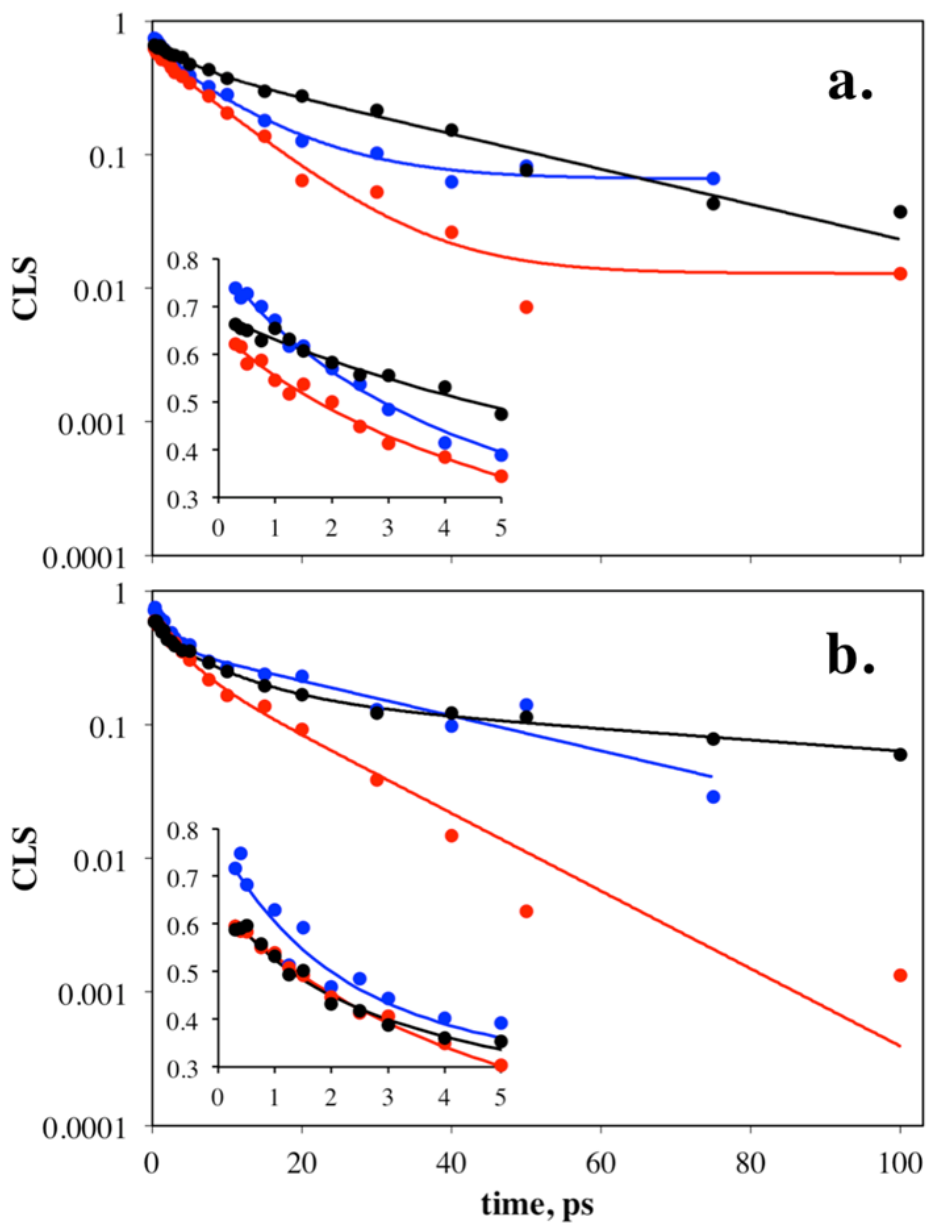
Figure 3.4: CLS as a function of T_w for a) VC and b) VC-O_2 in d_6-benzene (black), chloroform (red), and DMF (blue). Lines with matching colors represent multiexponential fits to the data shown as markers. Inset plots show zoom of early time data on a non-logarithmic scale.

Figure 3.3 similarly shows the 2D-IR spectra for VC-O_2 in d_6-benzene (Figs. 3.3a – 3.3c), chloroform (Figs. 3.3d – 3.3f) and DMF (Figs. 3.3g – 3.3i). Again, the full 2D-IR datasets for VC are shown in Figures 3.7, 3.9 and 3.11. Qualitatively, it is clear from

the degree of roundness of the 10 ps spectra in the three solvents that the dynamics in chloroform are generally faster than in either d_6-benzene or DMF. Also, it is worth noting that in a comparison between Figures 3.2 and 3.3, VC-O$_2$ is generally less elongated at the later T_ws, particularly in d_6-benzene and chloroform, indicating that faster dynamics are playing a dominant role in dephasing.

The evolution of the 2D-IR spectra in each solvent due to solvation dynamics can be characterized by the extent to which the peak shapes vary from diagonally elongated to round. The inverse center line slope (CLS) method described previously by Park and coworkers is a convenient approach to quantify this dynamical information.[117] The center line for a 2D-IR peak is found by taking slices of a given spectrum parallel to the ω_τ axis, calculating the peak value for each slice, then fitting those peak points to a line. The slope of this line is an indication of the extent to which the peak is elongated along the diagonal. At early values for T_w and in the limit that no spectral diffusion has occurred, the slope is expected to be close to unity. As T_w increases and the 2D-IR peak shape approaches its round limit, the CLS (the inverse of the center line slope) approaches zero. It has been shown that the CLS is proportional to the FFCF discussed above.[117] By examining how the CLS changes with T_w, we can gain insight into the amplitudes and time scales of the dynamics causing the decorrelation of the vibrational frequency.

The CLS decays (or the normalized FFCFs) with T_w for both VC and VC-O$_2$ in the three solvents are shown in Figure 3.4. None of the decays begins at 1, which indicates that there is significant homogenous broadening as well as solvent dynamics occurring on a time scale faster than we are able to resolve. These are likely to be of

similar origins to the fast rotational dynamics or intermolecular librational motions that have been identified by optical Kerr effect (OKE) measurements.[128, 131, 185-186] These solvent dynamics are completed by a few hundred fs in benzene and chloroform. Examining the initial heights for the CLS decays (see zoomed insets in Figures 3.4a and 3.4b), it is clear that for all of the solvents studied, the oxygenated form has decayed more than the deoxygenated by the first T_w (0.3 ps). This disparity between the two forms is most obvious in the case of d_6-benzene (black), which starts at 0.7 for VC but only 0.6 for VC-O$_2$. This indicates that these very fast solvent motions more strongly influence ν_{CO} on VC-O$_2$, and can be explained by the fact that the VC-O$_2$ carbonyl responds strongly to changes in and around the O$_2$ ligand, which acts as an antenna for the solvent dynamics and translates those solvent motions into frequency fluctuations in the iridium-bound CO through its effect on metal backbonding. Thus, these fast solvent motions have an additional mechanism by which they can eliminate the carbonyl frequency correlation for VC-O$_2$. Both forms of VC have the largest initial CLS in DMF (see insets in Figures 3.4a and 3.4b), the lowest in chloroform, and the intermediate in d_6-benzene (though these last two are very close for VC-O$_2$). These trends track the solvent viscosities illustrated in Table 3.1 supporting the notion that the dynamical information in this offset is related to the viscoelastic properties of the pure solvents.[27, 187-188]

Examining the inset plots in Figures 3.4a and 3.4b, five of the six complexes have very similar CLS decays over the first 5 ps. The outlier among these is VC in d_6-benzene, which is slower on this time scale. In order to quantify these time scales, the CLS decay for each complex in each solvent was fit with a multiexponential function that

is overlaid in Figure 3.4 as a solid line of matching color. The parameters for these functions along with the fit uncertainties are shown in Table 3.2. VC-O_2 in DMF and chloroform as well as VC in d_6-benzene were all fit with a double exponential. VC in chloroform and DMF were fit to a double exponential with a static offset (Δ_0), indicating that there were dynamics occurring on time scales much longer than those of our experiment. VC-O_2 in d_6-benzene required a triple exponential. The time constants have been classified into τ_1 (on the order of a few ps), τ_2 (on the order of tens of ps), and τ_3 (on the order of hundreds of ps). A comparison of the τ_1 values confirms that the five similar looking CLS decays in the insets of Figures 3.4a and 3.4b have time constants that range from 1.4 to 3.5 ps, while that of VC in d_6-benzene is roughly twice as long as their average. The VC in d_6-benzene also experiences the most significant change in τ_1 upon oxidative addition, which suggests a more severe change in the solvation shell dynamics on this time scale.

Identifying the microscopic origins of the dynamics measured in 2D-IR spectroscopy is challenging and is usually achieved through a connection with the observables calculated from a molecular dynamics simulation.[153-155] In the following discussion, we draw parallels between our measured CLS decays and previously reported dynamics measured by OKE and NMR spectroscopies to categorize some of our results. Table 3.3 compiles the results of several studies performed on neat benzene, chloroform, and DMF. Within error, the majority of the decorrelation dynamics contained in τ_1 for VC and VC-O_2 are identical to time scales extracted from previous studies where they were assigned primarily to rotational and reorientational motions of the pure solvent. A

notable exception is the longer time constant (~5 ps) measured in DMF that does not appear to have a corresponding term in the CLS decays for VC or VC-O$_2$. This underscores the fact that different techniques may in some cases be sensitive to different dynamical aspects, and in this case, the CO frequency flcutuations may be poorly coupled to the molecular source of these slower dynamics. It is also worth noting that the majority of the time constants found for benzene are not from the deuterated form, and these times would be expected to lengthen slightly for d_6-benzene.[189] Nonetheless, there is a strong correspondence between the τ_1 values measured by 2D-IR and the neat solvent librational dynamics measured by OKE spectroscopy.

Table 3.2: Multiexponential fit parameters to CLS decays of VC and VC-O$_2$ in multiple solvents.

CLS fit parameter	d_6-benzene		chloroform		DMF	
	VC	VC-O$_2$	VC	VC-O$_2$	VC	VC-O$_2$
Δ_1	0.20 ($\pm$0.05)[a]	0.18 ($\pm$0.05)	0.09 ($\pm$0.05)	0.31 ($\pm$0.06)	0.23 ($\pm$0.08)	0.39 ($\pm$0.05)
τ_1	5 ($\pm$2)	1.4 ($\pm$0.6)	2 ($\pm$1)	3.5 ($\pm$0.6)	2.1 ($\pm$0.8)	1.9 ($\pm$0.6)
Δ_2	0.48 ($\pm$0.05)	0.31 ($\pm$0.05)	0.55 ($\pm$0.06)	0.31 ($\pm$0.06)	0.49 ($\pm$0.09)	0.39 ($\pm$0.05)
τ_2	33 ($\pm$4)	9 ($\pm$3)	10 ($\pm$1)	15 ($\pm$2)	11 ($\pm$2)	33 ($\pm$8)
Δ_3	-	0.16 ($\pm$0.04)	-	-	-	-
τ_3	-	100 ($\pm$40)	-	-	-	-
Δ_0	-	-	0.013 ($\pm$0.009)	-	0.06 ($\pm$0.01)	-

a. Numbers in parentheses represent standard errors of the fit.

Table 3.3: Comparison of short time scale dynamics to literature values (in ps) (290-303 K).

assignment (method)	d_6-benzene		chloroform		DMF	
	VC-O$_2$	VC	VC-O$_2$	VC	VC-O$_2$	VC
τ_1 (this work)	1.4 ± 0.6	5 ± 2	3.5 ± 0.6	2 ± 1	1.9 ± 0.6	2.1 ± 0.8
reorientation (OKE)[186]	0.98, 3.14, 3.19[a]		3.28, 1.2, 1.85			
rotation (NMR)[96]	1.17		1.62 (d)			
reorientation (RIKES)[32]	0.86, 2.84[a]		2.81, 1.07		1.53, 5.06	
intermolecular nuclear response (OKE)[185]			2.94			
vibrational response[185]			1.38, 1.11, 1.48			
reorientation (OKE)[130]					1.3, 6.22	
reorientation (RIKES)[189]					0.82, 4.72	
reorientation (MD)[190]	1.2, 1.5, 2.8, 4.5[a]					

a. Values for benzene, not d_6-benzene.

Although the CLS decays of VC-O$_2$ begin lower than VC in all three solvents (as mentioned above), at later T_ws the VCs become more decorrelated. This is shown more clearly in Figure 3.5 in which the fitted multiexponential functions are overlaid for VC and VC-O$_2$ in each solvent separately. The point at which the crossover occurs and the CLS for VC (solid line) drops below VC-O$_2$ (dashed line) is indicated with a vertical dashed line at 50, 18, and 7 ps in d_6-benzene, chloroform, and DMF, respectively. While the unresolved fast dynamics before the first T_w have more of an impact on VC-O$_2$, the

spectral diffusion in the first tens of ps more strongly affects the VC carbonyl, allowing it to become more decorrelated. This is borne out in the fits to the CLS decays in Table 3.2, which show that the Δ_2 values are always larger for VC than for VC-O$_2$. Figure 3.5 shows that the length of time required for the crossover is not correlated with solvent viscosity, which suggests that the molecular origins of these dynamics have more to do with the strength of solvent-solute interactions than the pure solvent-solvent interactions of τ_1. If these motions do arise from such interactions, this could explain the trend of Δ_2 mentioned above since the square planar geometry of VC is sterically more open to these kinds of interactions than VC-O$_2$.

On longer time scales, the dynamics contained in the FFCF (through the CLS decay) can still, in some cases, be related to the viscoelastic properties of the pure solvents. For example, the CLSs for VC and VC-O$_2$ in chloroform have decayed below those of the other solvents by five ps and remain the most dephased out to longer T_ws. It is clear that overall the dynamics in chloroform are the fastest for both VC and VC-O$_2$, which is consistent with it being the least viscous solvent. Other observations on the tens of ps time scale are less correlated with the pure solvent properties, such as the crossover time described above, and the fact that VC in d_6-benzene and DMF is more readily differentiated by solvent type than VC-O$_2$ (Figures 3.4a and 3.4b). In these cases, the dynamics are more likely to be intermolecular fluctuations that depend on the nature of the interactions between the solute and solvent. Similarly, Chang and coworkers showed that some of the dynamics reported by OKE spectroscopy could be modulated by the

presence of a solute,[130] and it has more recently been demonstrated with 2D-IR

spectroscopy that water reorientation in the vicinity of ions is significantly slowed.[191-192]
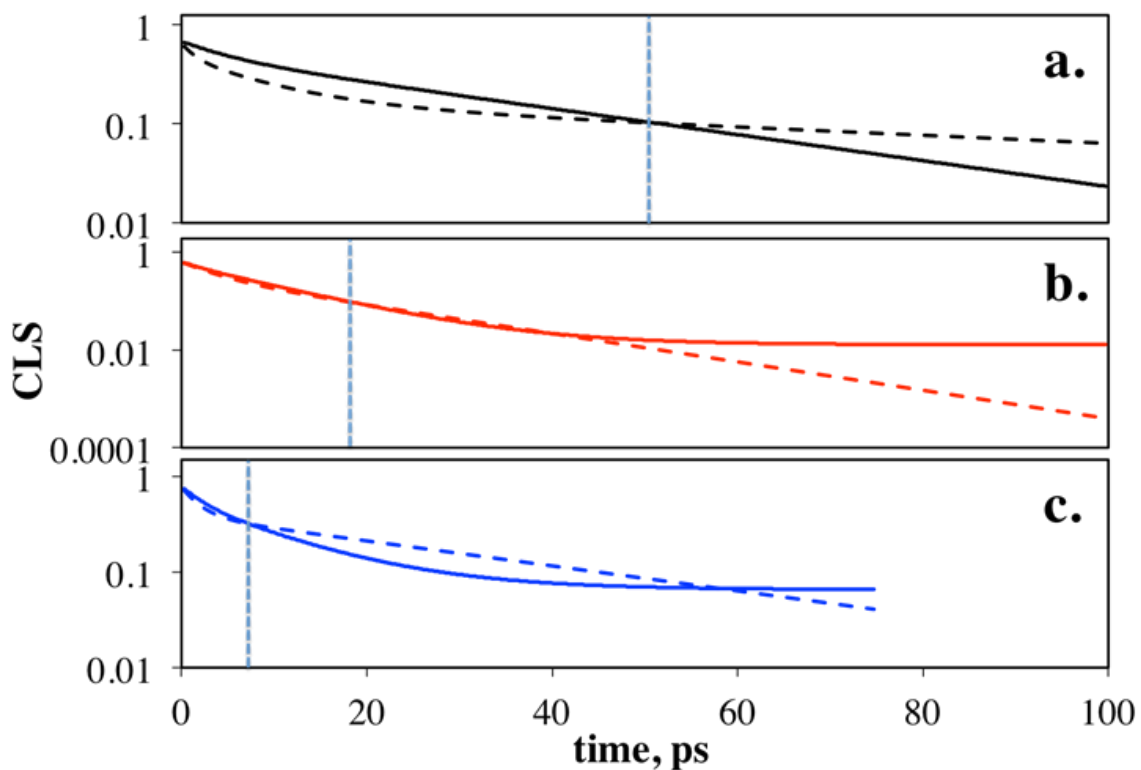
Figure 3.5: Comparison of multiexponential fits for VC (solid line) and VC-O_2 (dashed line) in a) d_6-benzene, b) chloroform, and c) DMF. Vertical dotted line in each frame indicates T_w at which VC decays below VC-O_2.

Even without precise knowledge of their origins, Table 3.2 shows that the τ_2

dynamics have a large impact on the loss of CO correlation for VC in all three solvents.

Regardless of solvent or VC form, the amplitudes (Δ_2) of these dynamics are equal to or

larger than the effect of any other time scale. However, there are differences in how the

contributions from τ_1 (few ps) and τ_2 (tens of ps) are balanced in each solvent.

Chloroform and DMF are similar, having their VC dynamics dominated by the τ_2

fluctuations (larger Δ_2s) and their VC-O$_2$ dynamics equally affected by the τ_1 and τ_2 dynamics. The CLS decays in d_6-benzene, on the other hand, are dominated by tens of ps dynamics for both VC and VC-O$_2$. Although the τ_1 and τ_2 time constants are not overly different in d_6-benzene compared to chloroform and DMF, their relative weights in the fit (Δ_1 and Δ_2), the necessity of a third exponential term (τ_3) in the CLS fits, and the greater change in the value of τ_1 with O$_2$ ligation make this solvent dynamically distinct from the other two. Notably, the reported rate of oxidative addition to VC in benzene is the smallest of the three solvents studied, which suggests that the solvation dynamics that we are resolving do have some influence on the overall reactivity of VC.

This connection between the chemical reactivity of VC and its ultrafast dynamics is a challenging one to draw from these experiments alone. The trends in reaction rates do not track the solvent viscosity for the three solvents studied, but the dynamics reported by the iridium-bound CO on the time scale of a few ps (τ_1), which we believe to reflect the pure solvent motions, are not drastically different. What is certainly different across these solvents is the relative amplitudes of the τ_1 and τ_2 types of dynamics. The change to more favorable solvents for oxidative addition of O$_2$ moves towards a system in which the VC-O$_2$ has notably more of the τ_1 time scale fluctuations than the deoxygenated form, to the point that these contributions are balanced with the tens of ps fluctuations. One interpretation of this is that the more reactive solvents have stronger solvent-solute interactions with the dioxygen ligand that favor the bound state (and possibly the transition state as well), which is manifested in our measurements as a larger proportion

of CO decorrelation through the indirect effect of CO frequency modulation by the metal-carbonyl backbonding interactions.

In addition to this change in the balance btween τ_1 and τ_2, the τ_2 time constants have distinct trends across the solvents studied. Moving from benzene to chloroform to DMF, the rate of O_2 addition increases, the τ_2 for VC decreases, and the τ_2 for VC-O_2 increases. Therefore, based on the dynamics that we are sensitive to in these 2D-IR experiments, the transition to more favorable solvation environments for this reaction is accompanied by a shift to a solvent system that has somewhat faster solvent-solute interactions with the deoxygenated complex and slower dynamics with the oxygenated form. We hypothesize that the slower dynamics indicate a stronger interaction between the solvent and the bound O_2 ligand.

3.5. Conclusions

In this work, the ultrafast solvation dynamics were measured for VC and VC-O_2 in three solvent systems. The solvents chosen have been reported to support a range of reactivities towards the oxidative addition of O_2 to the complex. The FTIR spectra showed that the center frequency of the iridium-bound carbonyl of VC was fairly insensitive to the solvent, but ligation of dioxygen made it noticeably sensitive, which was interpreted as an indirect effect of the solvent interactions with the O_2 ligand. The vibrational relaxation rates of the CO ligand were measured and found to be dependent on solvent type as well as oxidation state, with VC-O_2 always relaxing slower than VC in a given solvent. While this is consistent with trends in their carbonyl frequencies, there

were more subtle variations in T_1 that did not follow the anticipated pattern that were ascribed to energy relaxation into solvent modes.

2D-IR spectra were collected on all of the VC samples and were used to extract the fast homogeneous and spectral diffusion dynamics from beneath the inhomogeneous lineshapes in the FTIR spectra. Dynamics on the time scale of a few ps and faster were found to be consistent with the viscoelastic properties and molecular dynamics of the pure solvents. On these early time scales, the decorrelation of the ensembles of VC-O_2 carbonyls was found to be more effectively mediated by very fast (unresolved) solvent dynamics, whereas VC was more sensitive to the few to tens of ps dynamics. Fluctuations on the time scale of tens of ps generally dominated the decorrelation of the VC carbonyls, but it was observed that the solvents in which the oxidative addition reaction had the largest rate constant also had dynamics that reflected a more balanced contribution from the faster (few ps, pure solvent) and slower (tens of ps, solute-solvent influenced) carbonyl frequency fluctuations. In the presence of such solute-solvent interactions, the O_2 ligand on VC-O_2 may act as an antenna that makes the carbonyl frequency fluctutations more sensitive to the pure solvent dynamics, which explains the trend towards balanced contribution of the faster and slower time scale motions. The time constants of the slower dynamics became longer for VC-O_2 as the solvent became

more favorable for oxidative addition, suggesting that the better solvents for this reaction stabilize the oxygenated complex through stronger interactions with the dioxygen ligand.[a]
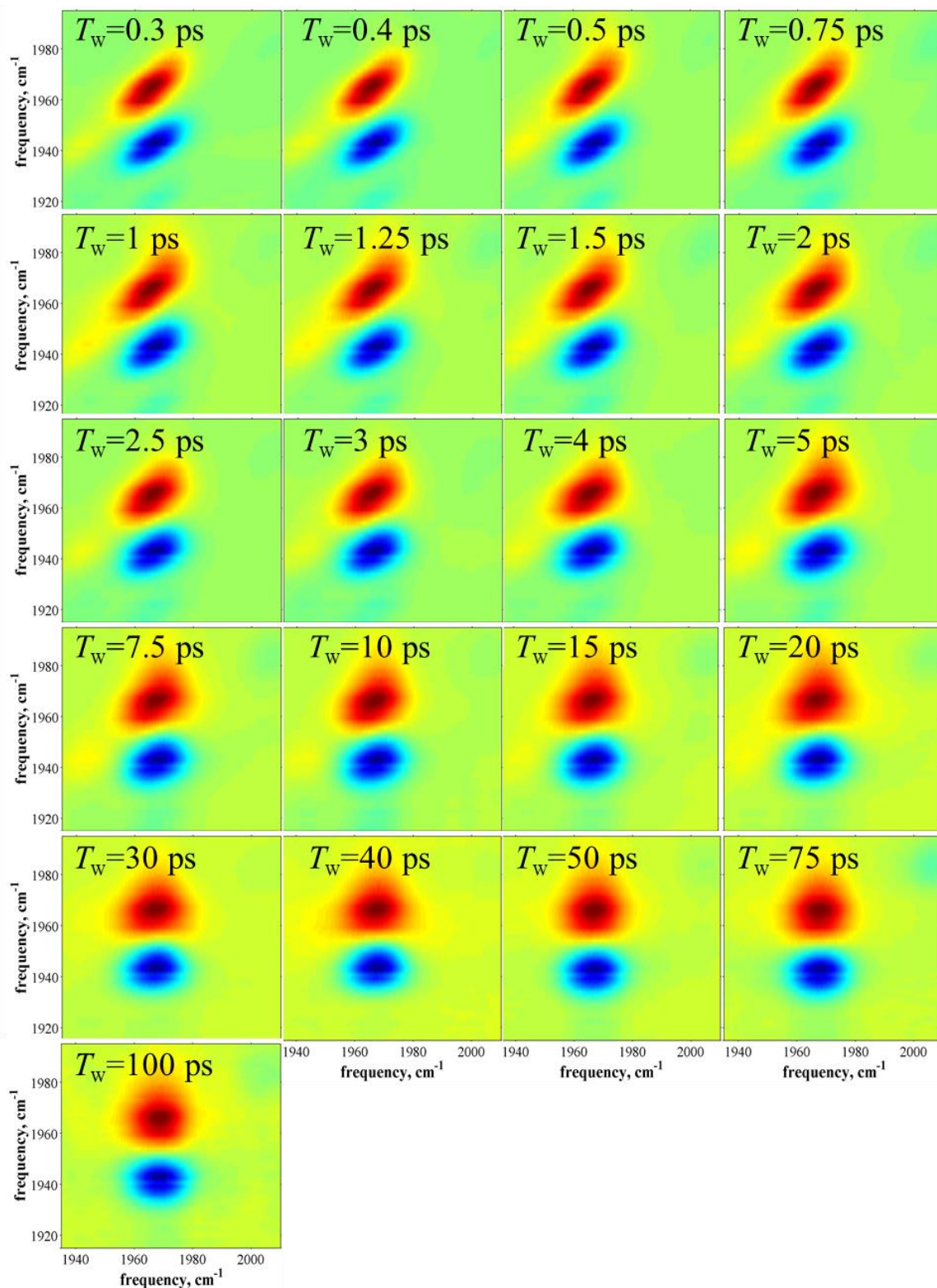
Figure 3.6. Full 2D-IR dataset for VC in d_6-benzene.
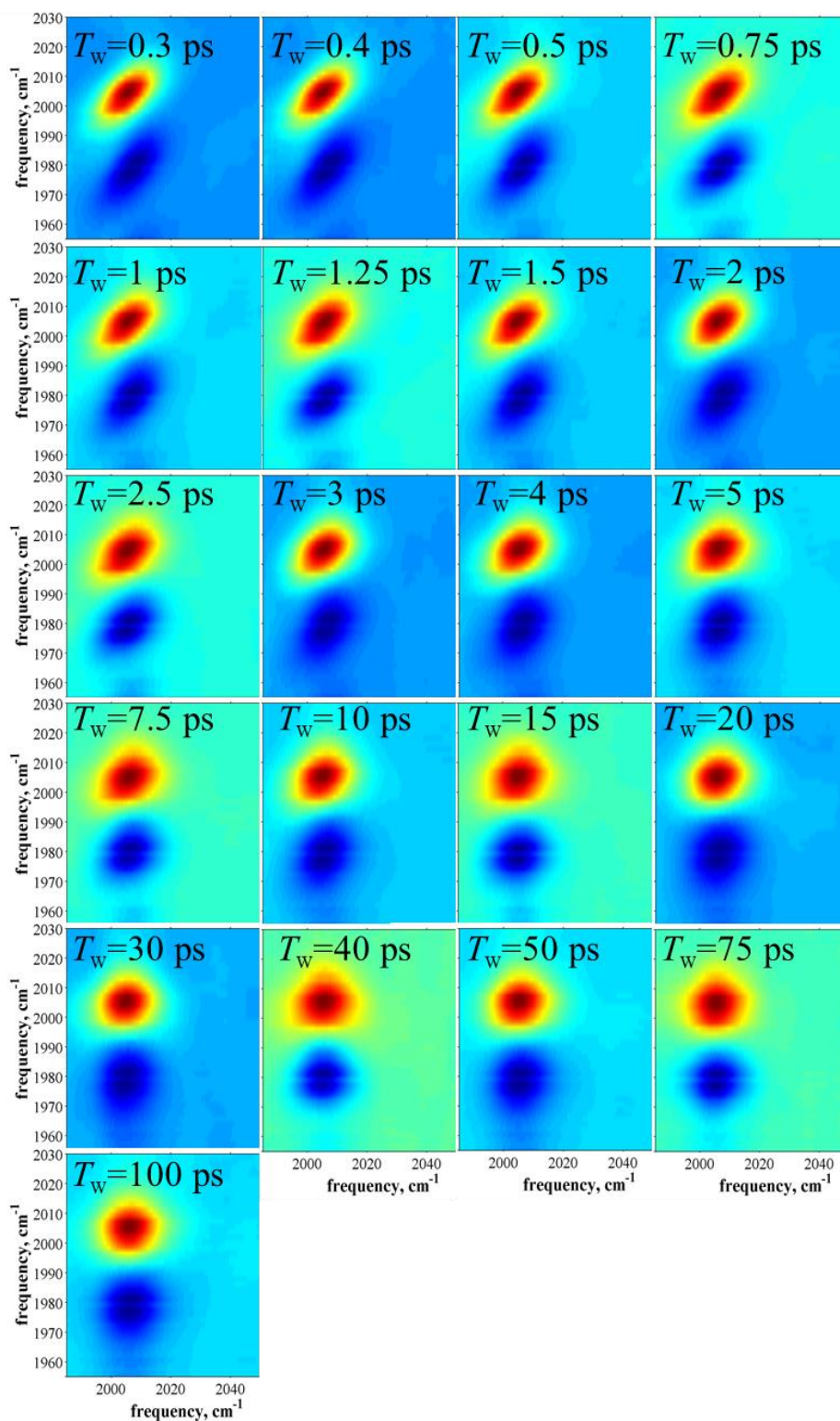
Figure 3.7. Full 2D-IR dataset for VC-O$_2$ in d_6-benzene.
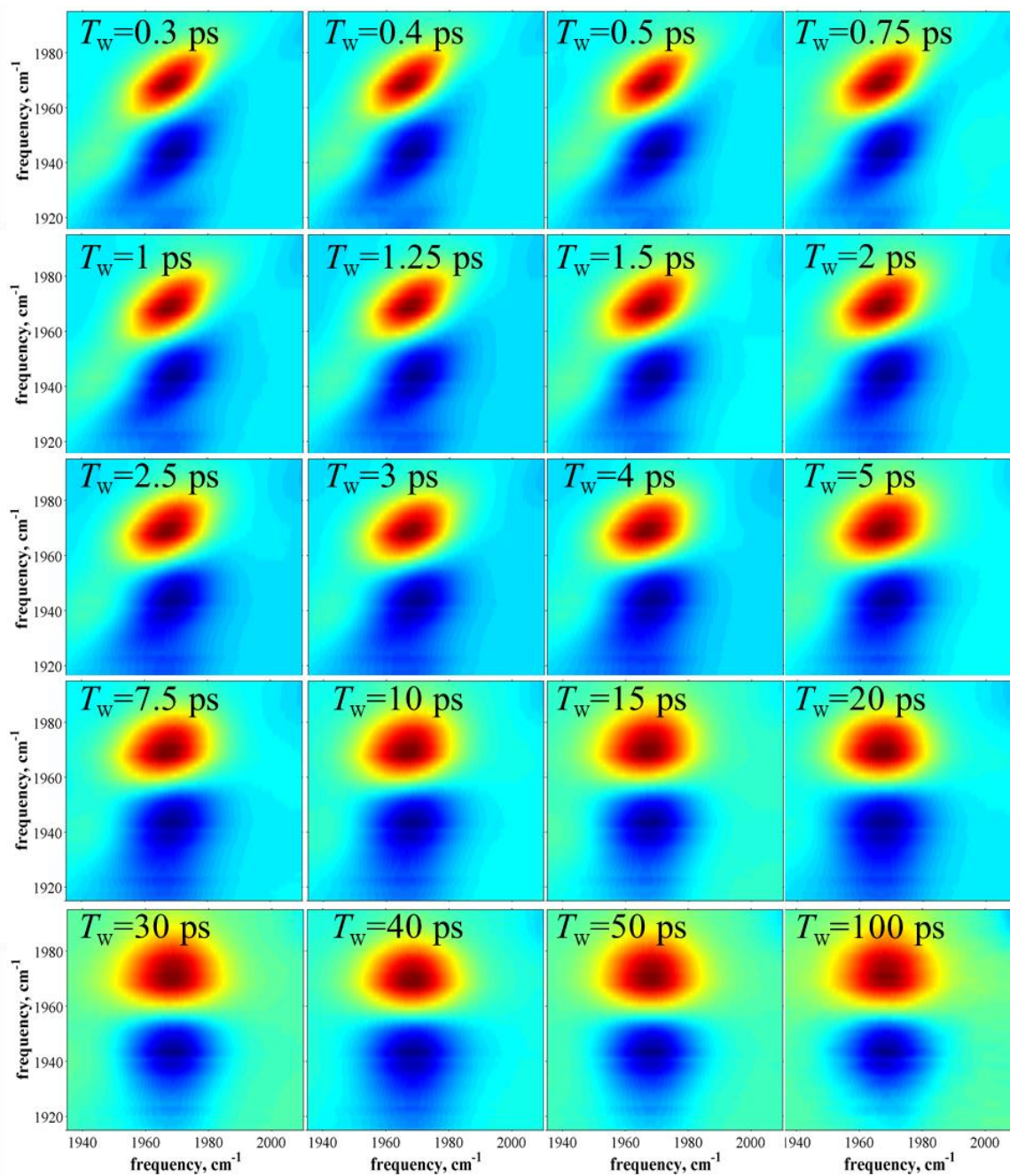
Figure 3.8. Full 2D-IR dataset for VC in chloroform.
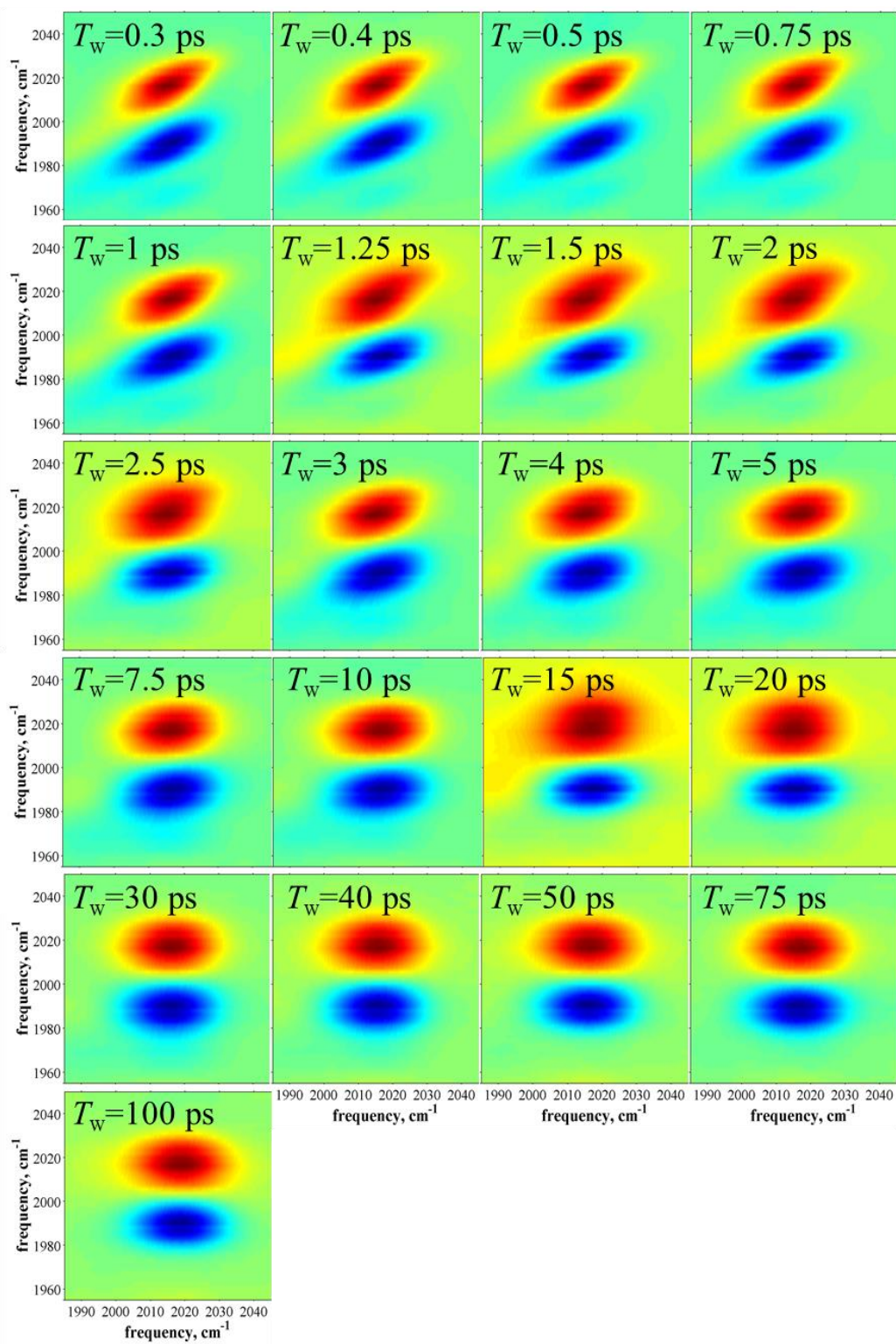
Figure 3.9. Full 2D-IR dataset for VC-O$_2$ in chloroform.
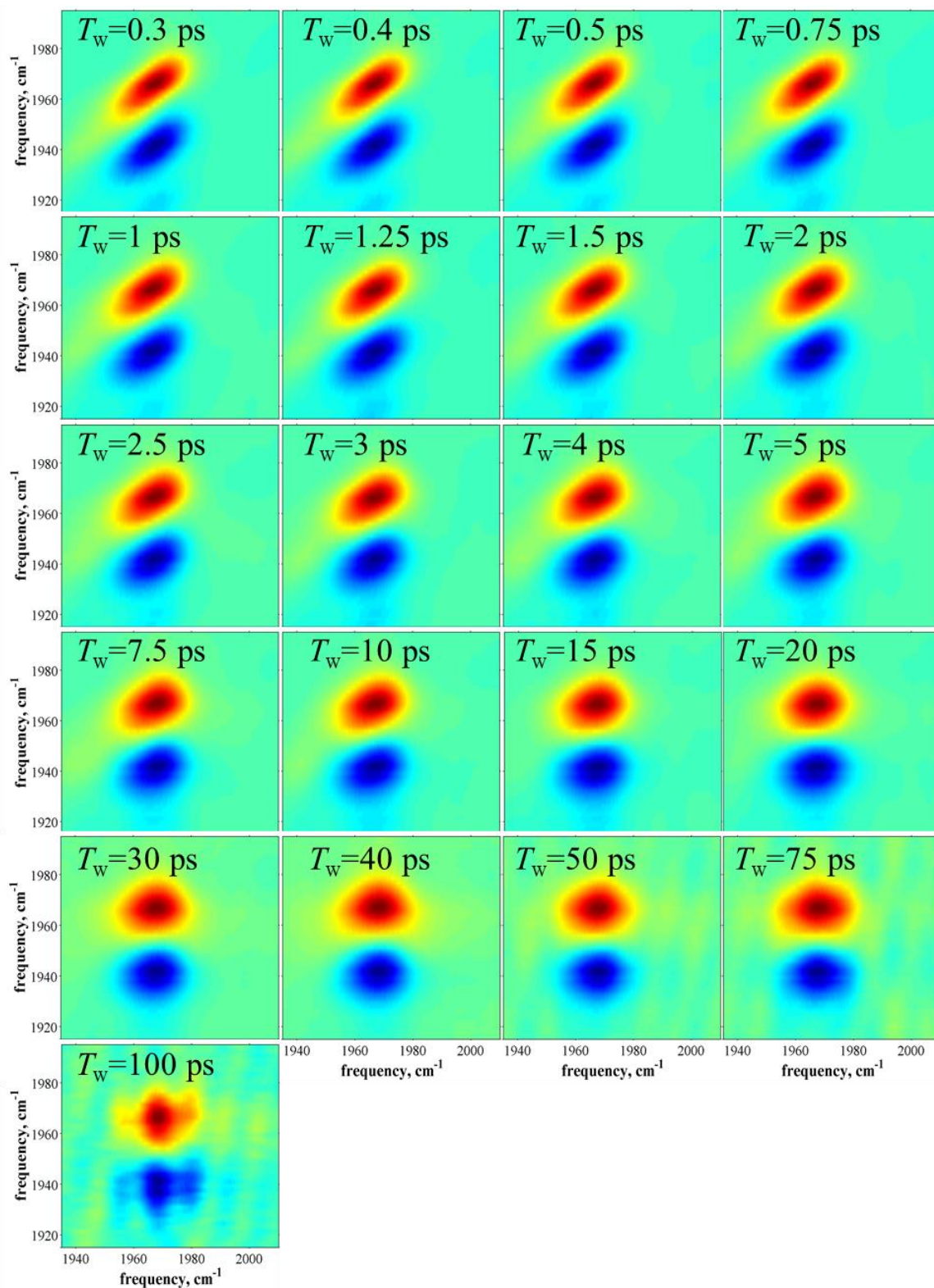
Figure 3.10. Full 2D-IR dataset for VC in DMF.
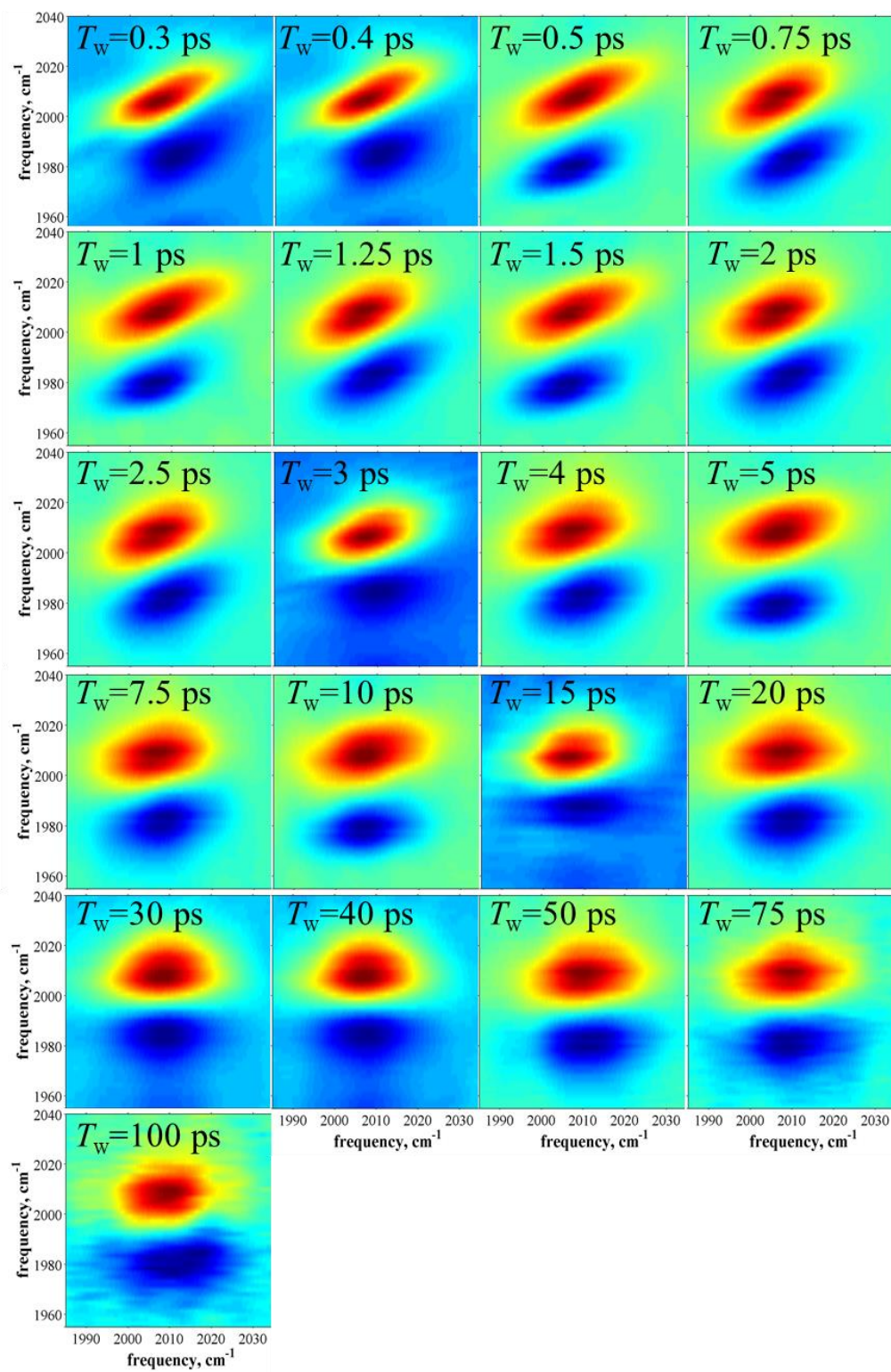
Figure 3.11. Full 2D-IR dataset for VC-O$_2$ in DMF.

Chapter 4: Solvent Mediated Vibrational Energy Relaxation From Vaska's Complex Adducts in Binary Solvent Mixtures

4.1. Chapter Summary

A vibrational pump-probe and FTIR study was performed on two different adducts of Vaska's complex in two different sets of binary solvent mixtures. The carbonyl vibrational mode on the oxygen adduct exhibits solvatochromic shifts of ~10 cm^{-1} in either benzyl alcohol or chloroform relative to d_6-benzene, whereas this vibration is nearly unchanged for the iodine adduct for the same three solvents. The width and center frequency of the carbonyl stretch for each adduct are compared to its vibrational lifetime in binary mixtures of d_6-benzene with either benzyl alcohol or chloroform. In neat solvents, the trends in linewidth, frequency, and vibrational lifetime are consistent for the two adducts, but complex relationships emerge when the trends in each property are compared as a function of mixed solvent composition. The ν_{CO} is more sensitive to the solvation environment around the *trans* ligand, while the linewidth and lifetime depend on the environment around the CO itself. The carbonyl frequency and width vary nonlinearly across the two binary solvent series indicating preferential solvation. In contrast, the vibrational lifetime is shown to change linearly with solvent composition, and is correlated with the mole fraction of chloroform but anti-correlated with the mole fraction of benzyl alcohol. The results are explained by differences in the densities of solvent modes that affect intermolecular relaxation of the carbonyl mode.

4.2. Introduction

Vaska's complex (bis(triphenylphosphine) iridium(II) carbonyl chloride, VC) is an organometallic catalyst that has served as a model system for exploring the mechanistic details of oxidative addition[42-43, 69, 157] and reductive elimination reactions,[159-160] as well as biomimetic O_2 binding to metal centers.[156, 158, 193] VC and its adducts possess a carbon monoxide ligand whose vibrational frequency (ν_{CO}) is a reporter of the oxidation state of the iridium.[171-172, 193] It is often cited as a textbook example of metal-to-ligand back-bonding whereby the ν_{CO} is effectively tuned by the extent of electron back-donation into its antibonding π^* orbital.[171]

In Chapter 3, we used this spectroscopic handle to report on the time scales of solvent shell rearrangement around VC in a series of solvents that were known to have different oxidative addition rate constants.[194] Oxidative addition to form an adduct is the first step in the catalytic cycle and this reaction restructures VC and its surrounding solvent shell. We found that the time scales on which the solvation shells fluctuate are different for these solvents around VC and its O_2 adduct (VC-O_2) and we hypothesized that these dynamic differences play a role in the catalytic rate. In both this study and a subsequent more exhaustive FTIR study, we showed that the ν_{CO} was generally insensitive to the surrounding solvent for VC and most of its adducts, including the I_2 adduct (VC-I_2), but was distinctly solvatochromic for VC-O_2.[104] We also found evidence that, for VC-O_2, the CO mode is influenced by the solvent motions around the O_2 ligand.[194] Based on this observation, we hypothesized that the O_2 ligand could contribute to the time-dependent frequency shifts of the ν_{CO} leading to its dephasing, making the

carbonyl on VC-O$_2$ a particularly sensitive probe of the local solvation dynamics in the vicinity of the active site of the catalyst. However, it is not clear to what extent the sensitivity of a static indicator like ν_{CO} translates to sensitivity in dynamic variables that affect the IR lineshape such as vibrational energy relaxation (VER) and pure dephasing.[106, 195-198] It has been shown that for certain classes of molecules that a linear correlation exists between the frequency of the excited vibrational mode and its population relaxation time[183] while in other cases this relationship is complicated by interactions with the solvent.[66, 199]

In this chapter, a detailed study of the solvent-solute interactions between two VC adducts in two series of binary solvent mixtures is presented. We focus our attention on the behavior of the frequency and width of the inhomogeneous lineshape, and the rate of VER of ν_{CO} for two specific VC adducts: the dioxygen adduct (VC-O$_2$) and the diiodide adduct (VC-I$_2$). Both molecules are octahedral iridium complexes with one chloride, one carbon monoxide, and two triphenylphosphine ligands, but the difference in electronegativity of the O$_2$ and I$^-$ ligands positions their ν_{CO} values 60 to 70 cm^{-1} apart. Although they are structurally similar, their frequencies exhibit the extremes of sensitivity and insensitivity to the nature of the solvent: the frequency on VC-O$_2$ can be perturbed up to 20 cm^{-1} by the solvent, while on VC-I$_2$ it is largely insensitive to all solvents that we have tested.[104] Hence, these VC adducts provide two cases in which the role of solvent on VER can be studied in the presence and absence of vibrational solvatochromism, giving us a way to examine the relationship between the solute-solvent interactions that perturb the ν_{CO} and those that affect the vibrational lifetime.

4.3. Experimental Materials and Methods

Bis(triphenylphosphine) iridium(II) carbonyl chloride, (Vaska's complex, 99.99%, Sigma Aldrich), chloroform ($CHCl_3$, 99.8%, Sigma Aldrich), benzyl alcohol (BA, ≥99%, Sigma Aldrich), perdeuterated (d_6-)benzene (99.5% D, Cambridge Isotope Laboratories, Inc), and iodine (99.8%, Fisher Scientific) were used as received.

VC-O_2 solutions were prepared by dissolving 6 mg of Vaska's complex in 2 mL of the desired solvent mixture (freshly prepared) and waiting for at least 24 hours to allow the oxygen dissolved in solution to bind. VC-I_2 solutions were prepared by dissolving 6 mg of Vaska's complex with 2 mg of iodine in 2 mL of solvent and sonicating for 1 hour in a water bath (vials were capped and parafilmed during sonication). All solutions were filtered before being placed in the sample cell. Typical VC concentrations were 4 mM. Solutions were used within 2 weeks (most within 1 week) of preparation. Solutions of the mixed solvents were stored in small vials with minimum headspace to minimize solvent composition changes due to evaporation. The sample cell had a path length of 150 μm for pump probe measurements.

Infrared spectra were collected on a Nicolet 6700 FTIR spectrometer (Thermo Scientific) with at least 16 scans and a typical resolution of 1 cm^{-1}. Path lengths of both 150 μm and 25 μm were used for FTIR measurements.

The IPP spectroscopy setup was similar to that described in Chapter 3, with the addition of polarization control. The probe beam was p-polarized and the pump beam was polarized to the magic angle (~54.7°) to remove any effects from orientational relaxation. For consistent results, it was necessary for the pump and probe beam polarizers to be

placed immediately before the sample.[118] The pump and probe beams were spatially overlapped and focused in the sample volume by an off-axis parabolic reflector. The transmitted probe beam passed through an analyzing polarizer placed directly after the sample (set to transmit p-polarized) and was then spectrally resolved in the same monochromator and detected with the same detector as in Chapter 3. The data were fit from 2 ps to 270 ps to determine the population relaxation times (lifetime, T_1) for the v=0-1 and 1-2 transitions. The vibrational relaxation times for these two transitions consistently showed the same trends and the 0-1 values are used in the following discussion.

4.4. Results and Discussion

The solvent-subtracted FTIR spectra of the carbonyl stretch on VC-O$_2$ and VC-I$_2$ in neat d_6-benzene, CHCl$_3$, and BA are shown in Figures 4.1a and 4.1b, respectively. As expected, the ν_{CO} of VC-I$_2$ is considerably higher than that of VC-O$_2$ due to the electron withdrawing strength of the I$^-$ ligands.[103-104] The VC-O$_2$ carbonyl peak broadens and exhibits a strong hypsochromic shift from 2003.6 cm^{-1} in d_6-benzene (black) to either 2014.0 cm^{-1} in CHCl$_3$ (blue) or 2013.2 cm^{-1} in BA (red). The ν_{CO} and linewidths in the latter two solvents are quite similar. It can be said that CHCl$_3$ and BA are two solvents that can lead to significant and nearly identical changes in the oxidation state of the iridium on VC-O$_2$.[158]

In contrast, VC-I$_2$ shows very little change in ν_{CO} but the peak width varies considerably between the three solvents, increasing from d_6-benzene (black) to BA (red) to CHCl$_3$ (blue). Comparing the two frames in this figure, the fact that the ν_{CO} of VC-I$_2$

is nearly insensitive to the change in solvents shows that there are no specific solvent-solute interactions with any of the ligands, including the CO, that influence the extent of metal-to-ligand back-bonding. For VC-I$_2$, the average oxidation state of the iridium is the same in all three solvents. Replacing the iodide ligands with O$_2$ activates solvatochromism through stronger specific interactions between this particular ligand and the solvent, as we have previously reported.[104, 194] DFT calculations showed that these interactions could be through hydrogen bond donation to the lone pairs on the O$_2$ ligand.[104] Yet CHCl$_3$ and BA have different hydrogen bonding strengths[176] and so the coincidence of their ν_{CO} values on VC-O$_2$ likely has some dependence on other nonbonding forces, such as dipole-dipole interactions.[15, 18] The broadening of the ν_{CO} lineshapes for both adducts suggests that their solvation environments in CHCl$_3$ and BA are more heterogeneous than that of d_6-benzene, although there may also be contributions to the lineshapes from changes in solvent shell dynamics and the T$_1$ that cannot be determined from the FTIR spectra alone.[110, 143]
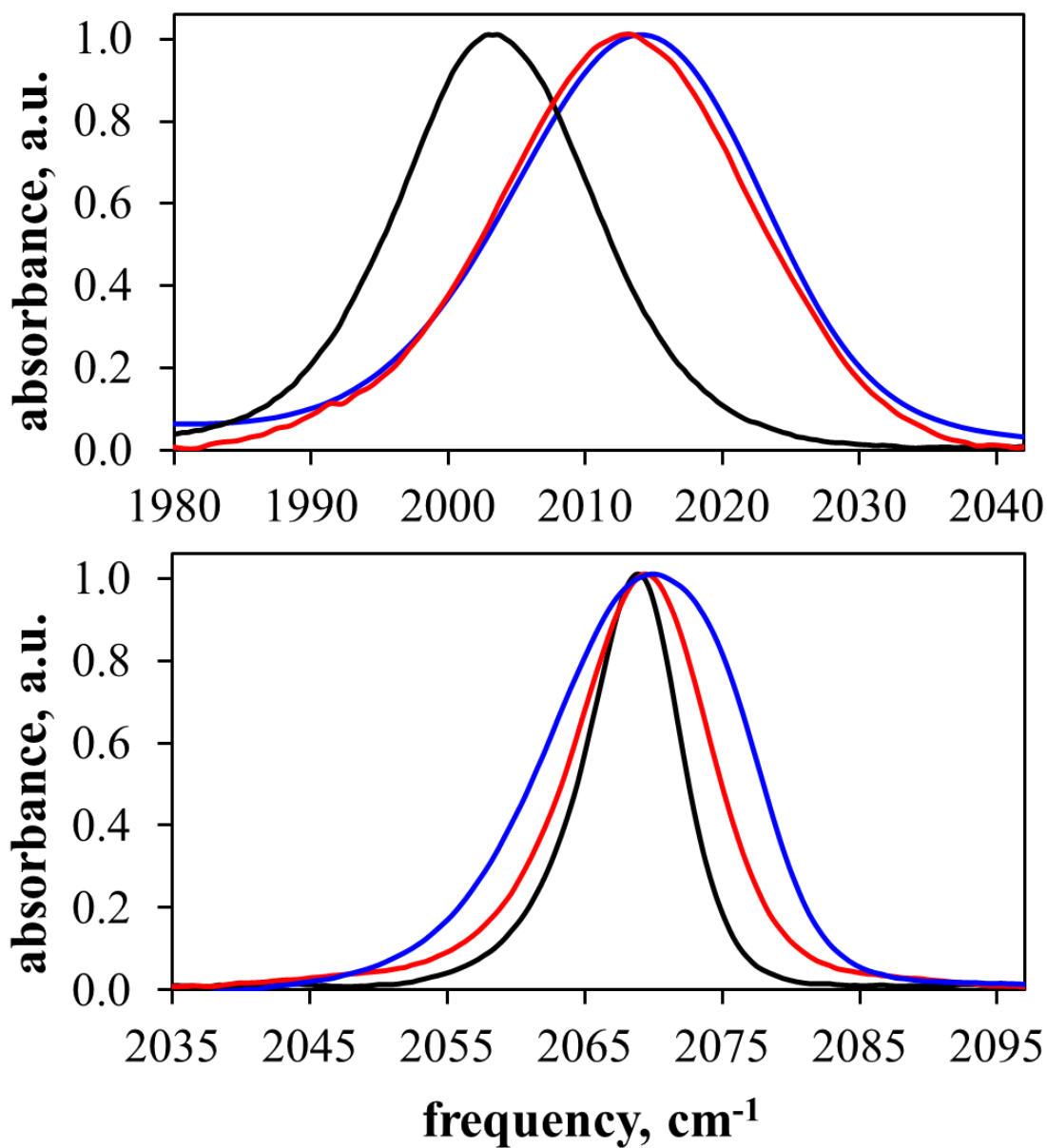
Figure 4.1: Solvent subtracted, baselined and normalized FTIR spectra of the CO vibrational mode on a) VC-O$_2$ and b) VC-I$_2$ in d_6-benzene (black), BA (red), and CHCl$_3$ (blue).

With the characteristics of ν_{CO} on the two adducts established in these pure solvents, we systematically varied the solvent composition from d_6-benzene to either CHCl$_3$ or BA. Binary solvent mixtures introduce a linear variation of the bulk solvent

composition as an independent variable onto which one can map spectroscopic changes to test for preferential solvation. In general, three types of preferential solvation can be described for binary solvent mixtures.[15, 18] First, the solvent and solute can have site-specific interactions such as hydrogen bonding. The second type of preferential solvation invokes non-structural solute-solvent interactions, such as dipole-dipole interactions. Alternatively, the solvent mixture itself may exhibit microheterogeneity in the bulk, and thus solvation would occur in small pockets or domains of one solvent or the other. In all cases, the mole fraction of the first solvation shell(s) is different from the mole fraction of the bulk solvent. If a particular spectroscopic observable, such as ν_{CO}, FWHM, or T_1 in the following measurements, has different values in two neat solvents, then a linear variation of that observable with the mole fraction of a binary mixture of the solvents would indicate that the solute experiences a solvation shell whose properties also vary linearly, at least from the perspective of the measured quantity. It is important to note that most properties of solvent mixtures do not vary linearly.[15, 18]

Figure 4.2a shows the ν_{CO} for VC-O$_2$ as the composition of the solvent mixture changes from pure d_6-benzene to either pure BA (black circles) or pure CHCl$_3$ (red squares). The ν_{CO} and FWHM values leading to Figures 4.2 and 4.3 are included in Table 4.1. The full FTIR spectra are provided in Figure 4.8. The change in the VC-O$_2$ ν_{CO} displayed in Figure 4.2a is not linear in mole fraction for either BA or CHCl$_3$ in d_6-benzene. In both types of mixtures, the non-benzene solvent has a stronger influence on the carbonyl frequency than would be anticipated from a linear projection between the pure solvents. This indicates that there is indeed preferential solvation of the O$_2$ ligand

by BA and CHCl$_3$ over d_6-benzene, which decreases the availability of metal electrons for back-bonding. The solvation shell is heterogeneously distributed around the ligated oxygen such that the local composition is not the same as that of the bulk solvent mixtures. While there certainly may be preferential solvation of other portions of the molecule as well, the lack of change in the ν_{CO} of VC-I$_2$ (Figure 4.2b) indicates that any change in solvation for the other ligands is not reflected in a frequency shift of the CO.

While neither plot is linear in Figure 4.2a, the BA mixtures exhibit a far less linear trend. We observed that VC-O$_2$ was much less soluble in BA than in either of the other two solvents; it thus seems unlikely that the solute is surrounded by entirely or even primarily BA molecules. What is far more probable is that any BA molecules present in the solvation shell have a stronger influence on the carbonyl stretch frequency than the benzene molecules. Considering that benzyl alcohol has a much greater dipole moment and hydrogen bond strength than d_6-benzene (or chloroform for that matter),[174, 176, 200-201] the more prominent deviation from linearity is thus due to a stronger solute-solvent interaction and/or heterogeneous solvent shell composition with BA preferentially solvating the O$_2$ ligand.[202] In CHCl$_3$, this interaction with dioxygen is weaker, even though the solvent readily dissolves VC-O$_2$, leading to a more linear trend in ν_{CO} as the mole fraction of CHCl$_3$ increases.
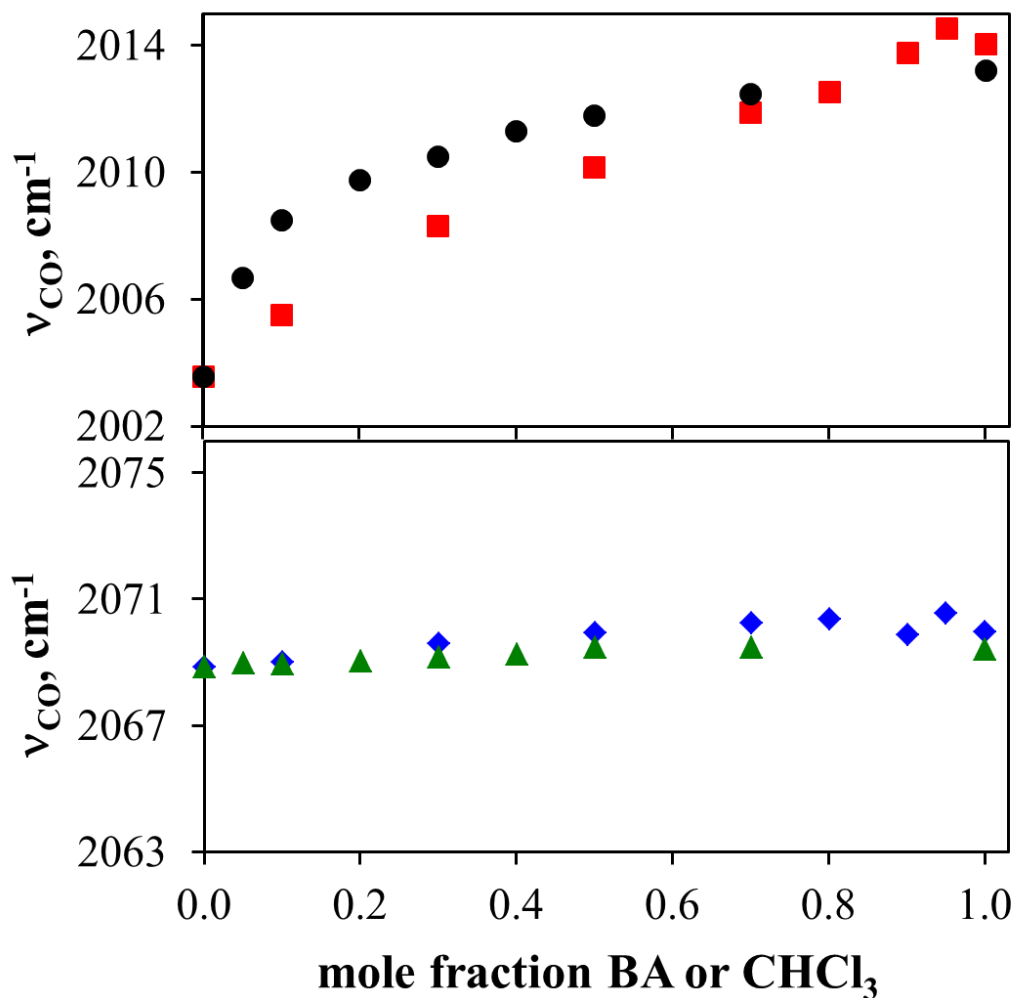
Figure 4.2: Carbonyl frequency (ν_{CO}) for VC-O$_2$ (a) and VC-I$_2$ (b) as a function of solvent composition in mixtures of d_6-benzene and BA (black circles, green triangles) and mixtures of d_6-benzene and CHCl$_3$ (red squares, blue diamonds).

The solvent insensitivity of ν_{CO} in VC-I$_2$ is apparent in Figure 4.2b, where the blue diamonds and green triangles show the center frequency in the CHCl$_3$ and BA mixtures, respectively. Since the three pure solvents have roughly the same ν_{CO} values, there is no variation of this parameter across the binary mixtures. The lack of a shift in the I$_2$ complex suggests that there are not specific solvent-solute interactions with any of

the ligands, including the I⁻ and CO, that modulate the electron density on the iridium

enough to change the extent of back-bonding to the CO ligand. Since the metal-to-CO

back-bonding is the primary factor dictating the carbonyl frequency, this does not imply

that the solvent shell composition is the same as that of the bulk.
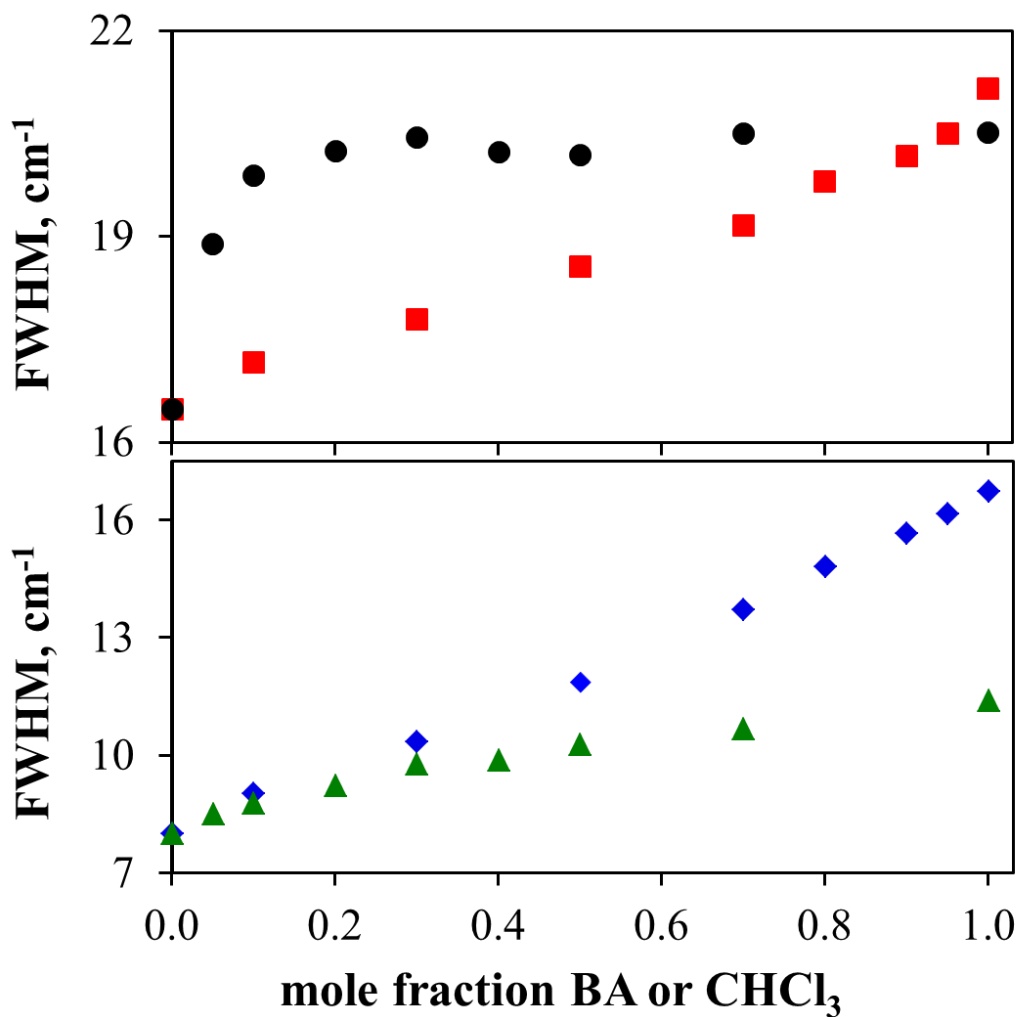
Figure 4.3: Full width at half maximum (FWHM) for the carbonyl stretch of VC-O$_2$ (a) and VC-I$_2$ (b) as a function of solvent composition in mixtures of d_6-benzene and BA (black circles, green triangles) and mixtures of d_6-benzene and CHCl$_3$ (red squares, blue diamonds).

As noted above, despite the insensitivity of ν_{CO} for VC-I$_2$, the spectral lineshapes are not independent of the solvent. Figure 4.3 shows the width (FWHM) for the carbonyl stretch of each adduct in both types of solvent mixtures. Here again, Figure 4.3a contains the values for VC-O$_2$ in BA mixtures (black circles) and CHCl$_3$ mixtures (red squares), while Figure 4.3b contains those for VC-I$_2$ in BA mixtures (green triangles) and CHCl$_3$ mixtures (blue diamonds). In some cases, the FTIR bands show some asymmetry (see Figure 4.8), and so the widths in Figure 4.3 are FWHMs of the raw absorbance bands, not Gaussian fit parameters. Both adducts show broadening as the mole fraction of d_6-benzene in the bulk decreases. In the BA mixtures, both VC-O$_2$ and VC-I$_2$ exhibit greater broadening at low mole fraction than would be expected from a linear variation in solvent composition. This is most pronounced for the VC-O$_2$ BA/d_6-benzene mixtures (black circles), which reach their maximum width at 0.1 mole fraction of BA and broaden very little at higher mole fractions. Combining this trend with that of the ν_{CO} in Figure 4.2a, it can be said that the carbonyl peak shifts and broadens at low mole fractions ($<$ 0.1), but then retains its linewidth and simply changes frequency over the rest of the range of solvent mixtures. In the CHCl$_3$ mixtures, both adducts broaden mostly linearly in relation to the mole fraction. In every solvent composition, the peak of VC-O$_2$ is consistently broader than that of VC-I$_2$ in the same solvent.

Based purely on the FTIR spectra discussed above, it is impossible to say whether the broadening in Figure 4.3 is due to changes in the homogeneous linewidth (arising from the vibrational lifetime and pure dephasing in the sample) or differences in the inhomogeneity of the systems (arising from the variety of solvent-solute configurations).

An increase in inhomogeneity would be a reasonable explanation of the broader peaks in the more polar $CHCl_3$ and BA (stronger intermolecular interactions generally mean a wider variety of environments) but the homogeneous lineshape can also be affected by the solvent. It is in these circumstances that nonlinear spectroscopies such as vibrational pump-probe spectroscopy can become useful in differentiating sources of broadening. The dynamic contributions to the lineshape are the vibrational relaxation time (lifetime, T_1), pure dephasing, and spectral diffusion.[106, 110] Here we measure only T_1, isolating that contribution to the homogeneous linewidth and giving insight into its role in lineshape broadening as well as the rate and possible mechanism of solvent influence on the relaxation of vibrational energy.

Preferential solvation has a peculiar manifestation in the dynamics of the solvation shell. Cichos and coworkers showed that the fluorescence Stokes shift that was characteristic of a coumarin dye in alcoholic solvents was achieved even at low concentrations of alcohols in alkane/alcohol mixtures. Time-resolving the fluorescence Stokes shift showed that the time scale for the solvation process around the excited state was notably slower than in neat alcohols.[23] Likewise, Luther and coworkers reported the time-resolved fluorescence Stokes shift of the same coumarin dye contained an abnormally slow solvation process in acetonitrile/benzene mixture solvents.[19] The mechanism of this process was elegantly described by Nguyen and Stratt as originating from the exchange of molecules from the first solvation shell to re-equilibrate around the excited state.[36] Hence, the preferential solvation of a solute by one component of a binary mixture over the other, which occurs for the VC adducts studied here (see Figures 4.2 and

4.3), could have an influence over the time dependent reorganization of the solvation shell molecules. Viewing the role of the solvent in VER as modulating the force applied to the solute,[203] it is conceivable that the preferential solvation might also affect the CO relaxation times. In the following measurements, we use vibrational pump-probe spectroscopy on VC adducts in binary solvent mixtures to test for this possibility, although 2D-IR spectroscopic studies underway in our lab are necessary to complete the dynamical picture of the solvation shell.

In each solvent mixture, it is possible that the CO peak consists of two or more populations corresponding to d_6-benzene and $CHCl_3$ or BA, and that these subensembles have different T_1 values. This could result from preferential solvation by domains that are rich in one of the two solvents, and might lead to a pronounced frequency dependence in the T_1. Alternatively, the v_{CO} peak may reflect a single heterogeneous population with a single relaxation time. For VC-O$_2$, the solvatochromic frequency shifts among the pure solvents (~10 cm^{-1}) allow for spectral distinction between uniform or binary solvation. In order to be certain that in choosing a particular frequency at which to report the lifetime we were not ruling out certain solvation environments, we compared the T_1 values at many frequencies.
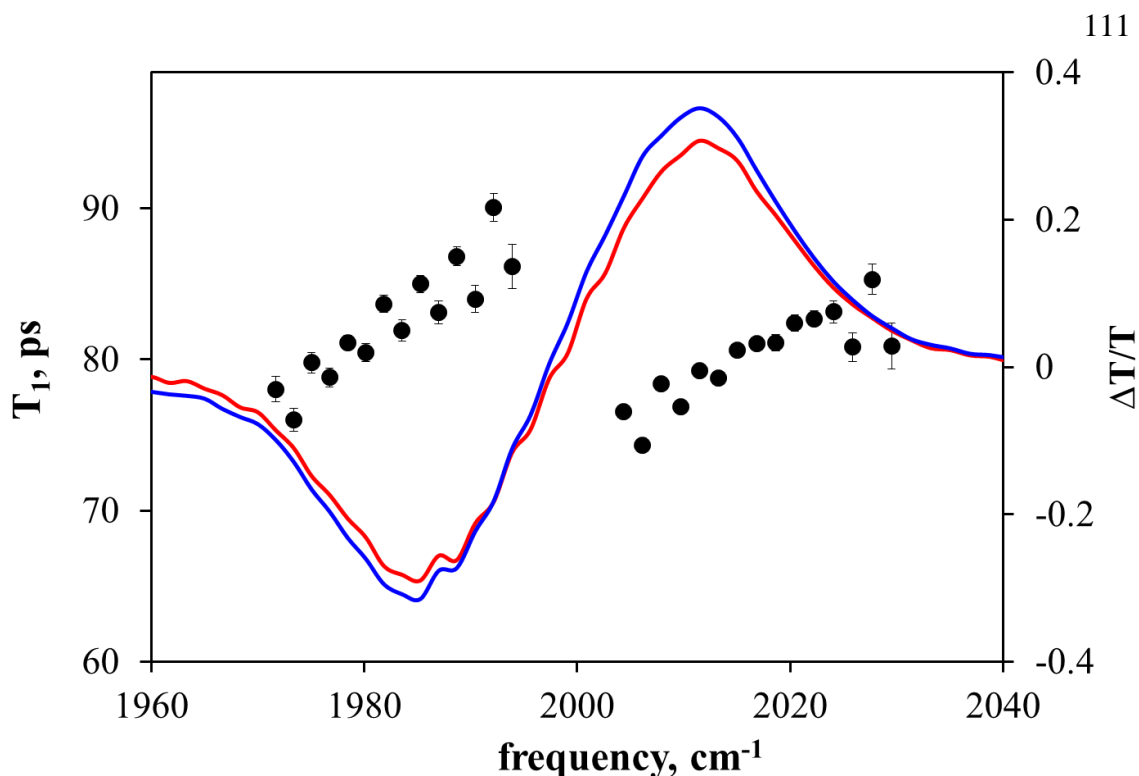
Figure 4.4: Vibrational lifetime (T_1) as a function of frequency for VC-O_2 in 0.3 mole fraction BA in d_6-benzene (black circles). Error bars represent the standard error of the fit. Overlaid are the pump probe spectra for the same sample at delay times of 1 ps (blue) and 100 ps multiplied by 3 (red). The gray area represents the region averaged in the reported values for T_1 (see text).

Figure 4.4 shows the values for the fits at most of the wavelengths (along with the standard error of the fit) as a function of frequency for the VC-O_2 sample in 0.3 mole fraction of BA in d_6-benzene. This mole fraction was chosen because it contains significant amounts of both BA and d_6-benzene and ν_{CO} in this mixture is some distance from its value in either pure solvent, giving a high probability that binary solvation, if present, would be visible. The spread of the data and the errors on the fits show that there are not statistical differences in T_1 across most of the 0-1 and 1-2 transitions. The slight increase in T_1 at a few of the higher frequencies was also present in the T_1 fits to the pump-probe spectra of the pure solvents. The T_1 of VC-O_2 in pure BA is almost 40 ps

faster than pure d_6-benzene (see Table 4.1). Therefore, if the higher frequency portion of the carbonyl peak was indeed from primarily BA-surrounded molecules, then in this particular d_6-benzene/BA mixture one would expect a decrease in T_1 with an increase in frequency. We conclude that the ν_{CO} peak is a single inhomogeneous population represented by a single T_1.

Overlaid in Figure 4.4, the pump-probe spectrum for this same sample is shown at 1 ps (blue) and 100 ps (red, ×3) delay times. The positive peak represents the bleach from the transient absorption from the ground state to the first excited state (0-1) and the negative peak represents the signal from the transition from the first excited state to the second excited state (1-2). The difference between the frequencies of these peaks is indicative of the anharmonicity of the system. If a binary population were present, we would expect the shape of the spectrum to change dramatically over this long time delay.[204] Instead, the shapes are nearly identical, confirming that the solvent mixture has a collective influence on the T_1 for these pump-probe spectral bands. For the remainder of the discussion, the T_1 values are reported as the average of the five points around the maximum of the positive (0-1) peak, shown in Figure 4.4 as the grayed area, for each trial (most data points have at least two trials associated with them). The T_1 values for both complexes in all solvents and solvent mixtures are compiled in Table 4.1.

Table 4.1. T_1, ν_{CO}, and FWHM values for binary solvent mixtures. Errors in parentheses indicate the standard deviation from the mean.

solvent(s)	mole fraction	ν_{CO} (cm^{-1})		FWHM (cm^{-1})		T_1 (ps)	
		VC-O$_2$	VC-I$_2$	VC-O$_2$	VC-I$_2$	VC-O$_2$	VC-I$_2$
CHCl$_3$ in d_6-benzene	0	2003.6	2068.9	16.5	8.0	92 (3)	194 (7)
	0.1	2005.5	2069.0	17.2	9.0	94 (2)	198 (8)
	0.3	2008.3	2069.6	17.8	10.3	101 (3)	205 (7)
	0.5	2010.2	2069.9	18.6	11.9	102 (1)	207 (6)
	0.7	2011.9	2070.2	19.2	13.7	106 (2)	214 (7)
	0.8	2012.5	2070.4	19.8	14.8	106 (2)	216 (6)
	0.9	2013.8	2069.9	20.2	15.7	109 (3)	219 (10)
	0.95	2014.5	2070.6	20.5	16.2	106 (2)	221 (6)
	1	2014.0	2070.0	21.2	16.7	108 (2)	216 (7)
BA in d_6-benzene	0	2003.6	2068.9	16.5	8.0	92 (2)	193 (7)
	0.05	2006.7	2069.0	18.9	8.5	87 (2)	189 (13)
	0.1	2008.5	2069.0	19.9	8.8	88 (2)	188 (13)
	0.2	2009.8	2069.0	20.2	9.2	84 (2)	181 (12)
	0.3	2010.5	2069.1	20.4	9.8	78 (1)	174 (11)
	0.4	2011.3	2069.2	20.2	9.9	76 (1)	165 (9)
	0.5	2011.8	2069.5	20.2	10.3	73 (2)	172 (10)
	0.7	2012.5	2069.5	20.5	10.7	66 (2)	150 (7)
	1	2013.2	2069.4	20.5	11.4	56 (2)	124 (10)
toluene	1	2003.6	2069.3	16.1	7.6	61 (4)	155 (5)
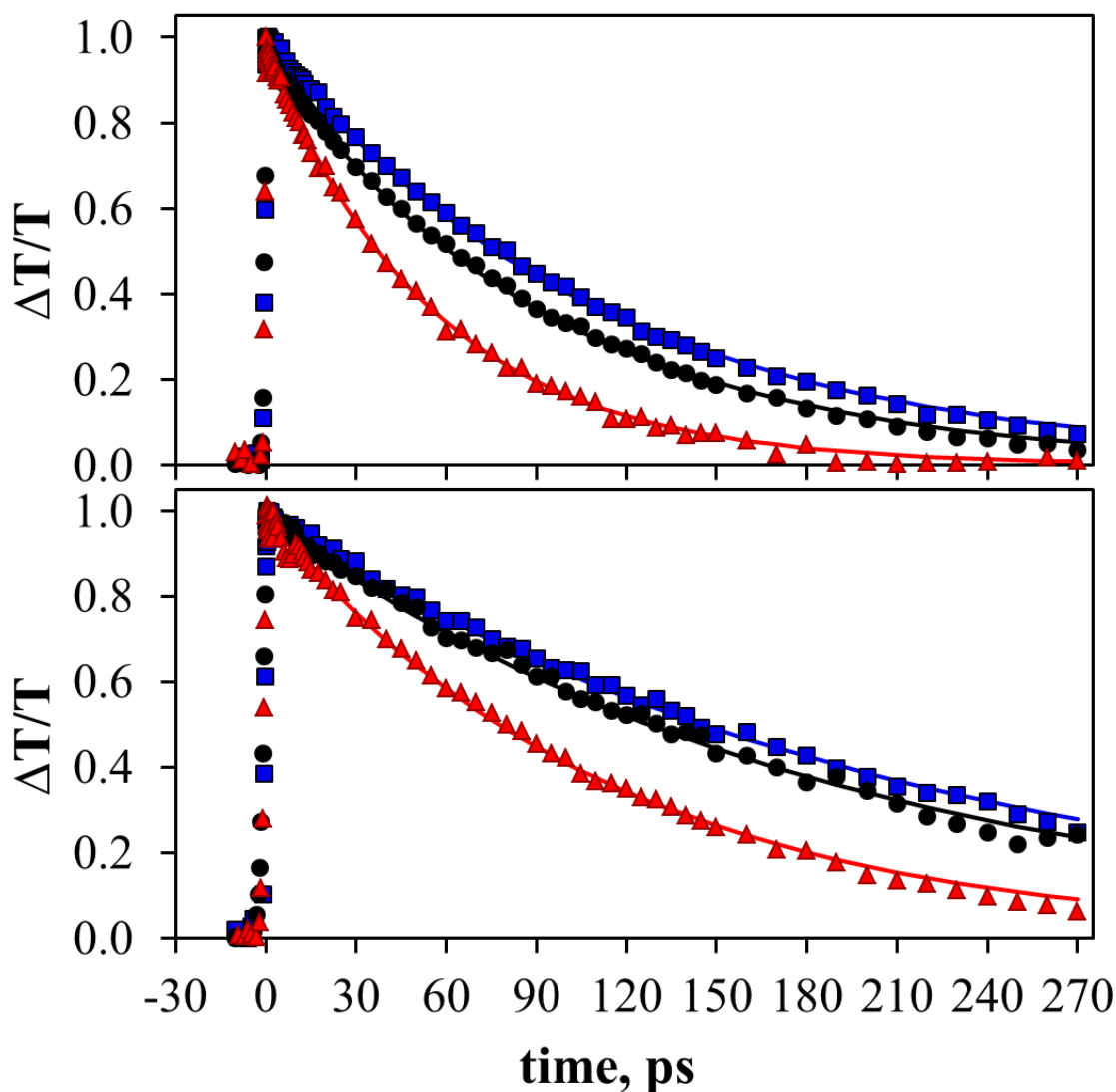
Figure 4.5: Representative normalized decays for VC-O_2 (a) and VC-I_2 (b) in neat d_6-benzene (black circles), BA (red triangles), and CHCl$_3$ (blue squares). Markers represent data points and lines illustrate the single exponential fits to the data.

Representative decays of the bleached 0-1 transition for VC-O_2 and VC-I_2 in pure solvents are shown in Figures 4.5a and 4.5b, respectively. Decays for all the mixtures with their fits are shown in Figures 4.9 and 4.10. The markers represent the normalized experimental data and the lines show the single exponential fits from which the T_1 was obtained. The signal-to-noise ratios for all datasets in this study are comparable to these

decays and the fits are of similarly high quality. The full data and fits are shown in Figures 4.9 and 4.10. For both adducts, BA has the fastest relaxation time, $CHCl_3$ has the slowest, and d_6-benzene is intermediate (though closer to $CHCl_3$).
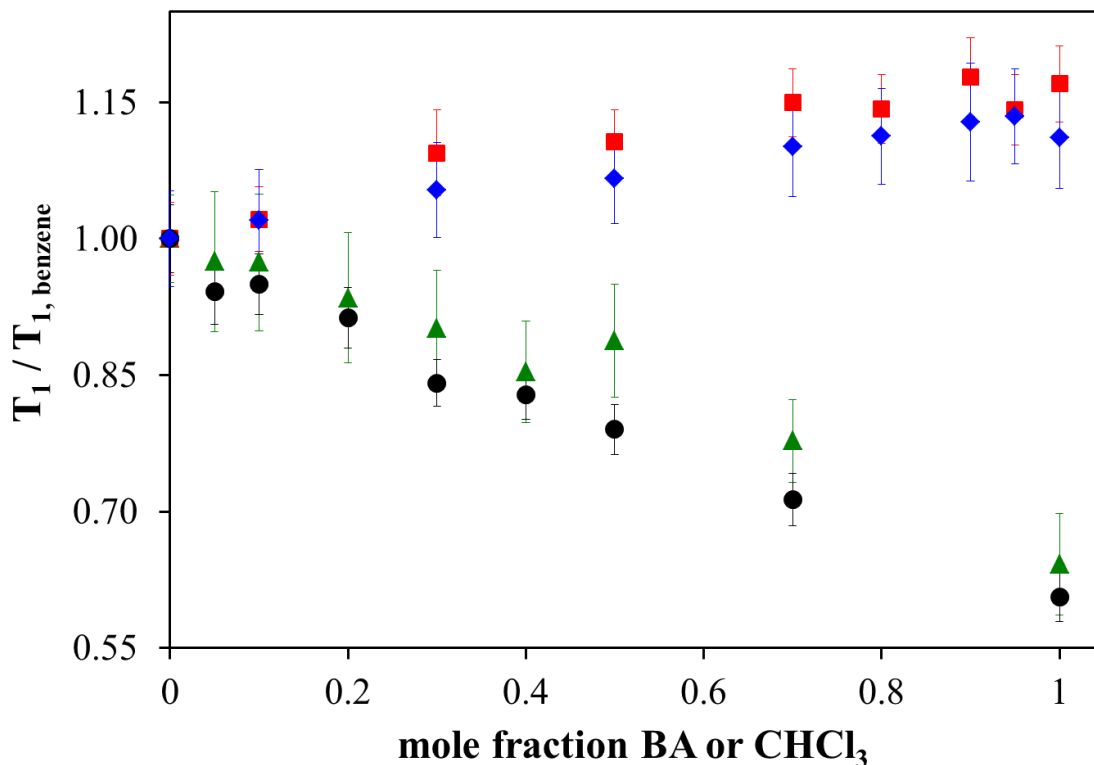
Figure 4.6: T_1 normalized by the lifetime of pure d_6-benzene ($T_1/ T_{1,benzene}$) as a function of solvent composition. VC-O_2 in BA mixtures (black circles), VC-O_2 in $CHCl_3$ mixtures (red squares), VC-I_2 in BA mixtures (green triangles), and VC-I_2 in $CHCl_3$ mixtures (blue diamonds) are shown. Error bars represent the standard deviation from the mean.

It was anticipated that the carbonyl would relax much more slowly on VC-I_2 compared to VC-O_2 in light of literature work on the relationship between vibrational frequency and relaxation time.[183] A high frequency mode relaxes primarily through intramolecular channels, whereby anharmonically coupled accepting modes in the solute become excited. For the intramolecular process, the solvent bath serves to modulate

these interactions and donates or absorbs additional quanta of energy that conserve energy in the overall process (solvent-assisted intramolecular relaxation).[203] If this relaxation process is inefficient, intermolecular relaxation into solvent accepting modes can also become a viable relaxation channel.[205-206] The intuitive picture is that, as long as the relaxation pathway remains the same, a higher energy mode should take longer to relax as more lower energy modes must be excited for relaxation to occur. Hill and coworkers demonstrated a linear relationship between the T_1 and ν_{CO} for a library of metalloporphyrins in which the lifetimes became longer with increasing frequency.[183] However, that trend was not consistently followed when the solvent alone was changed. For a series of simple chlorinated solvents they reported only minor changes in T_1 that were not correlated with ν_{CO}. They concluded that VER proceeded primarily through intramolecular channels from the carbonyl to the π-system of the porphyrin, and that the anharmonic coupling of these channels was not perturbed by the nature of the solvent. When a more structurally complex dibutylphthalate (DBP) solvent was used they observed a 40% decrease in T_1, which was partly attributed to intermolecular relaxation into the solvent on a time scale that was competitive with intramolecular relaxation due to the large density of states on DBP and its strong non-bonding interactions with the porphyrin.[183] It is worth noting that the relaxation times of their systems were on the order of 5-10 times faster than those for the molecules we studied here. Heilweil and coworkers reported drastic changes in T_1 with a change in solvent in their study of metal hexacarbonyls when only very small changes in ν_{CO} occurred.[66] In contrast, King and coworkers found minimal changes in the CO lifetime in a multi-carbonyl system, despite

changes in the number of hydrogen bonds that perturbed the CO frequencies and hindered intramolecular vibrational redistribution (IVR).[94]

The T_1 values for the VC adducts above are only partly consistent with these studies. All of the VC-I_2 decay times are longer than those of VC-O_2 in the same solvents. Yet, our results in Table 4.1 illustrate clearly that solvent effects on T_1 are not well-correlated with frequency changes for VC adducts. Comparing the frequencies and T_1s for the neat solvents, the ν_{CO} of VC-O_2 in BA and CHCl$_3$ are similar and higher in energy than in d_6-benzene, but the T_1 trend is BA $< d_6$-benzene $<$ CHCl$_3$. Additionally, VC-I_2 shows the same neat solvent trend in T_1 when there is virtually no change in center frequency. One explanation for these differences is that the solvent-assisted intramolecular relaxation process is enhanced by BA but inhibited by CHCl$_3$. However, based on the time scales of these T_1s (up to 200 ps), this channel is inefficient for these complexes, and intermolecular energy transfer to the solvent is probable. Since VER becomes faster as the solvent molecules increase in size, the process is apparently modulated by intermolecular relaxation into the manifold of solvent accepting modes, which has a greater density of states for the larger, more complex species.[205-206]

In order to more closely examine the connection between ν_{CO} and T_1, we determined the relaxation times across binary mixtures of d_6-benzene with BA or CHCl$_3$. Figure 4.6 shows the T_1 values normalized by the lifetime in neat d_6-benzene for VC-O_2 and VC-I_2 as a function of the mole fraction of BA or CHCl$_3$. This normalization was done to better enable comparison between adducts. Again, black circles represent VC-O_2 in BA mixtures, red squares represent VC-O_2 in CHCl$_3$ mixtures, blue diamonds

represent VC-I$_2$ in CHCl$_3$ mixtures and green triangles represent VC-I$_2$ in BA mixtures. The error bars represent the standard deviation of all frequency points averaged (five for each trial, see Figure 4.4 and discussion).

Comparing the trends shown by each adduct, VC-O$_2$ and VC-I$_2$ in both solvent mixtures show very similar proportional changes in T$_1$ with changing solvent composition. The CHCl$_3$ mixtures for VC-O$_2$ (red squares) and VC-I$_2$ (blue diamonds) show a monotonic increase in T$_1$ as the d_6-benzene is progressively replaced with CHCl$_3$. In the T$_1$ values for d_6-benzene/BA mixtures, unlike the CHCl$_3$ mixtures, VER is faster as the solvent moves toward a higher fraction of BA.

If the changes shown in Figure 4.6 for the BA (CHCl$_3$) mixtures were due to an increase (decrease) in the rate of IVR caused by a change in the density of states in the VC species, one would expect that the molecular structure and therefore the ν_{CO} would be perturbed. However, ν_{CO} for VC-I$_2$ is nearly unaffected by the nature of the solvent (Figure 4.2b). Therefore we attribute the decrease in T$_1$ to a change in the density of states in the solvent into which intermolecular relaxation occurs. This is not unexpected since BA is a larger molecule than benzene and should have more degrees of freedom. Despite the fact that the ν_{CO} for VC-O$_2$ shifts to higher energies on going from d_6-benzene to either BA or CHCl$_3$, the rate of carbonyl relaxation in BA *increases*, contrary to the expectation for a primarily intramolecular relaxation.[183] This is a further indication that VER is significantly affected by intermolecular relaxation into solvent modes for these adducts.

In order to further test this evidence, we also examined the relaxation times of VC-O_2 and VC-I_2 in toluene. The IR spectrum of toluene is similar to that of benzyl alcohol in the high frequency range of the spectrum close to the CO stretch (2000-1450 cm^{-1}) but similar to d_6-benzene and CHCl$_3$ in its lower frequency 500-650 cm^{-1} range (see spectra in Figure 4.7). This range was chosen to ascertain whether the relaxation pathway proceeds through the solute vibrations closest in energy to the carbonyl. In both VC-O_2 and VC-I_2 these vibrational peaks appear at ~1435 cm^{-1} (attributed to the triphenylphosphine ligands) and so 570 cm^{-1} and 635 cm^{-1} are the approximate differences between these vibrations and the CO stretch for VC-O_2 and VC-I_2 respectively. The resulting lifetimes are given in Table 4.1 and are much closer to the lifetimes in BA than either CHCl$_3$ or d_6-benzene, again supporting the intermolecular model of relaxation. Also shown in Table 4.1 are both the center frequency and FWHM of each adduct in toluene. The ν_{CO} for VC-O_2 in toluene is also very similar to that in neat d_6-benzene, another indication that frequency is not the determining factor in the value of the relaxation time for these systems.

Returning to Figure 4.6, we note that the T_1 values for both adducts in BA mixtures decrease in a linear fashion. In the CHCl$_3$ mixtures, they increase linearly. This shows that the solvation shell composition in the vicinity of the CO varies proportionately with the bulk solvent composition for both adducts in both mixtures. This is strikingly different from the behavior of ν_{CO} in Figure 4.2a and suggests that the specific stronger solvent-solute interactions that are responsible for changes in ν_{CO} do not have a noticeable effect on VER for the carbonyl. The evidence accumulated in Figure

4.6 and compared to Figure 4.2 indicates that the relaxation of the carbonyl vibration on VC-O_2 and VC-I_2 is not sensitive to the same influences as the solvatochromic response of ν_{CO}. The shape of the ν_{CO} versus mole fraction of diluent is not reflected in the T_1 plots with the same independent variable. Similar proportional changes in T_1 are observed over the full mole fraction range regardless of whether the ν_{CO} of the solute is sensitive (VC-O_2) or completely insensitive (VC-I_2) to the solvent. The vibrational frequency is tuned by the extent of back-bonding from the iridium, which is strongly tied to the strength of the solvent interactions (or lack thereof) with the *trans* ligand (O_2 or I^-). VER has a significant contribution from intermolecular relaxation channels that rely on coupling to the CO ligand rather than interactions with the *trans* ligand.

As mentioned previously, the lifetime is one of several variables that determines the linewidth of an absorbance. The homogeneous lineshape contains the T_1 as well as the pure dephasing time (T_2^*). If the lifetime decreases, with consistent pure dephasing, then the homogeneous linewidth will increase as dictated by the uncertainty principle. In spite of the fact that, in solution, the homogenous peak is usually buried under large amounts of inhomogeneous broadening, changes to its width can still contribute to the linear lineshape. This could explain the difference in the ranges of widths covered by the two adducts in Figure 4.3. The lifetimes of VC-I_2 as seen in Table 4.1 are always longer than VC-O_2 in the same solvents and so the homogeneous width of the VC-O_2 carbonyl stretch is expected to be consistently larger than its counterpart in VC-I_2. The VC-O_2 FWHM exhibits this expected trend. Without knowing that T_2^* is the same for the two adducts in the same solvent, it is impossible to say with certainty that this is the cause,

but there is at least a correlation between the linewidth differences and the T_1s for VC-I_2

and VC-O_2.
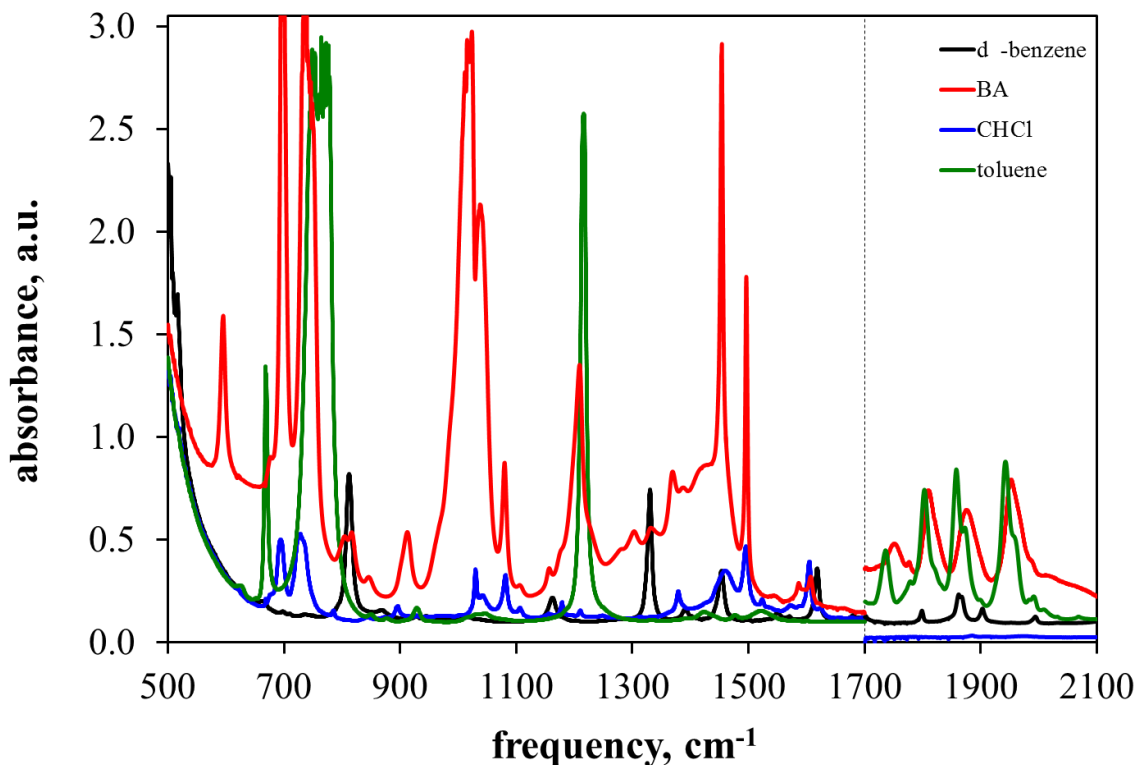
Figure 4.7: Neat solvent FTIR spectra for d_6-benzene(black), BA (red), CHCl$_3$ (blue), and toluene (green). Spectra to the left of the dotted line were collected with a 25 micron path length, spectra to the right of the dotted line were collected with a 150 micron path length.

Examining the trends in Figures 4.6 and 4.3 as the solvent composition changes, it is clear that something beyond the change in the T_1 is affecting the width. Both CHCl$_3$ and BA mixtures exhibit broadening in the FWHM, but only the BA mixtures show a corresponding decrease in vibrational lifetime. The contribution to the homogeneous linewidth from T_1 in the CHCl$_3$ mixtures is actually decreasing with increasing mole fraction. Furthermore, even in the BA mixtures the lifetime shows a gradual, linear

change while the width increases rapidly to its value at 0.1 mole fraction and then plateaus. We hypothesize that these differences are due to inhomogeneous broadening and/or dynamical differences induced by a range of solvent configurations and their interconversion; further experiments are required to affirm this.

4.5. Conclusions

We measured the FTIR and pump-probe spectra and decays of two different adducts of Vaska's complex in two sets of binary solvent mixtures. The oxygen adduct exhibited solvatochromism of the carbonyl stretch in the mixtures, while the iodine adduct did not. Although we observed higher v_{CO} values and longer T_1s for VC-I$_2$ complexes relative to VC-O$_2$, the positive linear correlation between these two variables that has been reported for a different class of compounds generally does not hold in this case. The frequency of the CO stretch is sensitive to the solvation environment of the O$_2$ ligand for VC-O$_2$, while the vibrational lifetime is sensitive only to the solvation environment of the CO. The dissimilarities between the T_1 and FTIR trends across the binary solvent mixtures and the similarity of the T_1 in toluene to that in BA show that the vibrational relaxation for these VC adducts is strongly affected by an intermolecular pathway involving the solvent vibrational modes rather than being dominated by solvent-mediated IVR.

The width of the CO stretch absorption is sensitive to configurational influences that elude the T_1, indicating that there is likely some inhomogeneous component to the broadening. But the consistent difference between VC-O$_2$ and VC-I$_2$ widths in the same solvent mixtures is possibly due to homogeneous broadening, since the T_1 also exhibits a

similar spread. From this and previous chapters, a picture is emerging of this carbonyl as an exquisitely sensitive probe of the equatorial solvation environment of the molecule. The linear spectrum is strongly affected by the solvation of the catalytic active site when a side-binding ligand like O_2 is present. Furthermore, since the relaxation time responds entirely to the environment around the carbonyl, it could be used to decouple the influences from the front and back sides of the molecule. This study shows that the dynamic influence of preferential solvation is not reflected in the VER of the carbonyl, though it may still be operational in other dynamical solvation processes. A 2D-IR study of these systems is given in Chapters 5 and 6, which will give further insight into the solvent influences on the carbonyl and the contributions of homogeneous and inhomogeneous broadening to the linear lineshape.[b]
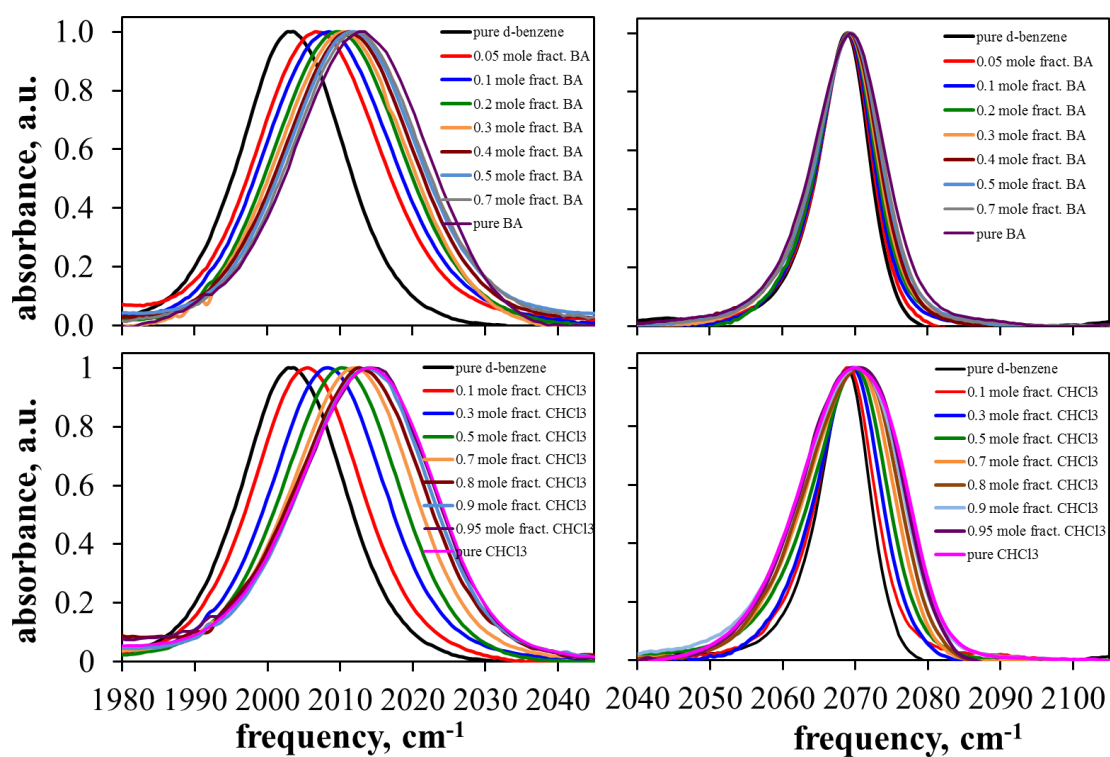
Figure 4.8: Baselined, solvent-subtracted, and normalized FTIR spectra for VC-O$_2$ in a) d_6-benzene/BA and b) d_6-benzene/CHCl$_3$ mixtures, and VC-I$_2$ in c) d_6-benzene/BA and d) d_6-benzene/CHCl$_3$ mixtures.
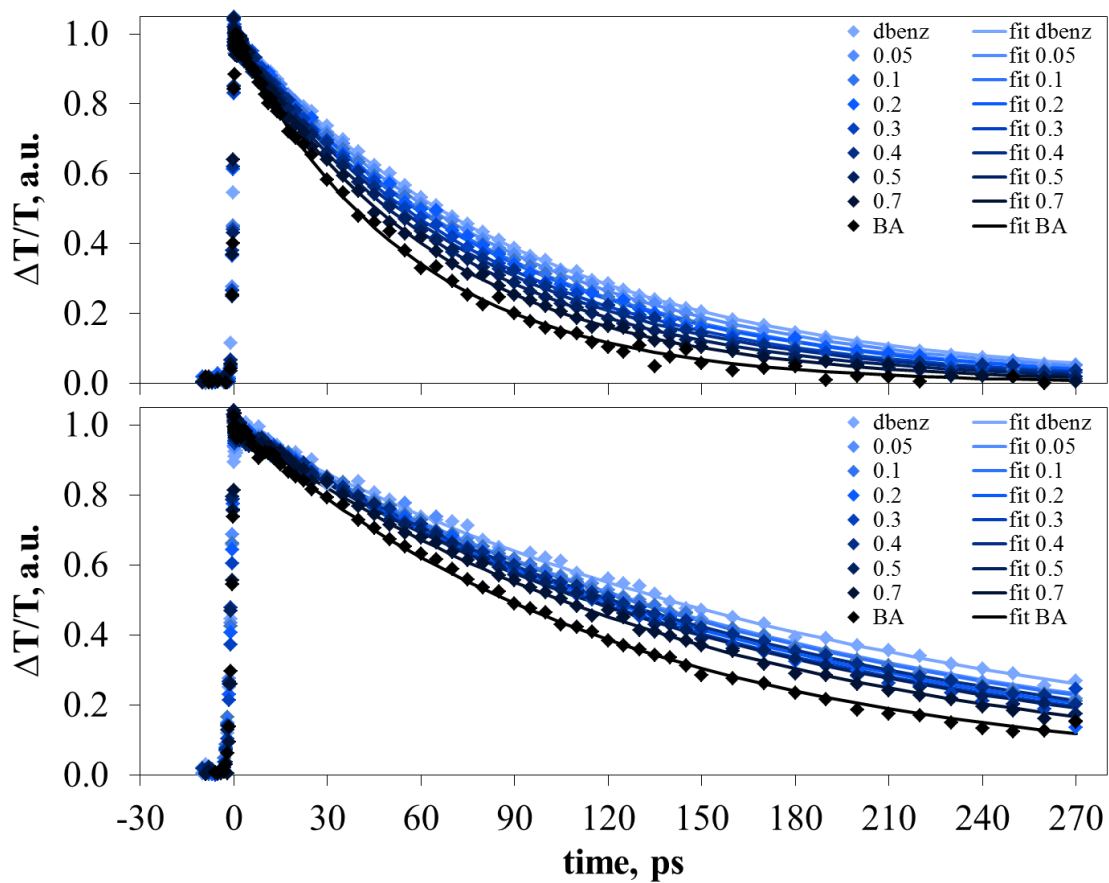
Figure 4.9: Pump-probe decays at the peak of the 0-1 transition in d_6-benzene/BA mixtures for a) VC-O_2 and b) VC-I_2
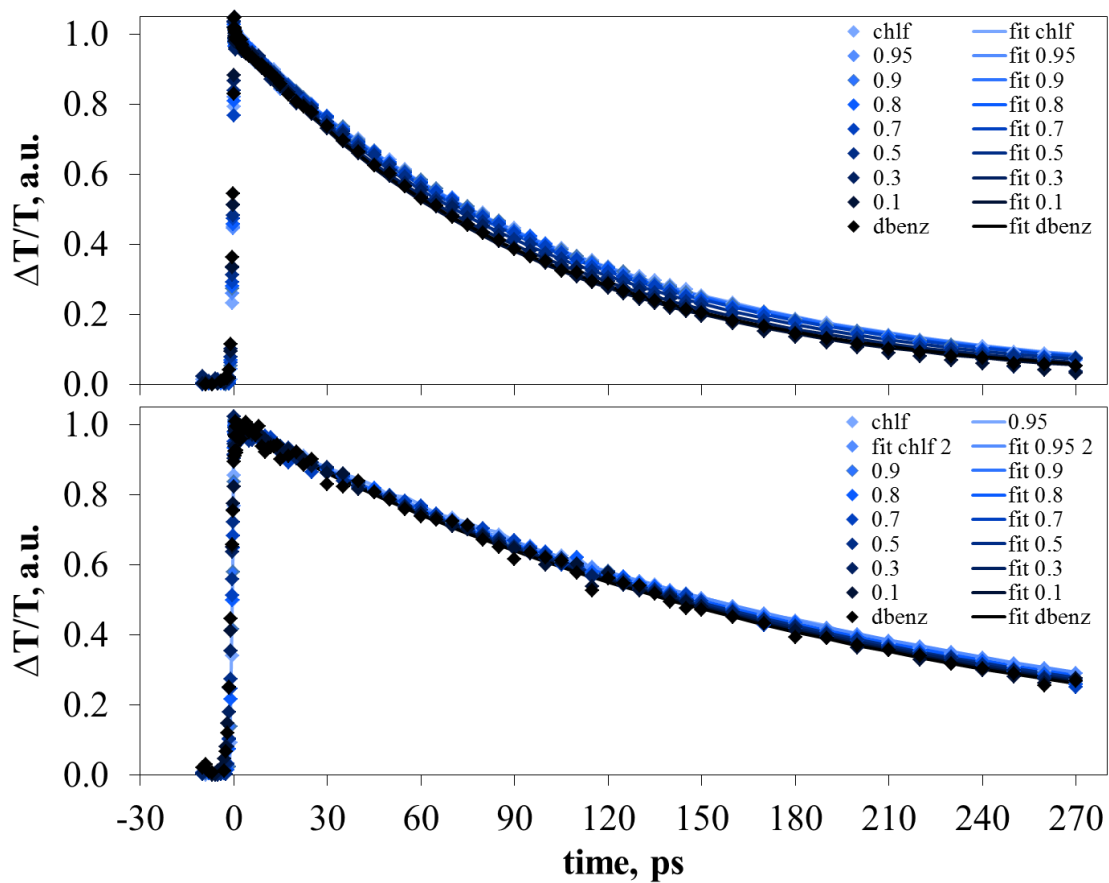
Figure 4.10: Pump-probe decays at the peak of the 0-1 transition in d_6-benzene/CHCl$_3$ mixtures for a) VC-O$_2$ and b) VC-I$_2$.

Chapter 5: Origins of Spectral

Broadening in Iodated Vaska's

Complex in Binary Solvent Mixtures

Reproduced in part with permission from:

 "Origins of Spectral Broadening in Iodated Vaska's Complex in Binary Solvent Mixtures" B.H. Jones, A.M. Massari, *J. Phys. Chem. B*, **2013,** *117* (49), 15741

5.1. Chapter Summary

As was seen in Chapter 4, linear absorption spectroscopy of the iridium-bound carbonyl on an iodated adduct of Vaska's complex has shown that the mean vibrational frequency is insensitive to solvation by a broad range of solvents while the spectral linewidth changes significantly. The spectral broadening is more significant in chloroform than benzyl alcohol, which is puzzling considering that benzyl alcohol is considerably more polar. In this study, 2D-IR spectroscopy was performed on this vibrational mode to dissect the linear lineshape into its homogeneous and inhomogeneous contributions in binary solvent mixtures of either chloroform or benzyl alcohol in d_6-benzene. The full frequency-frequency correlation function was determined, including the homogenous linewidth and fast spectral diffusion. We find that the magnitudes of frequency fluctuations and the time constants for spectral diffusion are the most notable changes in chloroform and benzyl alcohol, respectively, yet it is the fluctuation magnitudes in both solvent mixtures that most clearly explain the linear linewidths. The homogeneous contributions were found to either stay the same or decrease as the more polar solvent was added to d_6-benzene, thereby implicating inhomogeneous dynamics as the dominant broadening mechanism.

5.2. Introduction

Although it is often the average peak frequency that is used in vibrational analyses, there is a wealth of information contained in spectral lineshapes that is lost in linear spectroscopy, particularly the dynamic interactions of the solvation shell molecules with the solute of interest. In the condensed phase, the linear lineshape can be considered as a heterogeneous collection of sub-ensembles, each of which characterizes a particular solvent-solute configuration (see Figure 5.1). This inhomogeneous distribution is often well-approximated by a Gaussian lineshape whose width is notably larger than any of the underlying ensembles and describes the full range of solvent-solute configurations in the sample. These chemical microstates are dynamic – they have the potential to change their mean frequencies as solvent-solute configurations interconvert over a continuum of time scales. These time scales may be measurable as spectral diffusion or appear to be static for a given technique. As was discussed in Chapter 2, the contributions to the individual sub-ensemble linewidths (Γ) are also dynamic being dictated by pure dephasing (T_2^*), population relaxation (T_1), and solute reorientation (T_{orient}) according to:[116-117, 207-208]

$$\Gamma = \frac{1}{\pi T_2} = \frac{1}{\pi T_2^*} + \frac{1}{2\pi T_1} + \frac{1}{3\pi T_{orient}} \qquad (5.1)$$

Hence, the overall FTIR linewidth is a combination of inhomogeneous and homogeneous broadening phenomena, both of which are dynamic yet appear to be static through the lens of the FTIR measurement.

The convolution of inhomogeneous and homogeneous broadening contributions means that all of the dynamic solvent-solute interactions beneath the FTIR lineshape are indistinguishable. Fortunately, nonlinear IR spectroscopy can be used to recover this information. The T_1 and T_{orient} times can be measured directly by polarization-controlled IR pump-probe spectroscopy to reveal the mechanisms of energy relaxation and the role of the solvation environment in facilitating or inhibiting molecular rotation.[118, 209] T_2^* can be quantified by 2D-IR spectroscopy to determine the time scales on which the vibrational frequencies are modulated by their surrounding environments without relaxation.[108, 110, 145, 148-150, 194] In addition, this technique can be used to characterize the inhomogeneous dynamics of spectral diffusion, allowing full characterization of the origins of spectral broadening for a vibrational mode.[116-117]
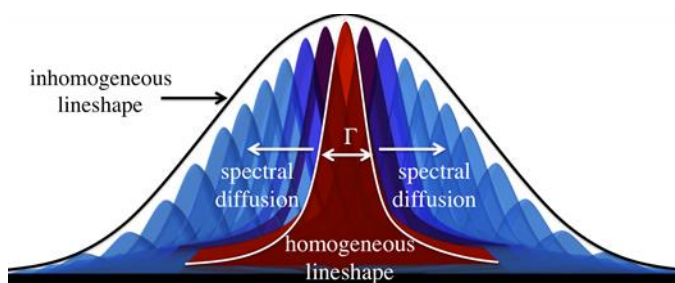
Figure 5.1. Diagram of an inhomogeneously broadened FTIR (linear) lineshape composed of numerous homogeneous (blue and red) sub-ensembles, each representing a solvent-solute configuration. The configurations have a homogeneous linewidth (Γ) and may spectrally diffuse to other mean frequencies as configurations interchange.

In this study, we use 2D-IR spectroscopy,[108, 110, 145, 148-150, 194] as well as the IR pump-probe results from Chapter 4,[210] to explore the origins of spectral broadening for a metal-bound CO vibrational mode across two binary solvent mixtures. The solute of

interest is bis(triphenylphosphine) iridium(I) carbonyl chloride, or Vaska's complex (VC),[81-82, 156] that has been converted to the iodated adduct by oxidative addition of iodine (VC-I$_2$).[103]

VC is an organometallic catalyst best known for its ability to reversibly bind and release oxygen, making it a model system for biomimetic oxygen transport.[156-158] It has also been shown to reversibly bind molecular hydrogen[43, 81] but irreversibly add iodine,[103] and to serve as an efficient catalyst for a number of chemical reactions following oxidative addition of the substrate.[43, 69, 157, 163-168] The carbonyl ligand on VC adducts is trans to the bound addend and is sensitive to the oxidation state of the iridium,[171-172] but also to the nature of the addend itself.[104, 194] VC-I$_2$ presents an interesting case in which the average vibrational frequency of the CO is unchanged for a broad range of solvents, indicating that the oxidation state of the metal is nearly constant, yet the spectral linewidth changes dramatically.[104, 210]

As stated above, nonlinear IR techniques can be used to separate the relative contributions to FTIR spectral broadening and will be used here to characterize the broadening influences for the CO on VC-I$_2$. Binary solvent mixtures of chloroform (CHCl$_3$) and benzyl alcohol (BA) in d_6-benzene were selected as two cases in which the extremes of spectral broadening were observed and a variety of solvent-solute interactions were present. By mapping the dynamical contributions to the lineshape onto a coordinate in which the bulk solvent composition was varied linearly, we were able to test for preferential solvation dynamics of the solute within the first solvent shell. Solvation dynamics studies have also shown that binary solvent mixtures may have

dynamical processes that are distinct from either of the pure solvents.[19, 23, 36] Such non-additive behavior can be valuable when attempting to use solvation interactions to tune the response of a solute.[211-217] By combining these results with our previous measurements of the linear spectroscopic changes and the vibrational lifetime of this mode discussed in Chapter 4, we are able to provide a complete picture of the factors that lead to spectral broadening for the carbonyl on VC-I_2 in these solvent mixtures.

5.3. Experimental Materials and Methods

Bis(triphenylphosphine) iridium(I) carbonyl chloride, (Vaska's complex, 99.99%, Sigma Aldrich), chloroform ($CHCl_3$, 99.8%, Sigma Aldrich), benzyl alcohol (BA, ≥99%, Sigma Aldrich), perdeuterated (d_6-)benzene (99.5% D, Cambridge Isotope Laboratories, Inc), and iodine (99.8%, Fisher Scientific) were used as received.

VC-I_2 solutions were prepared by dissolving 6 mg of Vaska's complex with 2 mg of iodine in 2 mL of solvent. These solutions were first capped and parafilmed and then sonicated for at least 1 hour in a water bath. All solutions were filtered through a 0.2 µm syringe filter before being placed in the sample cell. Typical VC concentrations were 4 mM. Solutions were used within 9 days of preparation. Solutions of the mixed solvents were stored in small vials with minimal headspace to reduce possible solvent composition changes due to evaporation. The sample cell had a path length of 150 µm.

Infrared spectra were collected on a Nicolet 6700 FTIR spectrometer (Thermo Scientific) with at least 16 scans and a typical resolution of 1 cm^{-1}. IR pump-probe

spectra were collected for all samples in a previous study and were used for phase corrections to the 2D-IR data.[210, 218]

The laser system used for 2D-IR and pump-probe spectroscopy was the same as that described in Chapters 2 and 3. The resulting spectra were then analyzed using the ω_m center line slope (CLS) procedure developed by Kwak and coworkers in order to extract the FFCF from the 2D-IR data directly, as described in Chapter 2.[116-117]

5.4. Results and Discussion

The frequency of the carbonyl stretch on VC-I$_2$ is effectively invariant to solvent composition for a wide range of solvents, including the three studied here.[104, 210] In contrast, the FTIR linewidth changes significantly as the bulk solvent composition is varied linearly in binary mixtures of either CHCl$_3$ or BA in d_6-benzene.[104, 210] Herein we define the solvent composition by the mole fraction metric, but we have also considered the data as a function of volume fraction and found the observed trends to be the same. Figure 5.2 shows the FWHM values for the CO vibration on VC-I$_2$ as a function of the mole fraction of CHCl$_3$ (black circles) and BA (red squares). The full linear spectra are available in previous publications.[104, 210] The change in spectral width is most drastic in the CHCl$_3$/d_6-benzene mixtures, varying monotonically and in a mostly linear fashion from 8 cm^{-1} in pure d_6-benzene to nearly 17 cm^{-1} in pure CHCl$_3$.[210] A linear variation of a spectral variable with the solvent mole fraction would indicate that the static and dynamic influences of the solvation shell(s) on the carbonyl frequency change in a proportional manner. This does not imply that the solvent shell composition is the same as the bulk

solvent mixture, which it likely is not, but simply that it changes uniformly as the bulk composition is varied. If nonlinear behavior is observed, this is interpreted as preferential solvation in which the solvent shell composition and/or dynamics are more heavily dominated by one solvent over the other.[15, 18-19, 23, 36]

A closer examination of the $CHCl_3$ data in Figure 5.2 reveals a slight variation in slope when only the first or last three points are fit to a line. The bulk composition of the surrounding solvent is changing linearly, but the influence on the linewidth is not perfectly linear over the entire range. We see that the broadening is slower (lower slope) at solvent compositions that have a majority of d_6-benzene than those that have a majority of $CHCl_3$. Whatever the underlying origins are for carbonyl FTIR lineshape broadening, which is the subject of this paper, they are preferentially affected by d_6-benzene over $CHCl_3$ and require higher bulk concentrations of $CHCl_3$ before the influence of this secondary solvent dominates. Using the point at which the trend lines cross we can say that between 0.5 and 0.6 mole fractions of $CHCl_3$ the linewidth trend begins to converge on the neat chloroform FWHM. Although the total broadening is smaller for the carbonyl vibration in BA mixtures in Figure 5.2 (note different y-axis scale), it is more clearly nonlinear indicating preferential solvation of VC-I$_2$ by this solvent over d_6-benzene. The low and high mole fraction trend lines cross between 0.1 and 0.2 mole fractions and the low mole fraction line has the higher slope, indicating that a small amount of BA has a disproportionately large influence on the FTIR linewidth over d_6-benzene.
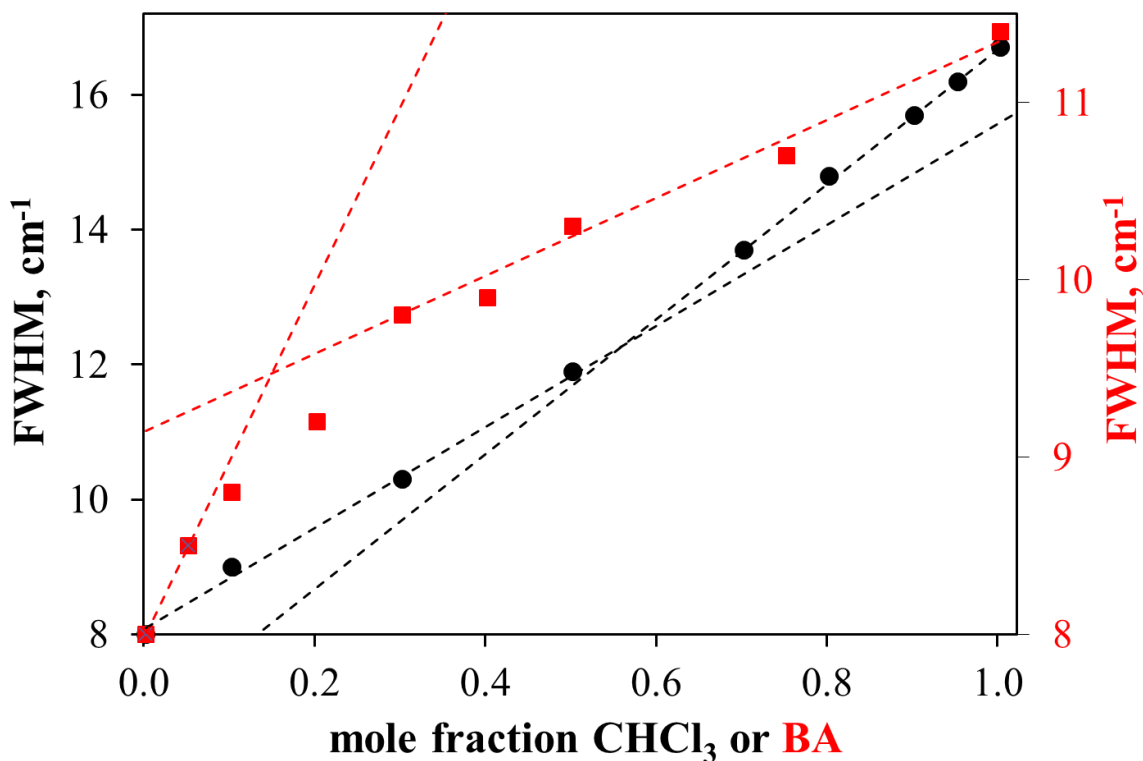
Figure 5.2. Full width at half maxima (FWHM) for the linear lineshapes of the CO on VC-I_2 in binary solvent mixtures of $CHCl_3$ (black circles) and BA (red squares) in d_6-benzene. Dashed lines are linear regression fits to the first or last points.

Understanding the reasons for the nonlinear evolution of the CO linewidth for VC-I_2 is the purpose of this study. As mentioned above, the dynamical variables that contribute to the spectral linewidths are T_2^*, T_1, and T_{orient}, and we can directly quantify these contributions with IR pump-probe and 2D-IR spectroscopies. We have previously reported the vibrational lifetimes for this complex in the $CHCl_3$ and BA binary mixtures with d_6-benzene.[210] It was shown that T_1 increases linearly in $CHCl_3$ but *decreases* linearly in BA, despite the fact that both show an increase in the overall linewidth (see Figure 5.2), indicating that some other factor is the likely cause of this broadening. In addition, the T_1 values for the VC-I_2 carbonyl in these solvents are so long that their

contribution to the overall lineshape is comparatively miniscule. For example, the vibrational lifetimes in neat d_6-benzene, $CHCl_3$, and BA are 193, 216, and 124 ps, respectively, which contribute 0.03, 0.02, and 0.04 cm^{-1} to the homogeneous linewidth. Based on its molecular size, we can estimate that T_{orient} is of order of hundreds of ps. Similarly-sized complexes were reported to have rotational times of 150 – 400 ps in solvents of similar viscosity to those used in this study, also giving a small linewidth contribution of 0.02 – 0.009 cm^{-1}.[219-220] This number would be similar in all solvent mixtures since the solute is the same throughout these studies. Moving forward, we conclude that the contributions of T_1 and T_{orient} to the homogeneous lineshape are negligible and focus our attention on determining the time scales of T_2* and spectral diffusion as measured by 2D-IR spectroscopy. As we will show below, this approximation is justified since these two terms contribute only a few percent of the homogeneous linewidth.

Representative 2D-IR plots give qualitative insight into the dynamics present in these systems. The 2D-IR spectra for every T_w measured for all binary solvent mixtures are provided in Figures 5.8-5.22. Figure 5.3 shows the 2D-IR spectra at a short (0.3 ps, top row) and a long (30 ps, bottom row) T_w for each of the three neat solvents and their corresponding 0.5 mole fraction mixtures. A 2D-IR spectrum is a frequency correlation plot for the subensembles beneath the FTIR lineshape.[108, 110, 145, 148-150, 194] The red positive-going peaks show the bleached v=0 to v=1 transition, while the blue negative-going peaks are the v=1 to v=2 vibrational excited state absorption that is shifted by the anharmonicity to lower frequencies. Assuming sufficient separation between the 0-1 and

1-2 peaks, the projection of a diagonal slice through the 0-1 peak onto either axis reflects

the linear lineshape, which is of course more easily obtained from an FTIR measurement.

However, new information is obtained along the antidiagonal dimension of the 2D-IR

spectrum.   In the absence of spectral diffusion of oscillators from one solvent

configuration to another, the antidiagonal width reports the homogeneous lineshape. In

most cases interconversion of molecular sub-ensembles driven by the reorganization of

solvent molecules in the first few solvation shells leads to broadening along the

antidiagonal dimension as T_w increases.   Even at short T_ws (top row, Figure 5.3),

presumably some spectral diffusion has occurred and an antidiagonal slice is already

broader than the homogeneous linewidth. After describing the qualitative features of the

2D-IR spectra below, CLS decay analysis will be used to quantitatively characterize the

homogeneous and inhomogeneous contributions to the VC-I_2 carbonyl lineshape for each

of the binary solvent mixtures.

Figure 5.3e (top middle frame) shows the early T_w 2D-IR spectrum for d_6-benzene

with characteristic diamond-shaped peaks that indicate that the lineshape is primarily

homogeneously broadened.[108, 221] At this T_w there is some elongation along the diagonal

due to inhomogeneity, but the peaks become symmetric by 30 ps (Figure 5.3f) through

spectral diffusion. Moving to the left, the d_6-benzene is progressively diluted with $CHCl_3$

and the lineshapes become diagonally elongated. The dramatic broadening with

increasing proportion of $CHCl_3$ shown in the FTIR spectra is reflected here.

Qualitatively, the lineshapes do not differ largely apart from the broadening and loss of

the diamond shape. At 0.3 ps, the frequencies of the CO stretch during the initial and

final coherences are strongly correlated with one another. By 30 ps this is no longer the case; each of the lower spectra shows a rounded lineshape. The same trend is observed moving to the right of the middle frames in Figure 5.3, diluting the d_6-benzene with a more polar solvent, though for BA the broadening is more modest. In contrast to the $CHCl_3$ mixtures, there are clear dynamical differences shown in these spectra. Notice particularly that the peak is slightly thinner along the antidiagonal dimension in pure BA (Figure 5.3i) as opposed to the 0.5 mole fraction mixture (Figure 5.3g). Comparing short to long T_ws for binary mixtures of $CHCl_3$ (Figures 5.3a-5.3d) to those of BA (Figures 5.3g-5.3j) shows that all of the dynamics have been sampled by 30 ps in $CHCl_3$, whereas the BA samples remain visibly elongated along the diagonal. The $CHCl_3$ and d_6-benzene solvation dynamics have enabled all of the carbonyl oscillators on $VC-I_2$ to sample all of the available frequencies under the linear lineshape by 30 ps, but in BA and BA/d_6-benzene mixtures some oscillators still remain partially correlated with their starting frequencies.
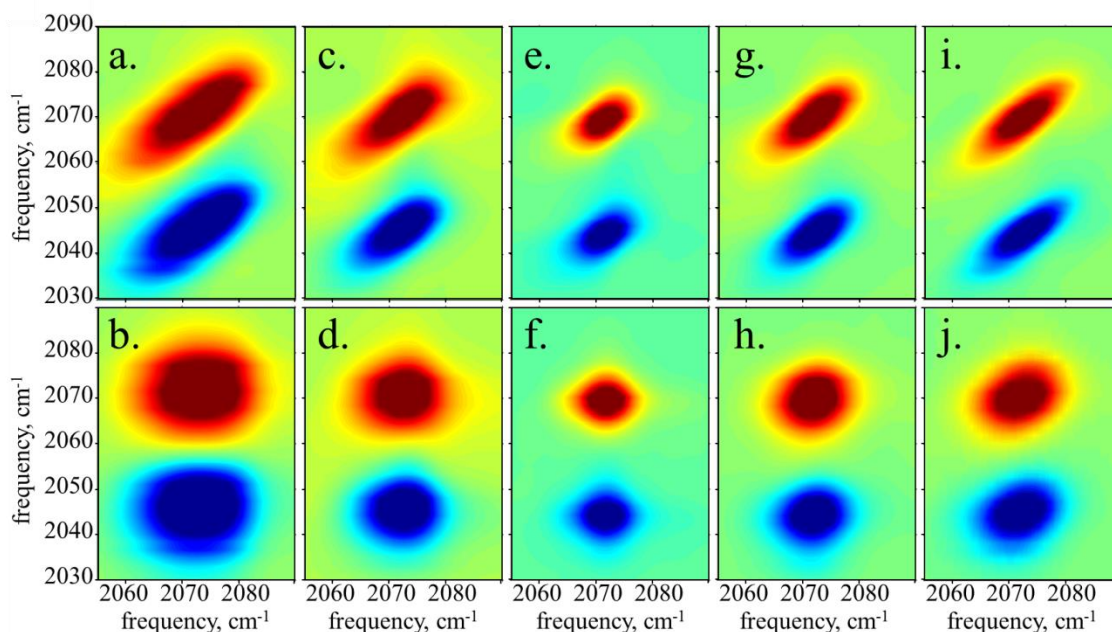
Figure 5.3. 2D-IR spectra collected at $T_w = 0.3$ ps (top row) and 30 ps (bottom row) for a) and b) neat $CHCl_3$, c) and d) 0.5 mole fraction $CHCl_3$ in d_6-benzene, e) and f) neat d_6-benzene, g and h) 0.5 mole fraction BA in d_6-benzene, and i and j) neat BA.

In order to quantify the data, we used the CLS:ω_m method outlined by Fayer and coworkers and previously mentioned in Chapter 2.[116-117] Recall that this method takes slices parallel to the y-axis (ω_m) in Figure 5.3 and fits the positive going maxima to a peak function. These peak points are then connected to form a line that tracks the ridge over the 0-1 transition. For these data, as T_w increased in the 2D-IR pulse sequence, the slope of this line evolved from a positive slope when the peak shape was elongated along the diagonal (e.g. Figure 5.3a) to a slope of zero when spectral diffusion was complete and the band shape was horizontally symmetric (e.g. Figure 5.3b). The CLS decay is commonly modeled as a sum of exponential decays and has been rigorously shown to provide a normalized analogue of the FFCF.[116-117] The FFCF also includes a

homogeneous term, which will be discussed below. In the limit of $T_w = 0$ (CLS y-intercept), deviations of the CLS from unity are the result of homogeneous broadening and very fast spectral diffusion. Using the linear spectrum, this normalized deviation can be used to determine the actual homogeneous linewidth and the unnormalized FFCF with amplitudes and time constants that are directly comparable to the results from MD simulations.[116-117, 153, 222]

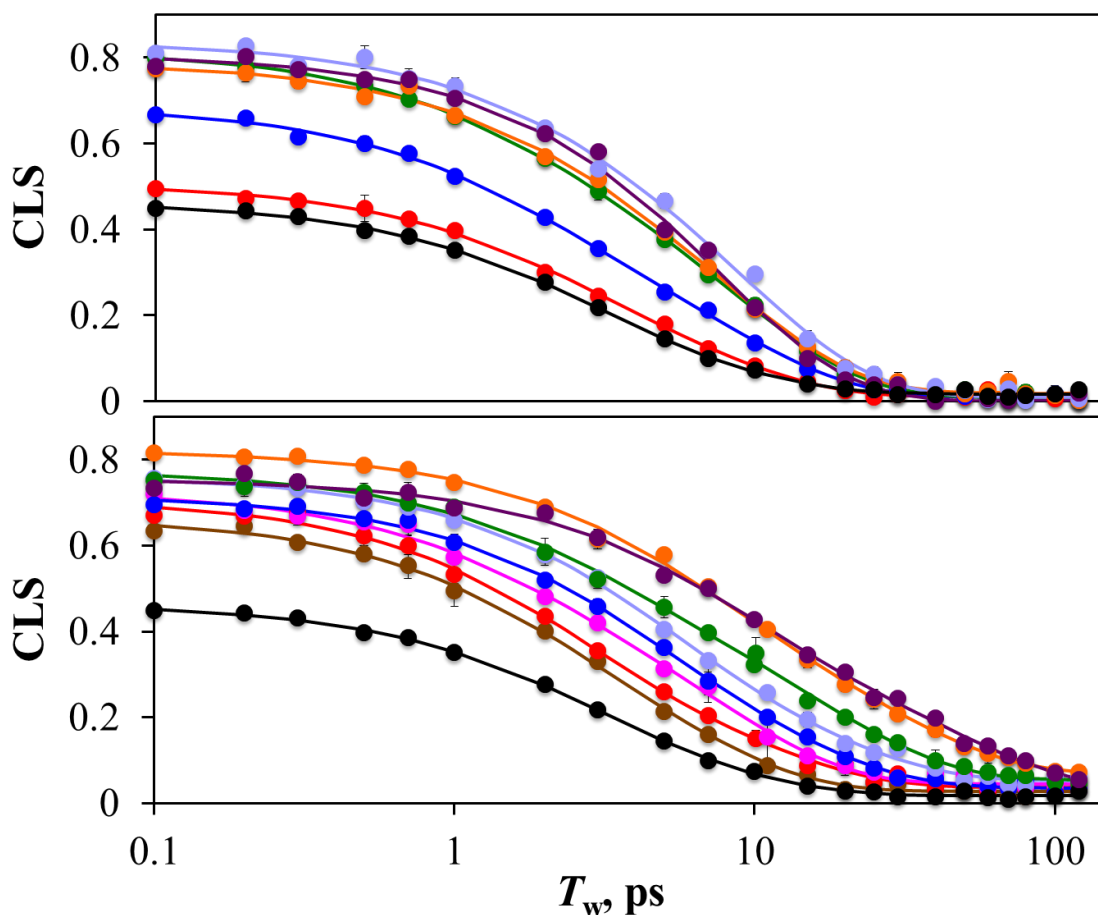**Figure 5.4:** CLS decays as a function of T_w for binary mixtures of a) 0 (black), 0.1 (red), 0.3 (blue), 0.5 (green), 0.7 (orange), 0.9 (lavender), and 1 (purple) mole fraction $CHCl_3$ in d_6-benzene; and b) 0 (black), 0.05 (brown), 0.1 (red), 0.2 (pink), 0.3 (blue), 0.4 (lavender), 0.5 (green), 0.7 (orange), 1 (purple) mole fraction BA in d_6-benzene. Overlaid solid lines are the multi-exponential fits to the data markers.

Figures 5.4a and 5.4b show the CLS values as a function of T_w overlaid with a multi-exponential fit for both types of binary solvent mixtures. The markers represent a mean CLS measured for between three to six different 2D-IR spectra and the error bars, which in many cases are smaller than the size of the markers, show the standard deviations from the mean. The solid lines are a multi-exponential plus a constant fit to the complete set of values (not simply the mean), and it can be seen that the signal-to-noise ratio is very high and the fits are very good. The black curve in each frame shows the CLS decay in neat d_6-benzene, and it is clear that both $CHCl_3$ and BA have the effect of increasing the y-intercept. Consistent with the 2D-IR spectral observations in Figure 5.3, the $CHCl_3$ mixtures show decays that reach their minimum values at similar times well before 50 ps. The BA mixtures take increasingly longer to decay, indicating that the dynamics are slower. The best fit parameters to these decays are given in Table 5.2. However, it is instructive to view these graphically to assess the dynamical trends.

The FFCF was modeled according to Equation 5.2, except in the case of pure chloroform, where only the first two terms were necessary:

$$FFCF(t) = \frac{\delta(t)}{T_2} + \Delta_1{}^2 \exp\left(\frac{-t}{\tau_1}\right) + \Delta_2{}^2 \exp\left(\frac{-t}{\tau_2}\right) + \Delta_0{}^2 \qquad (5.2)$$

The time constants (τ_1 and τ_2) in this equation were obtained directly from fitting the CLS decays in Figure 5.4, which has been shown to be highly accurate.[116-117] However, the amplitudes of each exponential contribution assume a FFCF normalized to unity and the y-intercept is likewise normalized and may include contributions from very fast spectral diffusion. Following the procedure by Kwak and coworkers, the amplitudes from the fits

to the CLS decays and the linear FWHMs were used to calculate approximate values for the unnormalized amplitudes (Δ_i) and T_2.[116-117] These starting values were then applied to a FFCF and the first order response function was used to reproduce the linear lineshape. The amplitudes, as well as the central frequencies, were iteratively varied to fit the linear lineshape. Only Δ values for those terms where the time constants were small compared with the free induction decay (FID, obtained from the Fourier transform of the linear spectrum) were allowed to float, where small is defined as less than five times the FID decay time. The CLS method was developed using the short-time approximation, which underestimates the values for Δ_i and T_2 due to the method's inability to distinguish between homogeneous terms and fast (compared with FID) spectral diffusion. Thus, the floated Δ_i and T_2 values were constrained to only increase from the estimated values. In all cases, the Δ_i values that were fit did not change from the initial guesses. The wings of the lineshapes of the linear spectra in mixtures containing the majority of $CHCl_3$ did not fit well due to the asymmetry of the peak,[104, 210] but the widths were well reproduced. The fit parameters are given in Table 5.1. The fitted center frequencies and T_2 values are given in Table 5.3. The homogeneous linewidths Γ were calculated from the T_2 values using Equation 5.1 and are also included in Table 5.1. The errors on each parameter are included in parentheses as a single ($\pm$) value or independent positive and negative (+/-) values.
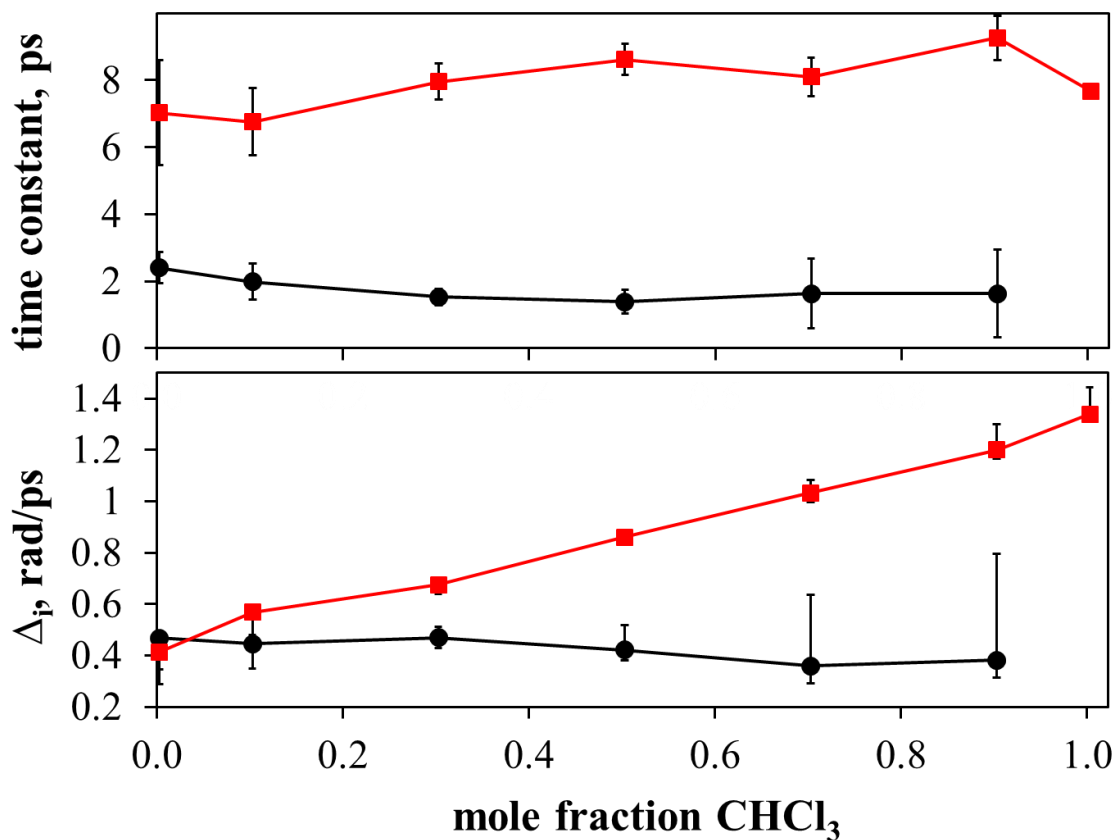
Figure 5.5: Graphical representation of full FFCF parameters for binary mixtures of CHCl$_3$ in d_6-benzene showing a) the τ_1 (black circles) and τ_2 (red squares) and b) Δ_1 (black circles) and Δ_2 (red squares). Error bars in a) represent the standard error of the fit. Positive error bars in b) show the range of values for which the FTIR lineshape is fit 98% as well as the best value. Since the amplitudes were constrained positively (see text), the negative error bars in b) represent the propagated error of the CLS fits.

Table 5.1: FFCF parameters for BA and CHCl$_3$ binary mixtures in d_6-benzene.

m. f.	Δ_1 (rad/ps)	τ_1 (ps)	Δ_2 (rad/ps)	τ_2 (ps)	Δ_0 (rad/ps)	Γ (cm^{-1})
			CHCl$_3$ in d_6-benzene			
0	0.47 (0.02/0.12)	2.4 (0.5)	0.41 (0.01/0.12)	7.0 (1.6)	0.12 (0.03/0.05)	2.3 (0.1/0.1)
0.1	0.44 (0.02/0.10)	2.0 (0.5)	0.57 (0.01/0.09)	6.8 (1.0)	0.10 (0.03/0.03)	1.9 (0.1/0.1)
0.3	0.49 (0.04/0.04)	1.5 (0.2)	0.68 (0.01/0.04)	8.0 (0.5)	0.10 (0.07/0.02)	2.3 (0.2/0.1)
0.5	0.42 (0.10/0.04)	1.4 (0.4)	0.86 (0.02/0.03)	8.6 (0.5)	0.10 (0.15/0.02)	2.2 (0.5/0.2)
0.7	0.36 (0.27/0.07)	1.6 (1.0)	1.03 (0.05/0.04)	8.1 (0.6)	0.17 (0.26/0.02)	1.9 (1.6/0.2)
0.9	0.38 (0.42/0.07)	1.6 (1.3)	1.20 (0.10/0.03)	9.3 (0.7)	0.13 (0.84/0.02)	2.1 (2.6/0.1)
1			1.34 (0.11/0.002)	7.7 (0.1)		2.2 (0.3/0.3)
			BA in d_6-benzene			
0	0.47 (0.02/0.12)	2.4 (0.5)	0.41 (0.01/0.12)	7.0 (1.6)	0.12 (0.03/0.05)	2.3 (0.1/0.1)
0.05	0.39 (0.02/0.19)	1.8 (0.7)	0.53 (0.01/0.18)	5.9 (1.1)	0.14 (0.02/0.07)	2.5 (0.1/0.1)
0.1	0.5 (0.01/0.1)	2.2 (0.4)	0.47 (0.01/0.1)	9.6 (1.8)	0.16 (0.02/0.04)	2.2 (0.1/0.1)
0.2	0.35 (0.03/0.09)	1.4 (0.6)	0.62 (0.01/0.07)	7.6 (0.8)	0.18 (0.02/0.03)	1.9 (0.1/0.1)
0.3	0.52 (0.01/0.12)	3.6 (0.8)	0.56 (0.01/0.12)	12.3 (2.1)	0.17 (0.03/0.05)	1.6 (0.2/0.1)
0.4	0.56 (0.01/0.08)	4.2 (0.6)	0.53 (0.01/0.08)	15.9 (2.4)	0.21 (0.02/0.03)	1.6 (0.2/0.1)
0.5	0.45 (0.02/0.04)	2.6 (0.5)	0.66 (0.01/0.04)	16.8 (1.5)	0.22 (0.02/0.02)	1.5 (0.1/0.1)
0.7	0.53 (0.01/0.05)	5.6 (0.9)	0.62 (0.01/0.06)	26.8 (3.6)	0.25 (0.02/0.03)	0.9 (0.1/0.1)
1	0.62 (0.01/0.05)	7.5 (1.0)	0.65 (0.01/0.04)	45.4 (9.3)	0.18 (0.03/0.06)	0.7 (0.1/0.1)

Figure 5.5 plots the time constants and Δ_i values of the exponential components of the determined FFCF. All decays were fit well with a biexponential (plus a constant offset) except for the neat $CHCl_3$, which was sufficiently modeled with a single exponential. Within error, the time constants for spectral diffusion are independent of the mole fraction of $CHCl_3$, having values of ~2 ps and ~8 ps in all mixtures. It is obligatory to state that connecting the time scales from the FFCF to microscopic events is not readily achieved with 2D-IR alone. What we can say is that the characteristic time scales for frequency decorrelation, regardless of their molecular origins, are unaffected by changing the $CHCl_3/d_6$-benzene composition. The Δ_i values (Figure 5.5b), however, show that there is a steady increase in the magnitude of the ~8 ps dynamics while the ~2 ps dynamic contribution diminishes and vanishes in neat $CHCl_3$. Conceptually, the Δ_i values indicate the magnitude of the frequency fluctuations that are being modulated on a time scale of τ_i. With no changes in the time scale of a dynamical process, increasing Δ leads to faster decorrelation of vibrational modes in the ensemble, a faster free induction decay, and therefore a broader linear lineshape. Taken together, these two frames paint a picture of spectral diffusion that is driven by two dominant processes in d_6-benzene, perhaps a molecular motion in VC-I_2 that modulates the carbonyl frequency and is coupled to the solvent shell and a proximal solvent motion that more directly affects the CO mode. Although this is conjecture in the absence of corroborating simulations, Figures 5.5a and 5.5b might then show the change in the intramolecular potential in the former case with additional $CHCl_3$ and the loss of the latter contribution as d_6-benzene is progressively diluted and replaced with $CHCl_3$ in the solvation shell. Within the error

bars of these measurements, the Δ_i values change in an effectively linear fashion with mole fraction, but it can be seen in Figure 5.5a that the longer time constants of spectral diffusion show a slight increase up to about the 0.5 mole fraction before leveling off. Here we see that the time constants for spectral diffusion are the only parameters in the FFCF that show any correlation with the change in the rate of broadening in Figure 5.2. It is a minor effect, but the time constant getting slightly longer would cause the rate of broadening to be somewhat slower up to 0.5 mole fraction.
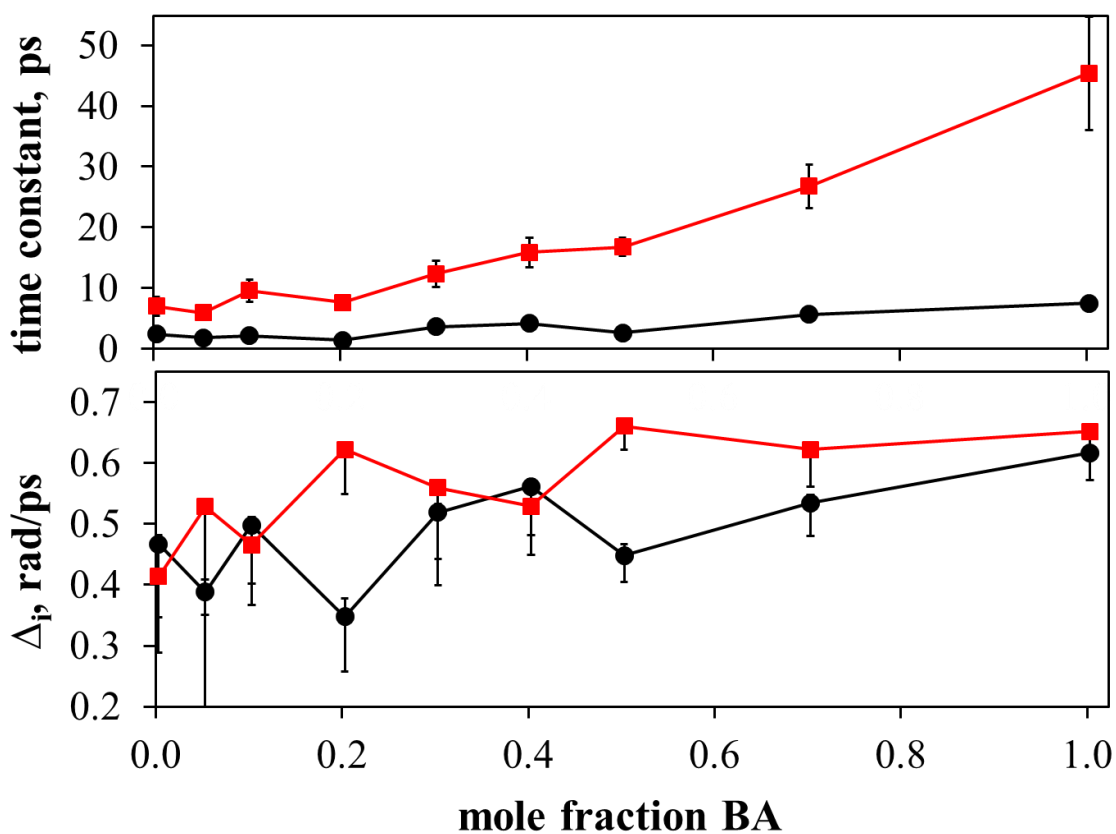
Figure 5.6. Graphical representation of full FFCF parameters for binary mixtures of BA in d_6-benzene showing a) the τ_1 (black circles) and τ_2 (red squares) and b) Δ_1 (black circles) and Δ_2 (red squares). Error bars in a) represent the standard error of the fit. Positive error bars in b) show the range of values for which the FTIR lineshape is fit 98% as well as the best value. Since the amplitudes were constrained positively (see text), the negative error bars in b) represent the propagated error of the CLS fits.

The dynamical behavior is notably different when d_6-benzene is diluted instead with the more polar BA, which we believe to preferentially solvate VC-I_2 over benzene. Figures 5.6a and 5.6b show the τ and Δ values of the FFCF. The time constants increase progressively while the magnitudes of the frequency fluctuations are anticorrelated and show very minor changes with mole fraction of BA. In comparison to the $CHCl_3$ mixtures, it can be said that the time scales of CO decorrelation progressively become much slower from ~2 ps and ~8 ps in neat d_6-benzene to ~8 ps and ~45 ps, respectively, in neat BA. Furthermore, both time constants only begin to increase significantly beginning around 0.2 mole fraction, the approximate area where the linear FWHM changed its slope (see Figure 5.2). This is accompanied by a mild nonlinear increase in the Δ_2 value in this same range in Figure 5.6b, indicating that while this process is becoming characteristically slower, the magnitudes of the frequency fluctuations become larger. Thus we can see in this graphical representation of the FFCF parameters that there is nonlinear behavior in the spectral diffusion with mole fraction of BA, showing that preferential solvation of VC-I_2 by BA over d_6-benzene leads to corresponding changes in the inhomogeneous dynamics.
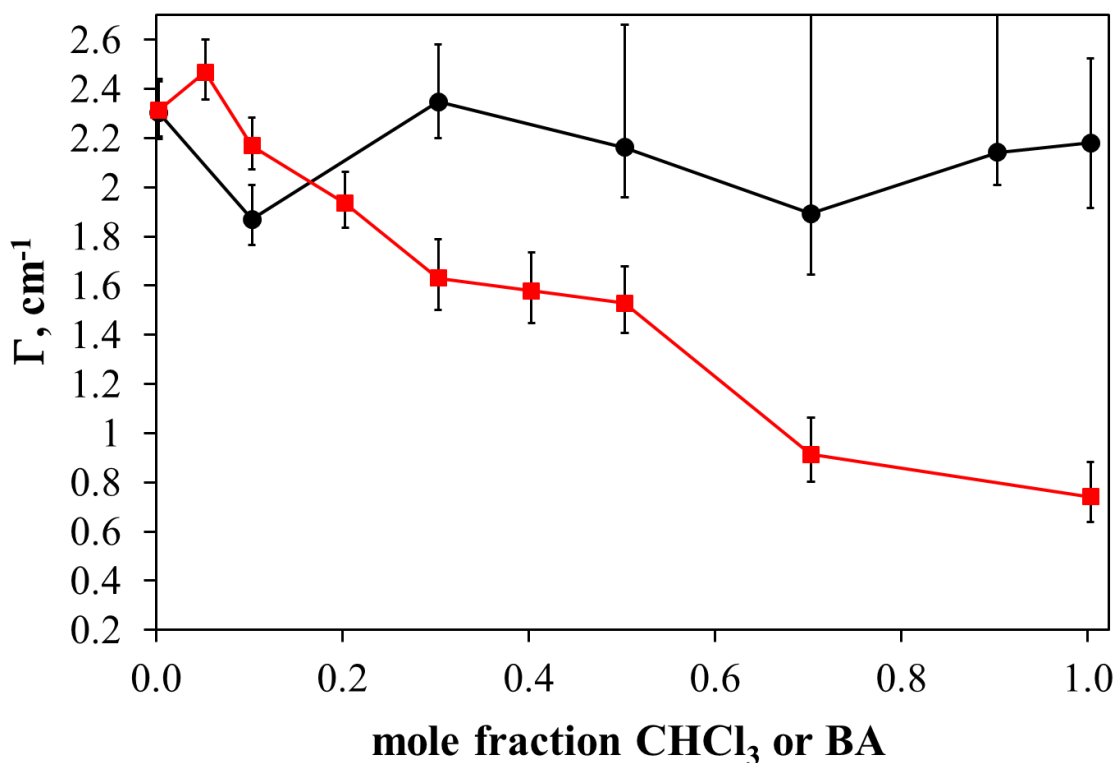
Figure 5.7. Homogeneous linewidth (Γ, cm^{-1}) as a function of mole fraction for CHCl$_3$ (black) and BA (red) mixtures. Error bars represent the range of values for which the FTIR lineshape is fit 99% as well as the best value (except where noted in Table 5.1).

The final piece in this spectral broadening puzzle is to consider the homogeneous contribution to the linewidth across both binary solvent mixtures. Figure 5.7 shows the homogeneous linewidth as calculated from T_2 for both sets of mixtures (CHCl$_3$ = black circles, BA = red squares) as a function of mole fraction. The values are typically on the order of a few wavenumbers. Considering the T_1 and T_{orient} contributions as they were calculated above, this demonstrates that the T_2^* contribution is dominant. Intriguingly, the CHCl$_3$ mixtures show virtually no change in Γ as the d_6-benzene is diluted with CHCl$_3$ in spite of the fact that the linear linewidth more than doubles! This reveals that this enormous and dramatic broadening shown in the FTIR is almost entirely due to an

increase in the variety of solvation environments and spectral diffusion. Since the time constants also remain nearly the same for this system over the entire range of solvent compositions, the most significant source of this inhomogeneous broadening (apart from the natural increase in the number of environments that occurs when adding a more polar solvent) is the increase in Δ_1, the magnitude of the frequency shifts for the slow spectral diffusion component. Closer examination of the FFCF parameters shows that there is also a corresponding small increase in the FFCF constant offset with mole fraction, showing that the increase in inhomogeneous broadening also includes some slow unresolved processes (see Table 5.1).

In contrast, the Γ for the BA mixtures shows considerable decrease throughout the range of solvent compositions from a value of ~2.3 cm^{-1} in pure d_6-benzene to ~0.7 cm^{-1} in pure BA. This is again consistent with the observations made concerning the 2D-IR spectra of the BA mixtures that the pure BA sample had a visibly thinner lineshape at the short T_ws. Considering that the FTIR linewidth increases by almost half, this is also a striking result. Again, the increased broadening is certainly not coming from the homogeneous linewidth, but rather from inhomogeneous broadening. The increase in the characteristic time scales of spectral diffusion shown in Fig. 5.6a would narrow the lineshape rather than broadening it, but this could be counteracted by increases in Δ. Therefore we must conclude that the nonlinear increase in linewidth up to 0.2 mole fraction of BA cannot be the result of homogenous broadening. Furthermore, the intuitive expectation that a more polar solvent should lead to greater inhomogeneous

contributions is recovered, despite a narrower linear lineshape in BA versus $CHCl_3$, since the BA induces a decrease in Γ that counters the increase in inhomogeneity.

5.5. Conclusions

Despite a lack of solvatochromism,[104, 210] the linear linewidth of the carbonyl on VC-I_2 varies dramatically and nonlinearly when d_6-benzene is systematically replaced by $CHCl_3$ or BA. The broadening is more pronounced in $CHCl_3$, which is surprising considering that BA is more polar. Herein we have used FTIR and 2D-IR spectroscopies to tease apart the major contributing factors to these lineshapes, in the process establishing the full FFCF for this vibration across a range of binary mixed solvents. With this information, the homogenous and inhomogeneous broadening contributions are determined. The primary contributor to the homogeneous linewidth is pure dephasing for VC-I_2, and we have shown that this contribution is unchanged across all mixtures of $CHCl_3$ in d_6-benzene while decreasing significantly for BA mixtures. This demonstrates that the gains in linear linewidth in both cases must have their origins in inhomogeneous contributions.

Using CLS decay analysis, we characterized the inhomogeneous broadening as well. The BA mixtures have much slower characteristic time scales for spectral diffusion than are present in d_6-benzene or any of the $CHCl_3$ mixtures. BA is about ten times more viscous than $CHCl_3$ or d_6-benzene, it is known to be a relatively strong hydrogen bond donor, and its higher dipole moment certainly strengthen the interactions with VC-I_2, and any of these factors could explain the slowed dynamics. Yet slower time constants in the

FFCF generally lead to lineshape narrowing, and so these temporal differences cannot be the reason for spectral broadening. The explanation lies in the corresponding increases in the magnitudes of the frequency fluctuations in the FFCF that correlate with the preferential solvation profile of the lineshapes in both types of solvent mixtures with mole fraction. Furthermore, ignoring contributions from spectral diffusion to the linewidth and simply taking the ratio of the FWHM to the homogeneous linewidth in each neat solvent, we obtain a value for d_6-benzene of 3.5, for chloroform of 7.4, and for benzyl alcohol 15.5. This trend, unlike that of the absolute FTIR width, is consistent with that expected for these solvents considering their relative dipole moments.

Overall, we have taken the vibrational mode on the adduct of a model catalyst and applied an in-depth evaluation of the origins of spectral broadening. Our results show how straightforward analysis of 2D-IR lineshapes can be used to uncover otherwise lost dynamical information about the solvation dynamics. A natural extension of these experiments would be to investigate the influence of changing the *trans* ligand to one that is perhaps more sensitive to its solvation environment in order to determine whether the dynamics sensed by the reporter reflect the active site of the catalyst. We will investigate this in the following chapter.[c]

Table 5.2: Fit parameters to CLS decays

mole frac.	A_1 (norm.)	τ_1 (ps)	A_2 (norm.)	τ_2 (ps)	A_0 (norm.)	A_{total} (norm.)
CHCl$_3$ in d_6-benzene						
0	0.25 (0.08)	2.4 (0.5)	0.20 (0.08)	7.0 (1.6)	0.017 (0.002)	0.46 (0.11)
0.1	0.19 (0.07)	2.0 (0.5)	0.31 (0.07)	6.8 (1.0)	0.010 (0.002)	0.51 (0.10)
0.3	0.22 (0.03)	1.5 (0.2)	0.46 (0.03)	8.0 (0.5)	0.009 (0.002)	0.69 (0.04)
0.5	0.16 (0.03)	1.4 (0.4)	0.65 (0.03)	8.6 (0.5)	0.009 (0.003)	0.82 (0.05)
0.7	0.08 (0.05)	1.6 (1.0)	0.69 (0.05)	8.1 (0.6)	0.019 (0.004)	0.775 (0.007)
0.9	0.08 (0.05)	1.6 (1.3)	0.75 (0.05)	9.3 (0.7)	0.009 (0.005)	0.821 (0.006)
1			0.808 (0.004)	7.7 (0.1)		0.808 (0.004)
BA in d_6-benzene						
0	0.25 (0.08)	2.4 (0.5)	0.20 (0.08)	7.0 (1.6)	0.017 (0.002)	0.46 (0.11)
0.05	0.22 (0.12)	1.8 (0.7)	0.42 (0.12)	5.9 (1.1)	0.027 (0.004)	0.67 (0.17)
0.1	0.36 (0.07)	2.2 (0.4)	0.31 (0.07)	9.6 (1.8)	0.036 (0.005)	0.71 (0.10)
0.2	0.16 (0.05)	1.4 (0.6)	0.52 (0.06)	7.6 (0.8)	0.045 (0.005)	0.73 (0.08)
0.3	0.32 (0.09)	3.6 (0.8)	0.37 (0.09)	12.3 (2.1)	0.035 (0.004)	0.718 (0.13)
0.4	0.38 (0.07)	4.2 (0.6)	0.33 (0.06)	15.9 (2.4)	0.052 (0.004)	0.763 (0.09)
0.5	0.23 (0.03)	2.6 (0.5)	0.49 (0.03)	16.8 (1.5)	0.054 (0.005)	0.774 (0.05)
0.7	0.32 (0.05)	5.6 (0.9)	0.43 (0.05)	26.8 (3.6)	0.069 (0.008)	0.822 (0.07)
1	0.34 (0.04)	7.5 (1.0)	0.38 (0.03)	45.4 (9.3)	0.028 (0.019)	0.756 (0.06)

Table 5.3: Additional fit parameters from linear response function to reproduce linear lineshape.

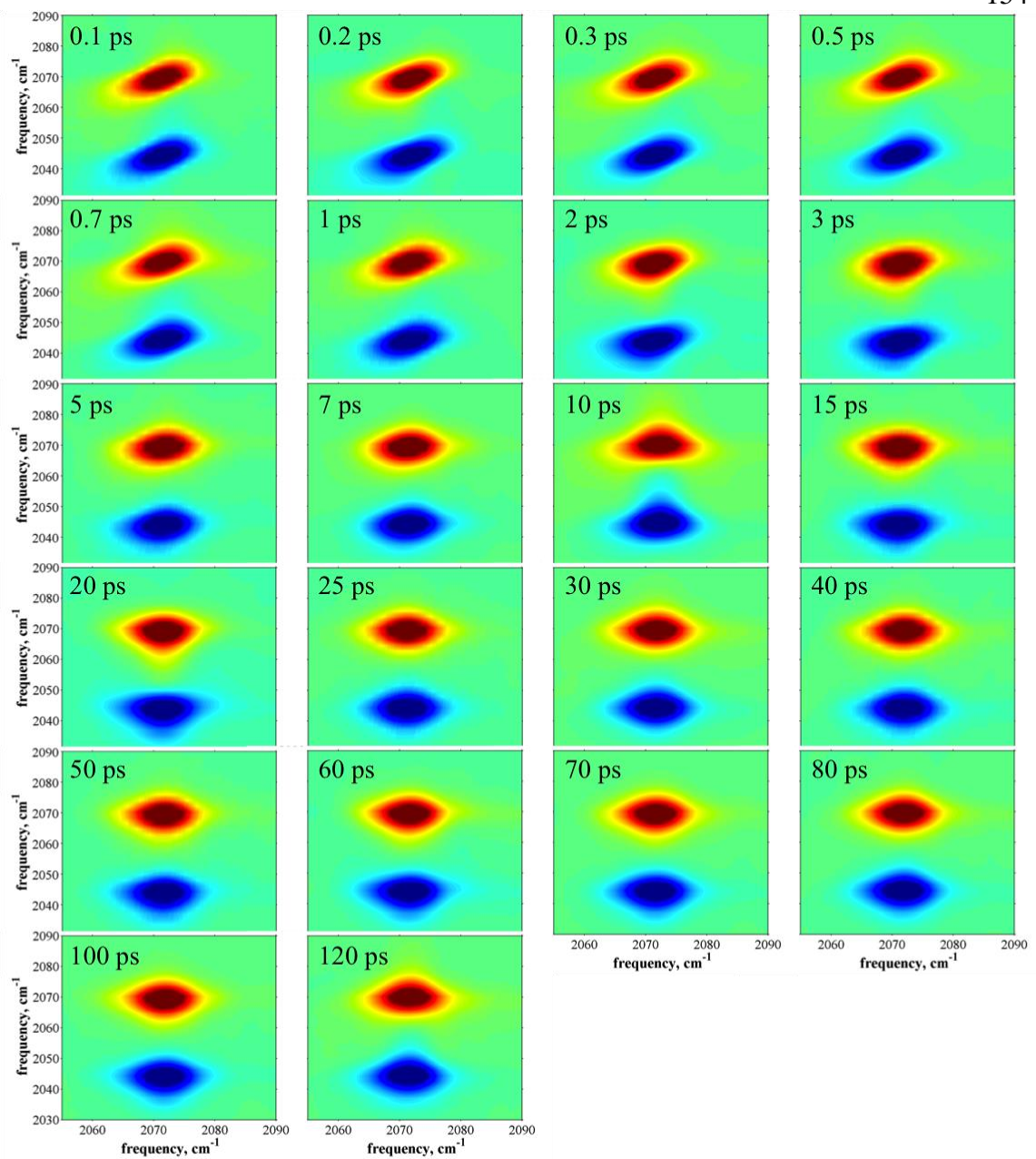| mole fraction	T_2 (ps)	ν_{CO} (cm^{-1})
CHCl$_3$ in d_6-benzene		
0	4.6 (0.3/0.2)	2068.6
0.1	5.7 (0.4/0.3)	2068.8
0.3	4.5 (0.4/0.3)	2069.1
0.5	4.8 (1.1/0.5)	2069.3
0.7	5.6 (4.6/0.7)	2069.4
0.9	5 (6.1/0.3)	2069.6
1	4.9 (0.8/0.6)	2069.7
BA in d_6-benzene		
0	4.6 (0.3/0.2)	2068.6
0.05	4.3 (0.2/0.2)	2068.7
0.1	4.9 (0.3/0.2)	2068.8
0.2	5.5 (0.4/0.3)	2068.9
0.3	6.5 (0.6/0.5)	2068.9
0.4	6.7 (0.7/0.6)	2069.0
0.5	6.9 (0.7/0.6)	2069.1
0.7	11.6 (1.9/1.4)	2069.1
1	14.3 (2.7/2.0)	2069.2

Figure 5.8: 2D-IR spectra for all T_w values for VC-I_2 in neat d_6-benzene.
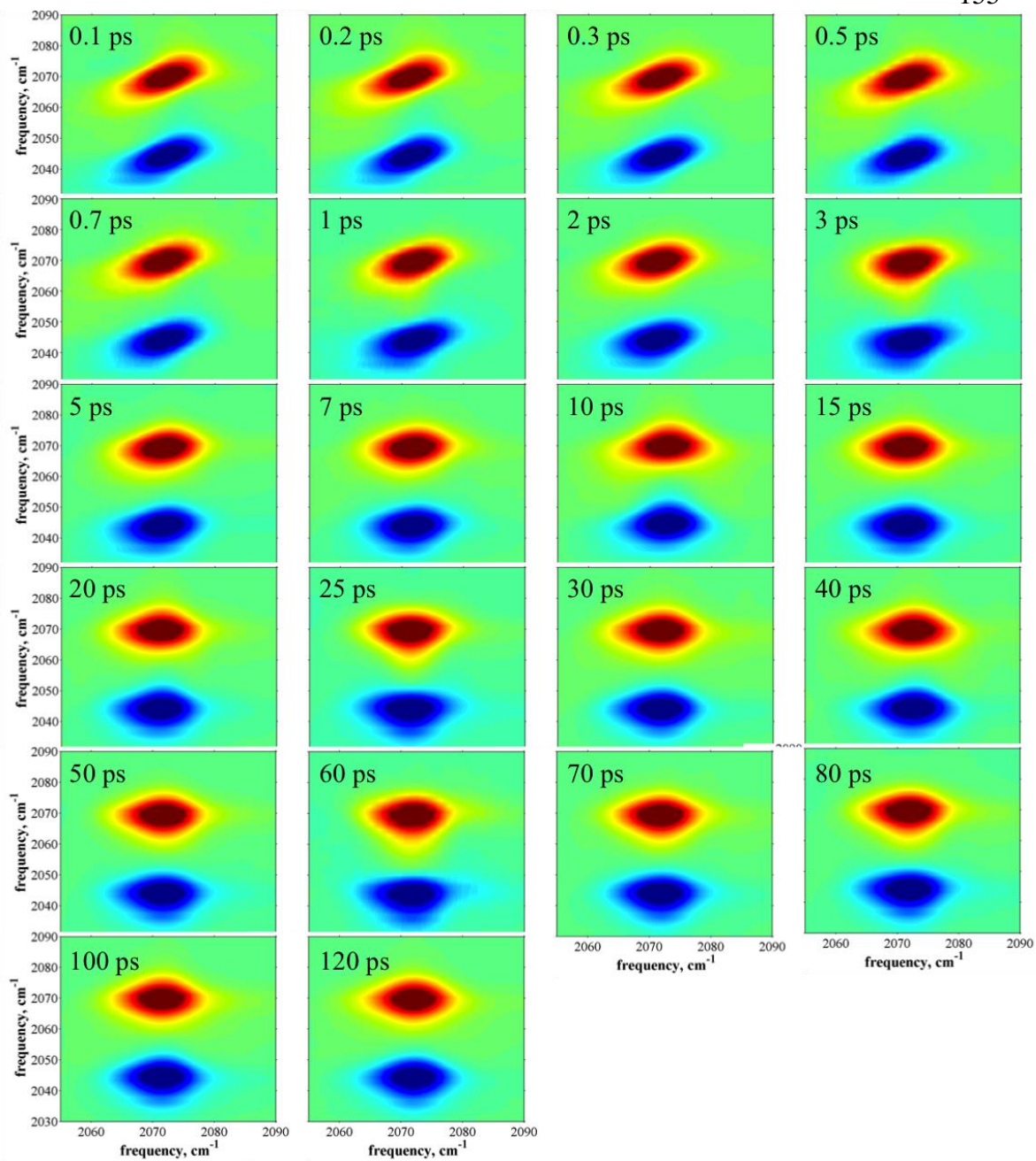
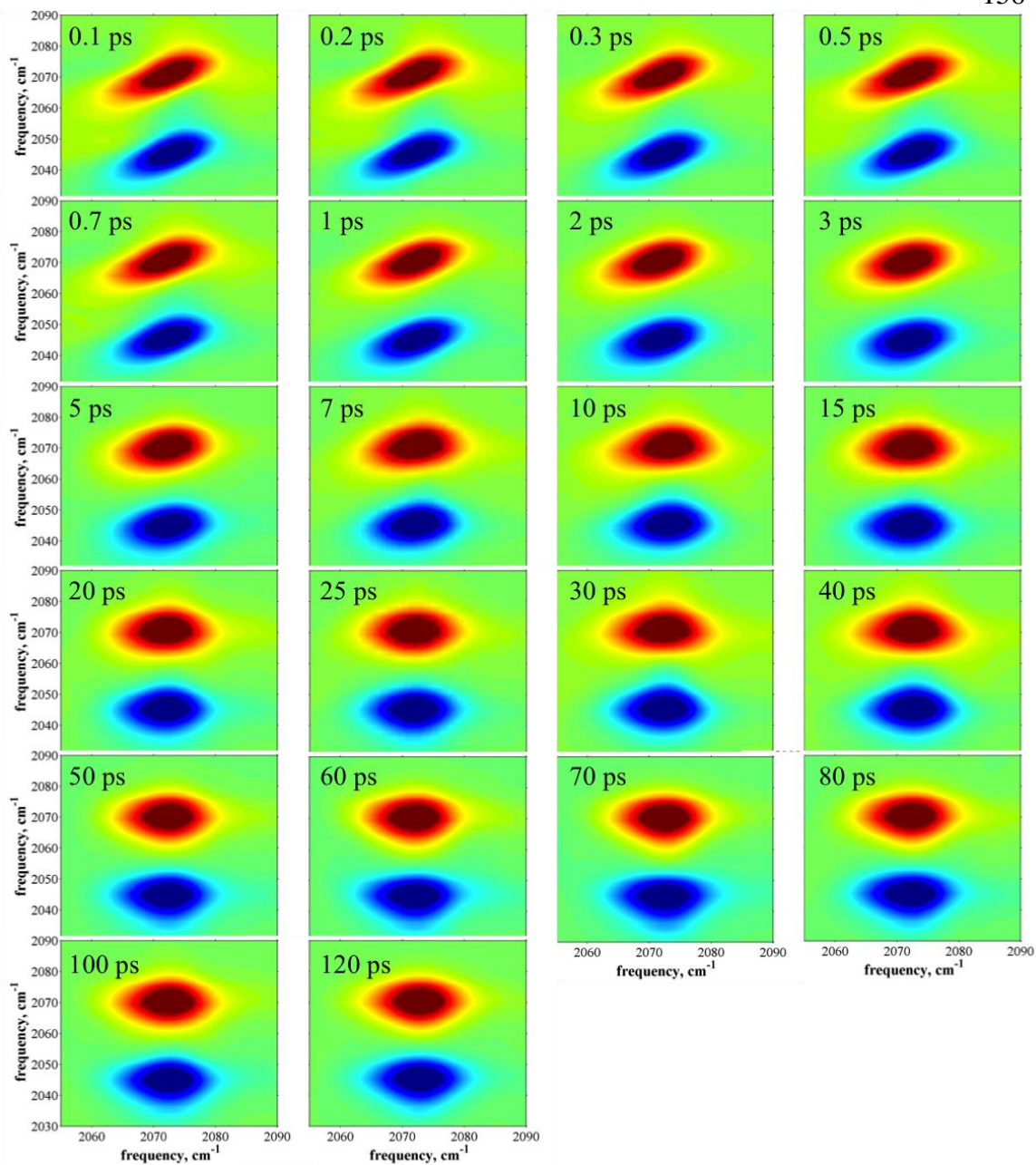**Figure 5.9:** 2D-IR spectra for all T_w values for VC-I_2 in 0.1 mole fraction $CHCl_3$ in d_6-benzene.

Figure 5.10: 2D-IR spectra for all T_w values for VC-I_2 in 0.3 mole fraction $CHCl_3$ in d_6-benzene.

Figure 5.11. 2D-IR spectra for all T_w values for VC-I$_2$ in 0.5 mole fraction CHCl$_3$ in d_6-benzene.

Figure 5.12. 2D-IR spectra for all T_w values for VC-I$_2$ in 0.7 mole fraction CHCl$_3$ in d_6-benzene.
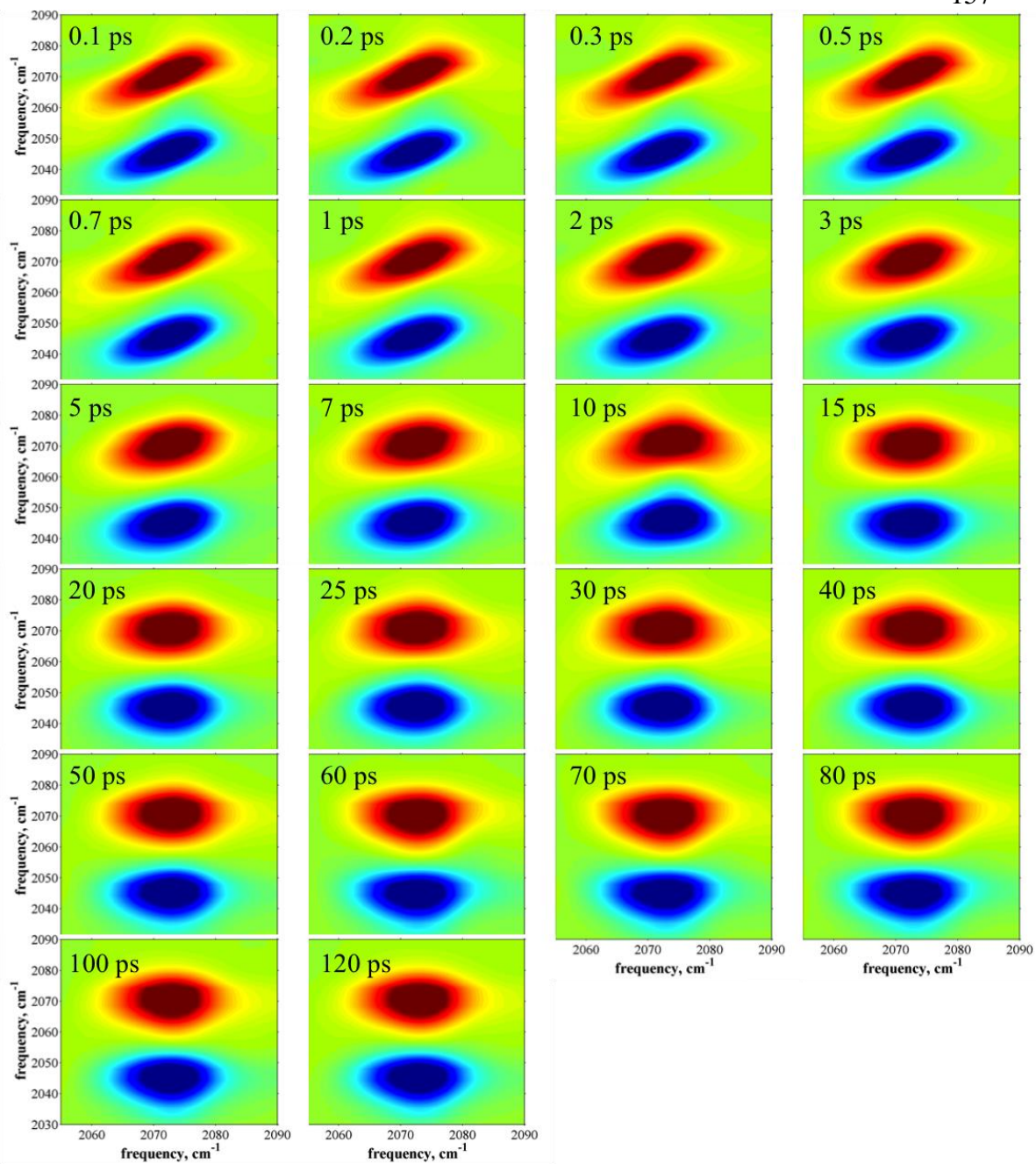
Figure 5.13. 2D-IR spectra for all T_w values for VC-I$_2$ in 0.9 mole fraction CHCl$_3$ in d_6-benzene.
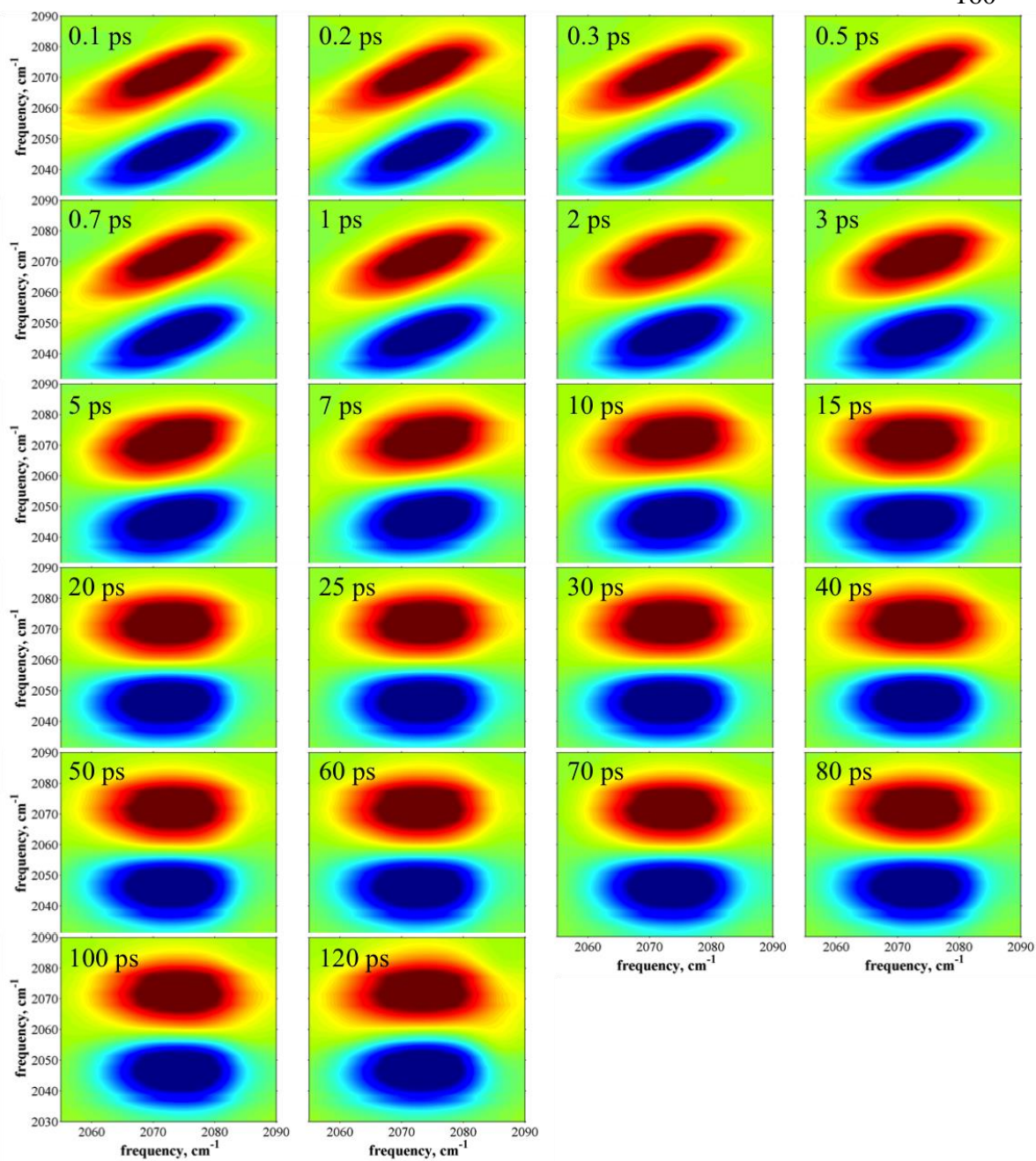
Figure 5.14. 2D-IR spectra for all T_w values for VC-I_2 in neat CHCl$_3$.

Figure 5.15. 2D-IR spectra for all T_w values for VC-I$_2$ in 0.05 mole fraction BA in d_6-benzene.

Figure 5.16. 2D-IR spectra for all T_w values for VC-I$_2$ in 0.1 mole fraction BA in d_6-benzene.
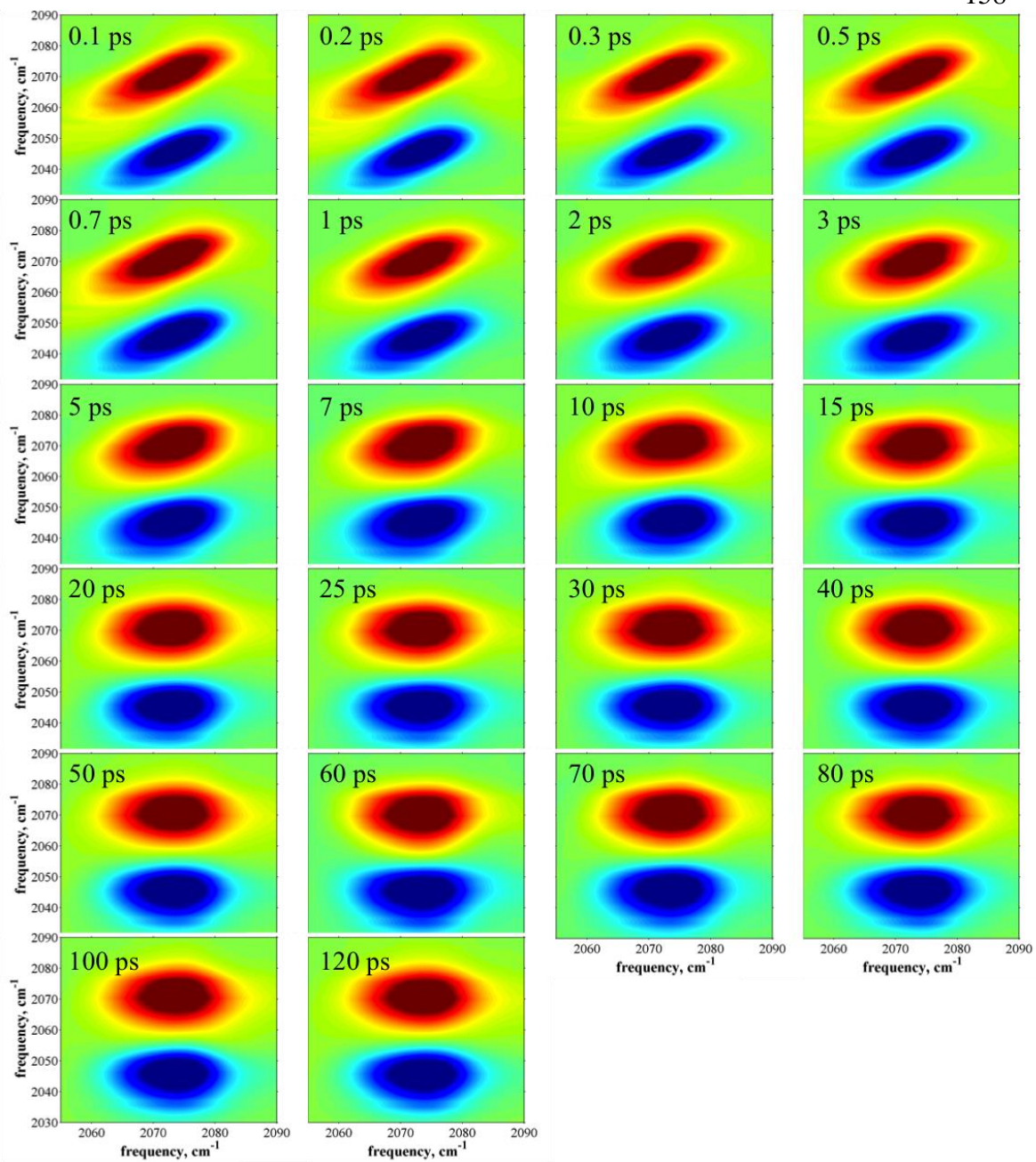
Figure 5.17. 2D-IR spectra for all T_w values for VC-I_2 in 0.2 mole fraction BA in d_6-benzene.
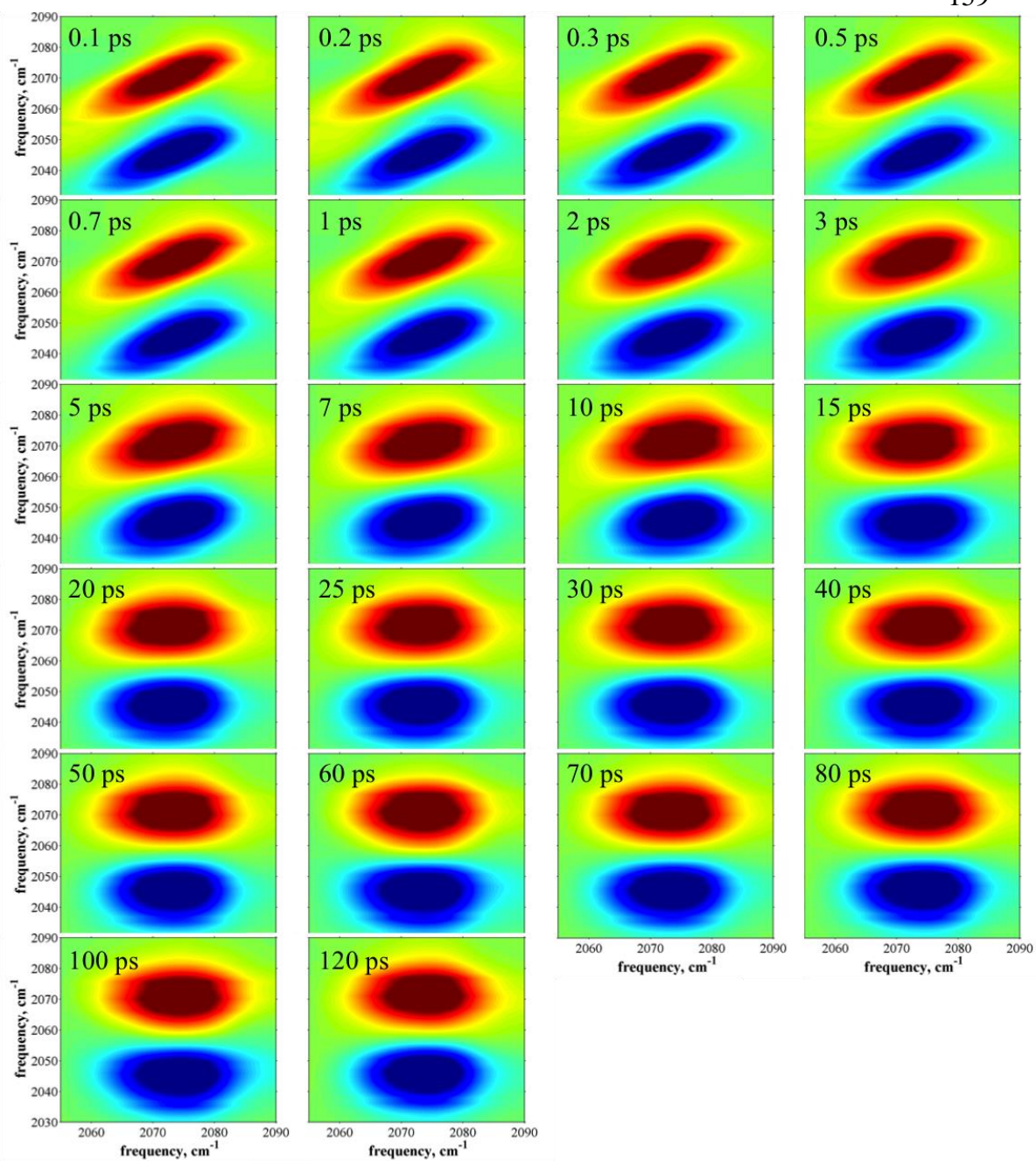
Figure 5.18. 2D-IR spectra for all T_w values for VC-I_2 in 0.3 mole fraction BA in d_6-benzene.

Figure 5.19. 2D-IR spectra for all T_w values for VC-I_2 in 0.4 mole fraction BA in d_6-benzene.
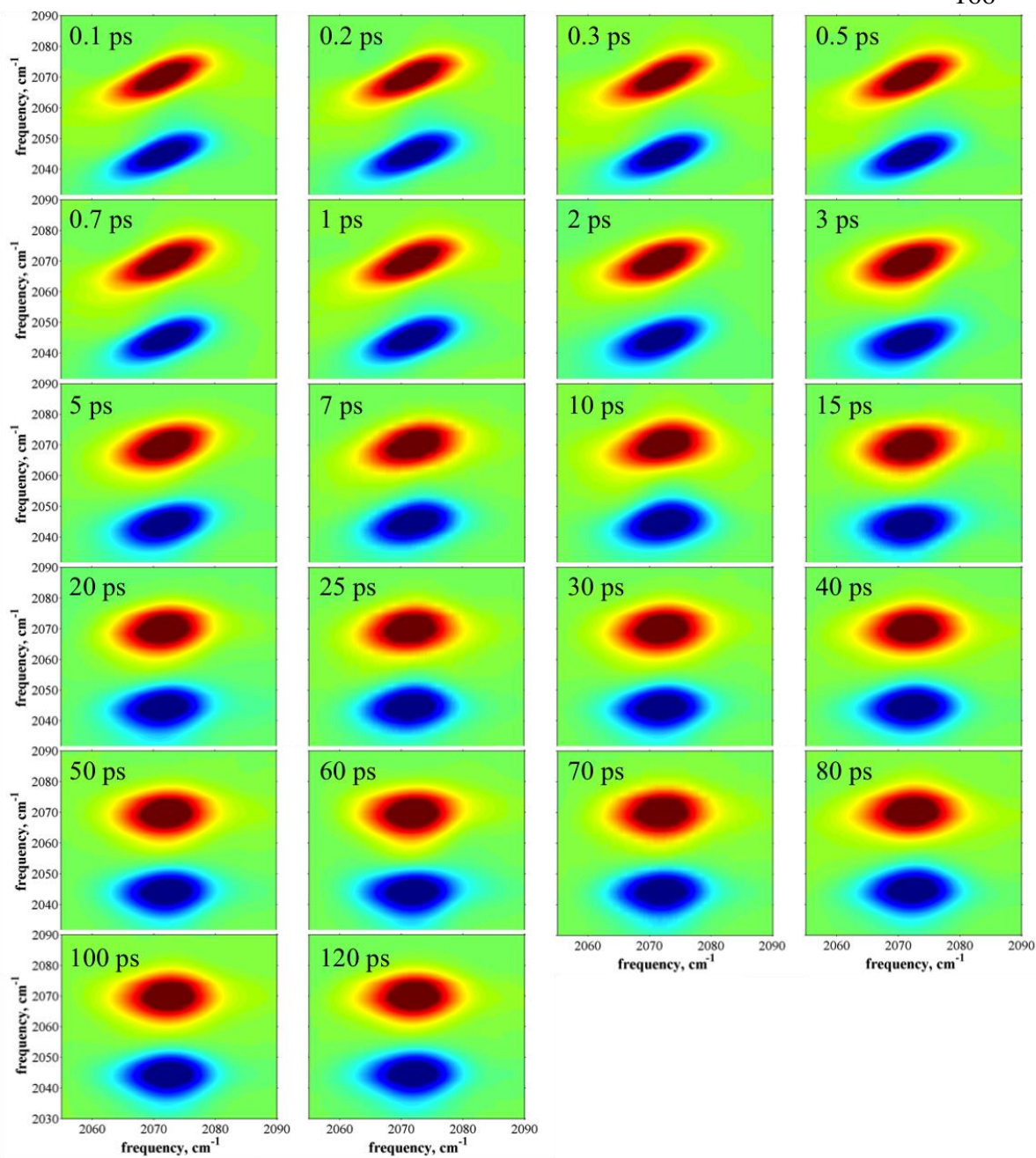
Figure 5.20. 2D-IR spectra for all T_w values for VC-I_2 in 0.5 mole fraction BA in d_6-benzene.
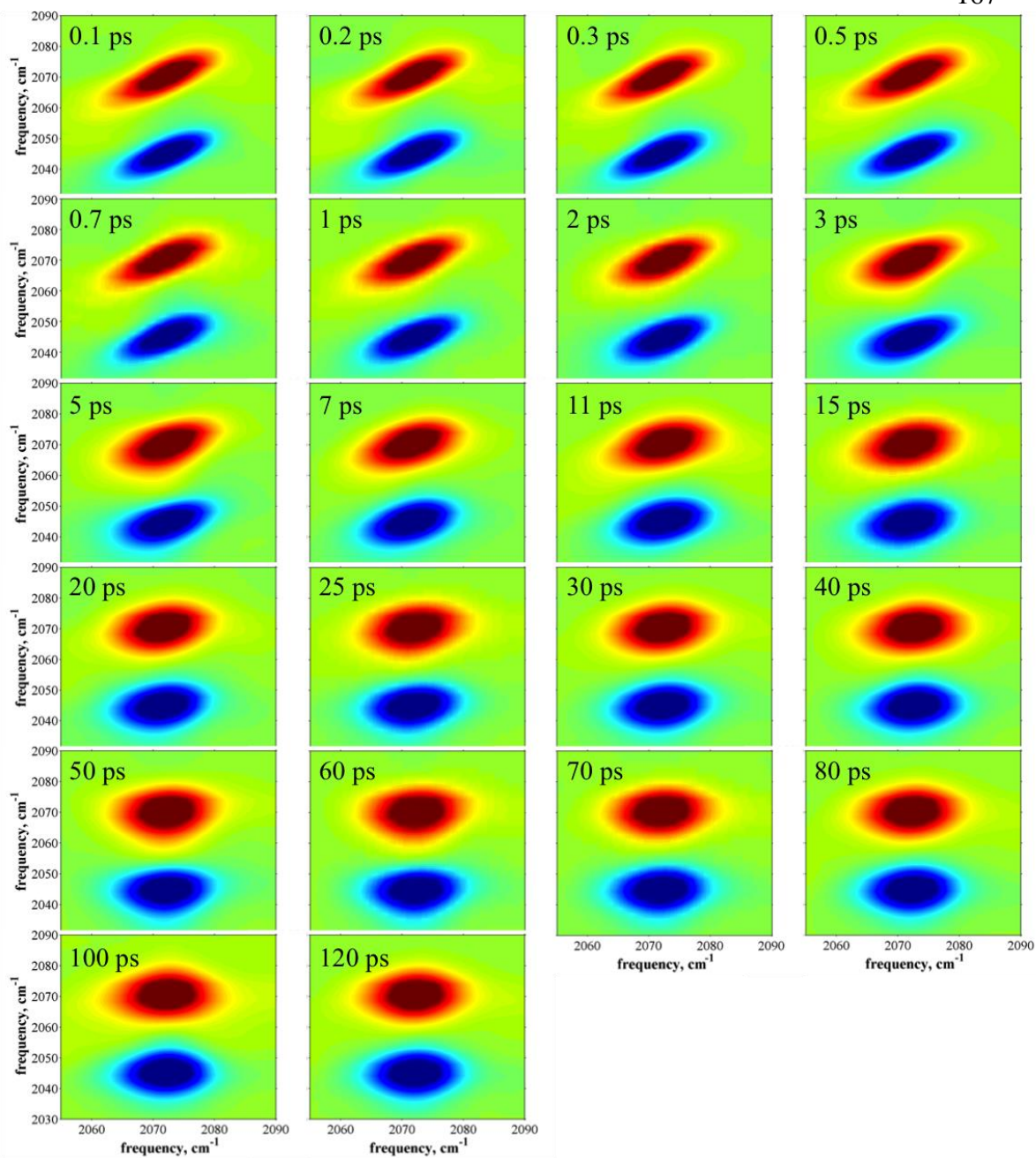
Figure 5.21. 2D-IR spectra for all T_w values for VC-I$_2$ in 0.7 mole fraction BA in d_6-benzene.
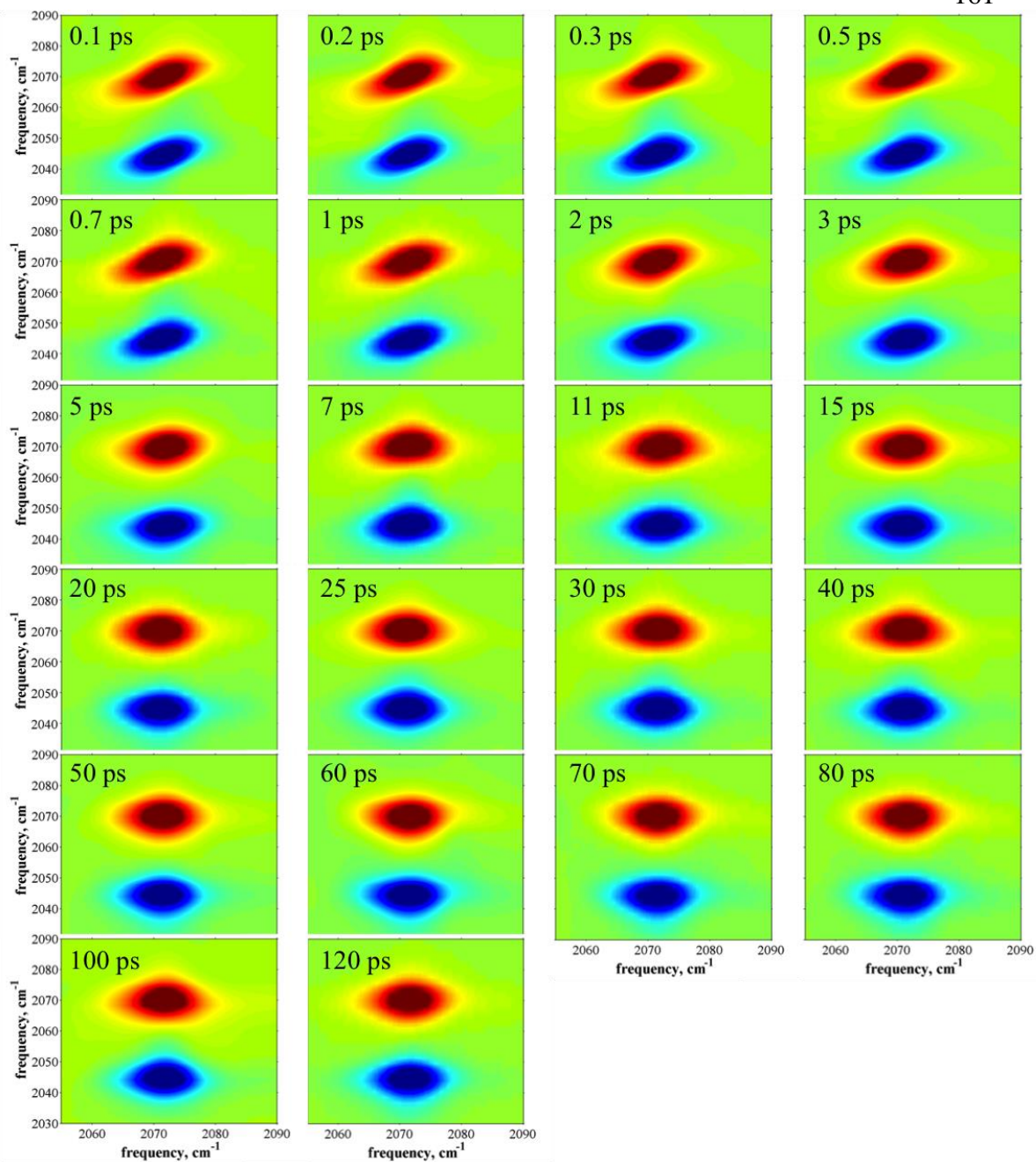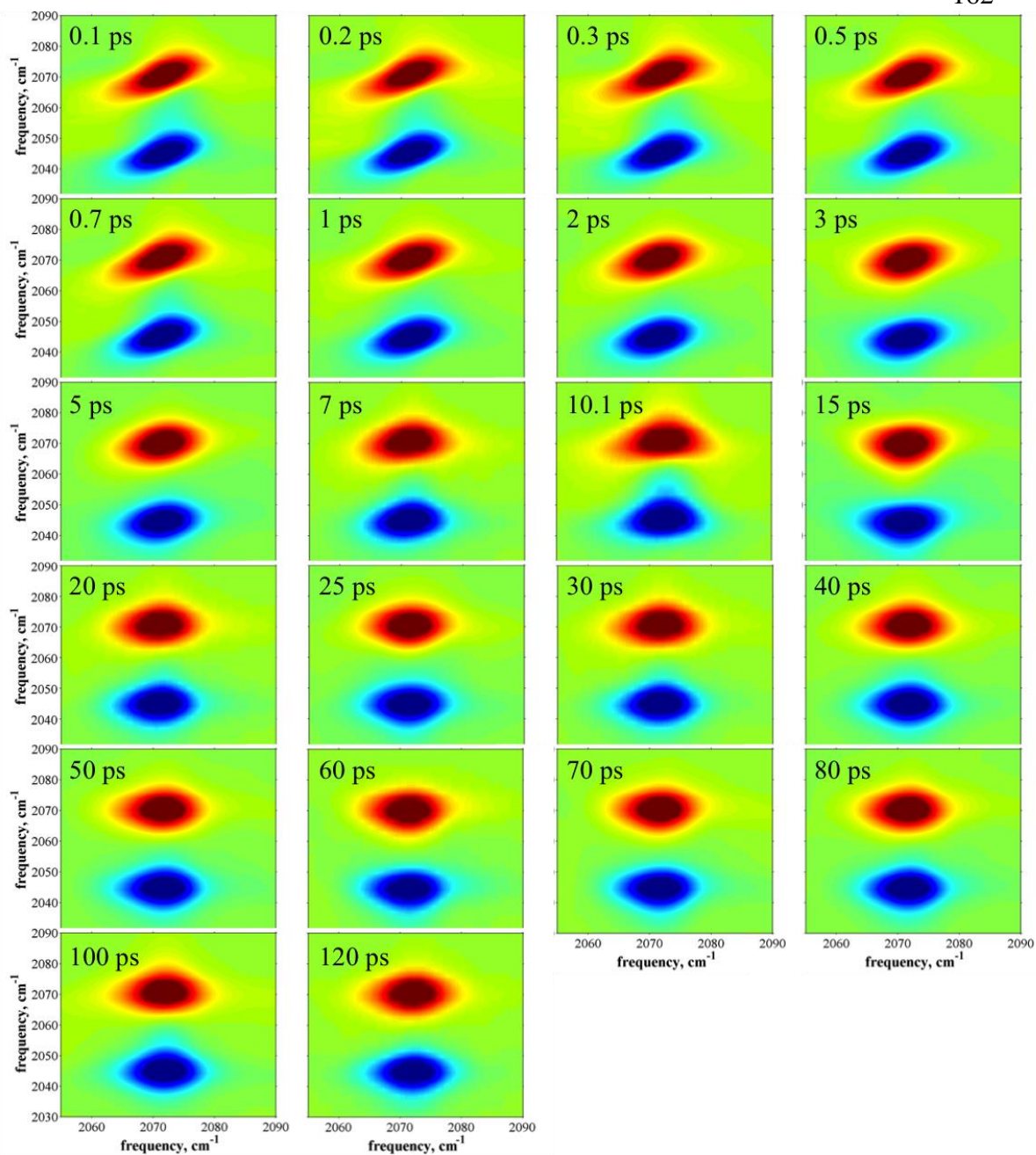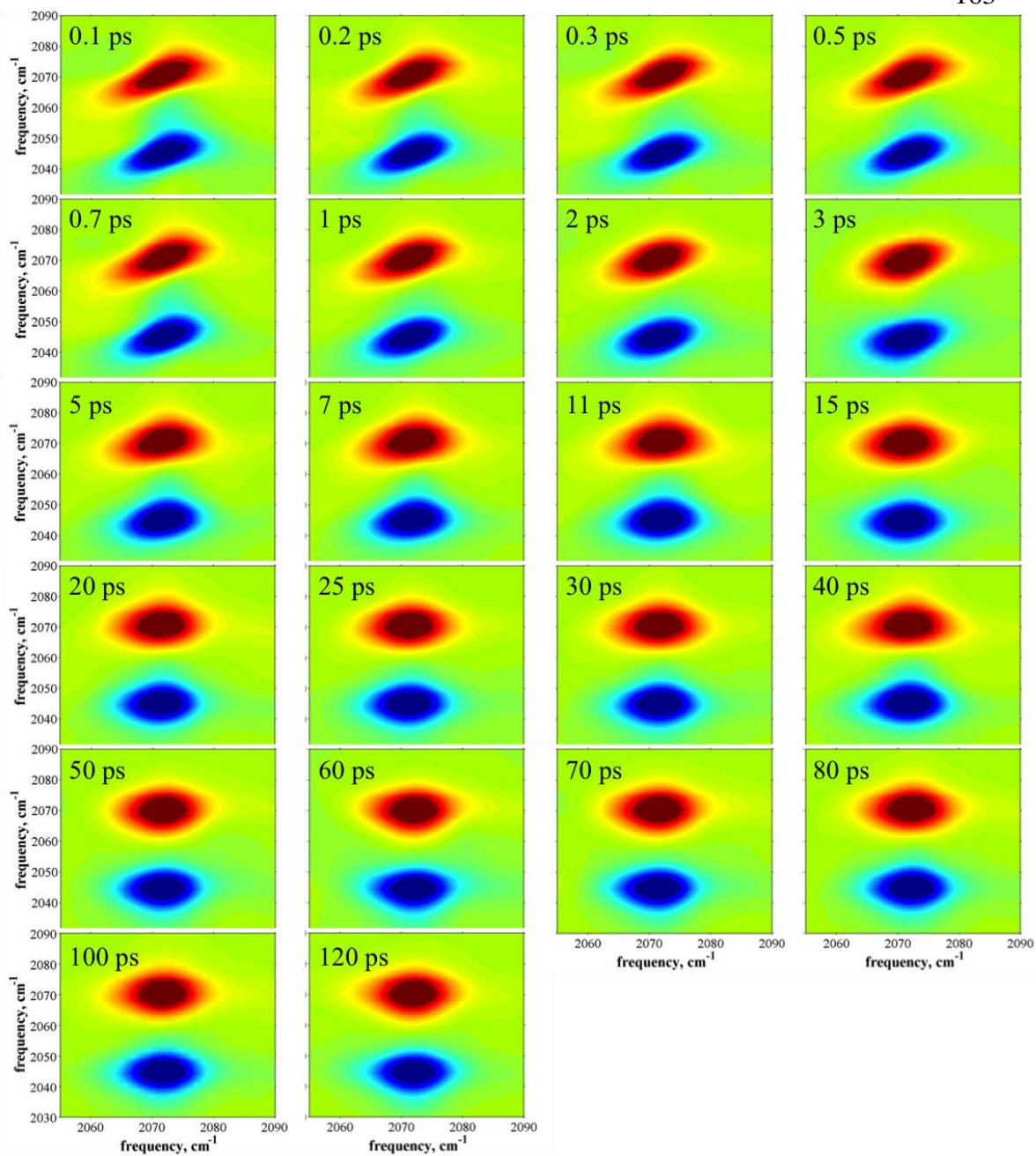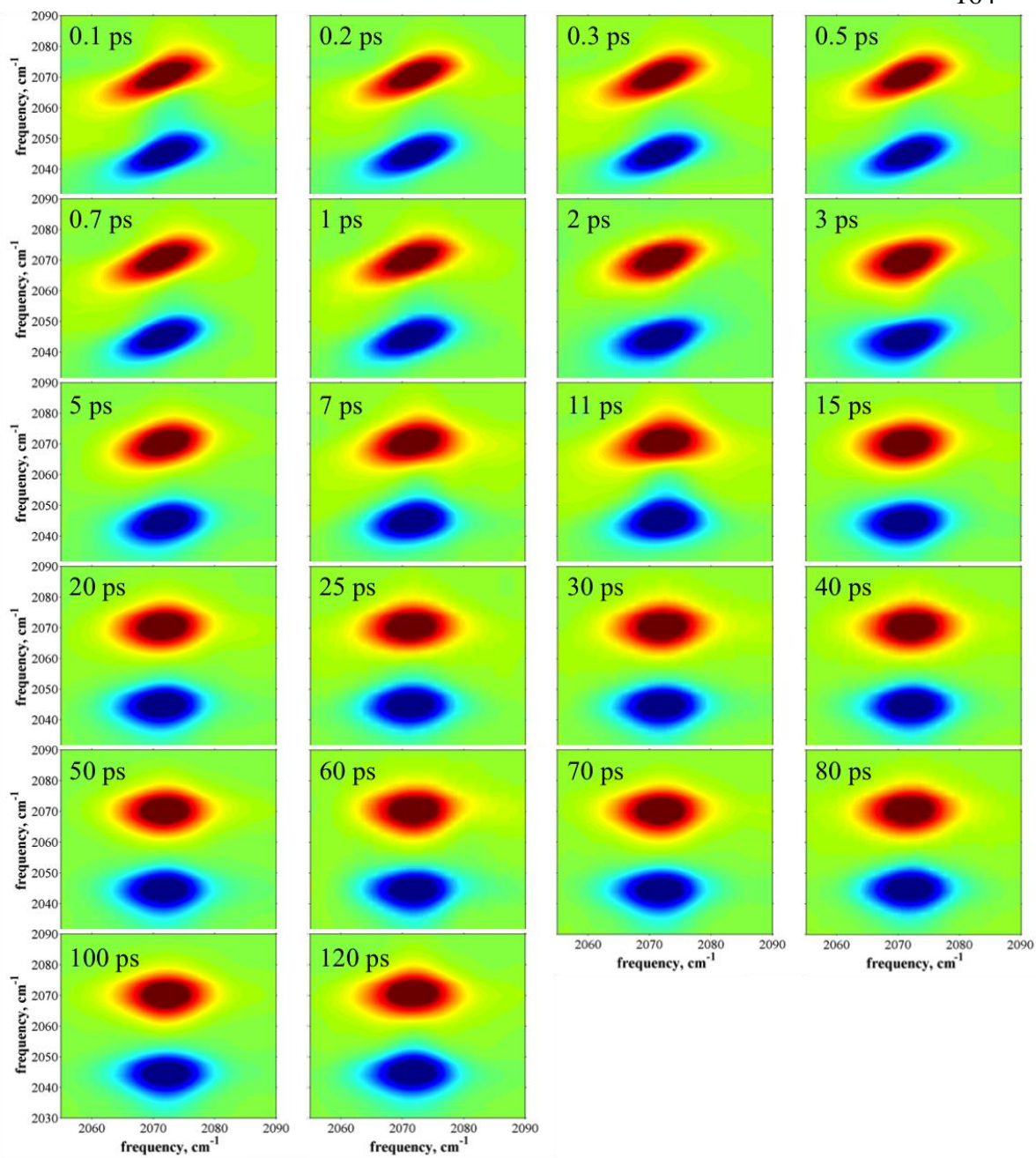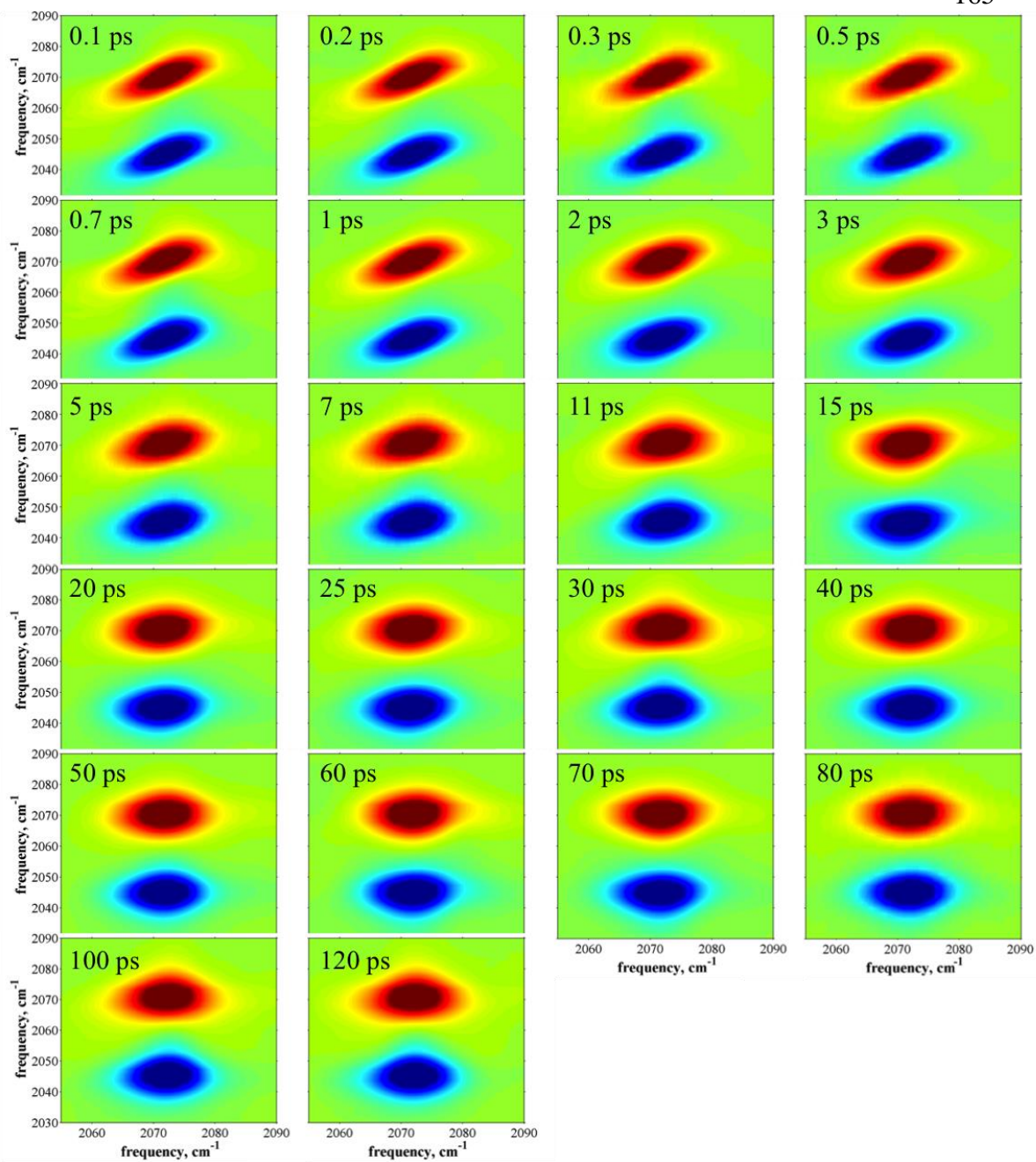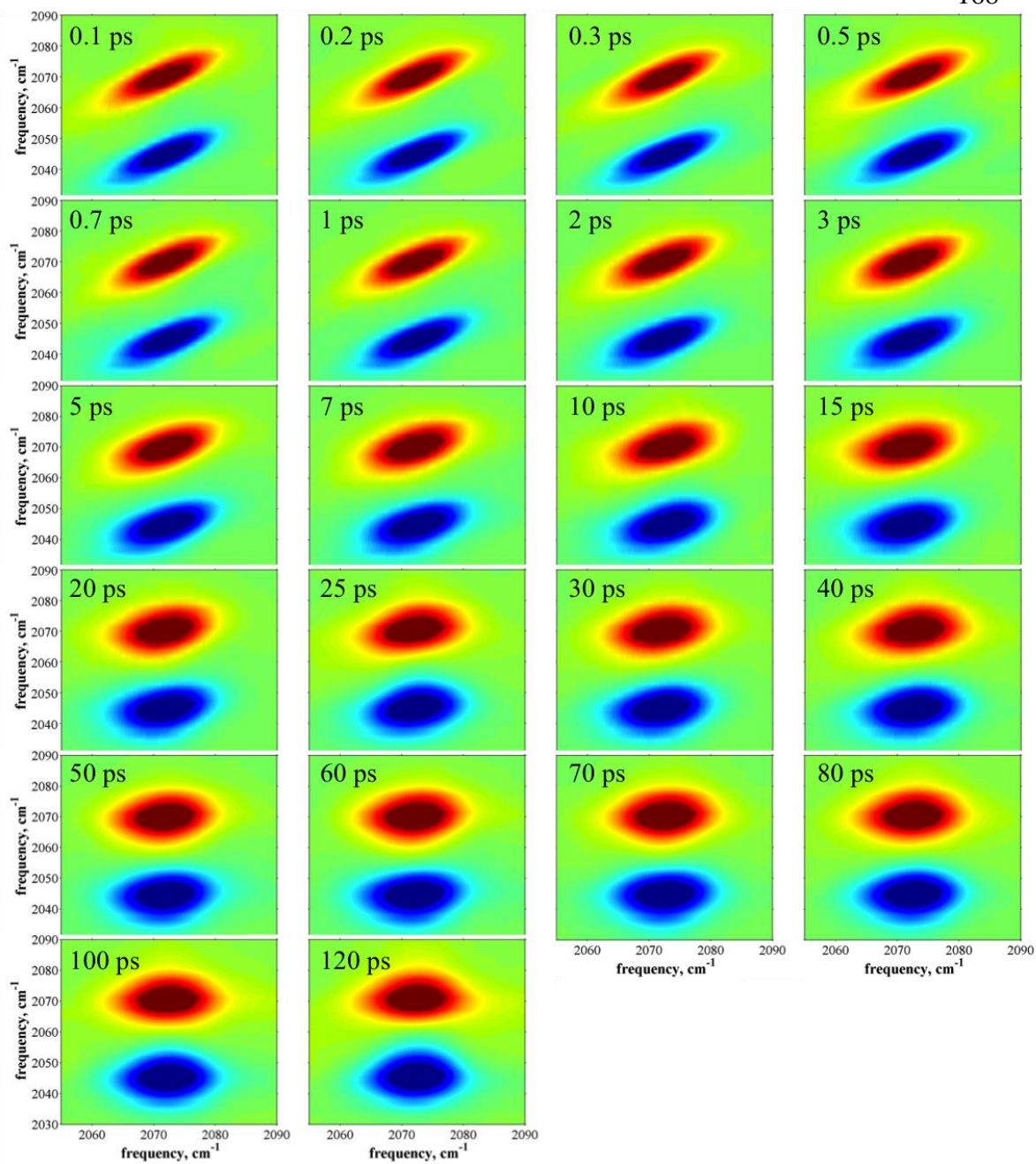
Figure 5.22. 2D-IR spectra for all T_w values for VC-I_2 in neat BA.

Chapter 6: Correlating Solvent Dynamics and Chemical Reaction Rates Using Binary Solvent Mixtures and 2D-IR Spectroscopy

6.1. Chapter Summary

In this chapter, a 2D-IR study was performed on VC and VC-O_2 in binary solvent mixtures of d_6-benzene with chloroform and benzyl alcohol. The rates of oxygenation were also measured in these mixtures. The rate constant for the chloroform mixtures shows a linear (within error) increase with increasing mole fraction. For the benzyl alcohol mixtures, however, the rate constants increase nonlinearly as a function of mole fraction. These rate constants as well as the macroscopic properties of the FTIR spectra were compared with the information extracted from the frequency-frequency correlation function using 2D-IR, particularly the homogeneous linewidth and the amplitude sum (inhomogeneity amplitude). VC shows a more linear trend than VC-O_2 in both of these parameters, and may be related to the linear portion of the increase. The nonlinearity of the trend in rate constant is reflected in both the inhomogeneity amplitude and the homogeneous linewidth of VC-O_2, against expectations of transition state theory. This suggests that VC-O_2 is similar to the transition state.

6.2. Introduction

Bis(triphenylphosphine)iridium(I)carbonyl chloride, or Vaska's complex (VC), has been extensively studied for its catalytic ability and its willingness to oxidatively bind small molecules.[42-43, 69, 157-168] The kinetics and mechanism of O_2 addition to form the VC-O_2 adduct (Scheme 1) have been the focus of many previous studies.[42-43, 69] The reversible side-on binding of O_2 to VC provides a small molecule mimic of biological oxygen transport systems,[156-158] but is also a simple model of the first mechanistic step in a catalytic cycle wherein the substrate is bound to the active site of a catalyst. As is true for most chemical reactions, the rate of O_2 addition to VC is sensitive to the nature of the solvent.[42-43, 69, 82] The entropy of this process was found to be negative and the rate constant increased with increasing solvent polarity, suggesting the presence of a polar transition state, similar to a Menshutkin reaction.[43] This interpretation was disputed by early studies analyzing electronic ligand effects,[44, 223-224] and more recently it has been shown by Wilson and coworkers that ligand properties can dictate relative rates for this and analogous compounds.[67] Thus, for the same reactant in different solvents the mere increase in rate with polarity does not in and of itself give enough information to determine whether a polar transition state was present. A further computational study modeled the mechanism and calculated transition states for the reaction of O_2 with the trimethylphosphine analogue of VC.[68] This study showed that the mechanism begins with an end-on triplet O_2 approach, proceeds via a pincer motion of the CO and Cl ligands through a side-on O_2 position (as surmised by Ugo),[44] passes through another end-on state, then undergoes intersystem crossing to the side-on singlet product.[68] The

largest energy cost (the transition state) comes at the pinching step, which was calculated to be structurally similar to the product and still fairly nonpolar.[68] In this light, the role of the solvent in dictating the reaction kinetics is not immediately clear.

An alternate explanation is that the dynamics of the molecules in the immediate solvation shell around the solute impact the rate of barrier crossing. The generalized Langevin equation provides a reasonable model for motion in the case of a reaction with a barrier, and describes the solvent effect as a time dependent frictional force.[47] This force is represented as a time correlation function of solvent fluctuations exerted in the direction of the reaction coordinate.[47] Though transition state theory predicts that only the energies of the reactants and transition state will matter to the final rate, it is important to note that, for our system, the product gives more information relevant to the reaction coordinate: the CO frequency in VC-O_2 is uniquely attuned to the environment around the O_2 ligand.[104, 194] It has also been shown in accordance with Onsager's linear regression hypothesis, that the molecular motions that comprise solvation dynamics (the movement of solvent molecules in response to a change in the solute) are strongly related to the solvent dynamics (the movement of solvent molecules around a solute).[39] With this understanding, it seems reasonable to hypothesize that the dynamics that might be measured experimentally could at least partly capture the same dynamics that facilitate chemical reactivity, as long as the observable has the appropriate sensitivity.

With this in mind, in Chapter 3 we used 2D-IR to characterize the solvent dynamics experienced by the carbonyl ligand on VC and VC-O_2 in pure solvents that had different oxidative addition kinetics.[194] While we were able to extract time scales and

amplitudes of some solvent shell rearrangements for the reactant and product species, extrapolating these results to explain the reactivity trends was speculative.   However, building on the approaches of others,[14-15, 18-19, 23, 29, 36, 225] we found that binary solvent mixtures were extremely useful in identifying which solvent shell properties were correlated.[210]

Binary solvents provide a common coordinate along which to map many observables, both static and dynamic. In a mixture of two solvents, it is generally true that the composition of the first shell of solvent molecules around a solute is different than that of the bulk solvent. This is due to the relative interaction strength of the each solvent with the solute and neighboring solvent molecules, and the dynamics of solvent exchange into and out of the solvent shell.[3, 18-19, 23, 36] If an observable varies linearly with the mole fraction of the second solvent in a binary mixture, this indicates that the composition of the solvation shell in the regions that influence that variable match the bulk values. For example, the vibrational lifetimes of the metal-bound carbonyl on VC-O_2 and the iodine adduct (VC-I_2) in binary solvent mixtures of d_6-benzene with chloroform ($CHCl_3$) or benzyl alcohol (BA) showed a linear variation with mole fraction of either $CHCl_3$ or BA.[210] As a counter example, the center frequency of the carbonyl vibrational on VC-O_2 varies in a highly nonlinear fashion in d_6-benzene/BA mixtures, with a small mole fraction of BA causing most of the frequency shift.[194, 210] This shows that there is preferential solvation of VC-O_2 by BA in ways that perturb the frequency of the metal-bound CO, though not its vibrational lifetime. These two examples illustrate that for the same solute in the same binary solvent mixtures two different observables can

report the absence and presence of preferential solvation. The solvatochromic frequency shift is achieved through electrophilic interactions with the O_2 ligand, which has π bonds that interact with the back-bonding orbitals on the iridium,[104, 194, 226] whereas vibrational relaxation is primarily solute-to-solvent energy transfer in the vicinity of the CO ligand.[210] It also highlights the possibility of drawing connections between quantities that might otherwise be difficult to correlate, such as solvent dynamics and reaction kinetics, when distinct nonlinear patterns are observed across the binary solvent coordinate.

In the following chapter, we have carried out a comprehensive binary solvent study of Vaska's complex and its oxygen adduct. The second order rate constants for O_2 addition were measured in binary solvent mixtures of d_6-benzene with $CHCl_3$ or BA to identify any preferential kinetic behaviors. Then numerous FTIR and 2D-IR spectroscopic observables were analyzed across the same solvent mixtures to identify correlations between the steady-state and dynamic quantities with the reaction kinetics.

6.3. Experimental Materials and Methods

Bis(triphenylphosphine)iridium(I)carbonyl chloride, (Vaska's complex, 99.99%, Sigma Aldrich, Strem Chemicals), chloroform ($CHCl_3$, 99.8%, Sigma Aldrich), benzyl alcohol (BA, ≥99%, Sigma Aldrich; puriss. Sigma Aldrich), and perdeuterated (d_6-)benzene (99.5% D, Cambridge Isotope Laboratories, Inc) were used as received without further purification for laser studies. (We found that the majority of commercially available ≥99% BA lots contained impurities that react with VC. Those who reproduce this work are advised to use only puriss. BA or to purify the solvent before use.) All

solutions were filtered prior to data collection. For solutions of VC, the solvents were

degassed by sparging with nitrogen prior to mixing and all subsequent steps of solution

preparation were performed under nitrogen.   For solutions of VC-O_2, mixing and

dissolution were carried out under ambient conditions. The solutions were capped and

covered with parafilm and stored until completion of the oxygenation reaction (24-48

hours). All measured samples were ~4 mM in VC or VC-O_2.

Infrared spectra were collected on a Nicolet 6700 FTIR spectrometer (Thermo

Scientific) with at least 16 scans and a typical resolution of 1 cm^{-1}. Path lengths of both

150 μm and 25 μm were used for FTIR measurements.

Kinetics data were measured by UV-visible spectroscopy (Perkin-Elmer Lambda

12).   Disappearance of the VC absorbance at 387 nm (ε = 4040 M^{-1}cm^{-1})[227] was

monitored over up to 33 hours under pseudo-first order conditions (ambient O_2, 0.1 and

0.05 mM VC). The solubilities of O_2 in the pure benzene and CHCl$_3$ were determined

from their Henry's Law constants (benzene = 9.24 10^{-3} M/atm,[228] CHCl$_3$ = 9.225 10^{-3}

M/atm,[229]). The Henry's Law constant for BA was not available, but we used the value

for toluene as has been reported by others[230] (toluene = 1.914 10^{-3} M/atm[228]).   The

Henry's Law constants for binary mixtures were determined as described by

Krichevsky.[231-232] An ambient O_2 partial pressure of 0.21 atm was used as the

concentration of O_2 in each solution. Under these conditions, the lowest concentration of

O_2 for any solution was 1.8 mM, which was at least an order of magnitude larger than the

concentration of VC or VC-O_2 to ensure pseudo first-order kinetics. The resulting decays

were fit well by a single exponential decay. Second order rate constants were determined using the method described by Corbett.[233]

The 2D-IR setup has been described in detail in Chapters 2 and 3. As was also mentioned in Chapter 2, since the pump-probe projection theorem was used in the phase correction process,[111] and since in our setup the probe beam passes through the sample while the local oscillator does not, the FTIR transmission spectrum was used as an absorption correction prior to phasing. The FFCF was obtained using the centerline slope/FTIR fitting method described in the literature and in Chapter 2.[116-117]

6.4. Results and Discussion

The second order rate constants for oxidative addition of O_2 to VC (refer back to Scheme 3.1) in binary solvent mixtures of d_6-benzene with $CHCl_3$ or BA are shown in Figure 6.1 (numerical values are provided in Table 6.1). To our knowledge, this is the first work to examine this reaction in mixed solvents. The rate constants in neat solvents follow the trends previously observed by Steiger and Chock,[42-43] increasing with solvent polarity index (benzene < $CHCl_3$ < BA)[176] as 1.9, 2.4, and 12 $M^{-1}min^{-1}$. It also follows the trend of anticorrelating with the solubility of Vaska's complex, which is often seen when there is not a polar transition state.[1] The rate constant in BA is considerably greater than in pure $CHCl_3$ or d_6-benzene. Although the Henry's law constant used here could affect this value, the toluene constant is generally considered a good surrogate for BA,[230] and even if the solubility of O_2 in BA were twice that of toluene the calculated rate constant would still be a factor of three higher than that of $CHCl_3$. Even at a mole fraction of only 0.05 BA, the k_2 is already considerably faster than in pure $CHCl_3$.
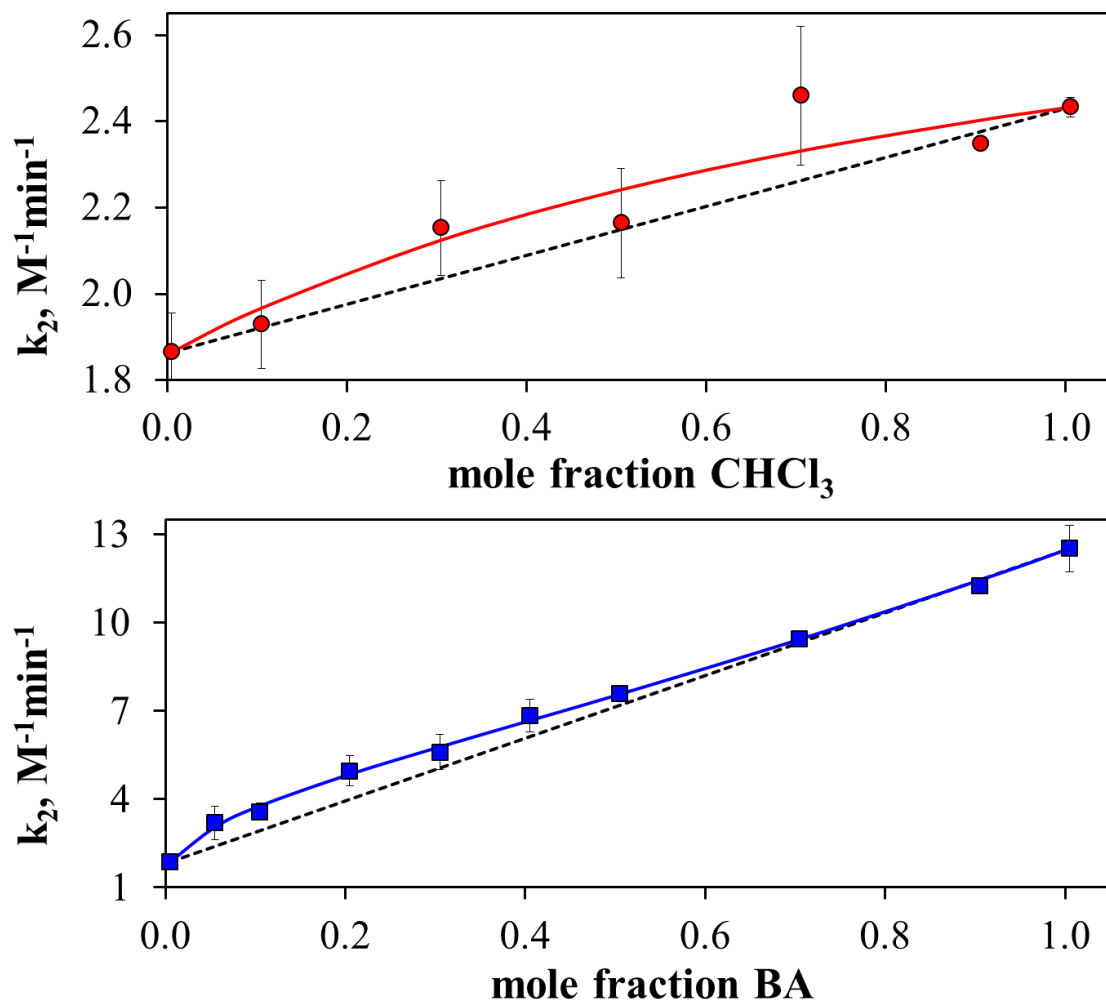
Figure 6.1. Second order rate constant for O_2 addition to VC as a function of mole fraction of a) $CHCl_3$ in d_6-benzene and b) BA in d_6-benzene. Error bars represent the standard deviation of four trials at two concentrations of VC. Black dashed lines are aids to the eye connecting the first and last points. Red and blue lines are the best fit to the data calculated from Equation 6.1 or 6.2 for $CHCl_3$ and BA mixtures, respectively.

Table 6.1. FTIR parameters and k_2 values for VC and VC-O_2 in BA and CHCl$_3$ binary mixtures in d_6-benzene.

mole fraction	k_2 (M^{-1} min^{-1})	ν_{CO} (cm^{-1})		FWHM (cm^{-1})		T_1 (ps)	
		VC	VC-O_2	VC	VC-O_2	VC	VC-O_2[a]
CHCl$_3$ in d_6-benzene							
0	1.86 (0.09)	1965.1	2003.2	16.7	16.8	52 (2)	92 (3)
0.1	1.9 (0.1)	1965.4	2005.7	17.9	17.5	51 (2)	94 (2)
0.3	2.1 (0.1)	1965.7	2008.3	19.4	18.2	50 (2)	101 (3)
0.5	2.2 (0.1)	1966.0	2010.5	20.8	18.9	50 (1)	102 (1)
0.7	2.4 (0.2)	1965.8	2012.3	22.1	19.8	49 (2)	106 (2)
0.9	2.348 (0.009)	1965.6	2013.8	23.4	20.7	48 (2)	109 (3)
1	2.43 (0.02)	1965.2	2014.3	24.1	21.5	49 (1)	108 (2)
BA in d_6-benzene							
0	1.86 (0.09)	1965.1	2003.2	16.7	16.8	52 (2)	92 (2)
0.05	3.2 (0.6)	1965.6	2006.9	17.3	19.8	49 (2)	87 (2)
0.1	3.6 (0.3)	1965.7	2008.4	17.7	20.2	45 (1)	88 (2)
0.2	5.0 (0.5)	1966.4	2009.7	18.6	20.6	42 (1)	84 (2)
0.3	5.6 (0.6)	1966.6	2010.5	18.8	20.5	41 (2)	78 (1)
0.4	6.8 (0.5)	1966.8	2011.1	19.2	20.7	38 (1)	76 (1)
0.5	7.6 (0.2)	1967.2	2011.6	19.9	20.6	36 (2)	73 (2)
0.7	9.45 (0.08)	1967.6	2012.4	20.6	21.0	31 (1)	66 (2)
0.9	11.2 (0.2)						
1	12.5 (0.8)	1968.2	2012.9	21.5	22.2	27 (3)	56 (2)

a: taken from Chapter 4 (Ref. 28) with permission.

Table 6.2 Preference parameters obtained by fitting various experimental observables to Equation 6.1 or 6.2. Each fit is deemed to have a preference or no preference based on the error.

observable	CHCl$_3$ in d$_6$-benzene		BA in d$_6$-benzene	
	VC	VC-O$_2$	VC	VC-O$_2$
k$_2$	$f_{2/1}$= 2.0 (0.6) no preference		$f_{2/1}^{below}$= 14 (9), X_C = 0.19 (0.07), $f_{2/1}^{above}$= 0.8 (0.1) preference	
ν_{CO}	$f_{2/1}$= N/A anomalous [a]	$f_{2/1}$= 2.0 (0.1) preference	$f_{2/1}$= 2.1 (0.1) preference	$f_{2/1}$= 9.0 (0.7) preference
FWHM ν_{CO}	$f_{2/1}$= 1.3 (0.1) no preference	$f_{2/1}$= 0.9 (0.1) no preference	$f_{2/1}$= 2.0 (0.1) preference	$f_{2/1}^{below}$= 76 (14), X_C = 0.71 (0.02), $f_{2/1}^{above}$= 0.11 (0.05), preference
Γ	$f_{2/1}$= 0.6 (0.5) no preference	$f_{2/1}$= 0.5 (0.5) no preference	$f_{2/1}$= 0.9 (0.3) no preference	$f_{2/1}^{below}$= 16 (4). X_C = 0.70 (0.04), $f_{2/1}^{above}$= 0.05 (0.04), preference
Ω	$f_{2/1}$= 1.0 (0.1) no preference	$f_{2/1}$= 0.73 (0.07) no preference	$f_{2/1}$= 2.3 (0.4) no preference	$f_{2/1}^{below}$= 92 (21), X_C = 0.17 (0.05), $f_{2/1}^{above}$= 0.69 (0.02), preference

a. ν_{CO} for VC in CHCl$_3$ mixtures is nearly the same in pure d$_6$-benzene and CHCl$_3$, but increases in the intermediate mole fractions. This shape cannot be modeled by Equation 6.1 or 6.2.

Examining the shapes of the kinetics data in mixed solvents, neither shows a fully linear trend with mole fraction. This is highlighted by the black line connecting the first and last data points. Positive deviation, or deviation above the black line, generally indicates that the higher endpoint solvent has a stronger effect on the observable, whereas for negative deviation the opposite is true. Considering the error bars, $CHCl_3$ mixtures only show significant deviations from linearity for 0.7 and 0.9 mole fraction (notably in opposite directions), whereas BA mixtures show a sharp increase in k_2 with just a small increment in mole fraction but then continue to increase more linearly as the BA concentration is increased.

It is useful to define a preference parameter following the approach of Roses and coworkers.[14] In the simplest case, some measured observable, y, displays a preference for one solvent over the other that is constant over the entire range of solvent mole fractions, allowing the data to be modeled with a single preference parameter, $f_{2/1}$,:[14, 234-235]

$$y = y_1 + \frac{f_{2/1}(y_2 - y_1)X_2}{(1 - X_2) + f_{2/1}X_2}$$

(6.1)

where y_1 and y_2 are the values of the observable in pure solvents 1 and 2, respectively, and X_2 is the mole fraction of solvent 2 in solvent 1 in the bulk solution. For this study, we consider solvent 1 to be d_6-benzene and solvent 2 is either $CHCl_3$ or BA. Since the solvation shell influences the stability of molecular configurations, it is possible that the preference parameter is not constant over the entire mole fraction range but undergoes a crossover between two molecular configurations, and after that structural change presents a different solvent preference. It is also possible that any hydrogen-bonded species have

a more polar configuration than either solvent on its own,[234] which can lead to a similar situation for observables connected to the polarity. For this more complex case, we can define a crossover mole fraction, X_C, and then modify Equation 6.1 using preference parameters below ($f_{2/1}^{below}$) and above ($f_{2/1}^{above}$) this point.

$$y = y_1 + \frac{f_{2/1}^{below} X_C (y_2 - y_1) X_2}{(1 - X_2) + f_{2/1}^{below} X_2} + \frac{f_{2/1}^{above} (y_2 - y_1 - X_C (y_2 - y_1)) X_2}{(1 - X_2) + f_{2/1}^{above} X_2} \qquad (6.2)$$

As expected, Equation 1 is recovered when the crossover mole fraction is set to unity. This equation can be used to quantify the preference of a given observable for solvent 2 (CHCl$_3$ or BA) versus solvent 1 (d_6-benzene). For the simple single preference case, the data can be fitted by floating only a single preference parameter, $f_{2/1}$, while three adjustable parameters are needed when a crossover is included ($f_{2/1}^{below}$, $f_{2/1}^{above}$, and X_C). Preference parameters for the rate constants, as well as those for other observables discussed later, are listed in Table 6.2.

Returning to the kinetics data in Figure 6.1, the overlaid dashed lines show fits to Equation 2 for each solvent mixture. The data in CHCl$_3$ mixtures (Figure 6.1a) were modeled by a single $f_{2/1}$ of ~2. For such a value, the rate of addition of O$_2$ to VC increases in going from pure d_6-benzene to pure CHCl$_3$, but something about the properties of the solvation shell enables this to occur about twice as fast as would be expected from the bulk solvent composition. However, in light of the error bars on these data points it is difficult to positively declare that the rate constant increase is not linear in mole fraction. Though the function with an $f_{2/1}$ of 2 is the best fit, and although the majority of deviations from linearity occur above the line between the endpoints, within

the standard deviation the majority of the points do not deviate significantly from that line.

The kinetics in d_6-benzene/BA mixtures in Figure 6.1b are not modeled well by a single preference parameter. If this were the case, the fast initial rise in k_2 would have quickly saturated at its maximum value. Instead, the initial increase is followed by a more gradual rise with added BA. The addition of small amounts of BA increases k_2 with a preference for BA over d_6-benzene by more than 13:1. This shows that small quantities of BA preferentially modify the composition and/or dynamics of the solvation shell in ways that favor O_2 addition to VC. Beyond a crossover point of about 0.2 mole fraction BA, the solvation shell composition and/or dynamics continue to be modified in ways that have a smaller impact on the reactivity of the solute, exhibiting almost no solvent preference.

The nonlinearity of the BA kinetics could be because of preferential solvation, where the composition of the solvent shell is different than that of the bulk solvent. Alternately, the composition of the solvation shell may match that of the bulk solution, but be heterogeneously distributed about the solute in ways that preferentially impact the reactivity (energetics) of VC to O_2. Another possibility, which is not exclusive of the previous two, is that the dynamic behavior of the solvent shell and/or solute contributes to the addition reaction, and that these time dependent fluctuations are modified in a nonlinear fashion by the added mole fraction of BA.
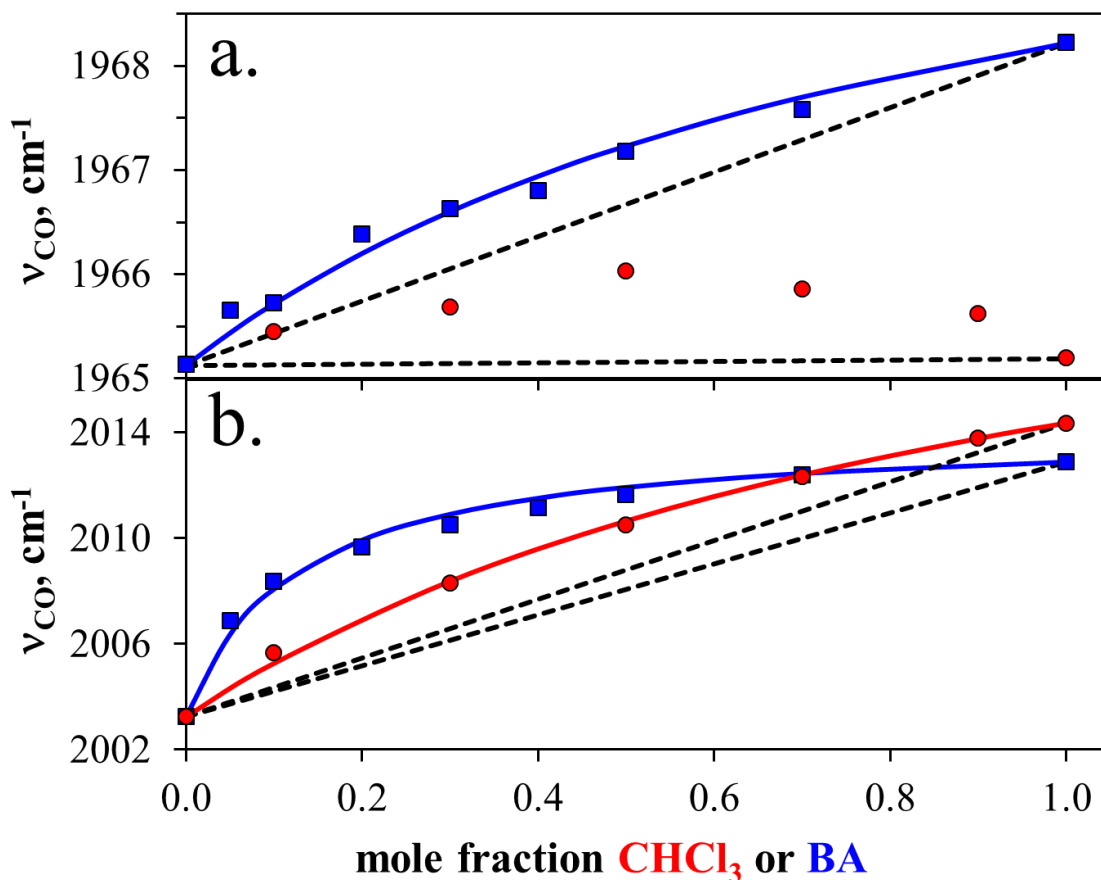
Figure 6.2. FTIR peak centers for the carbonyl stretch, ν_{CO}, on a) VC and b) VC-O$_2$ as a function of the mole fraction of CHCl$_3$ (red circles) or BA (blue squares) added to d_6-benzene. Black dashed lines are aids to the eye connecting the first and last points. Red and blue lines are the best fit to the data calculated from Equation 6.1 for CHCl$_3$ and BA mixtures, respectively.

Figure 6.2 shows the trends for the FTIR peak centers for the carbonyl stretching frequencies, ν_{CO}, on VC (top) and VC-O$_2$ (bottom) in mixed solvents. The vibrational spectra have been previously reported for VC in pure solvents[104] but not in binary solvent mixtures. Numerical values of ν_{CO} are provided in Table 6.1. Beginning with VC in Figure 6.2a, we see that although this mode is less solvatochromic than when it is bound to VC-O$_2$ (Fig. 6.2b), its frequency does shift nonlinearly with the mole fraction of the solvent system. The most unusual behavior is observed for VC in CHCl$_3$ mixtures, in

which the beginning and ending frequencies are nearly identical but in the intermediate

mole fractions the center blue-shifts by about 1 cm^{-1}. This clear, though small, increase

in frequency occurs only when both solvents are present. It seems likely therefore that it

is due to interactions between CHCl$_3$ and d_6-benzene occurring in the vicinity of the

solute. Such a change in observable that is outside of the range of the pure solvents

cannot be modeled by Equation 1 or 2; the ν_{CO} for VC in BA mixtures, however, provides

a case that can be analyzed. We find that the positive deviation from linearity for the ν_{CO}

indicates $f_{2/1}$ of 2.1, preferring BA over d_6-benzene for the characteristics of the

solvation shell that influence the carbonyl frequency.

Figure 6.2b shows that VC-O$_2$ exhibits larger solvatochromic carbonyl frequency

changes than VC due to changes in the iridium backbonding caused by electron density

changes at the O$_2$ ligand.[104] The FTIR spectra for VC-O$_2$ have been published and

discussed in Chapters 3 and 4 for some neat solvents[104] and binary solvent mixtures,[210]

but were reanalyzed here with improved solvent subtraction. The trends with mole

fraction are readily fit by Equation 2 using $f_{2/1}$ values of 2 and 9 for CHCl$_3$ and BA,

respectively. The positive deviation from linearity is notably greater for BA. The center

frequency always has a greater influence from the more polar solvent (positive

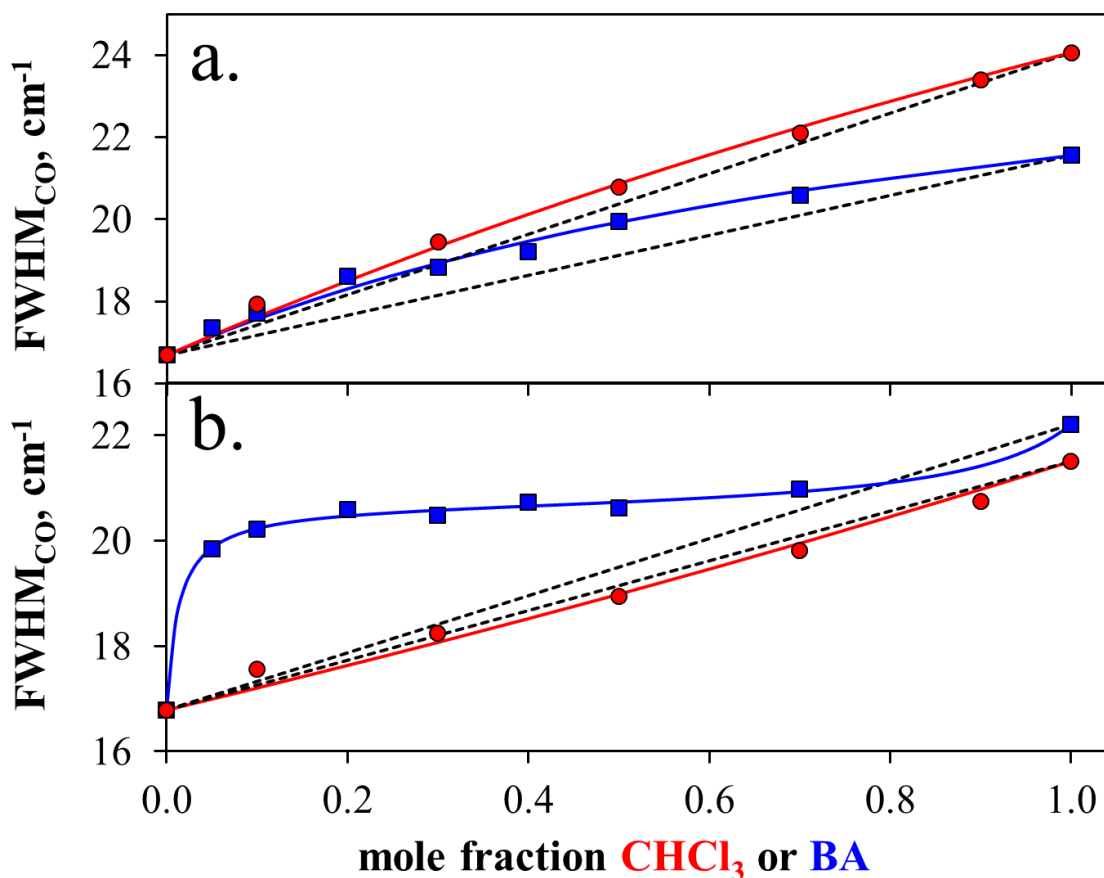deviation), but to differing degrees depending on the adduct.[104]

Figure 6.3. FTIR full widths at half maximum (FWHM) for the carbonyl vibration on a) VC and b) VC-O_2 as a function of the mole fraction of $CHCl_3$ (red circles) or BA (blue squares) added to d_6-benzene. Black dashed lines are aids to the eye connecting the first and last points. Solid (red and blue) lines are the best fit to the data calculated from Equation 6.1 or 6.2 for $CHCl_3$ and BA mixtures, respectively.

The FWHMs in Figure 6.3 show an increase in width with increasing mole fraction of either $CHCl_3$ or BA. This could be due to an increased number of environments around the carbonyl ligand with a more polar solvent, however it is impossible to distinguish inhomogeneous broadening from an increase in the width due to homogeneous broadening (faster dephasing or relaxation). In $CHCl_3$ mixtures, VC shows only a slight preference ($f_{2/1}$= 1.3) and VC-O_2 is effectively linear. Clearly whatever

produces the nonlinearity in the frequency does not have as strong an influence on the width for these mixtures.

In BA mixtures, VC shows a similar preference to the center frequency ($f_{2/1} = 2$), but VC-O$_2$ shows a strong bimodal preference as described above with $f_{2/1}^{below} = 76$ and $f_{2/1}^{above} = 0.11$ and a crossover of 0.7 mole fraction. This is a considerably greater preference at low mole fractions than the frequency shows in Figure 6.2b. The VC-O$_2$ carbonyl FWHM values in BA mixtures all have very similar widths, which is considerably wider than the value in pure d_6-benzene but narrower than that in pure BA. This may possibly indicate a strong interaction with BA that is inhibited by even small amounts of benzene. It is worth noting that the widths of both VC and VC-O$_2$ are similar in value; VC-O$_2$ is always slightly larger than VC in BA mixtures and the reverse is true in CHCl$_3$ mixtures. Neither VC nor VC-O$_2$ show the dramatic width changes exhibited by VC-I$_2$.[210] Surprisingly, considering the more open square planar configuration, the VC FTIRs show less preferential solvation in both width and frequency than those of VC-O$_2$. This is likely a reflection of the preferential solvation of the dioxygen ligand, communicated via changes in electron density of the iridium.

These trends in the carbonyl FTIR parameters can be compared to those observed in the kinetics traces. First, the v_{CO} for VC in either solvent system in Figure 6.2a shows no qualitative resemblance of the k_2 changes with solvent mole fraction, so we can conclude that the factors that increase the rate constants in Figure 6.1 are likely unrelated to those that impact the center frequency of the reactant species. Next, we note that although the linewidth on VC is responsive to the change in solvent composition (Figure

6.3a), it exhibits no particular behavior that would correlate it with the kinetic trends. On the other hand, the ν_{CO} for VC-O_2 shows a mild preference for $CHCl_3$ and a strong preference for BA (Figure 6.2b), which at least matches the kinetics fits qualitatively. The FWHM perhaps shows the stronger relationship (Figure 6.3b) with a mostly linear trend in $CHCl_3$ mixtures and a fast rise at low mole fractions of BA with a crossover point at higher concentrations.

Based on these correlations, one could hypothesize that the changes in the solvation shell of VC-O_2 that perturb the ν_{CO} and FWHM when small amounts of BA are added to benzene are also important to facilitating the addition of O_2. As noted in the introduction, calculations by Yu and coworkers indicated that the VC-O_2 structure is a better surrogate for the transition state structure and therefore might be influenced by the solvent composition in similar ways.[68]

The vibrational lifetimes (T_1) of the CO stretch were also found and are recorded in Table 6.1. Those for VC-O_2 have been published previously[210] and discussed at length in Chapter 4, but the lifetimes for VC have not been measured in these mixtures before. In keeping with previous observations, all of the carbonyl lifetimes are significantly shorter for VC than those of VC-O_2 or VC-I_2 due to the lower frequency of the vibration. The range over which the lifetimes change in the same mixtures is also considerably smaller than either of the octahedral adducts. Curiously, the lifetime decreases slightly in the $CHCl_3$ mixtures, rather than increasing. This may indicate a more intramolecular mechanism than was suggested for VC-O_2 and VC-I_2. For the current study, we are most interested in dynamic parameters that vary nonlinearly with mole fraction so that distinct

correlations might be found with kinetic data. The trends in T_1 for VC are similar to the adducts in that they change linearly with mole fraction and will not be discussed further here.
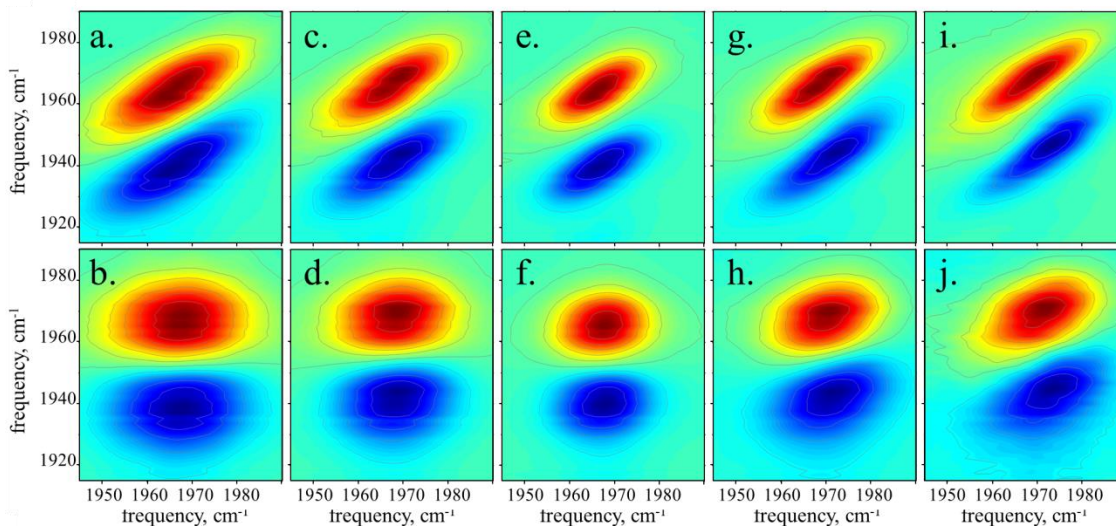

Figure 6.4. 2D-IR spectra collected for VC at $T_w = 0.3$ (top row) and 30 ps (bottom row) for (a,b) neat CHCl$_3$, (c,d) 0.5 mole fraction CHCl$_3$ in d_6-benzene, (e,f) neat d_6-benzene, (g,h) 0.5 mole fraction BA in d_6-benzene, and (i,j) neat BA.

Figure 6.4 shows representative 2D-IR plots for VC at short ($T_w = 0.3$ ps, top row) and long ($T_w = 30$ ps, bottom row) waiting times. In each 2D-IR spectrum, the positive peak (red) arises from the vibrational coherence between the ground and first excited state for the metal-bound carbonyl, and the negative peak (blue) arises from the coherence between the first and second excited states. The horizontal axis is the excitation frequency and the vertical axis is the vibrational echo emission frequency. Starting with the neat d_6-benzene spectra (center column, e and f), it is clear that increasing the T_w causes both peaks to evolve from diagonally elongated to symmetric

and round. At T_w = 0.3 ps, the vibrational oscillators are correlated with their starting frequencies, but by T_w = 30 ps they have diffused spectrally and sampled nearly the entire FTIR linewidth. These dynamics that are normally obscured by the inhomogeneous FTIR lineshape can be characterized by analyzing the centerline slope (CLS) from each 2D-IR spectrum as a function of T_w, which has been shown in many cases to be proportional to the frequency-frequency correlation function (FFCF).[116-117]

To the left from the center column in Figure 6.4, the 2D-IR spectra are shown for 0.5 mole fraction and pure $CHCl_3$. To the right from the center are 0.5 mole fraction and pure BA. The increase in FTIR linewidth in Figure 6.3a is manifested in the increase of the diagonal widths with addition of either $CHCl_3$ or BA in Figure 6.4. Comparing the antidiagonal widths in Figure 6.4a to 6.4i shows that the dynamical contributions to the lineshape are different for these two solvents. The narrowing along the antidiagonal direction for BA mixtures indicates that the homogeneous linewidth is growing narrower, a trend seen previously for VC-I_2.[28] The antidiagonal broadening for $CHCl_3$ mixtures cannot immediately be attributed to a homogeneous linewidth change since the diagonal width is also increasing, however, this will be determined below in the quantitative analysis of the CLS plots.[116-117] It is also apparent that spectral diffusion dynamics are different for these solvents since the long T_w data in Figures 6.4b and 6.4j show the $CHCl_3$ spectrum to be symmetric and round while the BA spectrum is still diagonally elongated. We can predict that the some of the spectral dynamics will exhibit preferential behavior since the 0.5 mole fractions of both solvents (Figures 6.4c, 6.4d, 6.4g, and 6.4h) look quite similar to the neat solvent spectra. Hence, whatever dynamics result in

frequency fluctuations of the carbonyl ligand, they appear to have been mostly developed
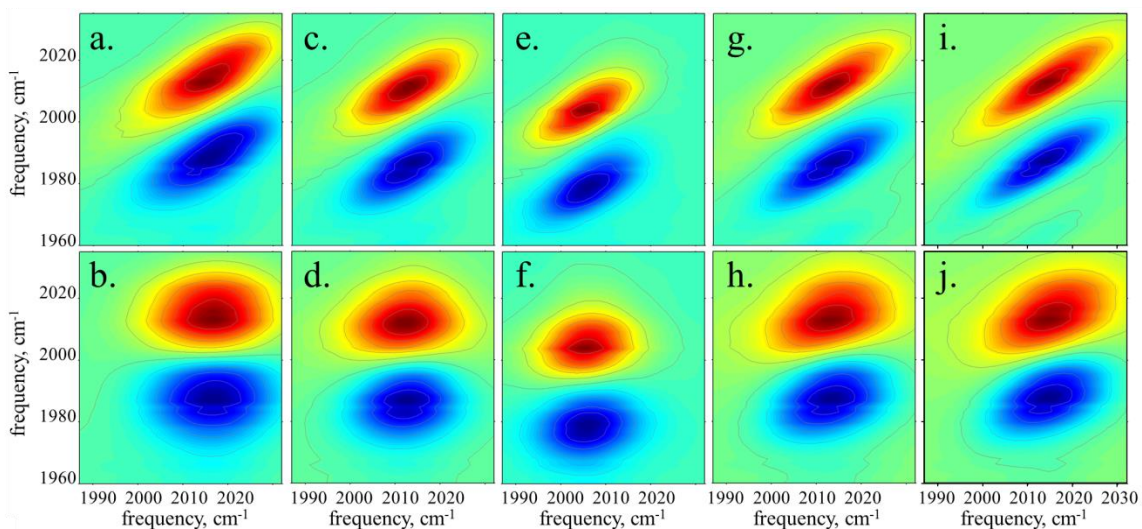
by this mole fraction.

Figure 6.5. 2D-IR spectra collected for VC-O$_2$ at T$_w$ = 0.3 (top row) and 30 ps (bottom row) for (a,b) neat CHCl$_3$, (c,d) 0.5 mole fraction CHCl$_3$ in d_6-benzene, (e,f) neat d_6-benzene, (g,h) 0.5 mole fraction BA in d_6-benzene, and (i,j) neat BA. Note the distinct differences in center wavelength.

The same 2D-IR plots for the VC-O$_2$ adduct are shown in Figure 6.5. In both solvent mixtures, the same qualitative trends hold as were described for VC. In total, for VC and VC-O$_2$ in all solvent mixtures studied at all T$_w$ values, more than 600 2D-IR spectra were collected and analyzed. All spectra are shown in Figures 6.11-6.40. The CLS treatment was applied to the 0-1 carbonyl transition in every spectrum to distill this enormous dataset into a tractable form.
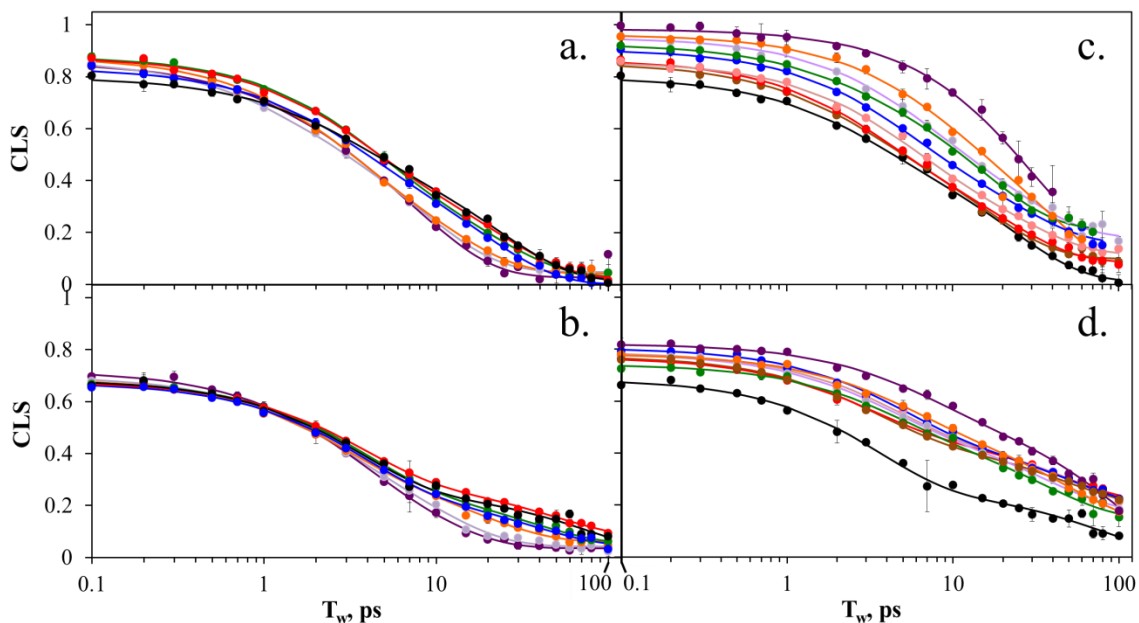
Figure 6.6. CLS decays for VC (top row) and VC-O$_2$ (bottom row) as a function of T$_w$ for binary solvent mixtures of CHCl$_3$ (left column) and BA (right column). Panels a and b show binary mixtures of 0 (black), 0.1 (red), 0.3 (blue), 0.5 (green), 0.7 (orange), 0.9 (lavender), and 1 (purple) mole fractions CHCl$_3$ in d_6-benzene; panels c and d show 0 (black), 0.05 (brown), 0.1 (red), 0.2 (pink), 0.3 (blue), 0.4 (lavender), 0.5 (green), 0.7 (orange), and 1 (purple) mole fractions BA in d_6-benzene. Overlaid solid lines are the multiexponential fits to the data markers. Error bars on each point represent the standard deviation of two or three trials.

Figure 6.6 shows the CLS decays as a function of T$_w$ for each of the mixture series and adducts. A first observation is that the addition of CHCl$_3$ (Figures 6.6a and 6.6b) has a notably smaller effect on the dynamics than addition of BA. In general, CHCl$_3$ mixtures look more similar to pure d_6-benzene than BA mixtures, with any deviations appearing at longer T$_w$ values. Spectral diffusion in BA (Figures 6.6c and 6.6d) is considerably slower than in d_6-benzene or CHCl$_3$. Intriguingly, the overall spectral diffusion for VC-O$_2$ in BA shows the same regime breakdown as was obvious in the FTIR FWHM; the endpoints are very distinct while the mixtures are very similar. Also the y-intercept of the CLS, which in some situations is related to the homogeneous linewidth, is higher for BA mixtures than for CHCl$_3$. It is also generally higher in VC

mixtures than in VC-O$_2$, so the homogeneous linewidth could be larger for VC-O$_2$. Looking at Figure 6.6 as a whole, aside from differences in the y-intercepts, the dynamical data extracted from the 2D-IR spectra look fairly similar for VC and VC-O$_2$ in a given solvent system. This supports the notion that the carbonyl vibrational mode mostly reports on the dynamics of the proximal solvation shell rather than the intramolecular dynamics of the molecule to which it is bound.

The full FFCFs were found by fitting to the FTIR spectra as well as the CLS decay.[116-117] With only a few exceptions, the data in Figure 6.6 and their corresponding FTIR spectra were well fit by a double exponential function (Equation 3), including a motionally narrowed term (for the homogeneous lineshape) and a static offset as shown below.

$$FFCF(t) = \frac{\delta(t)}{T_2} + \Delta_1^2 e^{-t/\tau_1} + \Delta_2^2 e^{-t/\tau_2} + \Delta_0^2 \qquad (6.3)$$

A few of the datasets did not require a static offset to fit well and the neat BA 1966-centered CLS decay did not need a first exponential term. Since these measurements took place in the solution phase, it is unlikely that the static offset truly represents static inhomogeneity; it is more likely that there are motions which perturb the CO stretch that are slower than we can measure. The 2D-IR peaks for VC in the 0.7 mole fraction and pure BA mixtures do not run straight along the diagonal (see for example Figure 6.4i), and as a result the CLS shows a kink around 1970 cm^{-1}. This is indicative of non-Gaussian dynamics.[113] Though the CLS method is not strictly accurate when non-Gaussian dynamics are present,[116] it has been shown to give a reasonable approximation of the dynamics.[113] In these two cases, the CLS method was applied twice, once centered

around 1966 cm^{-1} and the other centered around 1973 cm^{-1}. The population at 1966 cm^{-1} represents the majority of the FTIR linewidth and so the CLS values from this region were plotted in Figure 6.6c. The end result of this analysis is a collection of amplitudes and time constants for spectral diffusion as well as the inhomogeneity and homogeneous linewidths of the carbonyl mode for both molecules in all solvent mixtures studied. These parameters are all tabulated in Tables 6.3 and 6.4; a few will be presented and discussed graphically below. Returning to the purpose of this study, we seek to determine how the dynamic parameters vary with the mole fraction of the solvent to identify similarities and correlations in the solvent dynamics with the reaction kinetics introduced in Figure 6.1. Since the strongest relationship of the FTIR parameters was with the FWHM, it seems reasonable to also carry out an inspection of the broadening sources, as was done previously for VC-I$_2$.[28]

Table 6.3. FFCF parameters for VC in BA and $CHCl_3$ binary mixtures in d_6-benzene.

mole frac.	Δ_1 (rad/ps)	τ_1 (ps)	Δ_2 (rad/ps)	τ_2 (ps)	Δ_0 (rad/ps)	Γ (cm^{-1})
			$CHCl_3$ in d_6-benzene			
0	0.76 (0.11/0.03)	2.7 (0.5)	1.09 (0.07/0.02)	23.2 (2.3)	0.15 (0.45/0.09)	1.1 (0.1/0.1)
0.1	0.93 (0.10/0.03)	3.1 (0.3)	1.07 (0.08/0.02)	22.6 (2.0)	0.22 (0.37/0.05)	1.31 (0.1/0.09)
0.3	0.94 (0.06/0.03)	2.7 (0.4)	1.25 (0.03/0.02)	18.6 (1.1)	-	1.2 (0.1/0.1)
0.5	1.12 (0.02/0.05)	3.6 (0.5)	1.19 (0.02/0.05)	20.5 (2.8)	0.29 (0.07/0.06)	1.1 (0.1/0.1)
0.7	1.10 (0.02/0.10)	2.3 (0.6)	1.34 (0.01/0.08)	11.2 (1.8)	0.39 (0.05/0.05)	1.5 (0.1/0.1)
0.9	0.90 (0.14/0.04)	1.2 (0.2)	1.57 (0.05/0.02)	8.5 (0.4)	0.439 (0.154/0.007)	1.9 (0.1/0.1)
1	0.82 (0.90/0.20)	1.5 (1.0)	1.73 (0.02/0.09)	8.1 (1.1)	0.35 (0.07/0.06)	1.7 (0.1/0.1)
			BA in d_6-benzene			
0	0.76 (0.11/0.03)	2.7 (0.5)	1.09 (0.07/0.02)	23.2 (2.3)	0.16 (0.45/0.09)	1.1 (0.1/0.1)
0.05	0.75 (0.12/0.04)	2.3 (0.4)	1.09 (0.07/0.03)	15.8 (1.3)	0.48 (0.15/0.02)	1.25 (0.09/0.08)
0.1	0.87 (0.01/0.03)	3.0 (0.4)	1.029 (0.009/0.02)	20.5 (1.9)	0.44 (0.02/0.02)	1.24 (0.06/0.06)
0.2	0.94 (0.02/0.06)	4.4 (0.7)	1.02 (0.02/0.05)	24.2 (4.8)	0.54 (0.03/0.04)	1.0 (0.1/0.1)
0.3	0.915 (0.007/0.07)	4.2 (0.8)	1.029 (0.005/0.06)	23.7 (5.5)	0.627 (0.008/0.051)	0.99 (0.09/0.07)
0.4	0.85 (0.01/0.18)	5.1 (2.2)	1.088 (0.007/0.122)	25 (10)	0.66 (0.01/0.10)	0.53 (0.1/0.09)
0.5	0.56 (0.03/0.06)	1.9 (0.6)	1.296 (0.009/0.020)	15.3 (0.9)	0.77 (0.01/0.02)	0.78 (0.1/0.09)
0.7 1966	0.86 (0.03/0.07)	7.0 (1.6)	1.31 (0.02/0.04)	42.5 (4.2)	-	0.42 (0.01/0.01)

	1973	0.51 (0.07/0.05)	2.8 (0.8)	0.91 (0.03/0.02)	22.7 (6.5)	0.58 (0.05/0.03)	0.61 (0.02/0.02)
1	1966	-	-	1.5825 (0.0001/0.01)	30.0 (5.1)	0.5674 (0.0004/0.205)	0.20 (0.06/0.06)
	1973	0.42 (0.05/0.03)	2.8 (0.9)	0.99 (0.02/0.01)	57.1 (4.4)	-	0.47 (0.01/0.01)

Values in parentheses represent (positive error/negative error). Errors for τ values represent the standard error of the fit. For Δ values, the positive errors show the range of which that parameter could be increased while the other parameters floated to fit the FTIR line shape 98% as well as the best value (with all parameters floating). The negative errors represent the propagated error of the CLS fits.

Table 6.4. FFCF parameters for VC-O$_2$ BA and CHCl$_3$ binary mixtures in d_6-benzene.

mole frac.	Δ_1 (rad/ps)	τ_1 (ps)	Δ_2 (rad/ps)	τ_2 (ps)	Δ_0 (rad/ps)	Γ (cm^{-1})
			CHCl$_3$ in d_6-benzene			
0	1.058 (0.004/0.02)	3.5 (0.4)	0.828 (0.004/0.02)	82 (12)	-	1.50 (0.08/0.07)
0.1	1.044 (0.005/0.02)	3.6 (0.2)	0.818 (0.005/0.02)	50 (12)	0.448 (0.009/0.1)	1.45 (0.1/0.09)
0.3	1.128 (0.005/0.02)	3.5 (0.3)	0.854 (0.005/0.02)	34.7 (7.1)	0.36 (0.01/0.08)	1.55 (0.09/0.08)
0.5	1.152 (0.005/0.03)	3.6 (0.4)	0.892 (0.005/0.03)	34.5 (9.2)	0.40 (0.01/0.1)	1.45 (0.09/0.08)
0.7	1.10 (0.01/0.04)	2.5 (0.3)	1.05 (0.01/0.04)	17.1 (2.3)	0.47 (0.02/0.03)	1.6 (0.1/0.1)
0.9	0.97 (0.04/0.1)	2.2 (0.6)	1.28 (0.02/0.07)	9.6 (1.3)	0.41 (0.06/0.04)	1.7 (0.1/0.1)
1	1.1 (0.1/0.2)	2.6 (0.7)	1.3 (0.1/0.1)	8.9 (2.3)	0.38 (0.3/0.05)	1.7 (0.2/0.1)
			BA in d_6-benzene			
0	1.058 (0.004/0.02)	3.5 (0.4)	0.828 (0.004/0.02)	82 (12)	-	1.50 (0.08/0.07)
0.05	1.02 (0.01/0.01)	3.3 (0.2)	0.94 (0.01/0.01)	48.0 (5.6)	0.79 (0.01/0.03)	1.1 (0.1/0.1)

0.1	0.97 (0.01/0.03)	2.9 (0.3)	0.977 (0.008/0.02)	43.1 (8.2)	0.843 (0.009/0.04)	0.92 (0.09/0.08)
0.2	1.052 (0.004/0.04)	4.5 (0.3)	1.056 (0.004/0.04)	70 (19)	0.697 (0.006/0.1)	0.73 (0.07/0.06)
0.3	1.040 (0.005/0.03)	4.6 (0.4)	0.994 (0.004/0.03)	50 (12)	0.796 (0.006/0.06)	0.80 (0.08/0.07)
0.4	0.968 (0.008/0.03)	3.6 (0.4)	1.098 (0.006/0.02)	36.2 (5.0)	0.773 (0.008/0.03)	0.71 (0.1/0.08)
0.5	0.940 (0.006/0.07)	4.1 (1.0)	1.146 (0.004/0.05)	36.0 (9.3)	0.725 (0.006/0.07)	0.72 (0.08/0.07)
0.7	0.952 (0.008/0.04)	4.8 (0.6)	1.213 (0.005/0.03)	48.4 (8.1)	0.672 (0.009/0.07)	0.69 (0.1/0.09)
1	0.97 (0.02/0.02)	6.3 (0.7)	1.48 (0.01/0.01)	91.1 (4.4)	-	0.26 (0.2/0.08)

Values in parentheses represent (positive error/negative error). Errors for τ values represent the standard error of the fit. For Δ values, the positive errors show the range of which that parameter could be increased while the other parameters floated to fit the FTIR line shape 98% as well as the best value (with all parameters floating). The negative errors represent the propagated error of the CLS fits.

For fits involving multiple exponentials (i.e. Eq. 3), it can often be difficult to claim uniqueness for a fit; the dynamic parameters can themselves be correlated. On some level, this is an expected result when there is a gradual change that occurs in a sample, such as diluting a pure solvent progressively with a second solvent. The dynamics that are captured in the Δ and τ values are an attempt to impose a biexponential categorization of dynamics onto what is realistically a continuum of time scales. Changing the sample in some way may cause all of the dynamics to become slower, which could shift the originally "slow" dynamics into the "static" category and shift the originally "faster" dynamics into the "slow" exponential. Likewise, dynamics that were at first too slow to resolve may then populate the "fast" exponential. It is not unreasonable to expect that a continuous variation of the mole fraction of a solvent would

cause the dynamics in one category to be counterbalanced by the appearance of amplitude in another category. Many of the error values on the parameters in Tables 6.3 and 6.4 reflect exactly this sort of uncertainty – they indicate how much one parameter can change, while letting all of the others compensate, and still obtain nearly the same goodness of fit.[28] Figures 6.41-6.44 show plots (in the left hand column) for all of the fit parameters as a function of mole fraction. In the right hand column, the differences between the data and the solid line connecting the first and last point is plotted. This difference is also scaled by the range of the data, that the right hand columns may be compared across all four figures. Examining Figure 6.41 as an example, specifically the right column plots for Δ_1 and Δ_2, it is immediately apparent that when one parameter decreases in a seemingly preferential way, the other increases to counter it. It is difficult to determine whether this correlation of parameters is a limitation of the way that the data are fit, or whether this is real preferential variation. There are many cases in these four figures in which the spikes and dips of preference in one parameter are balanced by a fluctuation in another parameter.
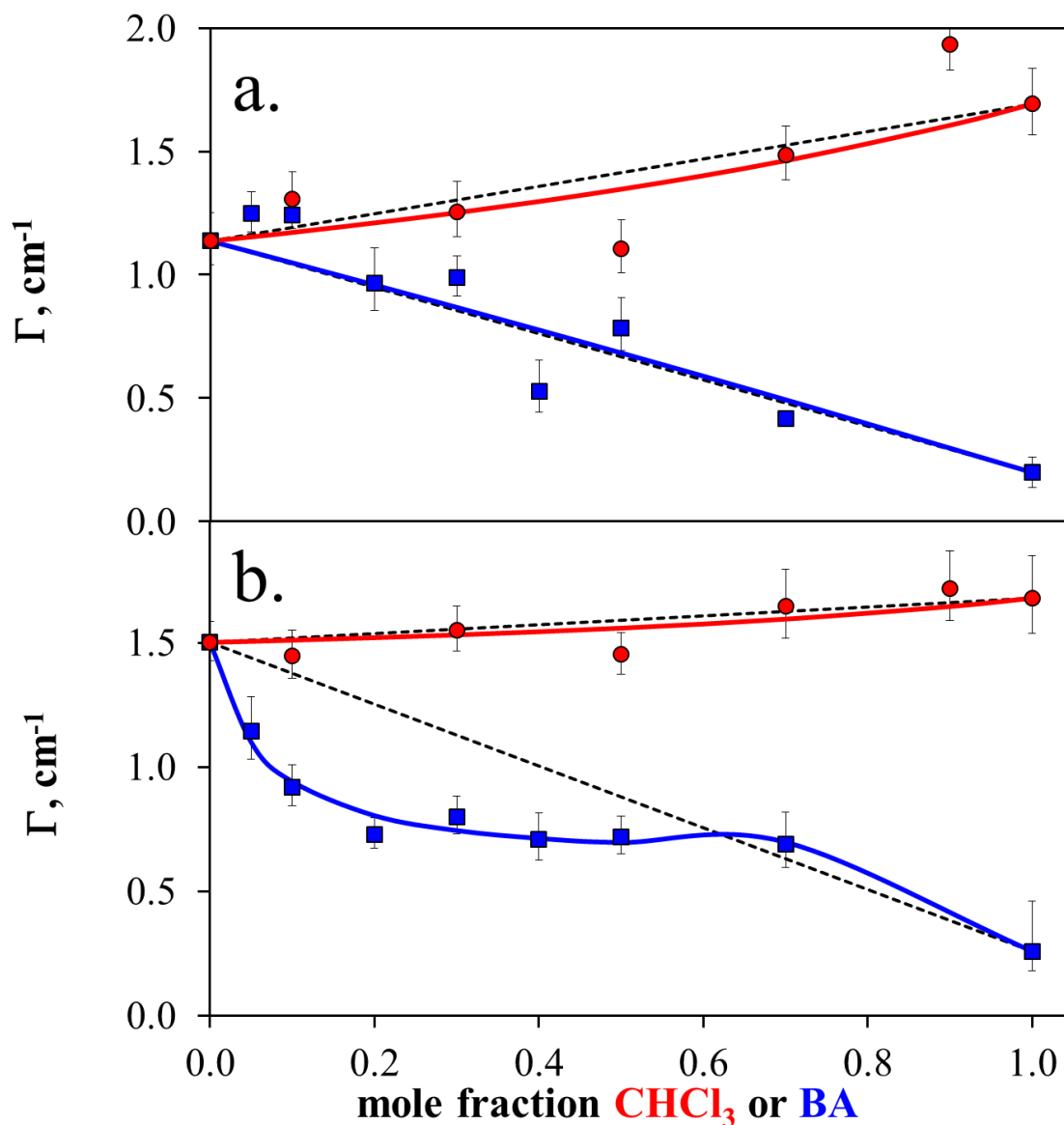
Figure 6.7. Homogeneous linewidth, Γ, for a) VC and b) VC-O$_2$ as a function of the mole fraction of CHCl$_3$ (red circles) or BA (blue squares) added to d_6-benzene. Black dashed lines are aids to the eye connecting the first and last points. Solid (red and blue) lines are the best fit to the data calculated from Equation 6.1 or 6.2 for CHCl$_3$ and BA mixtures, respectively.

In order to minimize the possibility of such errors influencing our correlation, we have chosen as our main parameters the homogeneous linewidth, Γ, and what we shall call the inhomogeneous amplitude, Ω, as defined in Equations 4 and 5.

$$\Omega = \sum_{n=0}^{2} \Delta_n^2 \qquad (6.4)$$

$$\Gamma = \frac{1}{\pi T_2} = \frac{1}{2\pi T_1} + \frac{1}{\pi T_2^*} + \frac{1}{3\pi T_{or}} \qquad (6.5)$$

In these equations, T_2^* is the pure dephasing time and T_{or} is the orientational relaxation time. Generally, T_{or} is on the order of hundreds of picoseconds for molecules of this size[15, 219] and so does not contribute significantly to Γ.

Figure 6.7 shows the values for Γ calculated from the CLS analysis of the 2D-IR spectra for VC and VC-O$_2$ in CHCl$_3$ (red circles) and BA (blue squares) mixtures. The general trends are very similar to those previously observed for VC-I$_2$,[28] where the homogeneous linewidth changes very little in CHCl$_3$ (red circles) and decreases in BA (blue squares) mixtures. In spite of the differences in y-intercepts for the CLS decays noted above, the homogeneous linewidths are not very different for the two solutes. In the CHCl$_3$ mixtures at low mole fraction, VC-O$_2$ is broader, but the distinction disappears after 0.7 mf, when the linewidth of VC rises slightly faster. The broadening noticed in the FTIR for VC with increasing amount of CHCl$_3$ could be partly coming from this increase in the homogeneous linewidth; however, it does not show the same preference for CHCl$_3$. The notable outlier in this figure is the Γ for VC-O$_2$ in BA mixtures (blue squares, Figure 6.7b). The variation of the homogeneous linewidth for this adduct and this solvent mixture is clearly nonlinear, displaying a quick decrease with the addition of a small amount of BA to d_6-benzene. The fitting the parameter to Equation 2 reveals a preference for BA in the solvation shell of about 16:1, which is the same within error as

the preference observed for rate constant for O_2 addition. There is a clear correlation

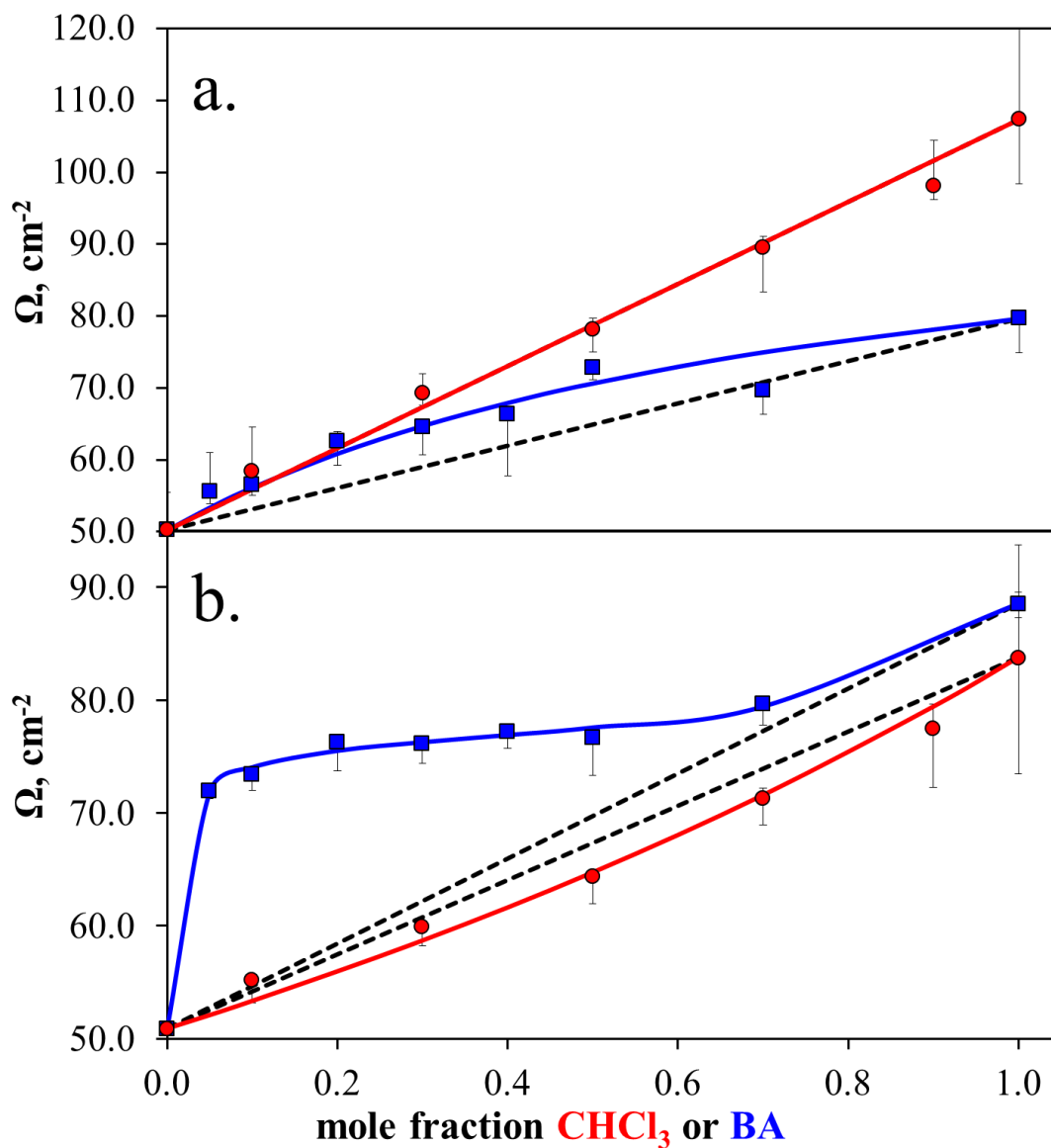between the homogeneous linewidth of the product complex and the reaction rate.

Figure 6.8. Inhomogeneous amplitude, Ω, for a) VC and b) VC-O_2 as a function of the mole fraction of $CHCl_3$ (red circles) or BA (blue squares) added to d_6-benzene. Black dashed lines are aids to the eye connecting the first and last points. Solid (red and blue) lines are the best fit to the data calculated from Equation 6.1 or 6.2 for $CHCl_3$ and BA mixtures, respectively.

Figure 6.8 shows that a complementary trend exists between the homogeneous linewidth and the inhomogeneous amplitude. The CHCl$_3$ mixtures vary linearly with mole fraction added for VC; VC-O$_2$ exhibits a possible slight preference for d_6-benzene, but the deviation from linearity is slight. The VC-O$_2$ values for BA mixtures in Figure 6.8b, however, show that Ω quickly increases with small additions of BA to d_6-benzene. Comparing Figure 6.8 to Figure 6.3, which showed the ν_{CO} FWHM values, it is quite clear that the changes in the FTIR linewidth with mole fraction track remarkably well with the changes in the inhomogeneous amplitude in the FFCF. This shows that linear and nonlinear behavior of the steady-state lineshape in different mole fractions of either solvent system is the result of increases in the inhomogeneity of chemical environments around the solute.

To help further elucidate the possible sources of such preferences as are exhibited by the many static and dynamic parameters hitherto discussed, and particularly those in Figure 6.8, Figures 6.9 and 6.10 show some of the steady-state hydrogen bonding properties of these mixtures. Figure 6.9 shows the center frequency (a) and FWHM (b) of the chloroform C-H stretching mode as a function of solvent composition. Obviously there is not a value for either of these parameters in pure d_6-benzene; the points marked with a dash here and in Figure 6.10 were found by fitting the three lowest mole fraction points and extrapolating to zero.
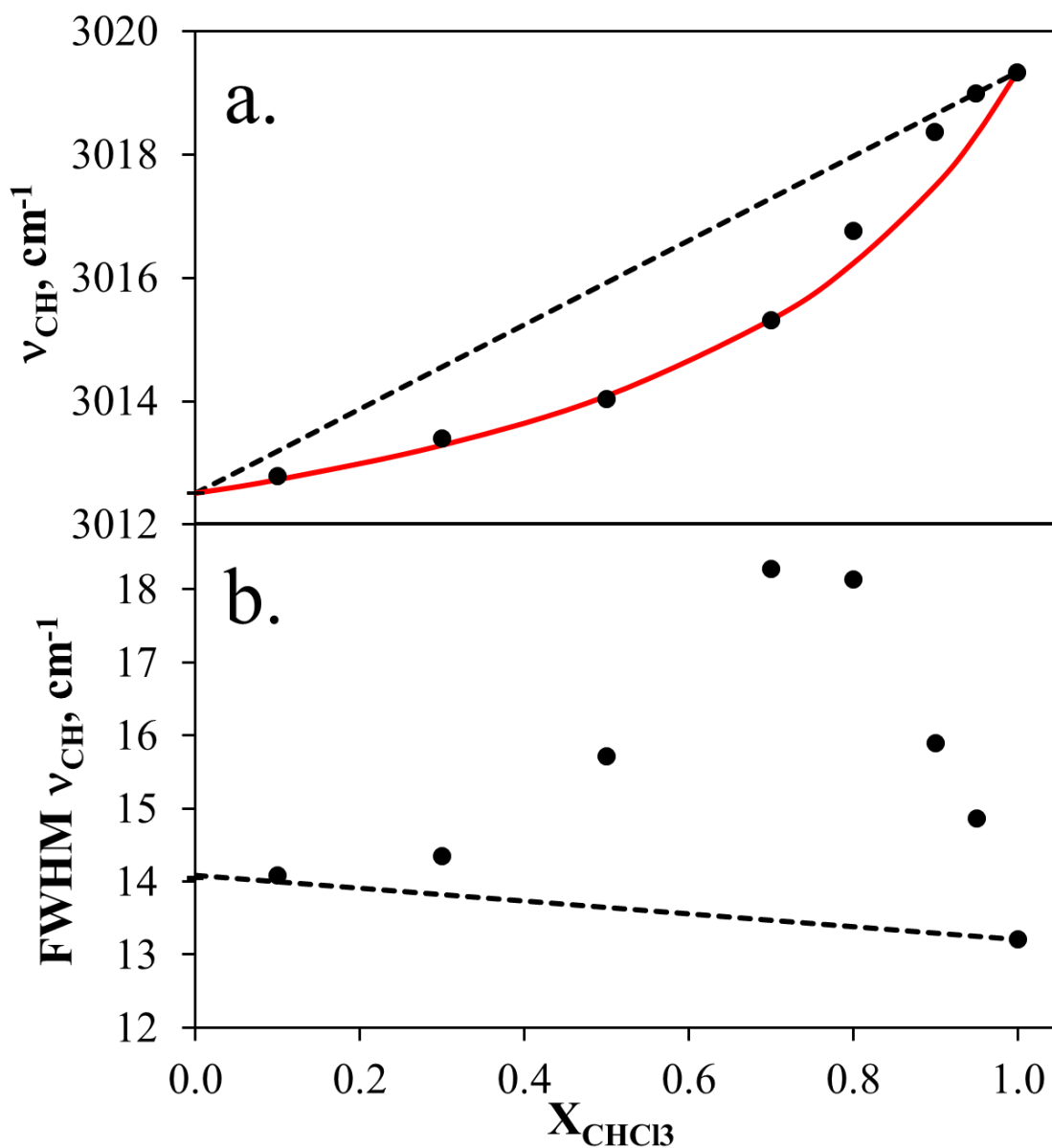
Figure 6.9. Frequency (a) and FWHM (b) of the C-H stretching mode of chloroform in chloroform/d_6-benzene. Points are the data values; the dash at 0 mole fraction comes from the extrapolation of a fit to the data points at the three lowest mole fraction values. Black dashed lines are aids to the eye connecting the first and last points. The solid (red) line shows the best fit to Equation 6.1.

As was previously mentioned in Chapter 1, the stretching frequency of a mode involved in hydrogen bonding undergoes a red shift. This is clearly seen in Figure 6.9a.

It is worth noting that this is one of the very few parameters that shows preference for d_6-

benzene rather than its more polar counterpart; this could possibly give some reasoning behind the preference shown in Ω by VC-O$_2$. The FWHM plot in Figure 6.9b gives some further insight into some of the subtler changes in Figure 6.9a; it shows a maximum around 0.7-0.8 mole fraction. In Figure 6.9a, the points on the low mole fraction side of this maximum are very similar in frequency to one another, as are those on the high mole fraction side. This implies a switch between two different regimes, occurring at around 0.7-0.8 mole fraction. It is possible that this may have some relationship to Δ_0 (see Tables 6.3 and 6.4), the amplitude of the motions slower than those we can resolve, which shows a maximum around 0.7 for both solutes. This could represent the effect of the chloroform molecules to which the solute C-O is sensitive switching between these different regimes.

The FTIR of benzyl alcohol shows two peaks in the O-H stretching region: a sharp (free OH) peak around 3560 cm^{-1} and a broad (H-bonded OH) peak centered around 3325 cm^{-1}. Figure 6.10a shows the FWHM of the sharp peak as a function of mole fraction; Figure 6.10b shows the integrated area ratio of the sharp peak to the sum of the sharp and broad peaks, also as a function of mole fraction. In neither of these plots do we see the nonlinearity moving to linearity shown in Figures 6.1, 6.7, and 6.8. Both are reasonably well fit by a single preference parameter; the slight maximum of the FWHM present at 0.5 mole fraction is a hindrance to the goodness of the preference fit. These measures of hydrogen bonding may be those properties that influence the inhomogeneous amplitude and FWHM of VC in the BA mixtures, as well as the frequency of both solutes.
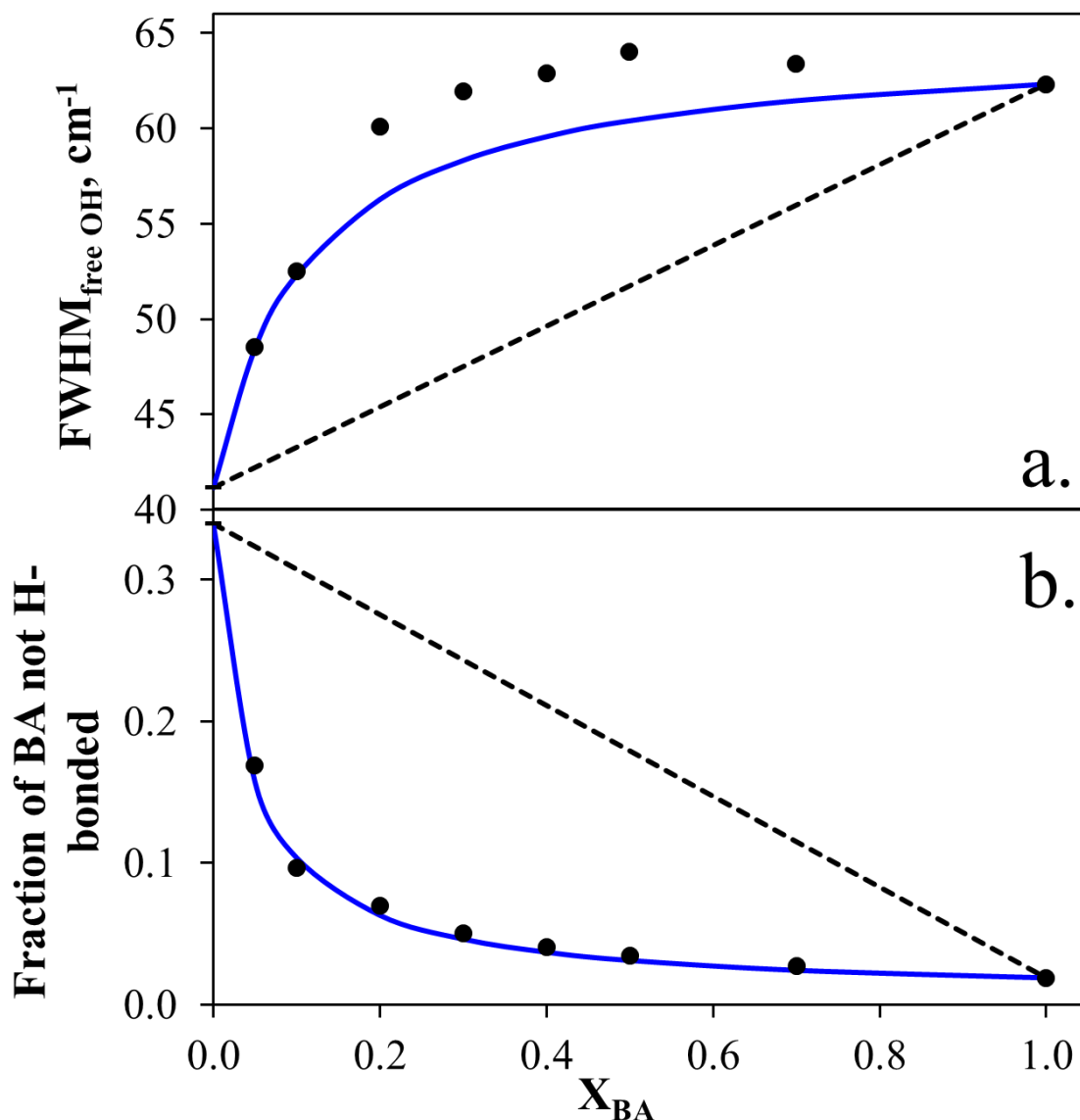
Figure 6.10. Hydrogen bonding parameters for benzyl alcohol in benzyl alcohol/d_6-benzene. Window a) shows the FWHM of the free OH stretching mode. Window b) shows the integrated area ratio of the free OH peak to the sum of the free and H-bonded peaks. Points are the data values; the dash at 0 mole fraction comes from the extrapolation of a fit to the data points at the three lowest mole fraction values. Black dashed lines are aids to the eye connecting the first and last points. Solid (blue) lines show the best fit to Equation 6.1.

The abrupt increase in k_2 with small quantities of BA in Figure 6.1 is accompanied by a corresponding increase in the spectral inhomogeneity around the product species (VC-O$_2$) in Figure 6.8. At the same time, beneath the inhomogeneous

lineshape, Figure 6.7 shows that the fast pure dephasing events that produce the homogeneous lineshape slow down. Returning to the view that VC-O$_2$ reflects the transition state structure,[68] the preferential behavior of the kinetics in BA/d_6-benzene mixtures appear to be mirrored by a general increase in chemical heterogeneity in the solvation shell and a slowing of fast solvent dynamics. It is curious that these very fast motions around the product should be correlated with the nonlinearity when those occurring around the reactant do not. This is again a confirmation that the "product-like" transition state calculated by Yu and coworkers seems to be an accurate picture of the actual reaction mechanism.[68] If these fast motions around the product carbonyl behave in the same fashion around the activated complex, then it may be that they somehow assist the pincer motion.

6.5. Conclusions

We performed an extensive spectroscopic and kinetic study on the oxidative addition of O$_2$ to Vaska's complex. We measured the solvent dynamics around both product and reactant at equilibrium. This provides a departure from the majority of 2D-IR/kinetics studies, as this reaction is not in the low-friction limit of solvent-solute interactions, and it thus provides an opportunity to examine a reaction that is squarely in the range where transition state theory works well.

We found that the kinetics for mixtures of d_6-benzene and chloroform showed a linear trend in mole fraction. This makes it difficult to assign correlation to any particular

parameter, but it showed strong correlation with the VC and VC-O_2 inhomogeneity amplitudes.

For mixtures of benzyl alcohol and d_6-benzene, the rate constant showed a mostly linear trend, with deviation at low mole fractions of benzyl alcohol. The linearity of the process could be coming from the reactant, which is far more linear in both inhomogeneity amplitude and homogeneous linewidth. This would be consistent with transition state theory's contention that the reactant should have the largest influence on the rate; however, similarly to the CHCl3 mixtures, since both parameters correlate linearly with mole fraction, correlation between the parameters cannot be currently asserted with any certainty.

The nonlinear deviation, however, corresponded to similar deviations for the VC-O_2 inhomogeneity amplitudes and the VC-O_2 homogeneous linewidth. This seems to indicate that the nonlinearity is somehow related to the dynamic inhomogeneity surrounding the product and also the slowing of fast solvent motions around the product. The greater variety of the solvation environments may give greater accessibility to favorable configurations, and a slowing of the fast pure dephasing motions may give such configurations greater time stability.

Further studies along these lines could be carried out; the kinetics of the addition of I_2 to VC are considerably faster than those of O_2 as well as being irreversible. Of course, the eventual goal would be to examine these dynamics in the context of a catalytic reaction, such as decarbonylation[80] or hydrogen atom transfer.[79]
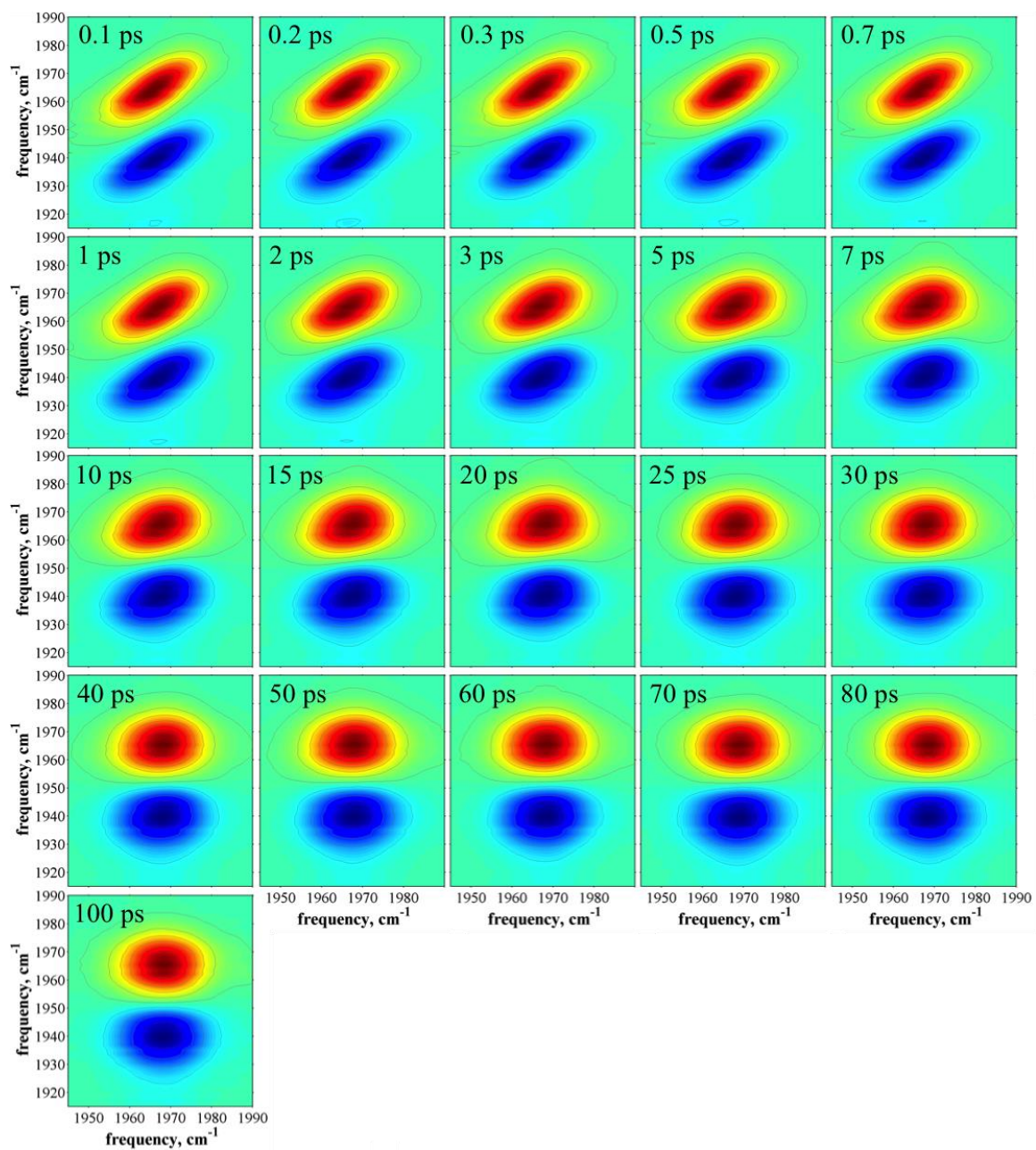
Figure 6.11. Full 2D-IR dataset for VC in all d_6-benzene.
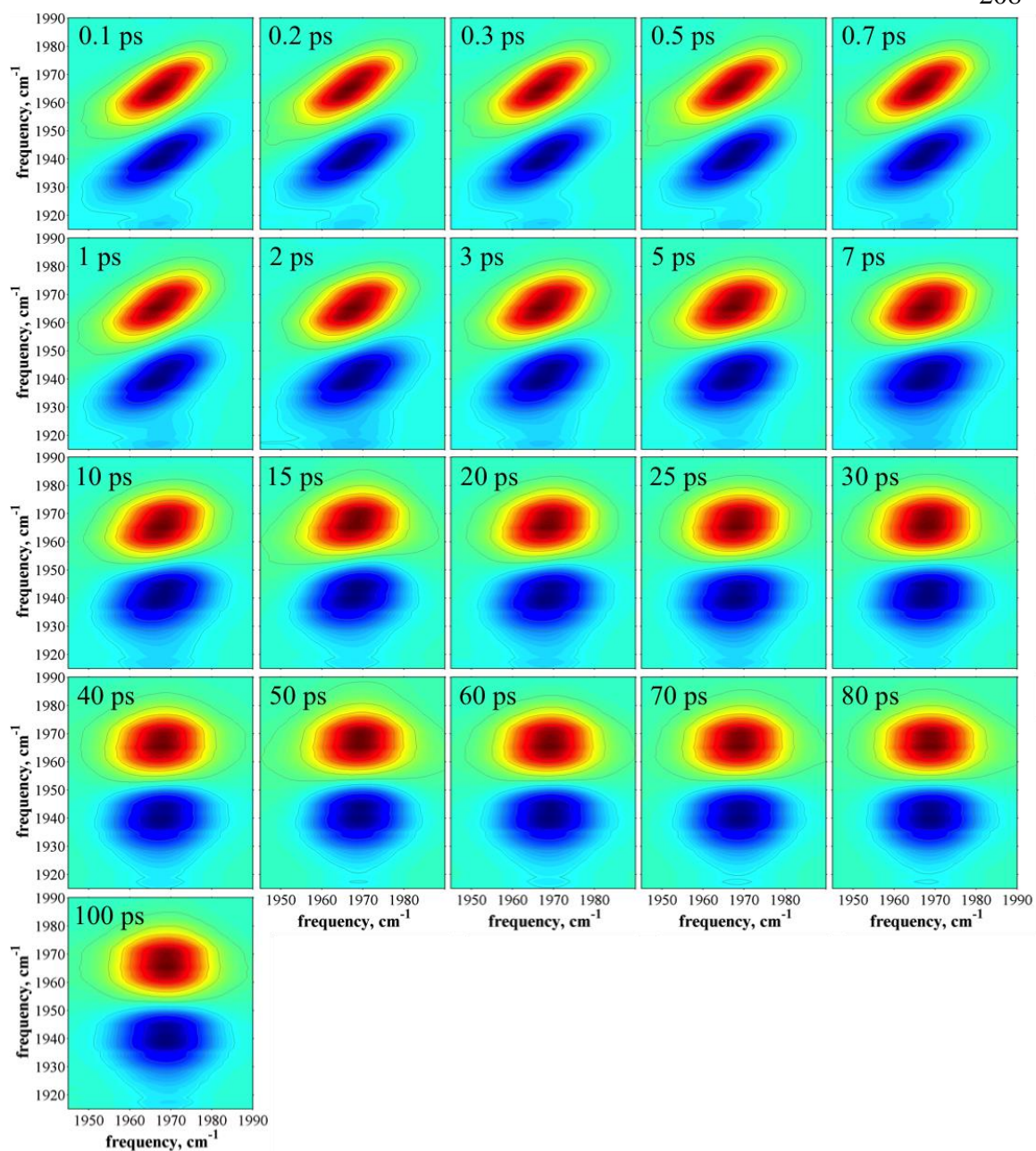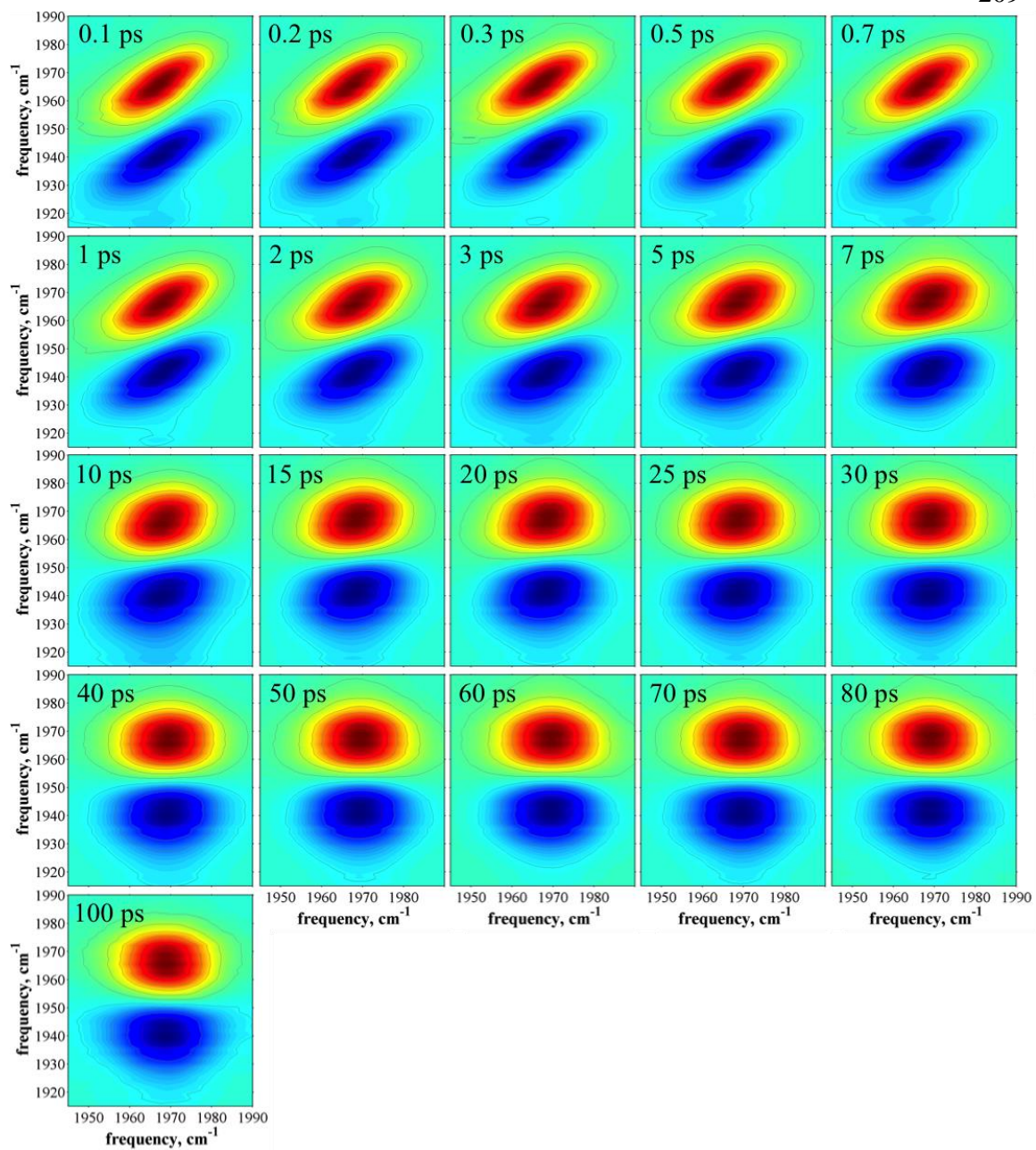
Figure 6.12. Full 2D-IR dataset for VC in 0.1 mole fraction CHCl₃.

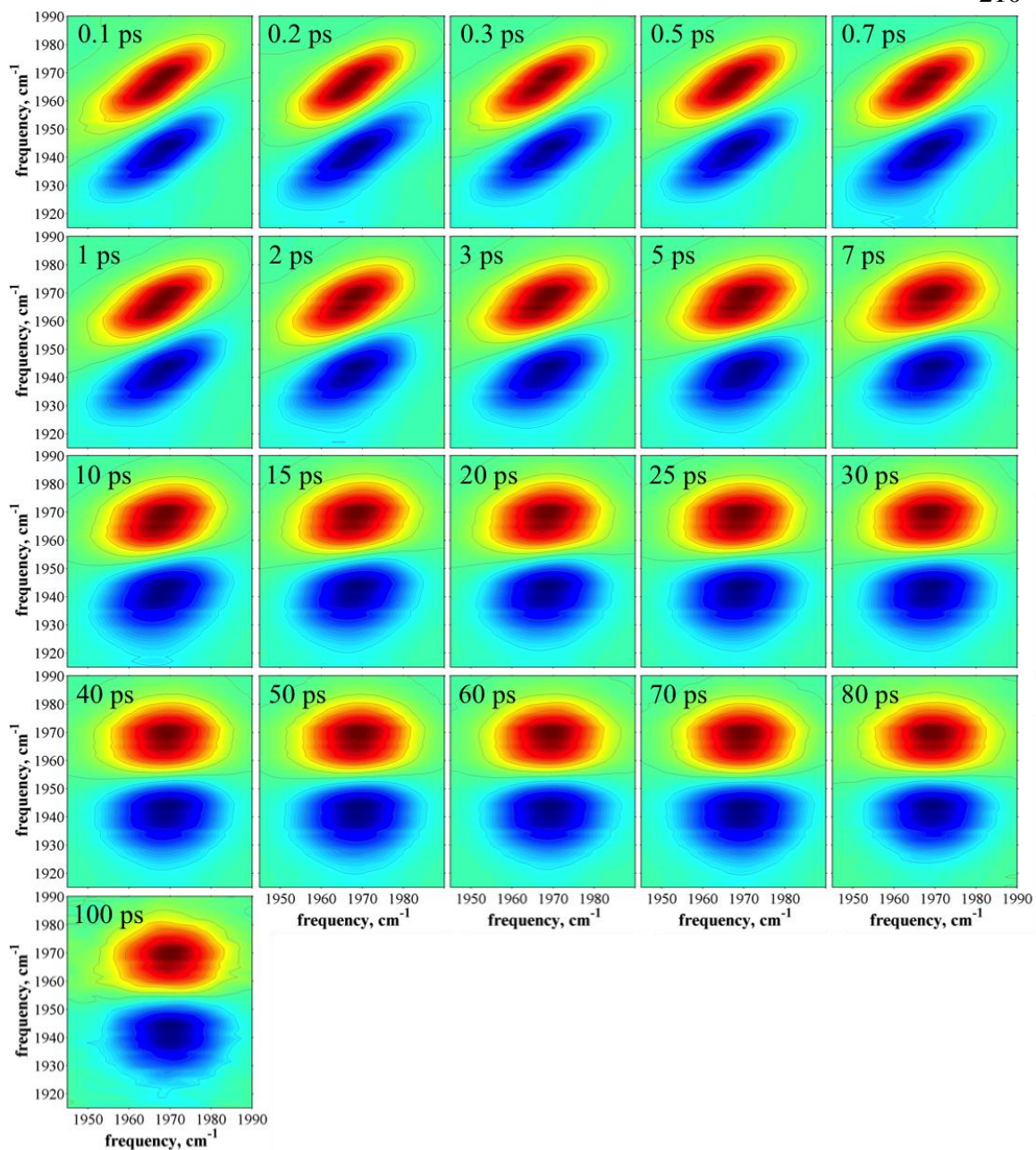**Figure 6.13.** Full 2D-IR dataset for VC in 0.3 mole fraction CHCl$_3$.

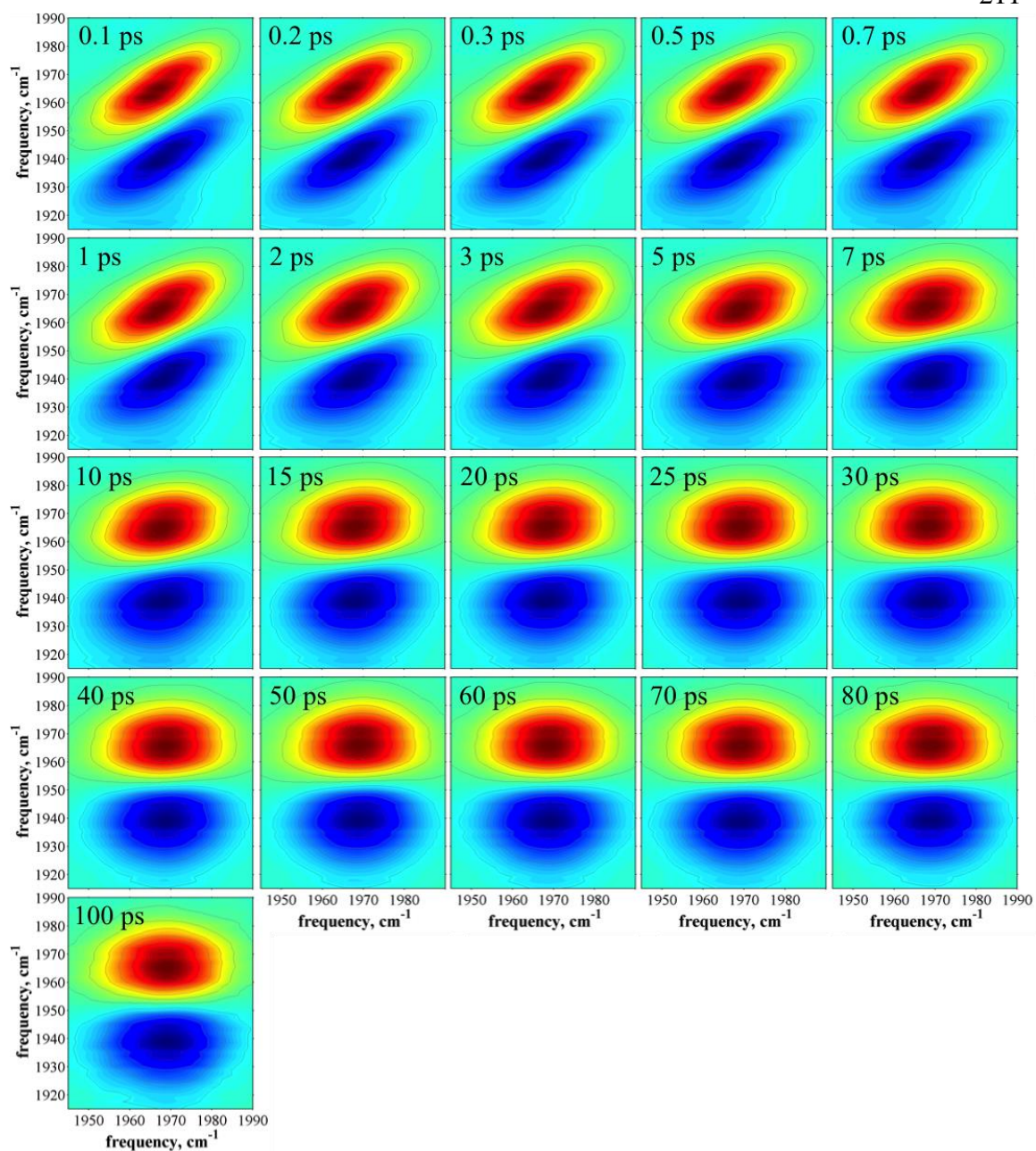**Figure 6.14.** Full 2D-IR dataset for VC in 0.5 mole fraction CHCl$_3$.

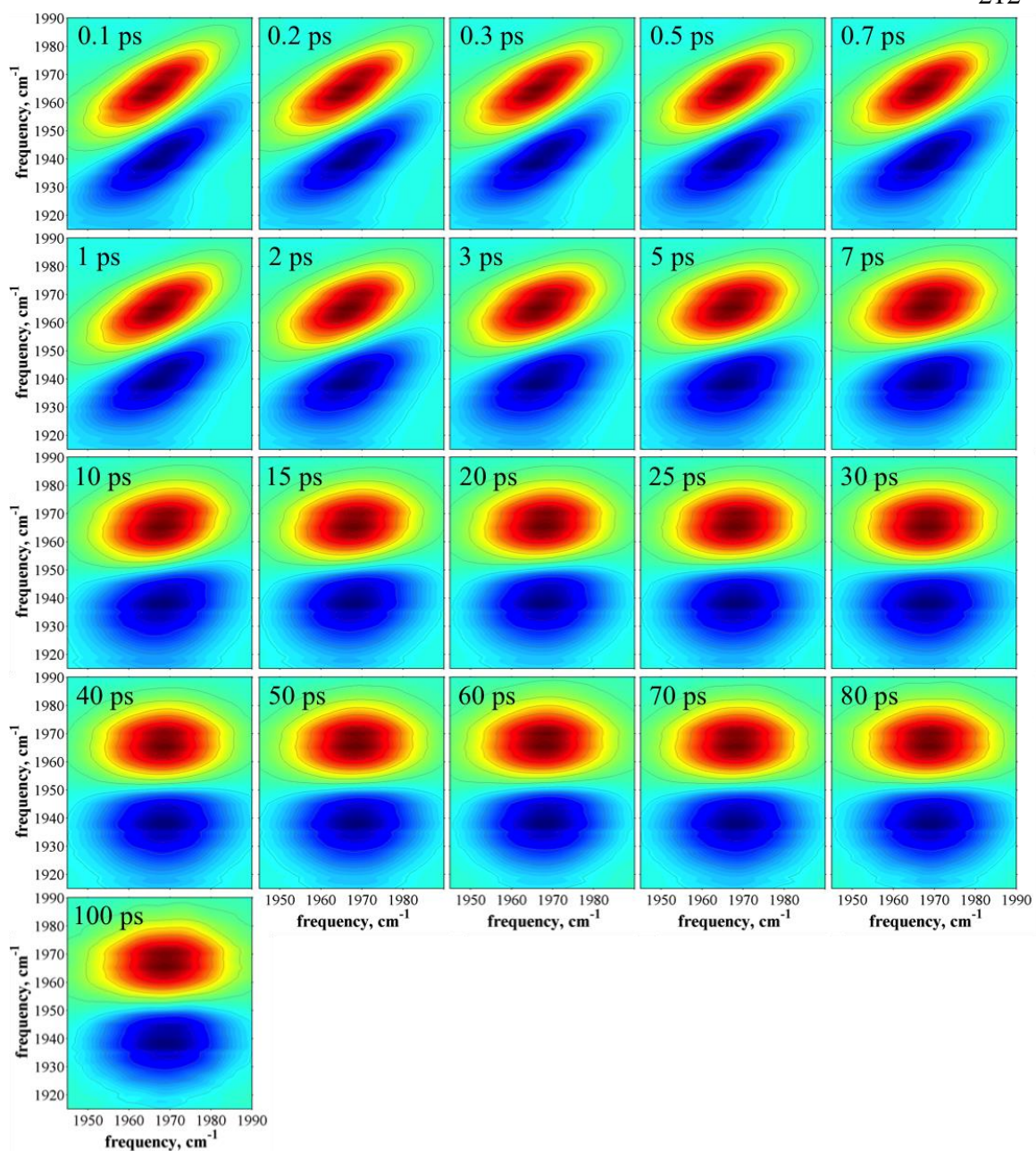**Figure 6.15.** Full 2D-IR dataset for VC in 0.7 mole fraction CHCl$_3$.

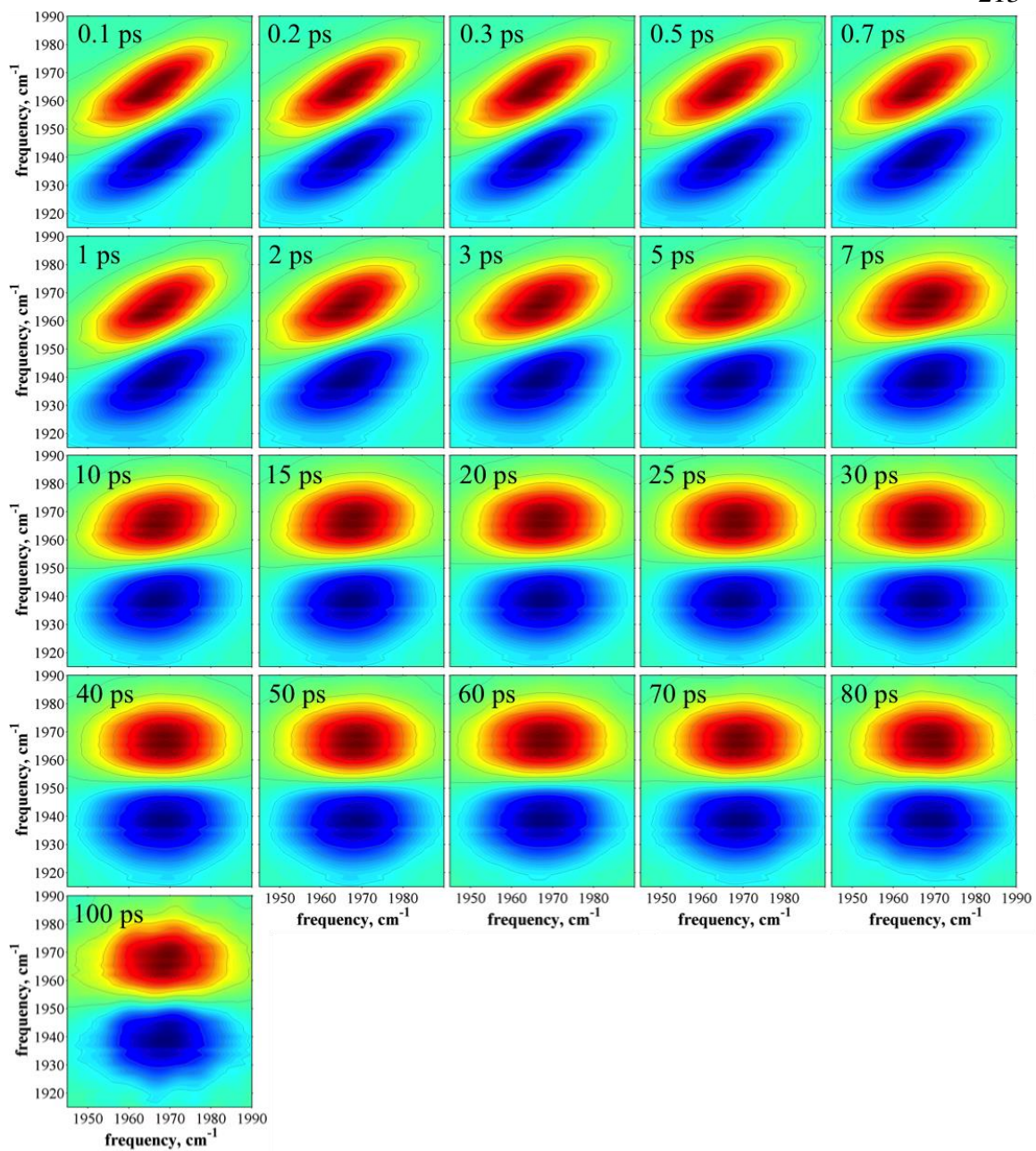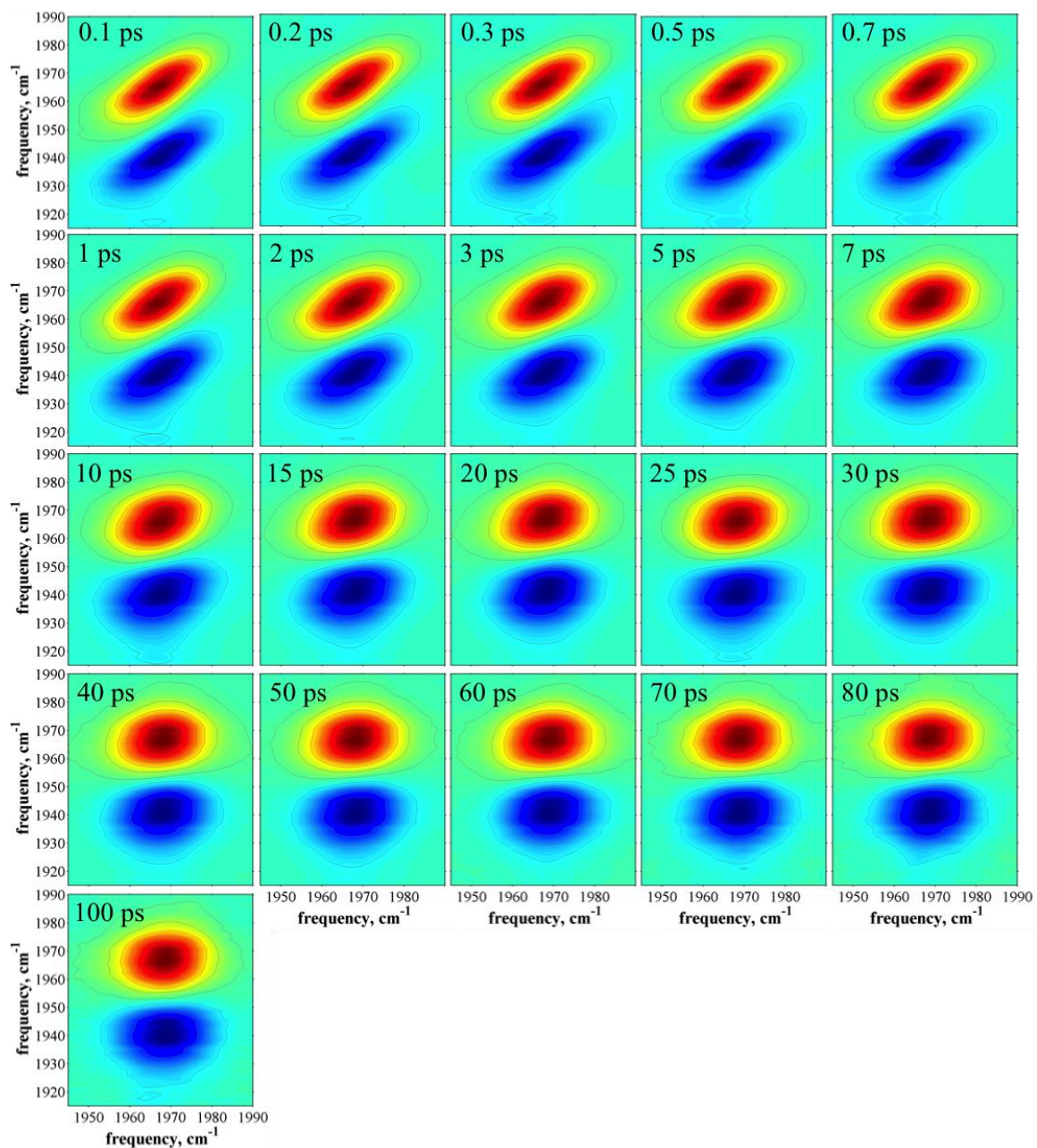**Figure 6.16.** Full 2D-IR dataset for VC in 0.9 mole fraction CHCl$_3$.

Figure 6.17. Full 2D-IR dataset for VC in all CHCl$_3$.

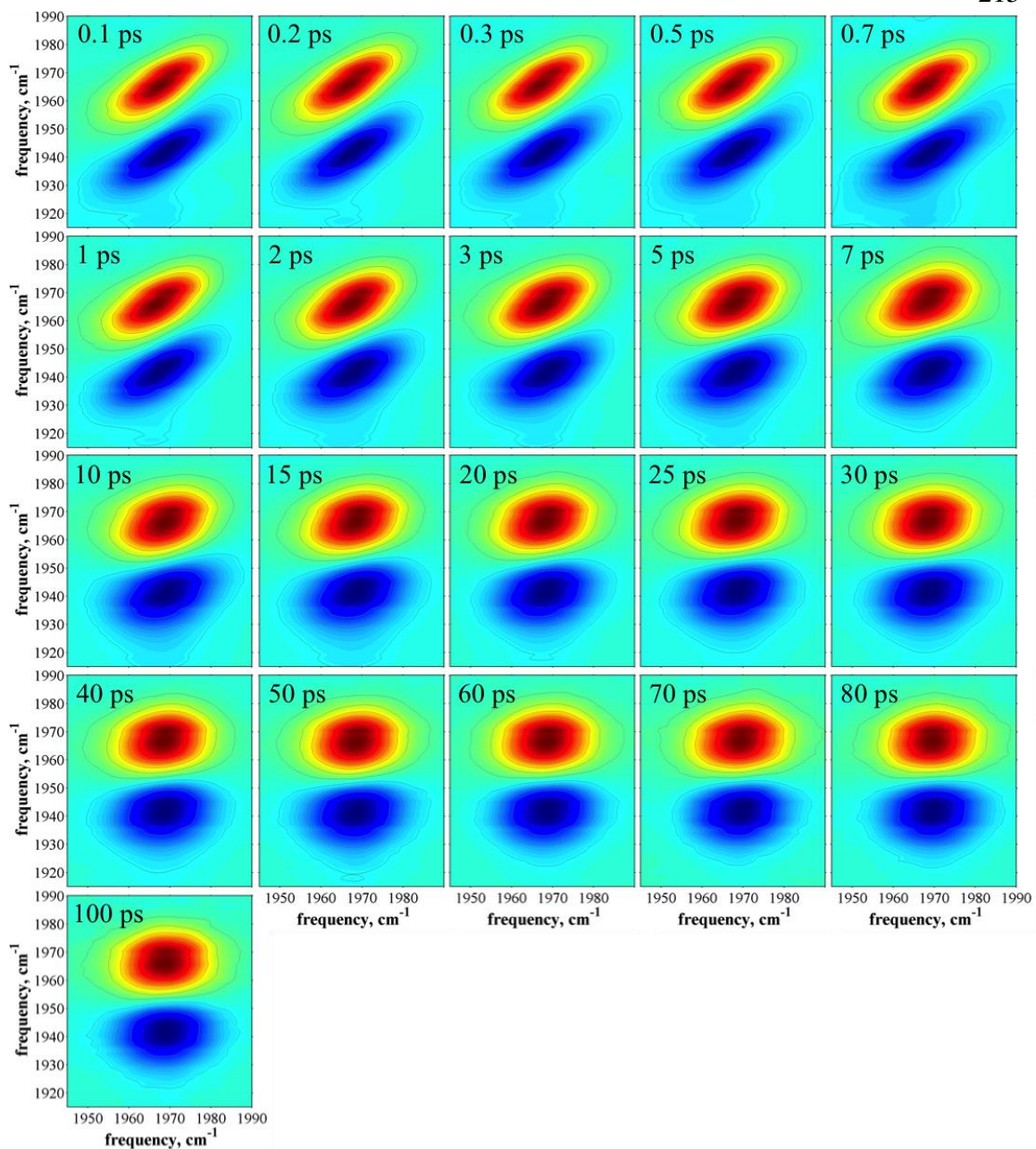**Figure 6.18.** Full 2D-IR dataset for VC in 0.05 mole fraction BA.

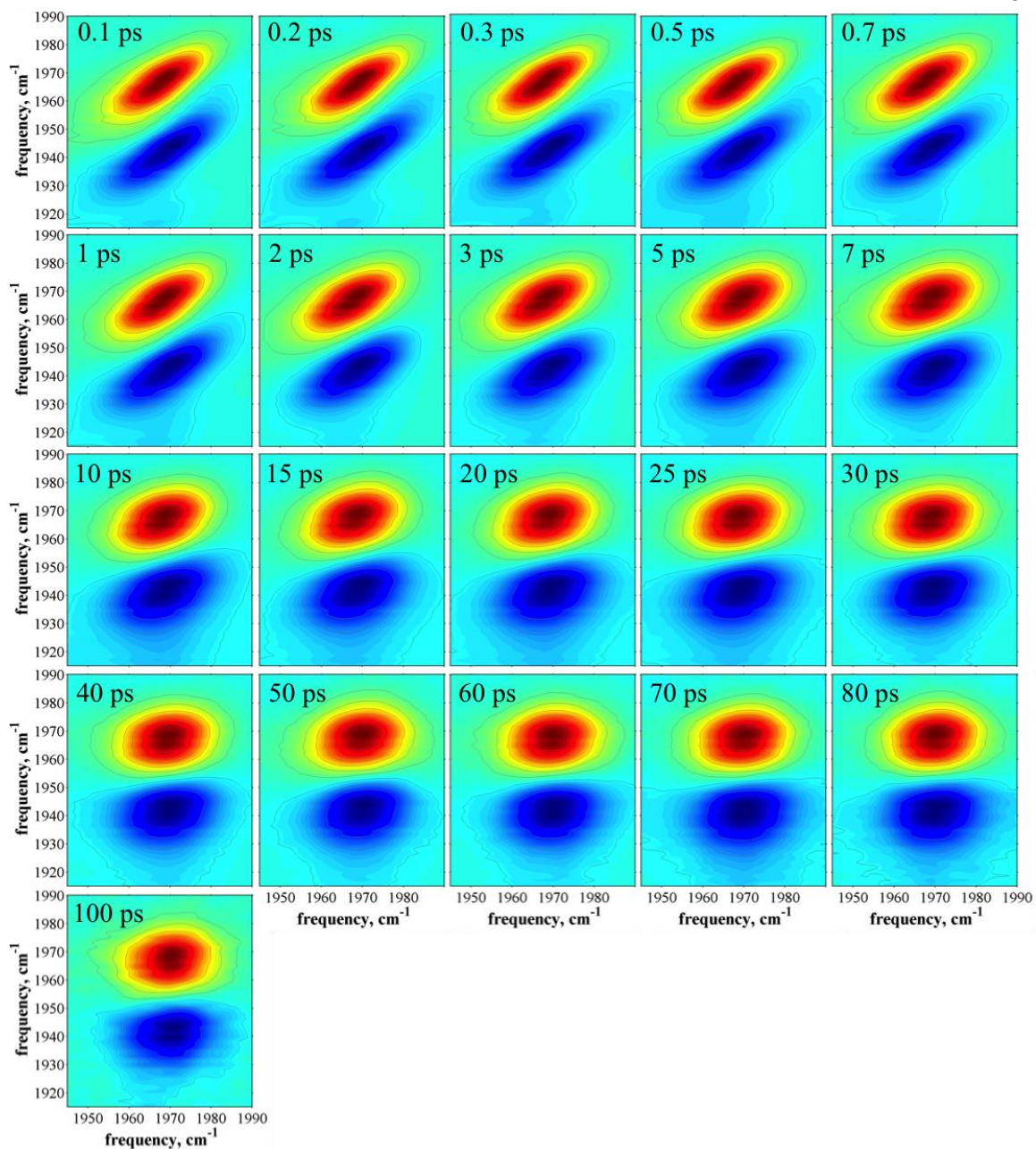**Figure 6.19.** Full 2D-IR dataset for VC in 0.1 mole fraction BA.

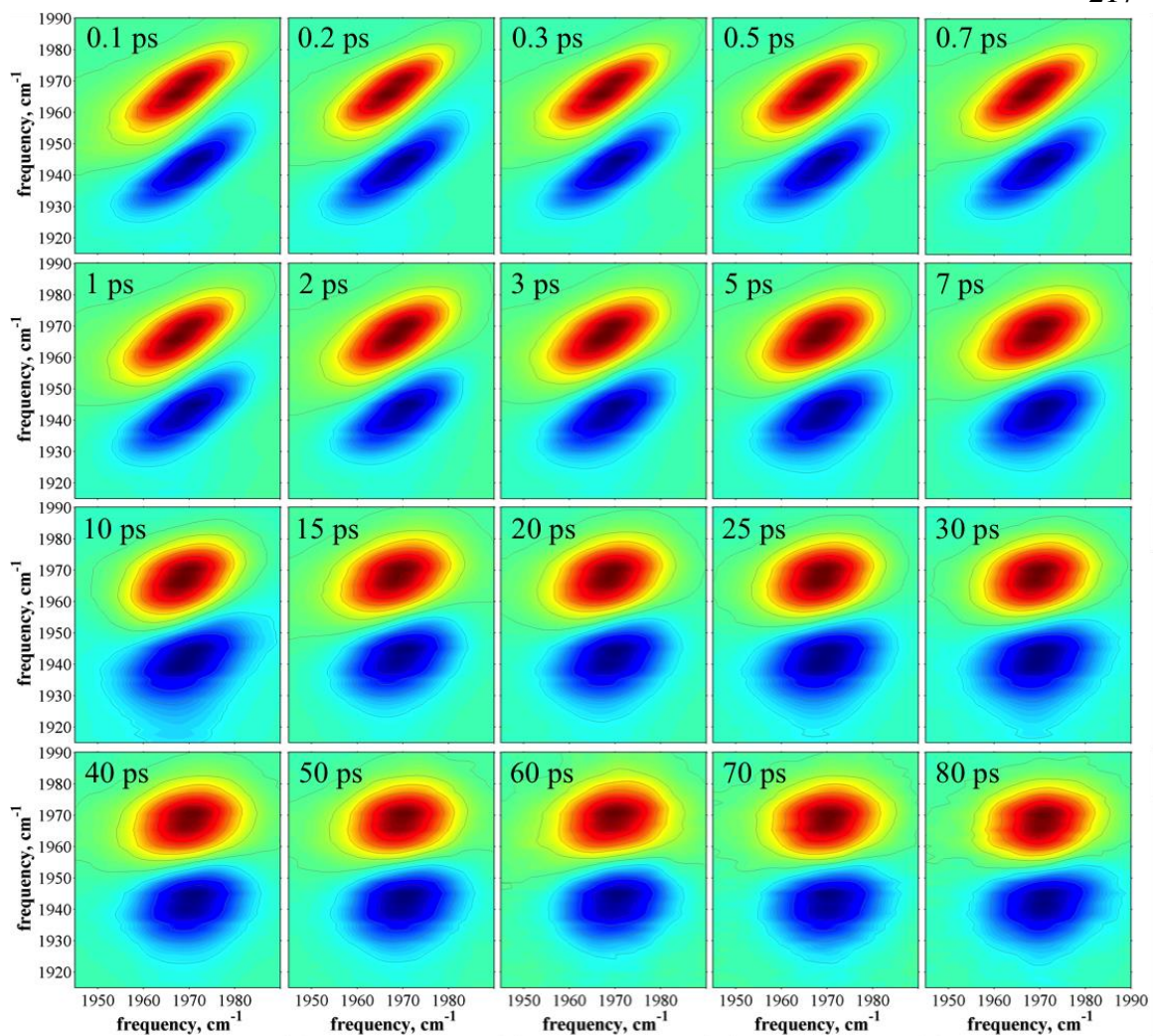**Figure 6.20.** Full 2D-IR dataset for VC in 0.2 mole fraction BA.

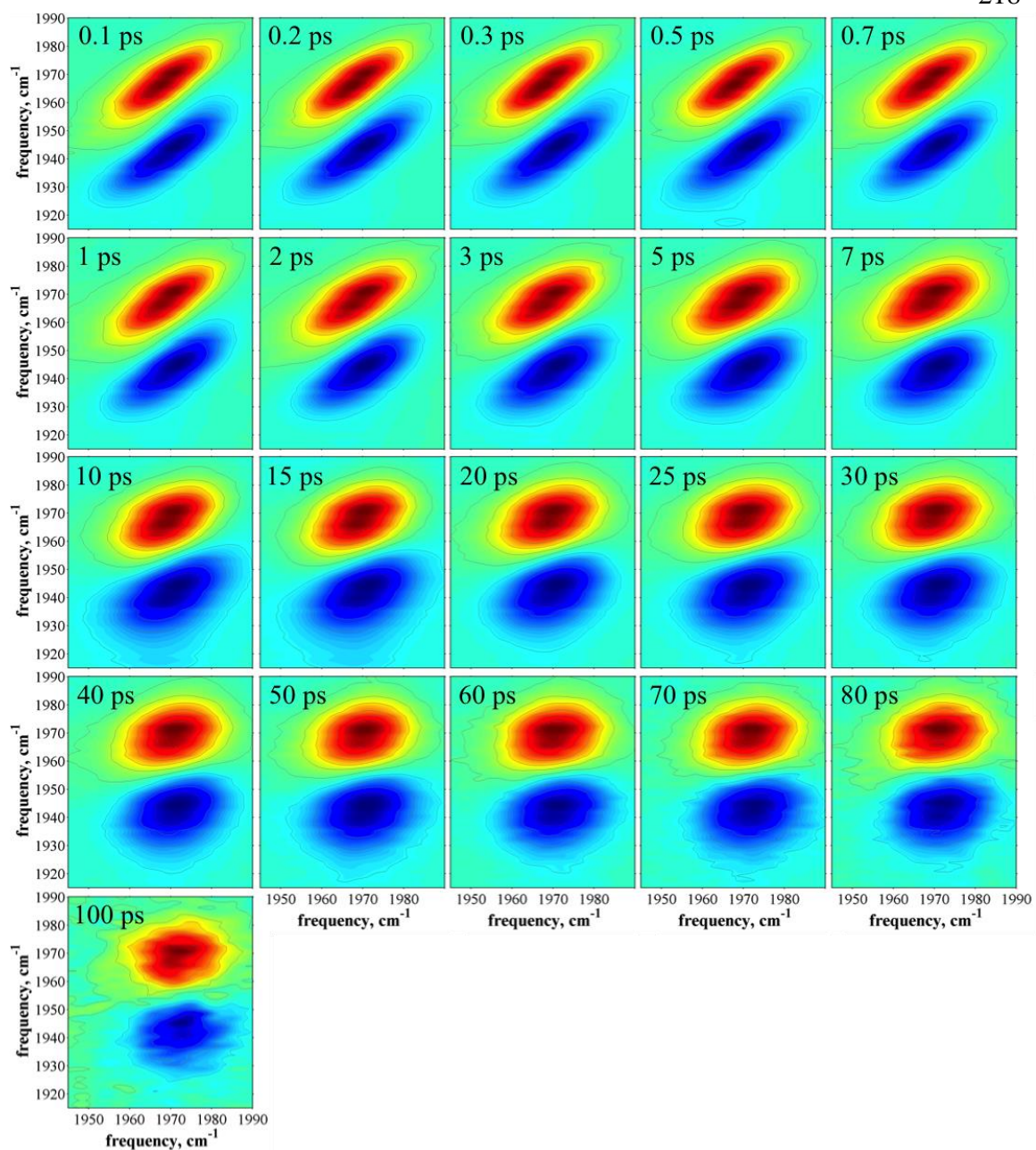**Figure 6.21.** Full 2D-IR dataset for VC in 0.3 mole fraction BA.

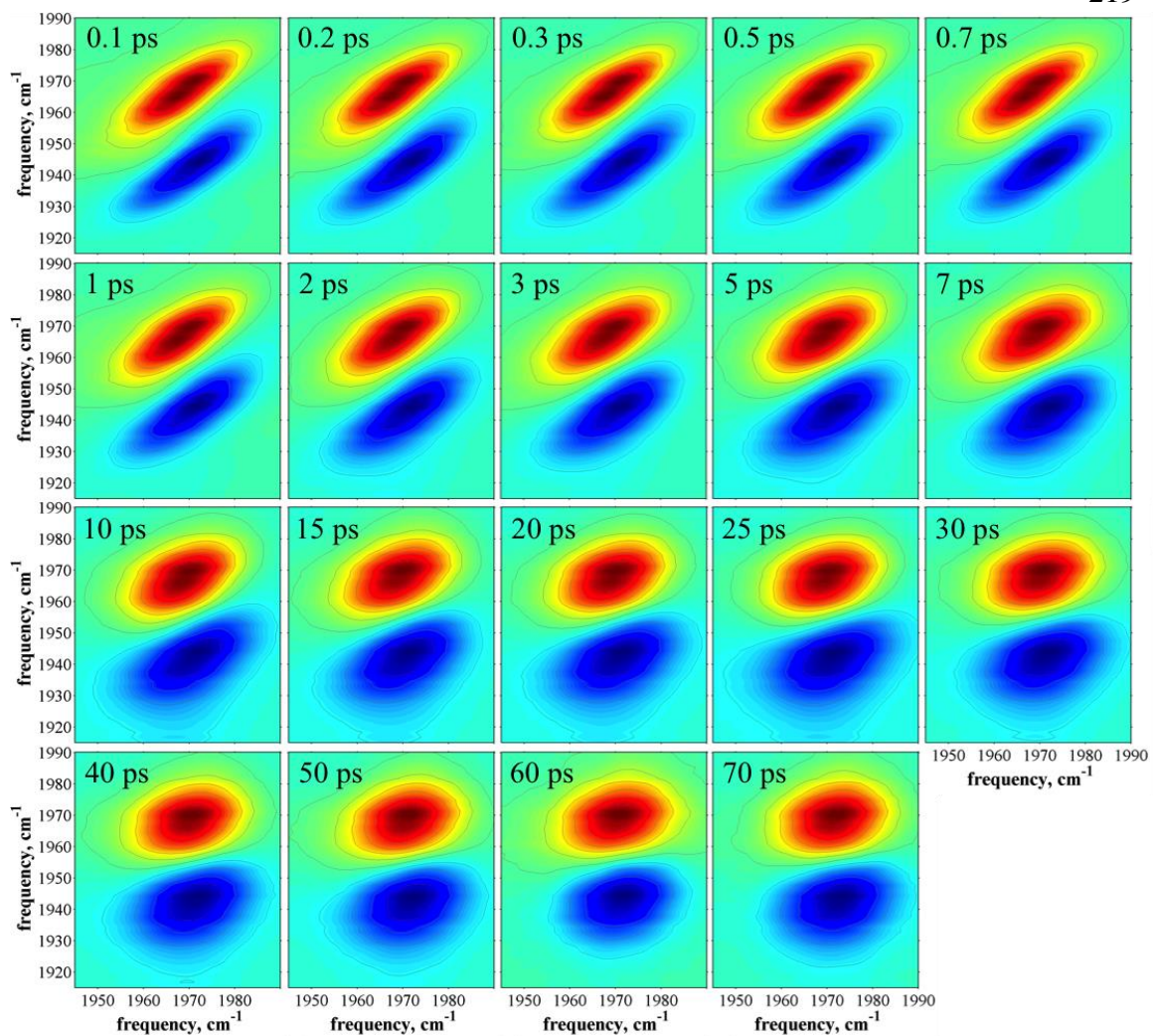**Figure 6.22.** Full 2D-IR dataset for VC in 0.4 mole fraction BA.

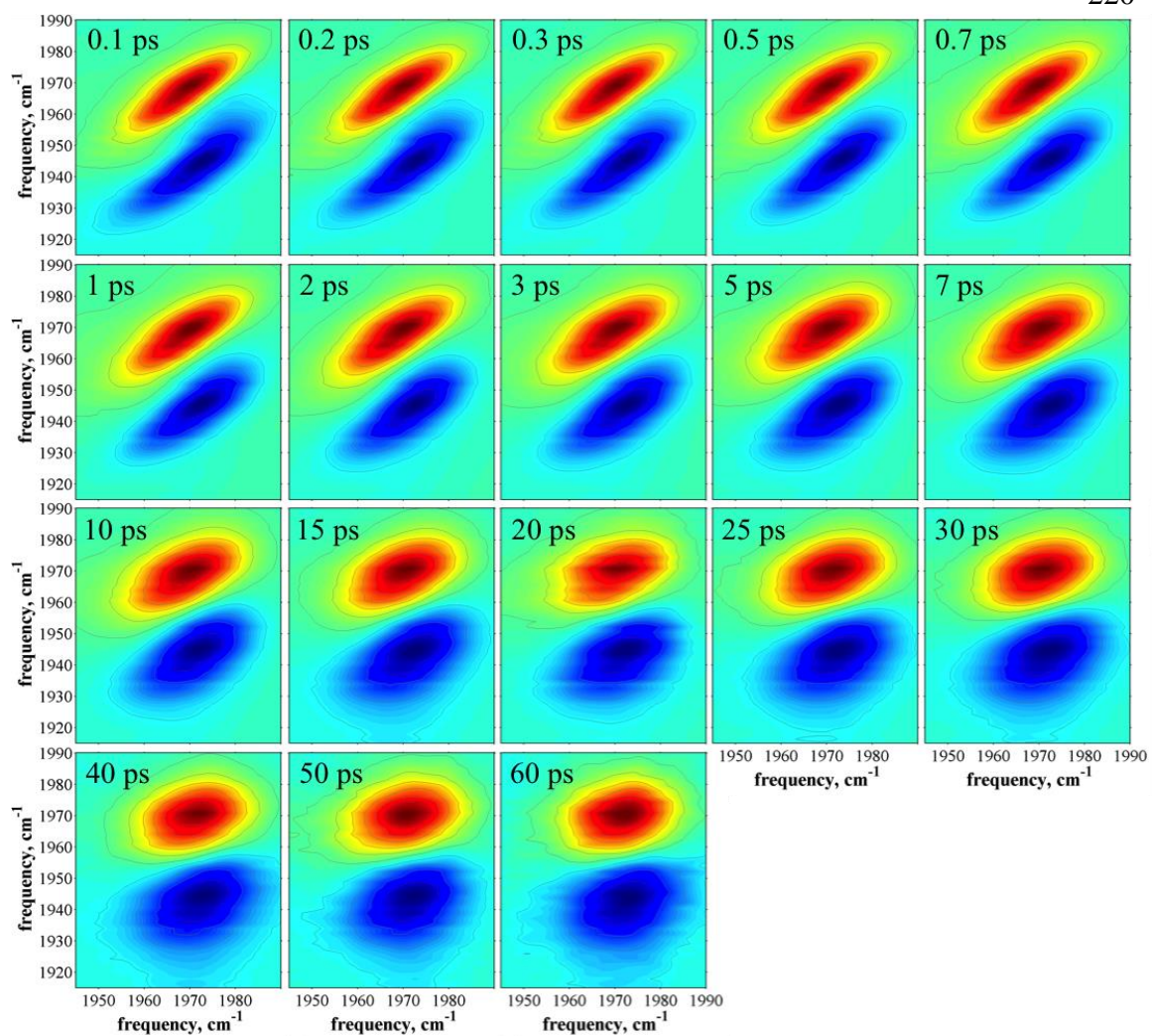**Figure 6.23.** Full 2D-IR dataset for VC in 0.5 mole fraction BA.

Figure 6.24. Full 2D-IR dataset for VC in 0.7 mole fraction BA.
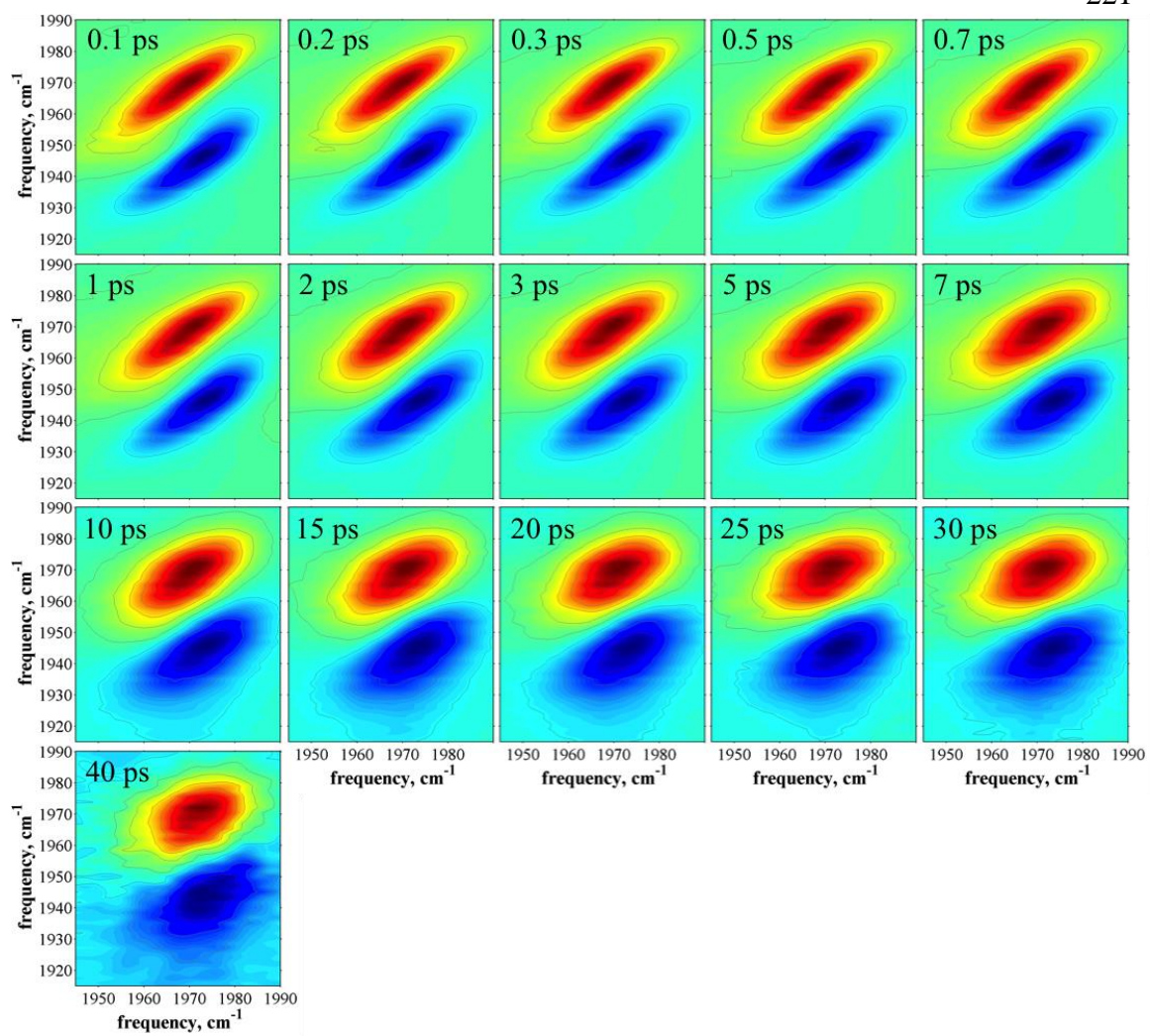
Figure 6.25. Full 2D-IR dataset for VC in all BA.
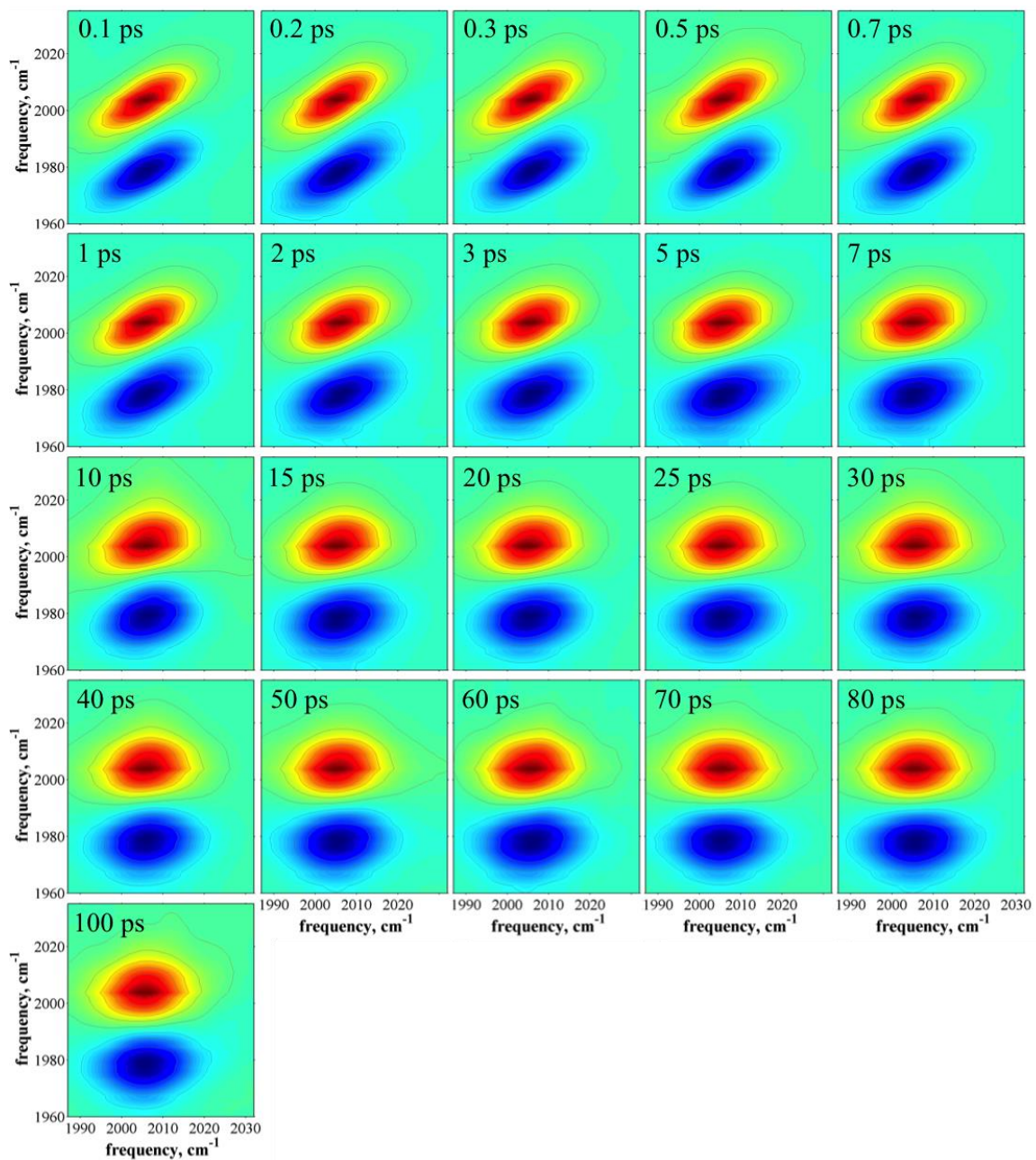
Figure 6.26. Full 2D-IR dataset for VC-O$_2$ in all d_6-benzene.
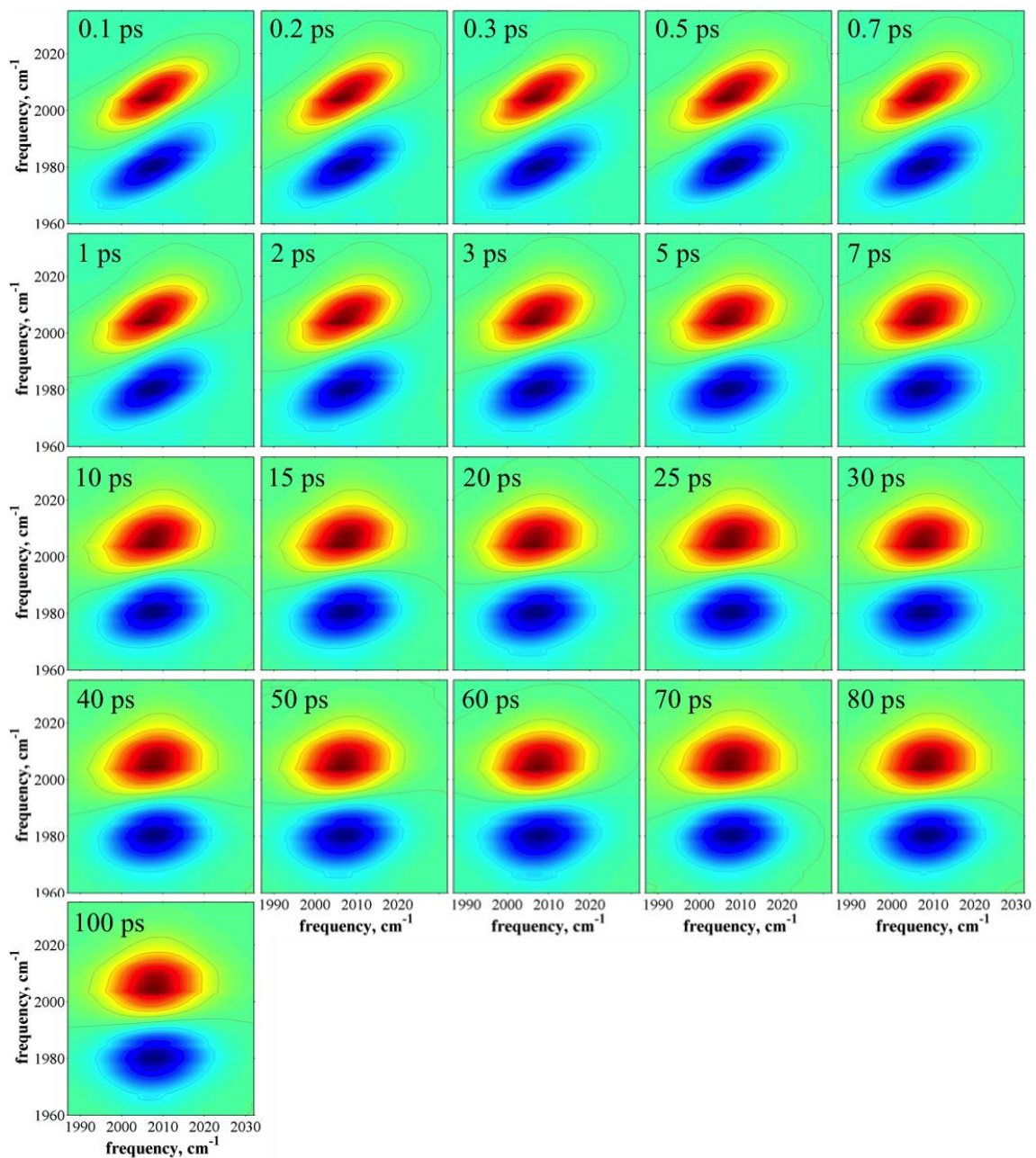
Figure 6.27. Full 2D-IR dataset for VC-O$_2$ in 0.1 mole fraction CHCl$_3$.
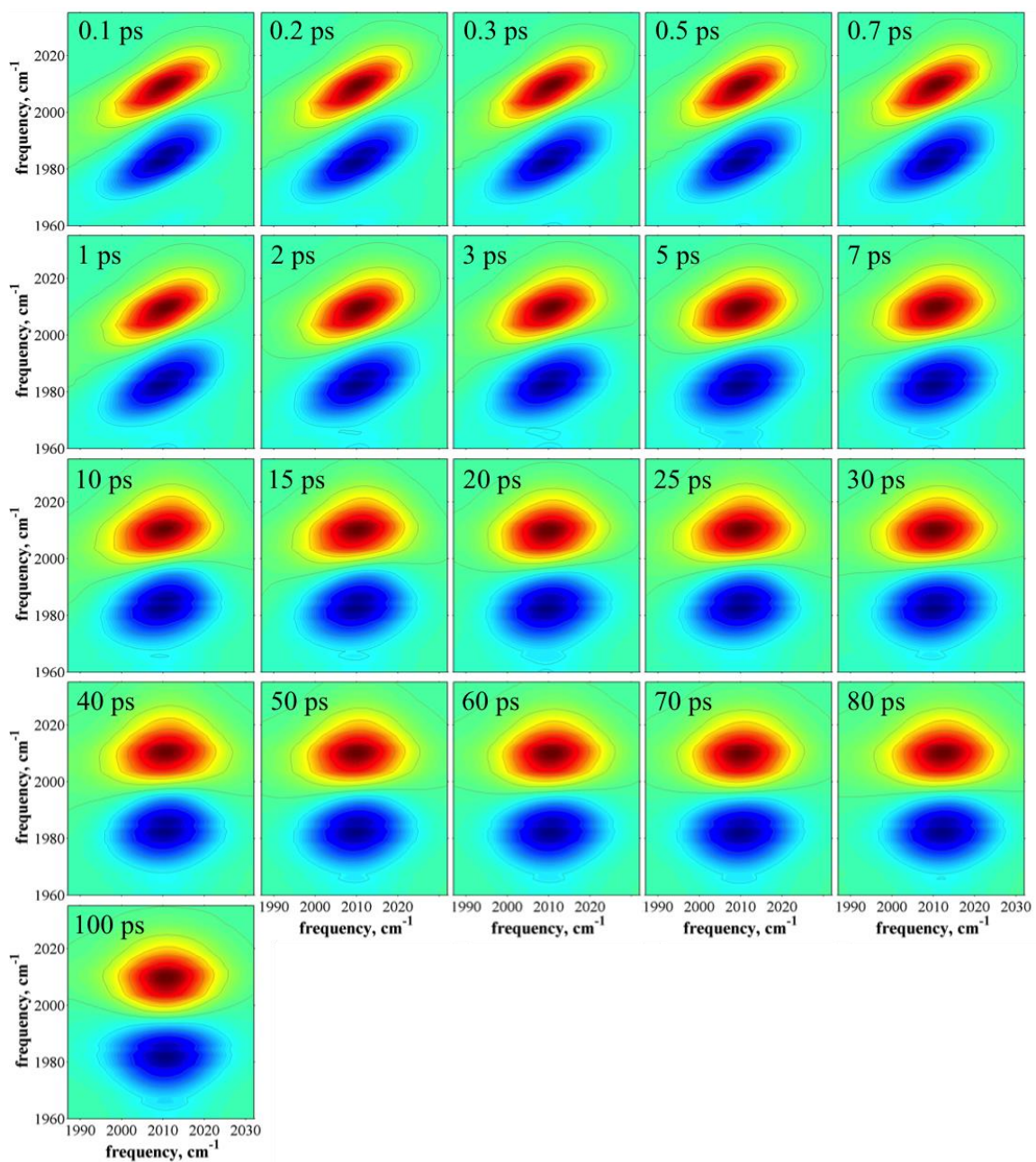
Figure 6.28. Full 2D-IR dataset for VC-O$_2$ in 0.3 mole fraction CHCl$_3$.
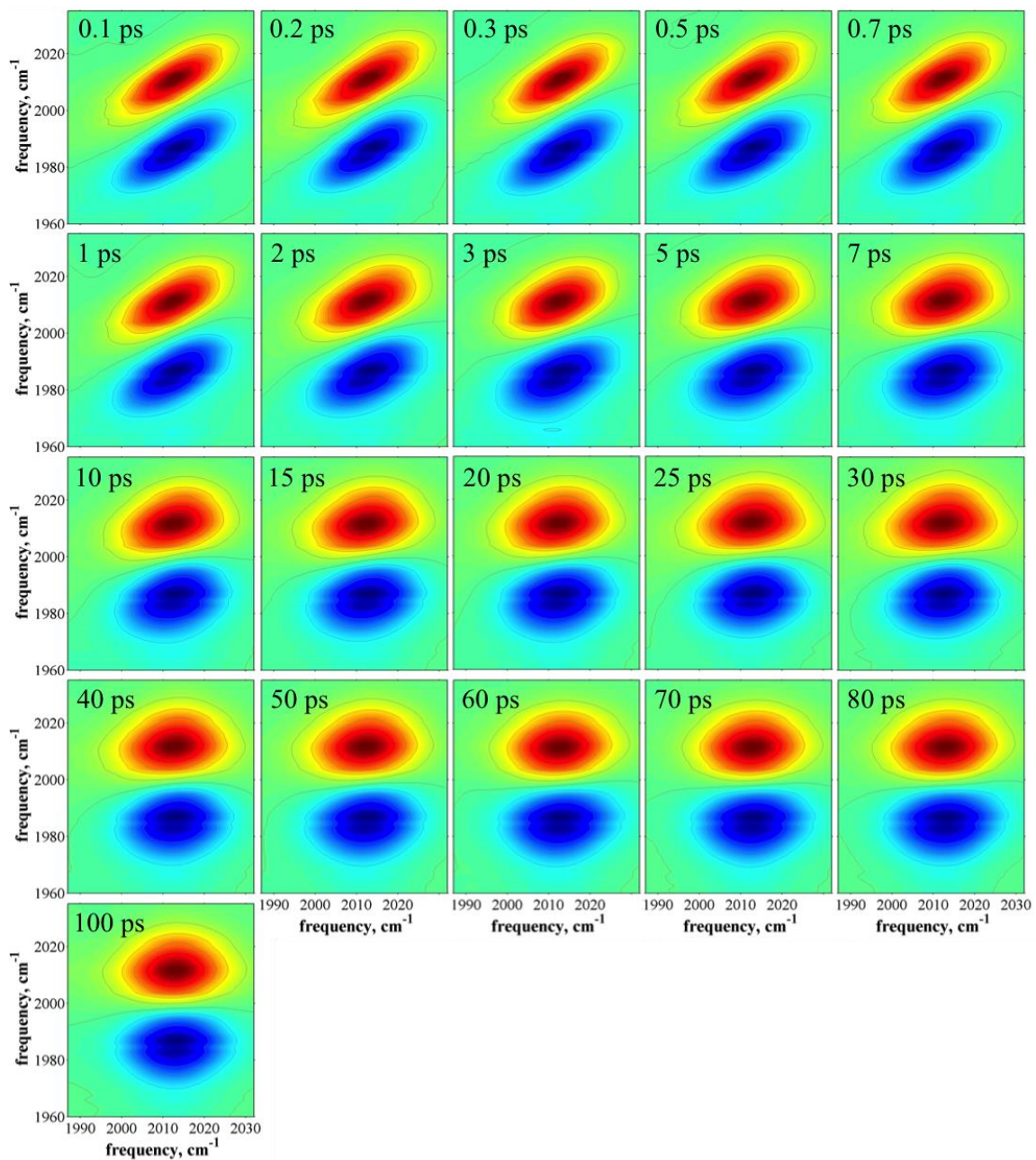
Figure 6.29. Full 2D-IR dataset for VC-O$_2$ in 0.5 mole fraction CHCl$_3$.
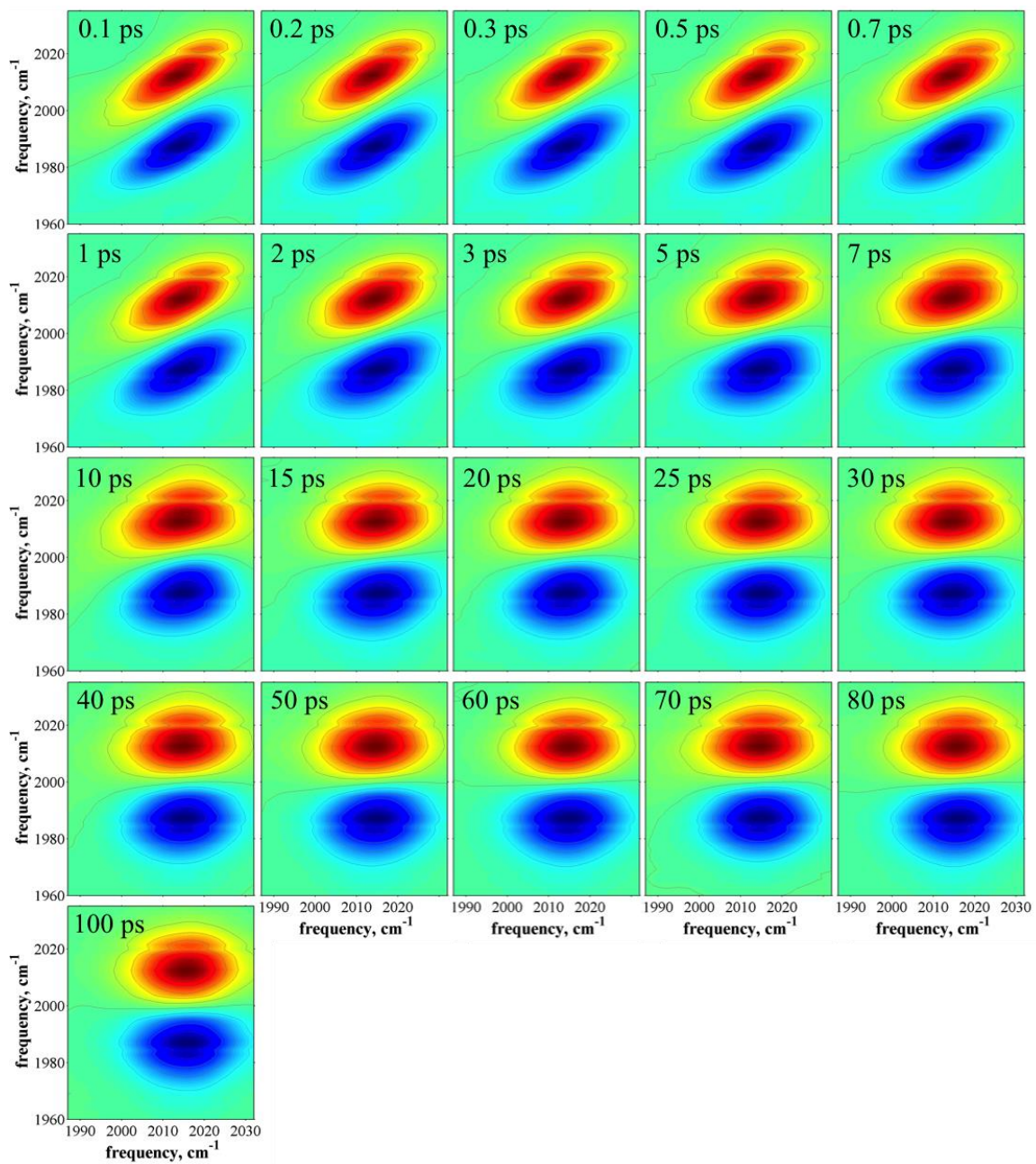
Figure 6.30. Full 2D-IR dataset for VC-O$_2$ in 0.7 mole fraction CHCl$_3$.
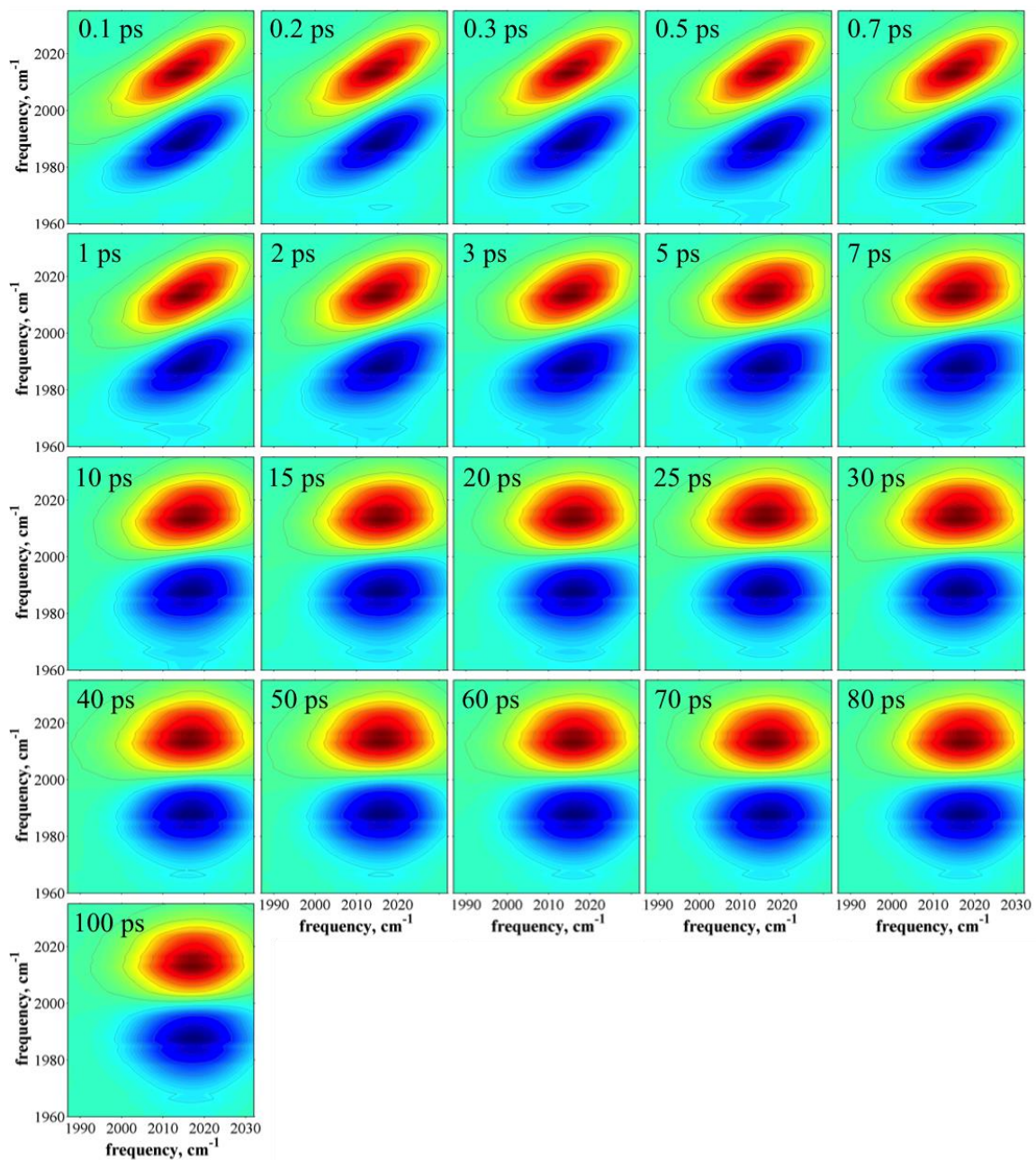
Figure 6.31. Full 2D-IR dataset for VC-O$_2$ in 0.9 mole fraction CHCl$_3$.
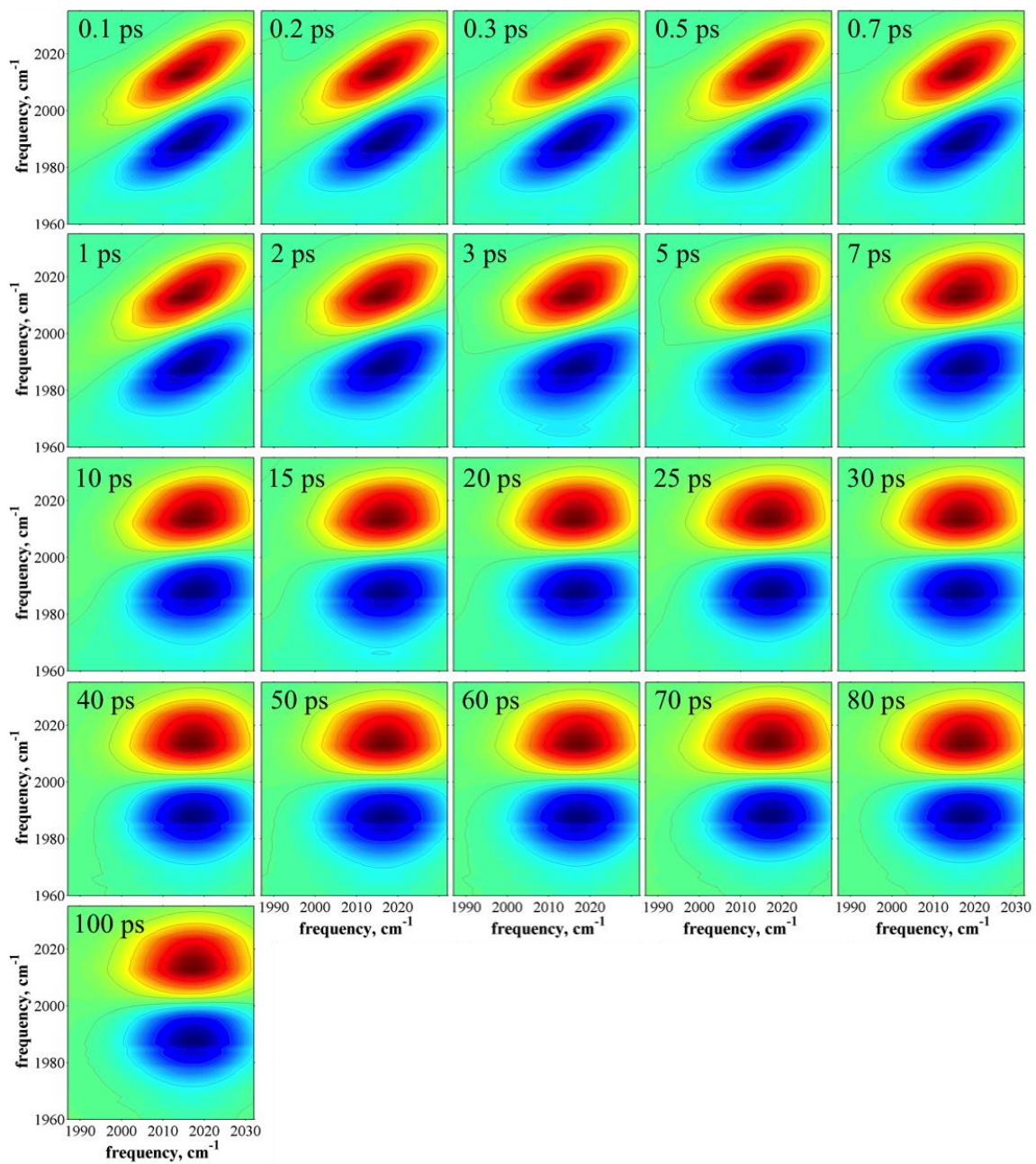
Figure 6.32. Full 2D-IR dataset for VC-O$_2$ in all CHCl$_3$.

.
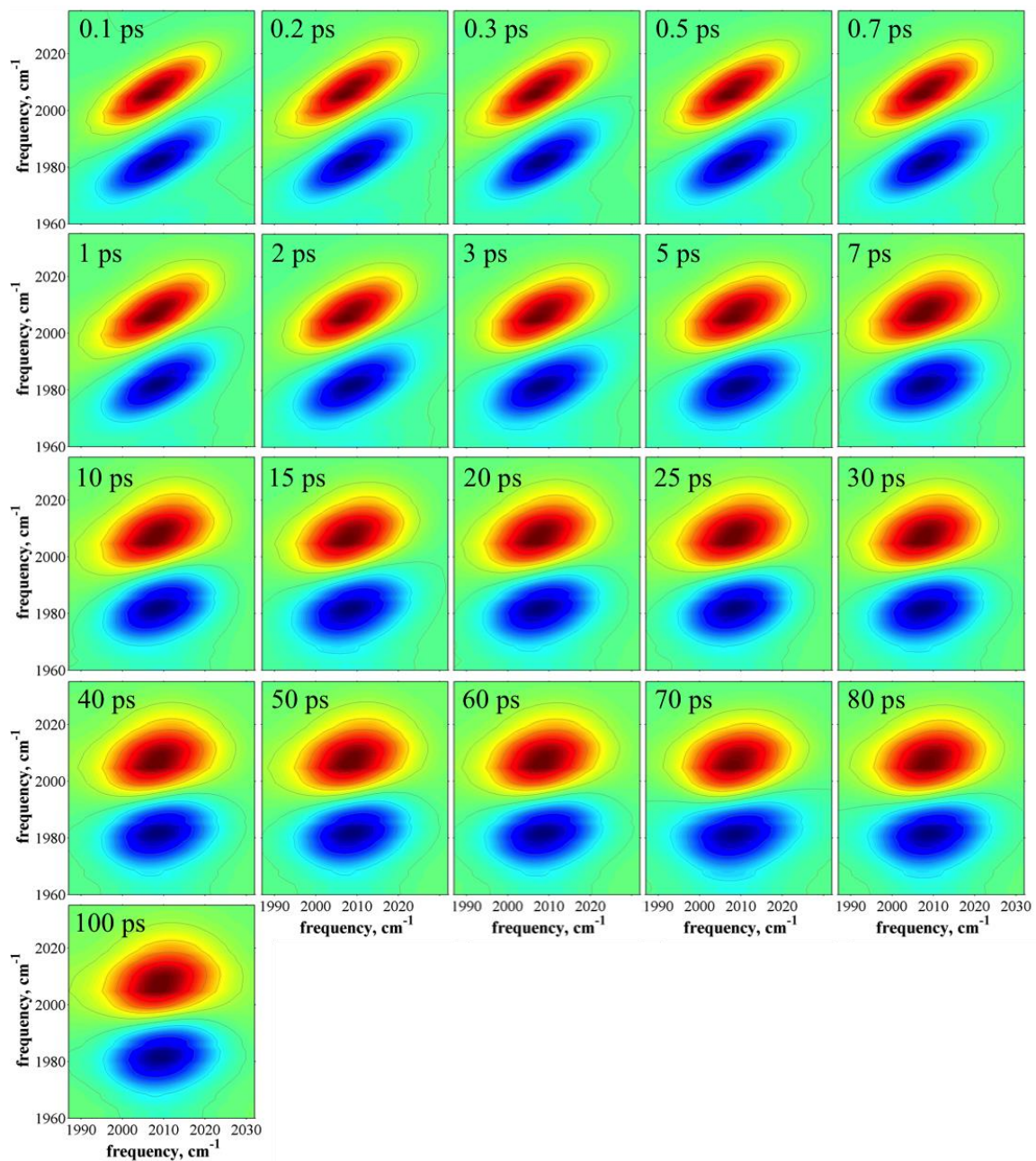
Figure 6.33. Full 2D-IR dataset for VC-O$_2$ in 0.05 mole fraction BA.
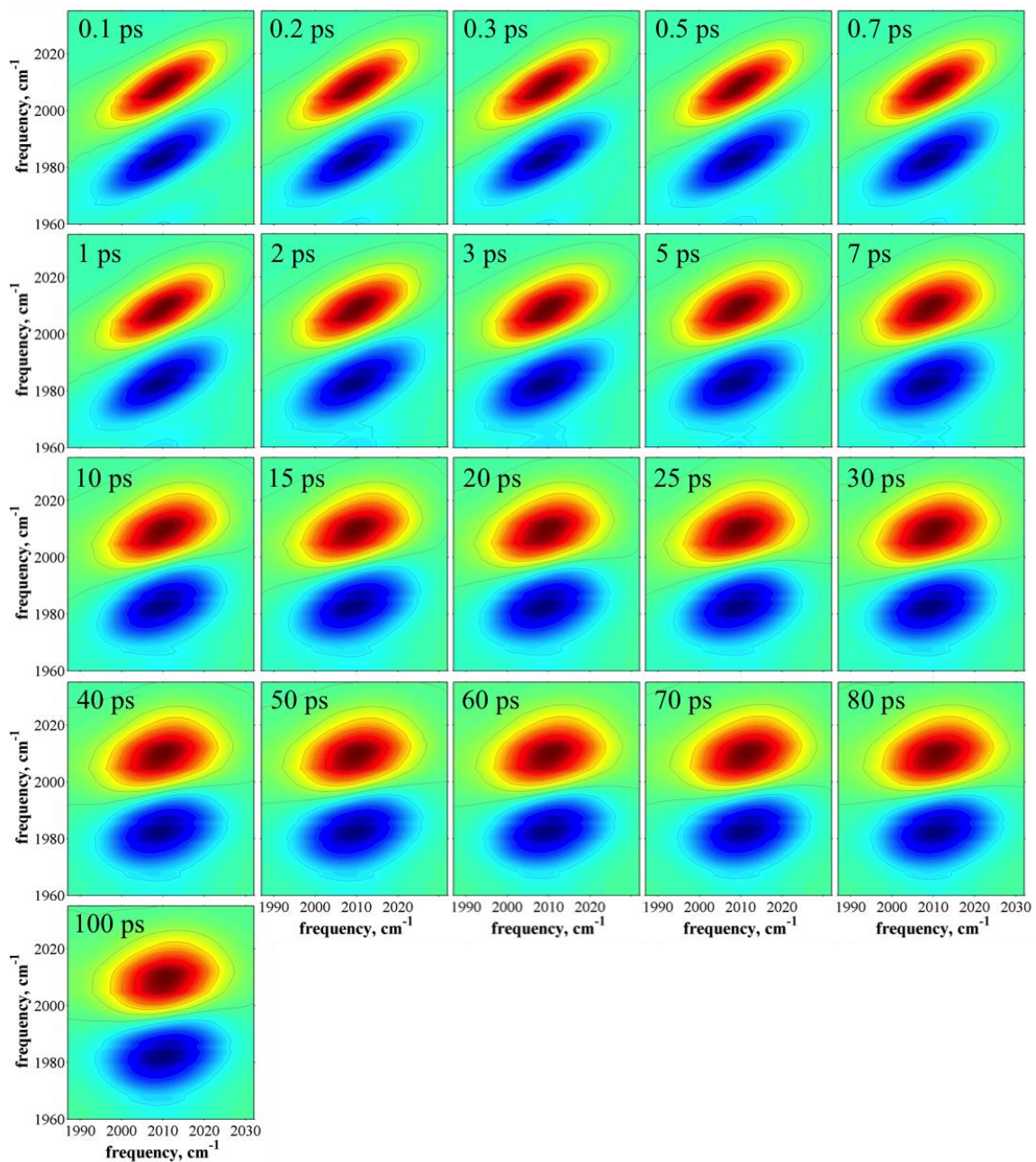
Figure 6.34. Full 2D-IR dataset for VC-O$_2$ in 0.1 mole fraction BA.
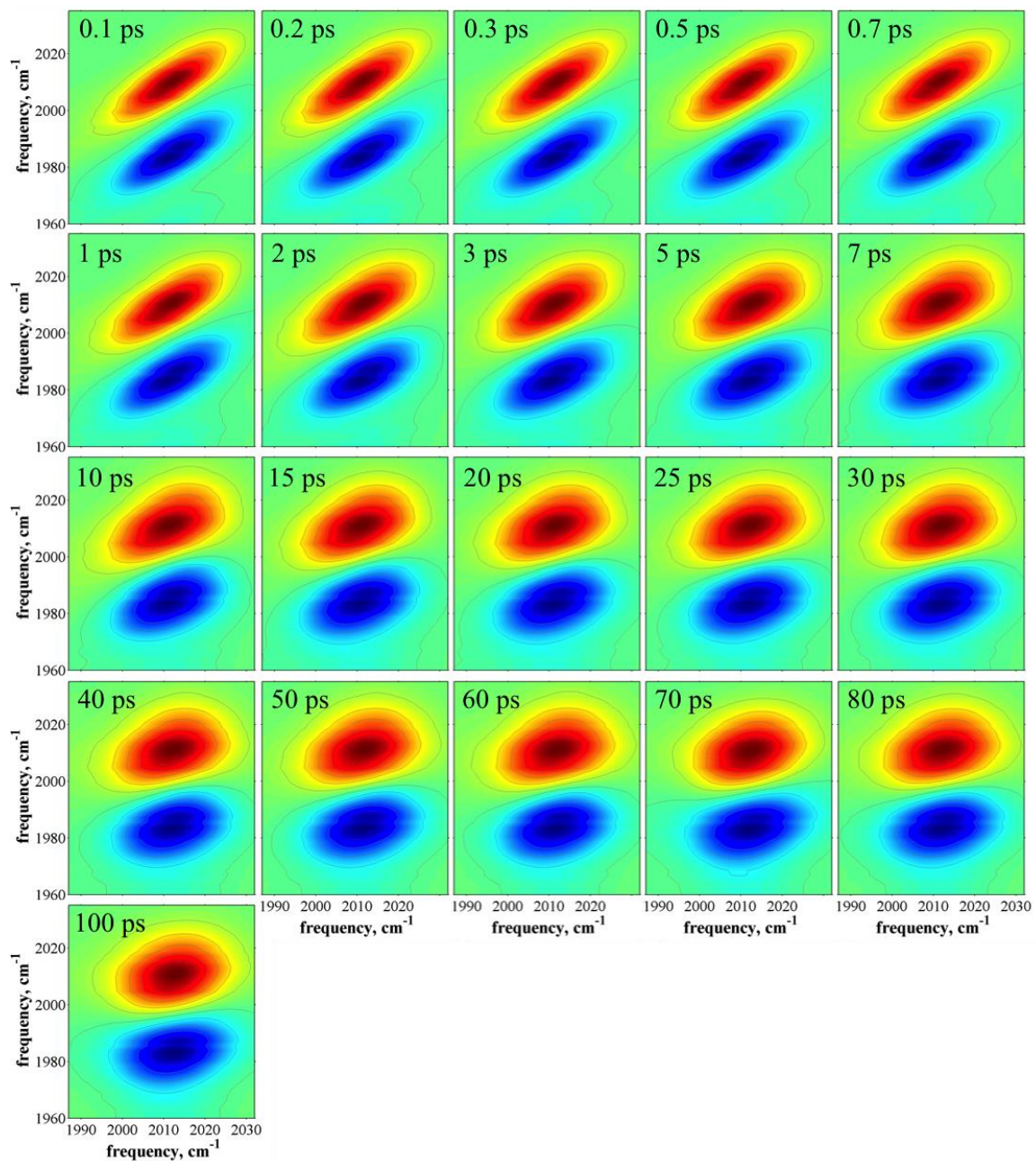
Figure 6.35. Full 2D-IR dataset for VC-O$_2$ in 0.2 mole fraction BA.
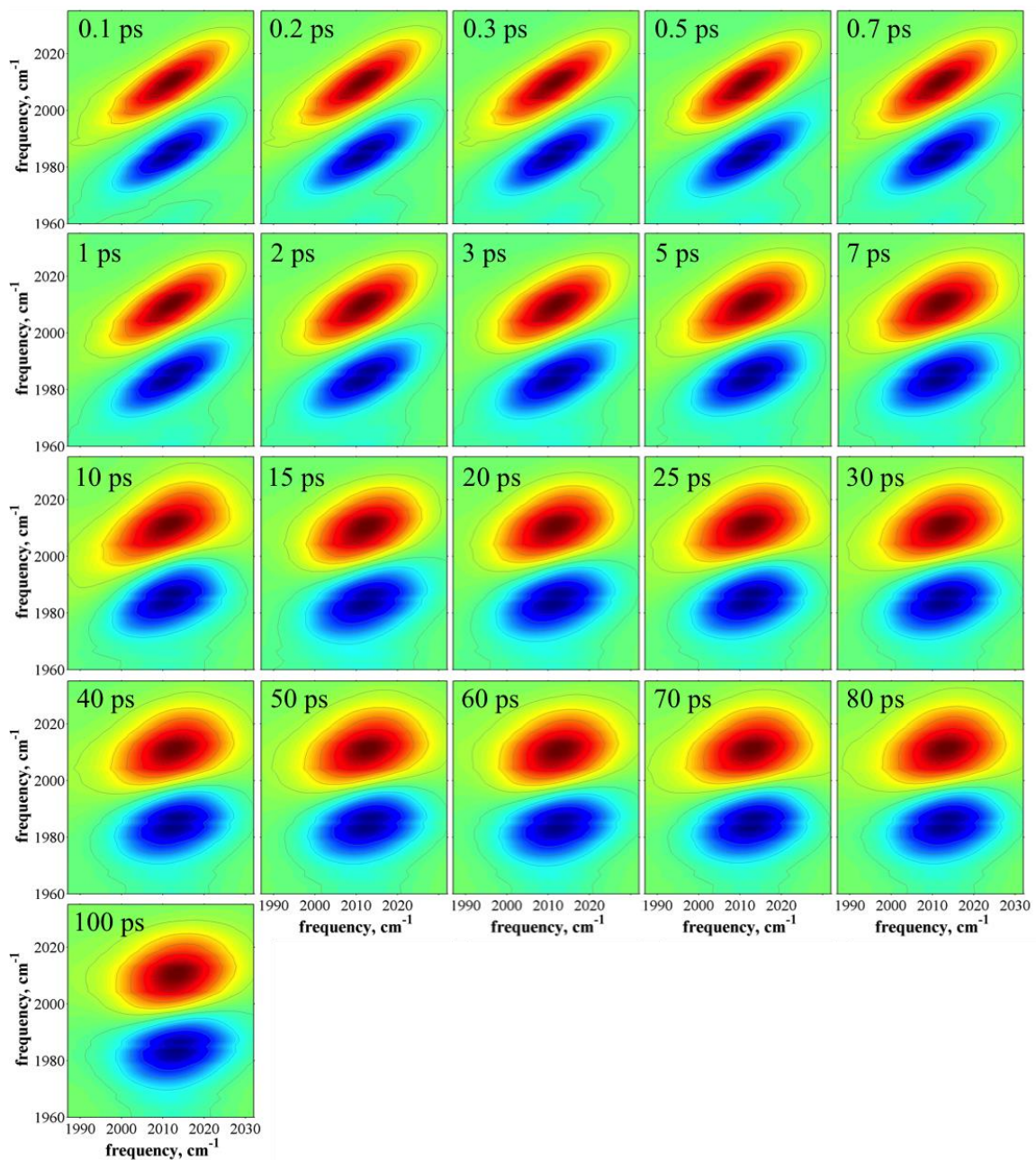
Figure 6.36. Full 2D-IR dataset for VC-O$_2$ in 0.3 mole fraction BA.
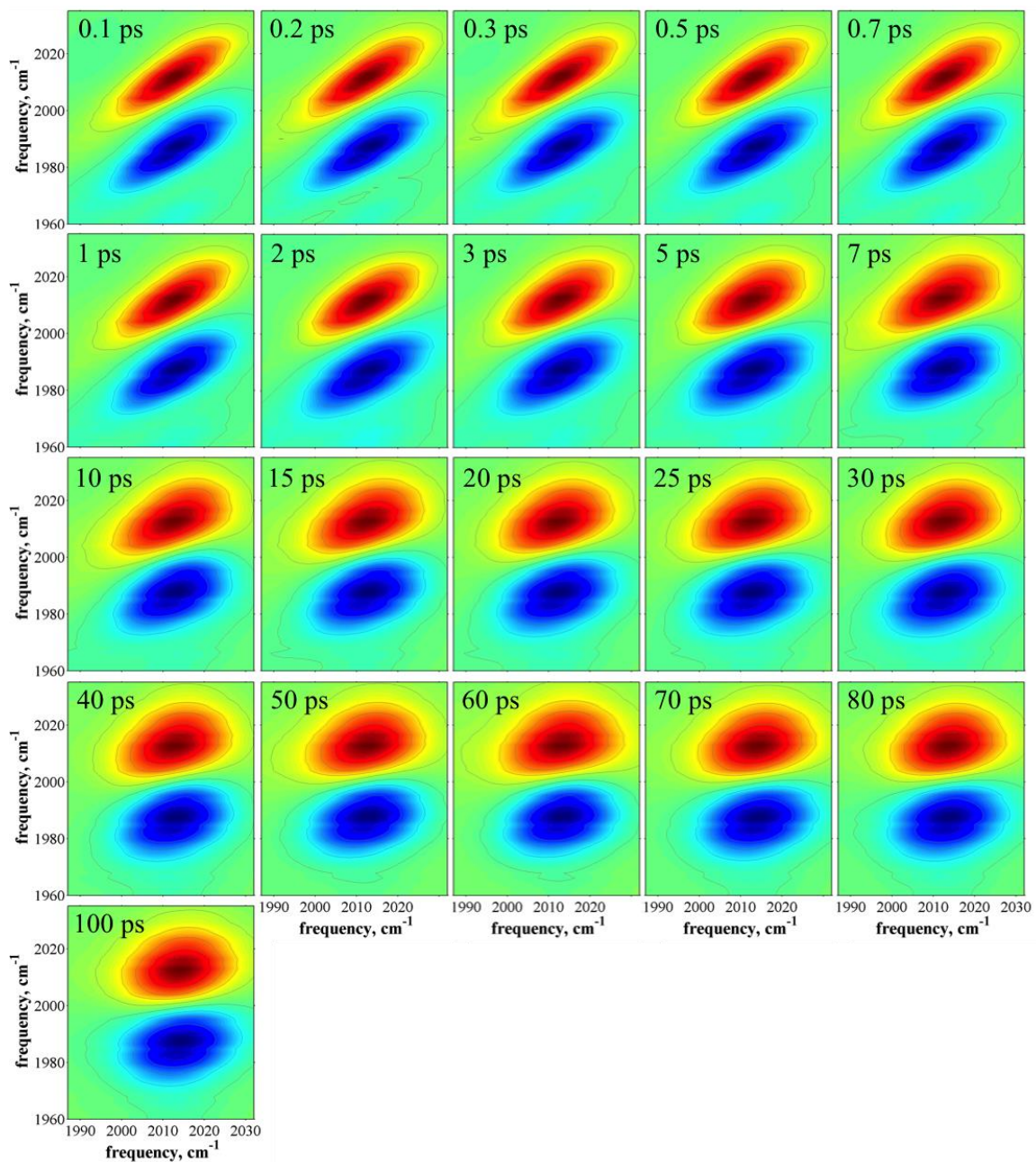
Figure 6.37. Full 2D-IR dataset for VC-O$_2$ in 0.4 mole fraction BA.
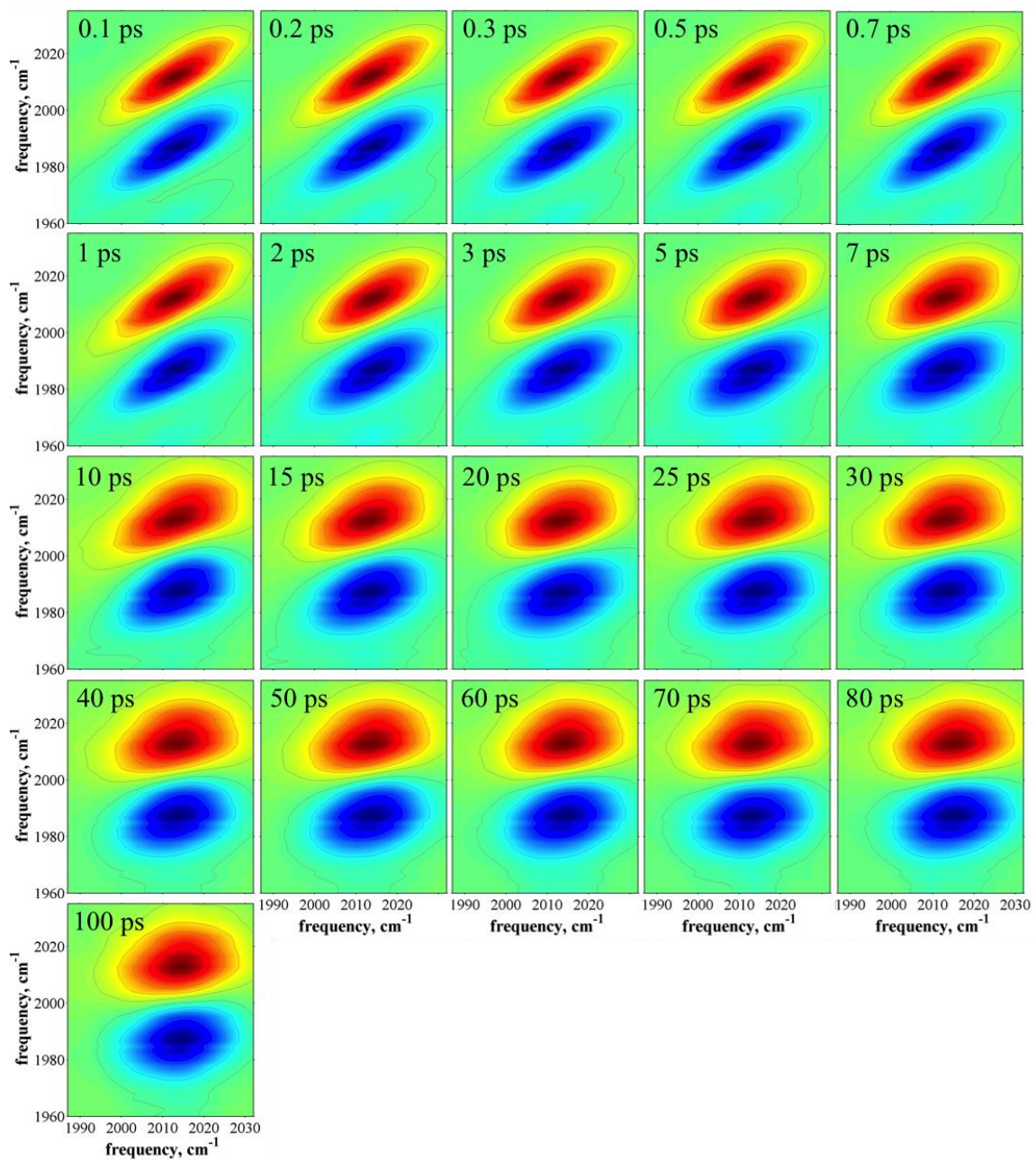
Figure 6.38. Full 2D-IR dataset for VC-O$_2$ in 0.5 mole fraction BA.
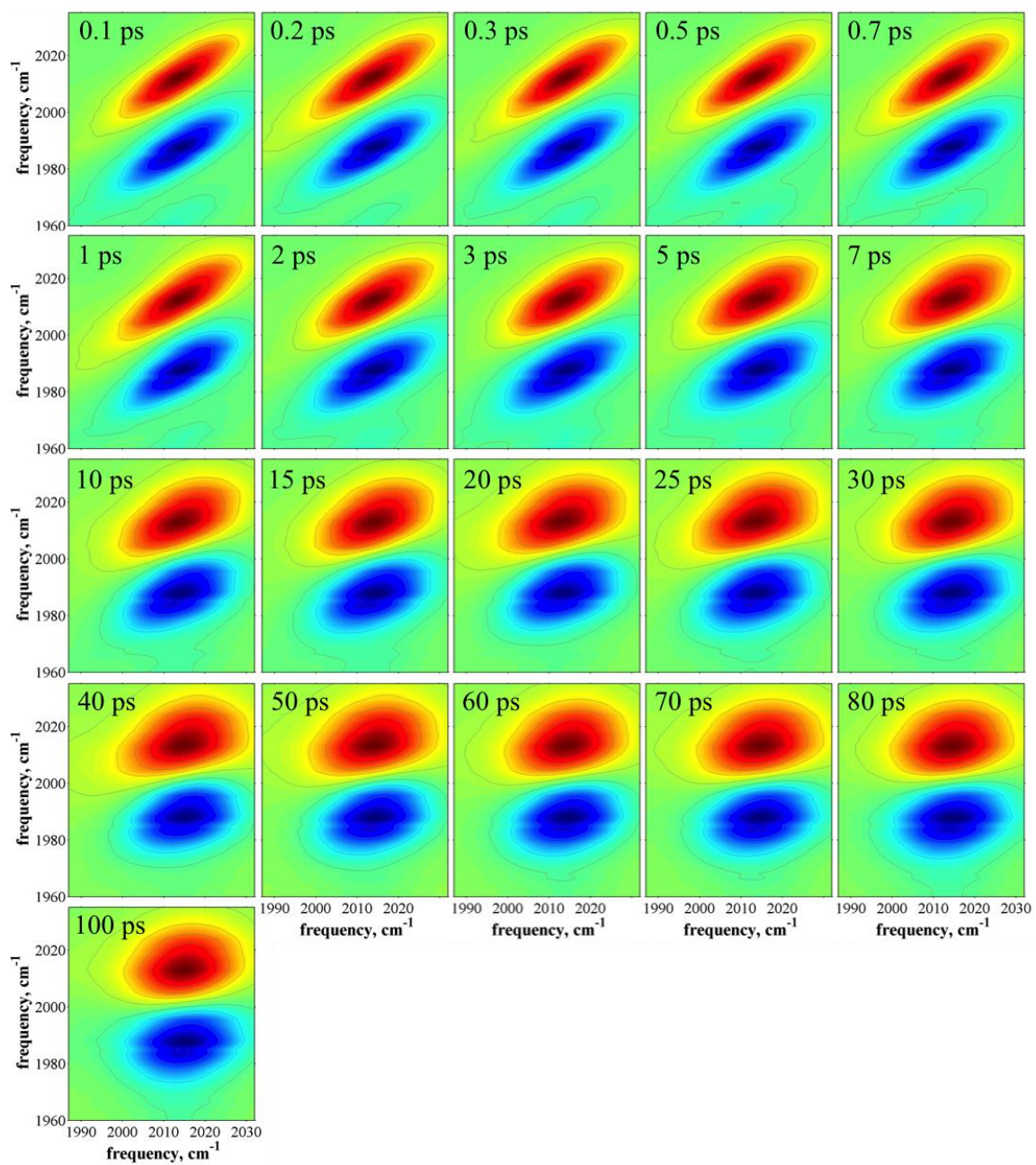
Figure 6.39. Full 2D-IR dataset for VC-O$_2$ in 0.7 mole fraction BA.
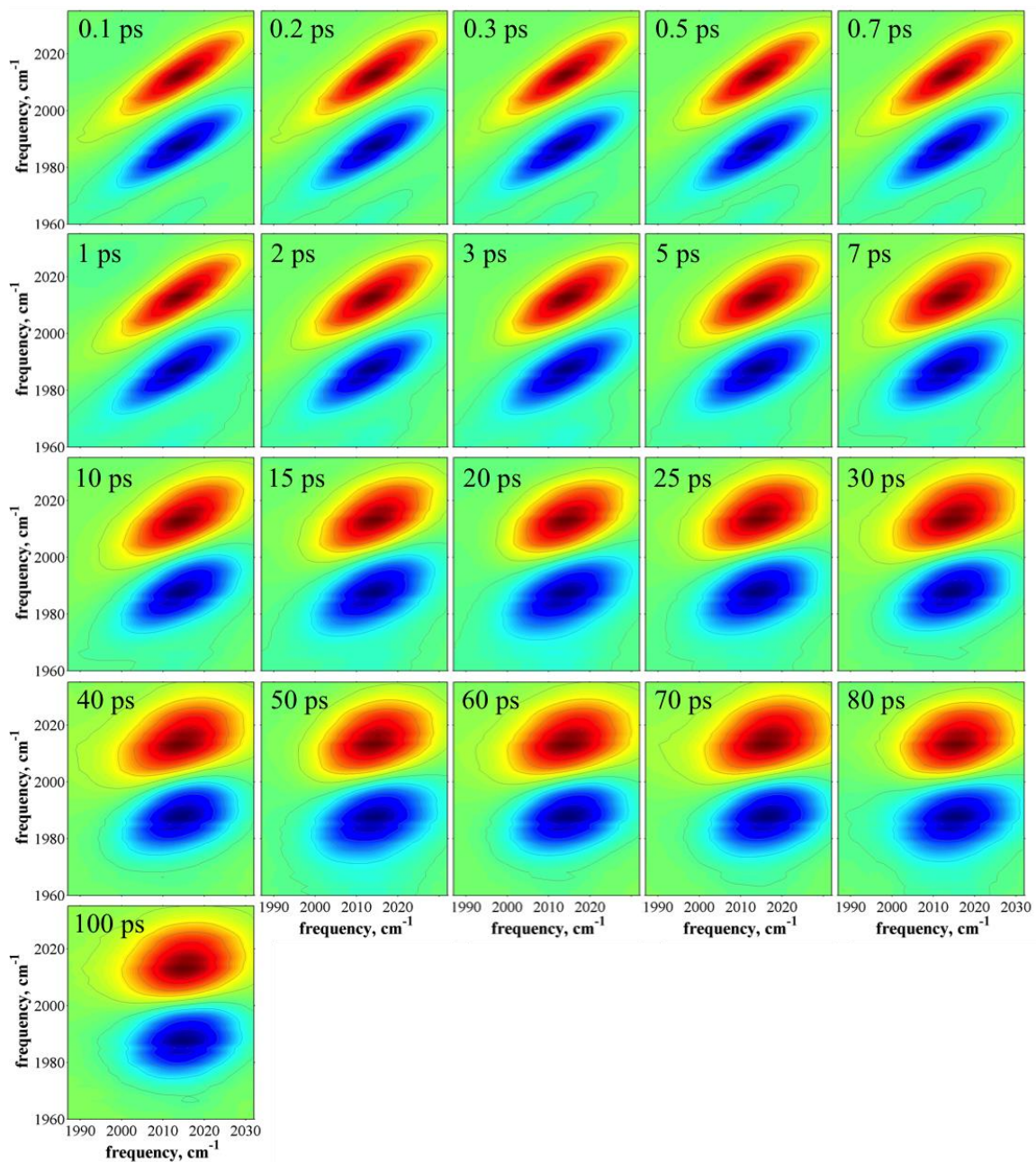
Figure 6.40. Full 2D-IR dataset for VC-O$_2$ in all BA.
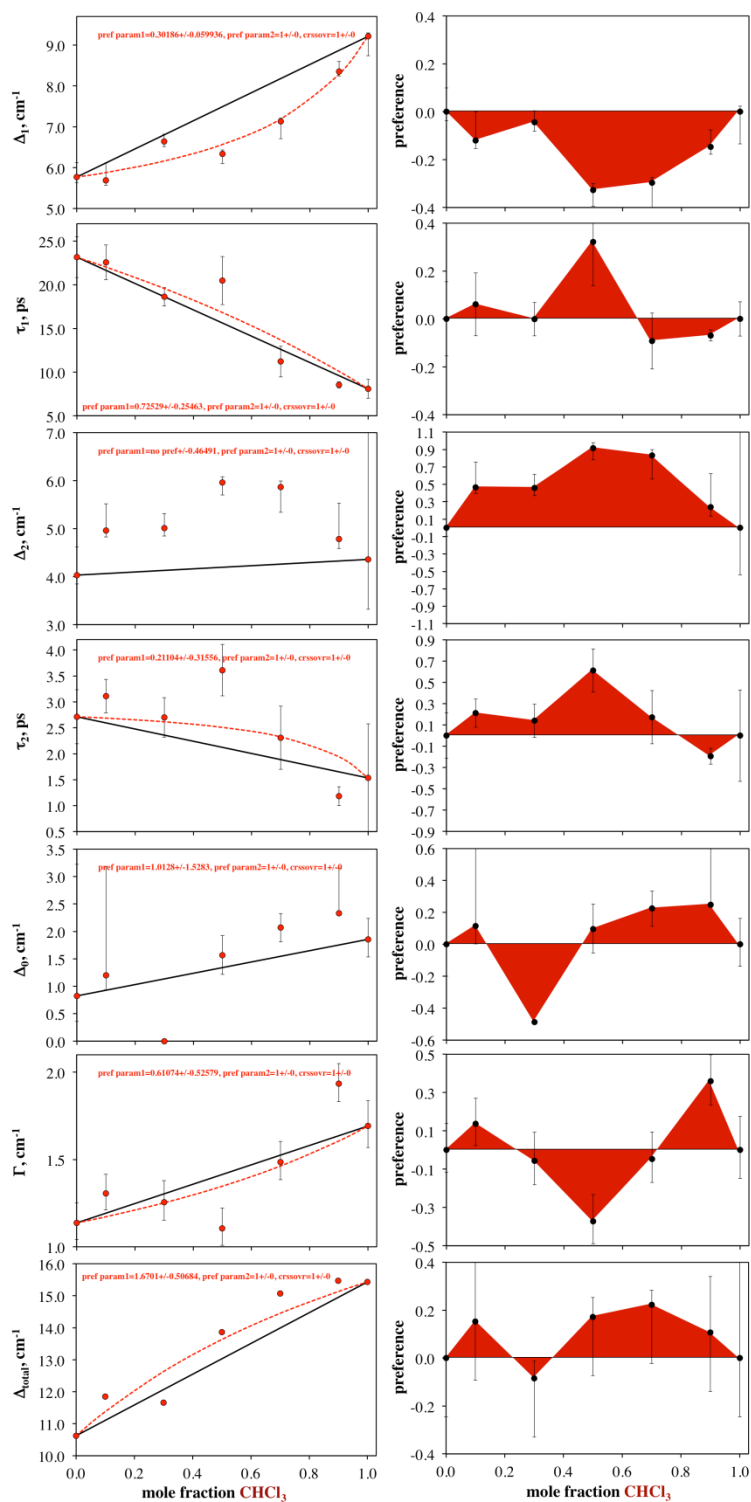
Figure 6.41. (left column) Parameters obtained by fitting CLS decays to obtain the full FFCF for VC in binary mixtures of $CHCl_3$ in d_6-benzene. (right column) The difference between the data in the left column and the straight line connecting the first and last point, normalized (for comparison) by the range of the data.
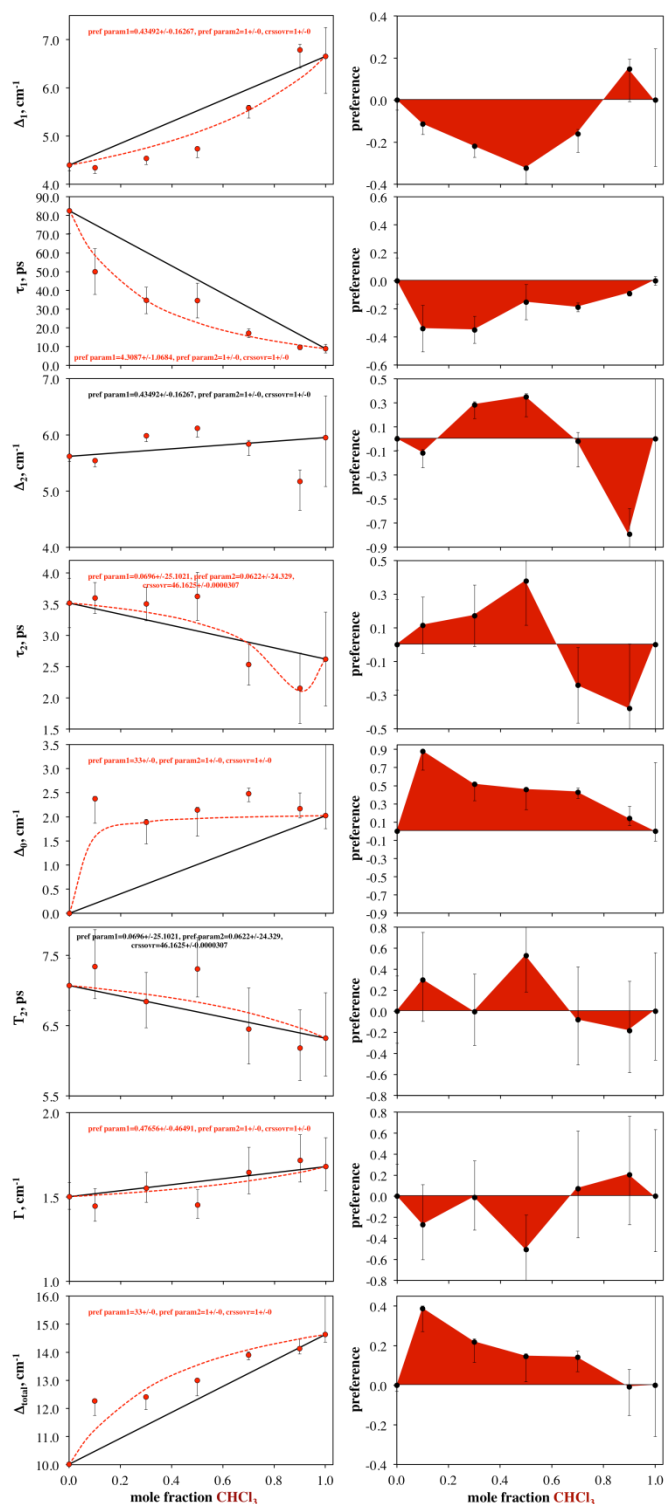
Figure 6.42. (left column) Parameters obtained by fitting CLS decays to obtain the full FFCF for VC-O$_2$ in binary mixtures of CHCl$_3$ in d$_6$-benzene. (right column) The difference between the data in the left column and the straight line connecting the first and last point, normalized (for comparison) by the range of the data (max minus min).
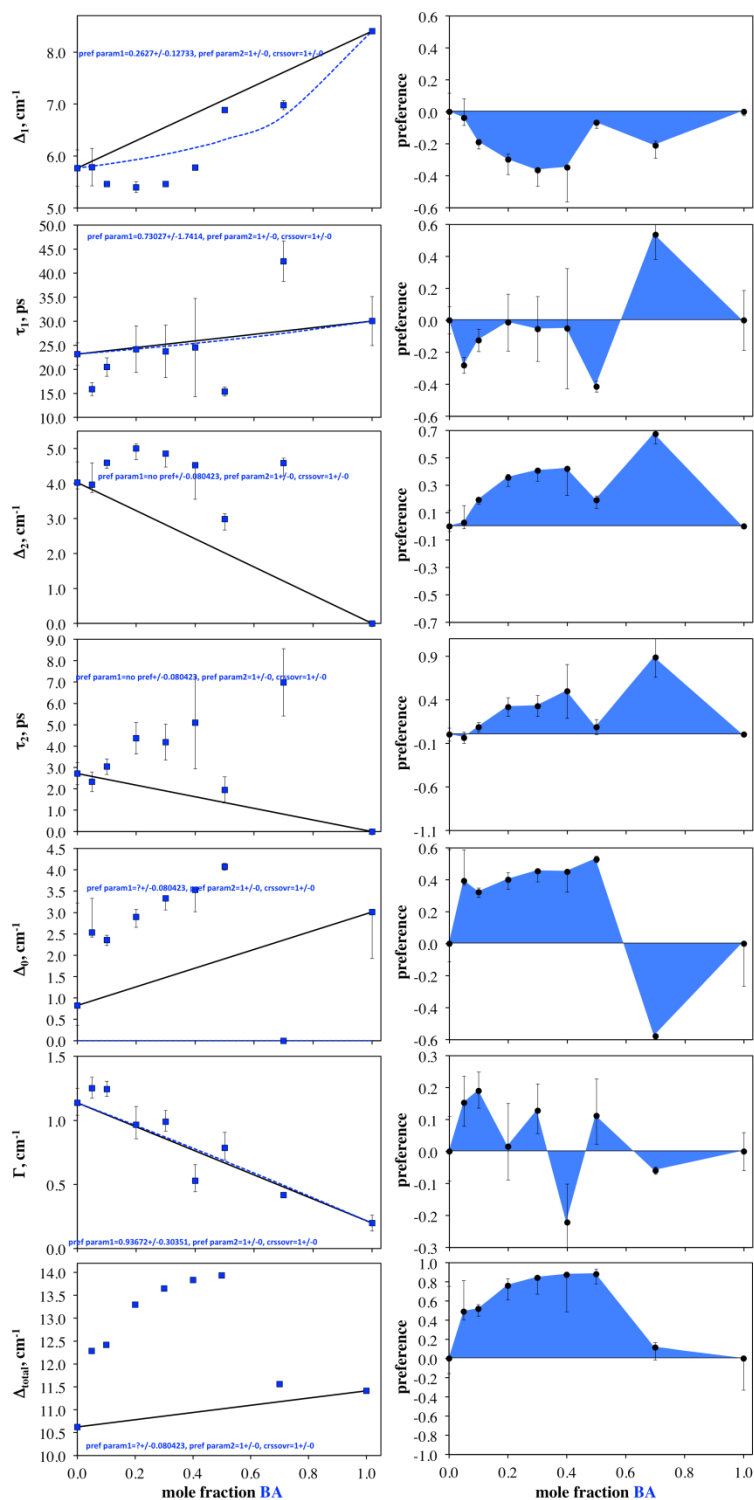
Figure 6.43 (left column) Parameters obtained by fitting CLS decays to obtain the full FFCF for VC in binary mixtures of BA in d₆-benzene. (right column) The difference between the data in the left column and the straight line connecting the first and last point, normalized (for comparison) by the range of the data (max minus min).
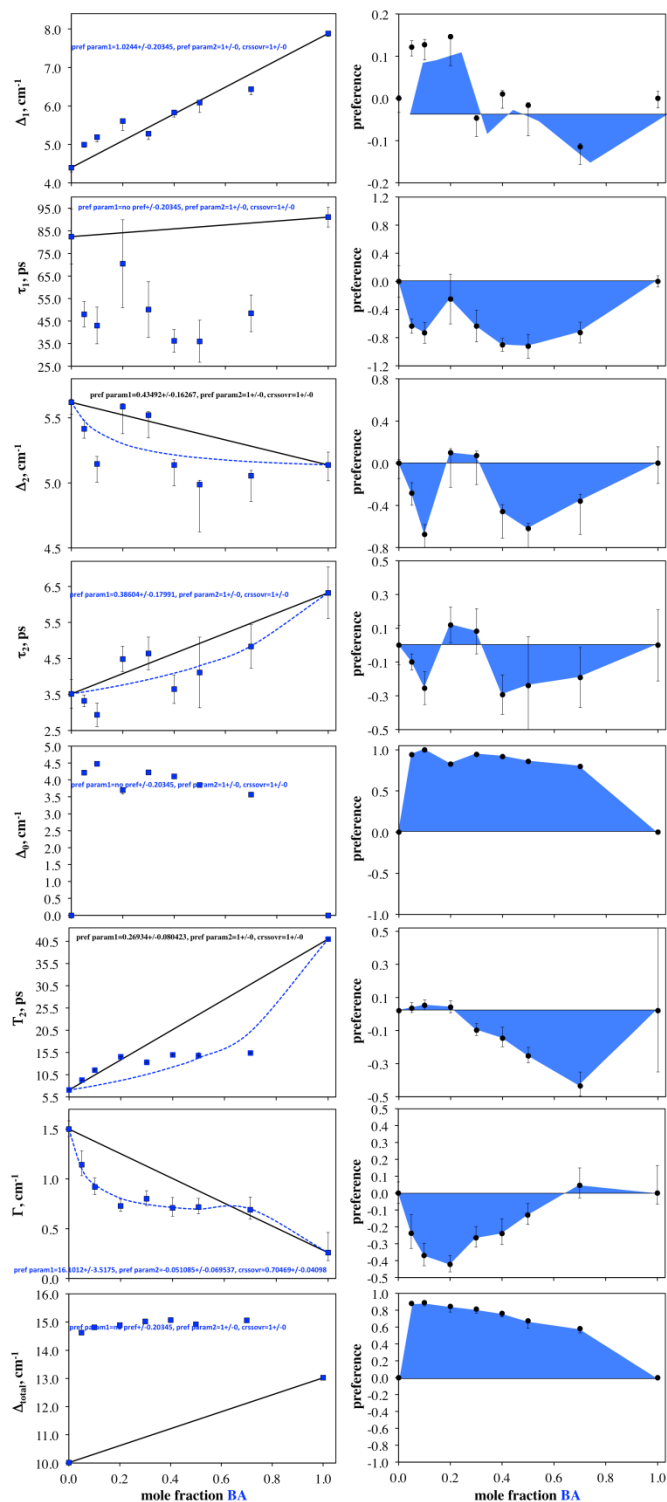
Figure 6.44. (left column) Parameters obtained by fitting CLS decays to obtain the full FFCF for VC-O$_2$ in binary mixtures of BA in d$_6$-benzene. (right column) The difference between the data in the left column and the straight line connecting the first and last point, normalized (for comparison) by the range of the data (max minus min).

Bibliography

1.   Reichardt, C., *Solvents and Solvent Effects in Organic Chemistry*, 2nd ed.; VCH: Weinheim, 1988.

2.   Gardecki, J. A.; Maroncelli, M., Solvation and Rotational Dynamics in Acetonitrile Propylene Carbonate Mixtures: A Binary System for Use in Dynamical Solvent Effect Studies. *Chem. Phys. Lett.* **1999**, *301*, 571-578.

3.   El Seoud, O. A., Understanding Solvation. *Pure Appl. Chem.* **2009**, *81*, 697-707.

4.   Bagno, A., Probing the Solvation Shell of Organic Molecules by Intermolecular 1H NOESY. In *J. Phys. Org. Chem.*, 2002; Vol. 15, pp 790-705.

5.   Matteoli, E., A Study on Kirkwood-Buff Integrals and Preferential Solvation in Mixtures with Small Deviations from Ideality and/or with Size Mismatch of Components. Importance of a Proper Reference System. *J. Phys. Chem. B* **1997**, *101*, 9800-9810.

6.   Sakurai, M.; Yoshimori, A., Selective Solvation Caused by Size Effects. *Chem. Phys. Lett.* **2003**, *371*, 23-28.

7.   Rastrelli, F.; Saielli, G.; Bagno, A.; Wakisaka, A., Preferential Solvation and Self Association in Alcohol-Acetonitrile Mixtures Observed through Mass-Spectrometric Analysis of Clusters: Influence of Alkyl Chain Length. *J. Phys. Chem. B* **2004**, *108*, 3479-3487.

8.   Shin, D. N.; Wijnen, J. W.; Engberts, J.; Wakisaka, A., On the Origin of Microheterogeneity: A Mass Spectrometric Study of Dimethyl Sulfoxide-Water Binary Mixture. *J. Phys. Chem. B* **2001**, *105*, 6759-6762.

9.   Bagno, A.; Campulla, M.; Pirana, M.; Scorrano, G.; Stiz, S., Preferential Solvation of Organic Species in Binary Solvent Mixtures Probed by Intermolecular 1H NOESY NMR Spectroscopy. *Chem. Eur. J.* **1999**, *5*, 1291-1300.

10.   Saielli, G.; Bagno, A., Preferential Solvation of Glucose and Talose in Water-Acetonitrile Mixtures: A Molecular Dynamics Simulation Study. *Phys. Chem. Chem. Phys.* **2010**, *12*, 2981-2988.

11.   Skaf, M. S.; Ladanyi, B. M., Molecular Dynamics Simulation of Solvation Dynamics in Methanol-Water Mixtures. *J. Phys. Chem.* **1996**, *100*, 18258-18268.

12.   Sahu, K.; Mondal, S. K.; Roy, D.; Karmakar, R.; Bhattacharyya, K., Slow Solvation Dynamics of 4-AP and DCM in Binary Mixtures. *J. Photochem. Photobiol. A-Chem.* **2005**, *172*, 180-184.

13.   Reichardt, C., Solvatochromic Dyes as Solvent Polarity Indicators. *Chem. Rev.* **1994**, *94*, 2319-2358.

14.   Roses, M.; Rafols, C.; Ortega, J.; Bosch, E., Solute-Solvent and Solvent-Solvent Interactions in Binary Solvent Mixtures .1. A Comparison of Several Preferential Solvation Models for Describing E_T-(30) Polarity of Dipolar Hydrogen-Bond Acceptor-Cosolvent Mixtures. *J. Chem. Soc.-Perkin Trans. 2* **1995**, 1607-1615.

15.   Silva, P. L.; Trassi, M. A. S.; Martins, C. T.; El Seoud, O. A., Solvatochromism in Binary Mixtures: First Report on a Solvation Free Energy Relationship between Solvent Exchange Equilibrium Constants and the Properties of the Medium. *J. Phys. Chem. B* **2009**, *113*, 9512-9519.

16.   El Seoud, O. A., Solvation Simplified. *Quim. Nova* **2010**, *33*, 2187-2192.

17.   da Silva, D. C.; Ricken, I.; Silva, M. A. D.; Machado, V. G., Solute-Solvent and Solvent-Solvent Interactions in the Preferential Solvation of Brooker's Merocyanine in Binary Solvent Mixtures. *J. Phys. Org. Chem.* **2002**, *15*, 420-427.

18.   El Seoud, O. A., Solvation in Pure and Mixed Solvents: Some Recent Developments. *Pure Appl. Chem.* **2007**, *79*, 1135-1151.

19.   Luther, B.; Kimmel, J.; Levinger, N., Dynamics of Polar Solvation in Acetonitrile–Benzene Binary Mixtures: Role of Dipolar and Quadrupolar Contributions to Solvation. *J. Chem. Phys.* **2002**, *116*, 3370-3377.

20.   Zurawsky, W.; Scarlata, S., Assessment of Dielectric Enrichment around 2 Fluorophores in Binary Solvents. *Photochem. Photobiol.* **1994**, *60*, 343-347.

21.   Dahlberg, M.; Laaksonen, A., Preferential Solvation of Phenol in Binary Solvent Mixtures. A Molecular Dynamics Study. *J. Phys. Chem. A* **2006**, *110*, 2253-2258.

22.   Reynolds, L.; Gardecki, J. A.; Frankland, S. J. V.; Horng, M. L.; Maroncelli, M., Dipole Solvation in Nondipolar Solvents: Experimental Studies of Reorganization Energies and Solvation Dynamics. *J. Phys. Chem.* **1996**, *100*, 10337-10354.

23.   Cichos, F.; Willert, A.; Rempel, U.; Von Borczyskowski, C., Solvation Dynamics in Mixtures of Polar and Nonpolar Solvents. *J. Phys. Chem. A* **1997**, *101*, 8179-8185.

24.   Nishiyama, K.; Okada, T., Relaxation Dynamics of Inhomogeneous Spectral Width in Binary Solvents Studied by Transient Hole-Burning Spectroscopy. *J. Phys. Chem. A* **1998**, *102*, 9729-9733.

25.   Kwak, K. W.; Park, S.; Fayer, M. D., Dynamics around Solutes and Solute-Solvent Complexes in Mixed Solvents. *Proc. Natl. Acad. Sci. U. S. A.* **2007**, *104*, 14221-14226.

26.   Kwac, K.; Lee, C.; Jung, Y.; Han, J.; Kwak, K.; Zheng, J. R.; Fayer, M. D.; Cho, M., Phenol-Benzene Complexation Dynamics: Quantum Chemistry Calculation, Molecular Dynamics Simulations, and Two Dimensional IR Spectroscopy. *J. Chem. Phys.* **2006**, *125*, 16.

27.   King, J. T.; Baiz, C. R.; Kubarych, K. J., Solvent-Dependent Spectral Diffusion in a Hydrogen Bonded "Vibrational Aggregate". *J. Phys. Chem. A* **2010**, *114*, 10590-10604.

28.   Jones, B. H.; Massari, A. M., Origins of Spectral Broadening in Iodated Vaska's Complex in Binary Solvent Mixtures. *J. Phys. Chem. B* **2013**, *117*, 15741-15749.

29.   Wong, D. B.; Sokolowsky, K. P.; El-Barghouthi, M. I.; Fenn, E. E.; Giammanco, C. H.; Sturlaugson, A. L.; Fayer, M. D., Water Dynamics in Water/DMSO Binary Mixtures. *J. Phys. Chem. B* **2012**, *116*, 5479-5490.

30.   Berg, M.; VandenBout, D. A., Ultrafast Raman Echo Measurements of Vibrational Dephasing and the Nature of Solvent-Solute Interactions. *Acc. Chem. Res.* **1997**, *30*, 65-71.

31.   Zhong, Q.; Fourkas, J. T., Optical Kerr Effect Spectroscopy of Simple Liquids. *J. Phys. Chem. B* **2008**, *112*, 15529-15539.

32.   Shirota, H.; Fujisawa, T.; Fukazawa, H.; Nishikawa, K., Ultrafast Dynamics in Aprotic Molecular Liquids: A Femtosecond Raman-Induced Kerr Effect Spectroscopic Study. *Bull. Chem. Soc. Jpn.* **2009**, *82*, 1347-1366.

33.   Sturlaugson, A. L.; Fruchey, K. S.; Lynch, S. R.; Aragon, S. R.; Fayer, M. D., Orientational and Translational Dynamics of Polyether/Water Solutions. *J. Phys. Chem. B* **2010**, *114*, 5350-5358.

34.   Elola, M. D.; Ladanyi, B. M.; Scodinu, A.; Loughnane, B. J.; Fourkas, J. T., Effects of Molecular Association on Polarizability Relaxation in Liquid Mixtures of Benzene and Hexafluorobenzene. *J. Phys. Chem. B* **2005**, *109*, 24085-24099.

35.   Day, T. J. F.; Patey, G. N., Ion Solvation Dynamics in Water-Methanol and Water-Dimethylsulfoxide Mixtures. *J. Chem. Phys.* **1999**, *110*, 10937-10944.

36.   Nguyen, C. N.; Stratt, R. M., Preferential Solvation Dynamics in Liquids: How Geodesic Pathways through the Potential Energy Landscape Reveal Mechanistic Details About Solute Relaxation in Liquids. *J. Chem. Phys.* **2010**, *133*, 124503.

37.   Chandra, A.; Bagchi, B., Molecular Theory of Solvation and Solvation Dynamics in a Binary Dipolar Liquid. *J. Chem. Phys.* **1991**, *94*, 8367-8377.

38.   Nitzan, A., *Chemical Dynamics in Condensed Phases*; Oxford University Press: New York, 2006.

39.   Fleming, G. R.; Cho, M. H., Chromophore-Solvent Dynamics. *Annu. Rev. Phys. Chem.* **1996**, *47*, 109-134.

40.   Bagchi, B.; Jana, B., Solvation Dynamics in Dipolar Liquids. *Chem. Soc. Rev.* **2010**, *39*, 1936-1954.

41.   Christian, S. D.; Lane, E. H., Solvent Effects on Molecular Complex Equilibria. In *Solutions and Solubilities Part I*, Dack, M. R. J., Ed. John Wiley & Sons: New York, 1975; pp 327-378.

42.   Steiger, H.; Kelm, H., Effect of Solvent and Pressure on the Rates of the Oxidative Addition Reactions of Methyl Iodide and Oxygen to Chlorocarbonylobis (Triphenylphosphine) Iridium (I). *J. Phys. Chem.* **1973**, *77*, 290-294.

43.   Chock, P. B.; Halpern, J., Kinetics of the Addition of Hydrogen, Oxygen, and Methyl Iodide to Some Square-Planar Iridium (I) Complexes. *J. Am. Chem. Soc.* **1966**, *88*, 3511-3514.

44.   Ugo, R.; Pasini, A.; Fusi, A.; Cenini, S., Kinetic Investigation of Some Electronic and Steric Factors in Oxidative Addition Reactions to Vaska's Compound. *J. Am. Chem. Soc.* **1972**, *94*, 7364-7370.

45.   Amis, E. S., *Solvent Effects on Reaction Rates and Mechanisms*; Academic Press: New York, 1966.

46.   Cainelli, G.; Galletti, P.; Giacomini, D., Solvent Effects on Stereoselectivity: More Than Just an Environment. *Chem. Soc. Rev.* **2009**, *38*, 990-1001.

47.   Hynes, J. T., Chemical Reaction Dynamics in Solution. *Annu. Rev. Phys. Chem.* **1985**, *36*, 573-597.

48.   Asperger, S., *Chemical Kinetics and Inorganic Reaction Mechanisms*, 2nd ed.; Kluwer Academic/Plenum Publishers: New York, 2002.

49.   Truhlar, D. G.; Hase, W. L.; Hynes, J. T., Current Status of Transition-State Theory. *J. Phys. Chem.* **1983**, *87*, 2664-2682.

50.   Buncel, E.; Stairs, R.; Wilson, H., *The Role of the Solvent in Chemical Reactions*; Oxford University Press: Oxford, 2003.

51.   van't Hoff, J. H., *Vorlesungen Uber Theoretische Und Physikalische Chemie*, 1 ed.; Vieweg: Braunschweig, 1898.

52.   Hughes, E. D.; Ingold, C. K., Mechanism of Substitution at a Saturated Carbon Atom. Part IV. A Discussion of Constitutional and Solvent Effects on the Mechanism, Kinetics, Velocity, and Orientation of Substitution. *J. Chem. Soc. (Res.)* **1935**, 244-255.

53.   Isaacs, N. S., *Physical Organic Chemistry*, 2nd ed.; Longman: Harlow, Essex, 1995.

54.   Yangjeh, A. H.; Gholami, M. R.; Mostaghim, R., Dual-Parameter Correlations on Rate of Dehydration Step of a Condensation Reaction in Aqueous Solutions of Ethanol, Propan-2-ol and 2-Methylpropan-2-ol. *J. Phys. Org. Chem.* **2001**, *14*, 884-889.

55.   Nobuoka, K.; Kitaoka, S.; Yanagisako, A.; Maki, Y.; Harran, T.; Ishikawa, Y., Stereoselectivity of the Diels-Alder Reaction in Ionic Liquids with Cyano Moieties: Effect of the Charge Delocalization of Anions on the Relation of Solvent-Solvent and Solute-Solvent Interactions. *RSC Adv.* **2013**, *3*, 19632-19638.

56.   Perkins, J.; Edwards, E.; Kleiv, R.; Weinberg, N., Molecular Dynamics Study of Reaction Kinetics in Viscous Media. *Mol. Phys.* **2011**, *109*, 1901-1909.

57.   Kramers, H. A., Brownian Motion in a Field of Force and the Diffusion Model of Chemical Reactions. *Physica* **1940**, *VII*, 284-303.

58.   Voth, G. A.; Hochstrasser, R. M., Transition State Dynamics and Relaxation Processes in Solutions: A Frontier of Physical Chemistry. *J. Phys. Chem.* **1996**, *100*, 13034-13049.

59.   Lee, M. Y.; Holtom, G. R.; Hochstrasser, R. M., Observation of the Kramers Turnover Region in the Isomerism of Trans-Stilbene in Fluid Ethane. *Chem. Phys. Lett.* **1985**, *118*, 359-363.

60.   Caldin, E. F.; Hasinoff, B. B., Diffusion-Controlled Kinetics in Reaction of Ferroprotoporphyrin-IX with Carbon-Monoxide - Reaction Studies as a Function of Pressure, Temperature and Solvent by Means of a Laser Flash-Photolysis High-Pressure Apparatus. *J. Chem. Soc.-Faraday Trans. I* **1975**, *71*, 515-527.

61.   Anna, J. M.; Baiz, C. R.; Ross, M. R.; McCanne, R.; Kubarych, K. J., Ultrafast Equilibrium and Non-Equilibrium Chemical Reaction Dynamics Probed with Multidimensional Infrared Spectroscopy. *Int. Rev. Phys. Chem.* **2012**, *31*, 367-419.

62.   Anna, J. M.; Kubarych, K. J., Watching Solvent Friction Impede Ultrafast Barrier Crossings: A Direct Test of Kramers Theory. *J. Chem. Phys.* **2010**, *133*, 12.

63.   Kanaan, N.; Ferrer, S.; Marti, S.; Garcia-Viloca, M.; Kohen, A.; Moliner, V., Temperature Dependence of the Kinetic Isotope Effects in Thymidylate Synthase. A Theoretical Study. *J. Am. Chem. Soc.* **2011**, *133*, 6692-6702.

64.   Horng, M. L.; Dahl, K.; Jones, G.; Maroncelli, M., Electron Transfer in a Donor-Substituted Acridinium Dye: Evidence for Dynamical Solvent Control. *Chem. Phys. Lett.* **1999**, *315*, 363-370.

65.   Orr-Ewing, A. J., Perspective: Bimolecular Chemical Reaction Dynamics in Liquids. *J. Chem. Phys.* **2014**, *140*, 12.

66.   Heilweil, E.; Cavanagh, R.; Stephenson, J., Population Relaxation of Co (V= 1) Vibrations in Solution Phase Metal Carbonyl Complexes. *Chem. Phys. Lett.* **1987**, *134*, 181-188.

67.   Wilson, M. R.; Liu, H. Y.; Prock, A.; Giering, W. P., Reinvestigation of the Oxidative Addition of MeI, H$_2$, and O$_2$ to Ir(CO)(Cl)L$_2$ - Quantitative-Analysis of Ligand Effects (QALE). *Organometallics* **1993**, *12*, 2044-2050.

68.   Yu, H. Z.; Fu, Y.; Guo, Q. X.; Lin, Z. Y., DFT Studies on Reactions of Transition Metal Complexes with O$_2$. *Organometallics* **2009**, *28*, 4443-4451.

69.   P'Pool, S. J.; Klingshirn, M. A.; Rogers, R. D.; Shaughnessy, K. H., Kinetic Study of the Oxidative Addition of Methyl Iodide to Vaska's Complex in Ionic Liquids. *J. Organomet. Chem.* **2005**, *690*, 3522-3528.

70.   Asbury, J. B.; Steinel, T.; Stromberg, C.; Gaffney, K. J.; Piletic, I. R.; Goun, A.; Fayer, M. D., Ultrafast Heterodyne Detected Infrared Multidimensional Vibrational Stimulated Echo Studies of Hydrogen Bond Dynamics. *Chem. Phys. Lett.* **2003**, *374*, 362-371.

71.   Fayer, M. D., Dynamics of Liquids, Molecules, and Proteins Measured with Ultrafast 2D IR Vibrational Echo Chemical Exchange Spectroscopy. *Annu. Rev. Phys. Chem.* **2009**, *60*, 21-38.

72.   Baiz, C. R.; Kubarych, K. J., Ultrafast Vibrational Stark-Effect Spectroscopy: Exploring Charge-Transfer Reactions by Directly Monitoring the Solvation Shell Response. *J. Am. Chem. Soc.* **2010**, *132*, 12784-12785.

73.   Anna, J. M.; Ross, M. R.; Kubarych, K. J., Dissecting Enthalpic and Entropic Barriers to Ultrafast Equilibrium Isomerization of a Flexible Molecule Using 2DIR Chemical Exchange Spectroscopy. *J. Phys. Chem. A* **2009**, *113*, 6544-6547.

74.   Lee, K. K.; Park, K. H.; Kwon, D.; Choi, J. H.; Son, H.; Park, S.; Cho, M., Ion-Pairing Dynamics of Li$^+$ and SCN$^-$ in Dimethylformamide Solution: Chemical Exchange Two-Dimensional Infrared Spectroscopy. *J. Chem. Phys.* **2011**, *134*, 10.

75.   Sun, Z.; Zhang, W. K.; Ji, M. B.; Hartsock, R.; Gaffney, K. J., Contact Ion Pair Formation between Hard Acids and Soft Bases in Aqueous Solutions Observed with 2DIR Spectroscopy. *J. Phys. Chem. B* **2013**, *117*, 15306-15312.

76.   Datta, P.; Sardar, D.; Mitra, P.; Sinha, C., Ir(I)-Carbonyl Complexes of Coumarinazoimidazoles: Synthesis Structure, Electrochemistry, Photophysical Properties and DFT Calculations. *Polyhedron* **2011**, *30*, 1516-1523.

77.   Kirchmann, M.; Fleischhauer, S.; Wesemann, L., Iridium Coordination Compounds of Stanna-Closo-Dodecaborate. *Organometallics* **2008**, *27*, 2803-2808.

78.   Ciriano, M. A.; Lopez, J. A.; Oro, L. A.; Pereztorrente, J. J.; Lanfranchi, M.; Tiripicchio, A.; Camellini, M. T., Oxidation of Substrates by an Iridium Dioxygen Complex - Intramolecular Oxidation of Carbon-Monoxide and Activation of a Carbonyl Group by Attack of a Heterocyclic Nitrogen. *Organometallics* **1995**, *14*, 4764-4775.

79.   Gansauer, A.; Otte, M.; Shi, L., Radical Cyclizations Terminated by Ir-Catalyzed Hydrogen Atom Transfer. *J. Am. Chem. Soc.* **2011**, *133*, 416-417.

80.   Maetani, S.; Fukuyama, T.; Suzuki, N.; Ishihara, D.; Ryu, I., Efficient Iridium-Catalyzed Decarbonylation Reaction of Aliphatic Carboxylic Acids Leading to Internal or Terminal Alkenes. *Organometallics* **2011**, *30*, 1389-1394.

81.   Vaska, L.; Rhodes, R. E., Homogeneous Catalytic Hydrogenation of Ethylene and Acetylene with Four-Coordinated Iridium and Rhodium Complexes. Reversible Catalyst-Substrate Adducts1. *J. Am. Chem. Soc.* **1965**, *87*, 4970-4971.

82.   Vaska, L.; Tadros, M., Catalytic Hydrogenolysis of Molecular Oxygen by Transition Metal Complexes in Nonaqueous Solution. *J. Am. Chem. Soc.* **1971**, *93*, 7099-7101.

83.   Casassas, E.; Fonrodona, G.; Dejuan, A., Solvatochromic Parameters for Binary-Mixtures and a Correlation with Equilibrium-Constants .1. Dioxane-Water Mixtures. *J. Solut. Chem.* **1992**, *21*, 147-162.

84.   Katritzky, A. R.; Fara, D. C.; Yang, H. F.; Tamm, K.; Tamm, T.; Karelson, M., Quantitative Measures of Solvent Polarity. *Chem. Rev.* **2004**, *104*, 175-198.

85.   Gutmann, V., Solvent Effects on Metal-Carbonyls and Related Compounds. *Mon. Chem.* **1977**, *108*, 429-435.

86.   Timpson, C. J.; Bignozzi, C. A.; Sullivan, B. P.; Kober, E. M.; Meyer, T. J., Influence of Solvent on the Spectroscopic Properties of Cyano Complexes of Ruthenium(II). *J. Phys. Chem.* **1996**, *100*, 2915-2925.

87.   Jauquet, M.; Laszlo, P., Influence of Solvents on Spectroscopy. In *Solutions and Solubilities Part I*, Dack, M. R. J., Ed. John Wiley & Sons: New York, 1975; pp 195-258.

88.   Matyushov, D. V.; Newton, M. D., Understanding the Optical Band Shape: Coumarin-153 Steady-State Spectroscopy. *J. Phys. Chem. A* **2001**, *105*, 8516-8532.

89.   Coleman, M. M.; Skrovanek, D. J.; Hu, J. B.; Painter, P. C., Hydrogen-Bonding in Polymer Blends .1. Ftir Studies of Urethane Ether Blends. *Macromolecules* **1988**, *21*, 59-65.

90.   Skrovanek, D. J.; Howe, S. E.; Painter, P. C.; Coleman, M. M., Hydrogen-Bonding in Polymers - Infrared Temperature Studies of an Amorphous Polyamide. *Macromolecules* **1985**, *18*, 1676-1683.

91.   Irish, D. E., Spectroscopic Measurements: Infrared and Raman Spectroscopy In *Physical Chemistry of Organic Solvent Systems*, Covington, A. K.; Dickinson, T., Eds. Plenum Press: London; New York, 1973; p 449.

92.   Rector, K. D.; Fayer, M. D., Infrared Vibrational Echo Experiments. In *Ultrafast Infrared and Raman Spectroscopy*, Fayer, M. D., Ed. Marcel Dekker, Inc.: New York, 2001; pp 227-272.

93.   Hamm, P.; Zanni, M., *Concepts and Methods of 2D Infrared Spectroscopy*; Cambridge University Press: New York, 2011.

94.   King, J. T.; Anna, J. M.; Kubarych, K. J., Solvent-Hindered Intramolecular Vibrational Redistribution. *Phys. Chem. Chem. Phys.* **2011**, *13*, 5579-5583.

95.   Wang, S. P.; Schwartz, M., Reorientational Diffusion of Tungsten Hexacarbonyl in Solution. *J. Mol. Liq.* **1990**, *47*, 121-128.

96.   Wakai, C.; Nakahara, M., Pressure Dependencies of Rotational, Translational, and Viscous Friction Coefficients in Water-D(2), Acetonitrile-D(3), Acetonitrile, Chloroform, and Benzene. *J. Chem. Phys.* **1994**, *100*, 8347-8358.

97.   Shelby, R. M.; Harris, C. B.; Cornelius, P. A., Origin of Vibrational Dephasing of Polyatomic Molecules in Condensed Phases. *J. Chem. Phys.* **1979**, *70*, 34-41.

98.   Gershgoren, E.; Wang, Z. H.; Ruhman, S.; Vala, J.; Kosloff, R., Investigating Pure Vibrational Dephasing of I-3(-) in Solution: Temperature Dependence of T-2(*) for the Fundamental and First Harmonic of Nu(1). *J. Chem. Phys.* **2003**, *118*, 3660-3667.

99.   Vohringer, P.; Westervelt, R. A.; Yang, T. S.; Arnett, D. C.; Feldstein, M. J.; Scherer, N. F., Solvent and Frequency-Dependence of Vibrational Dephasing on Femtosecond Time-Scales. *J. Raman Spectrosc.* **1995**, *26*, 535-551.

100.   Stenger, J.; Madsen, D.; Hamm, P.; Nibbering, E. T. J.; Elsaesser, T., Ultrafast Vibrational Dephasing of Liquid Water. *Phys. Rev. Lett.* **2001**, *87*, 4.

101.   Mukamel, S., *Principles of Nonlinear Optical Spectroscopy*; Oxford University Press: New York, 1995.

102.   Smith, B. C., *Infrared Spectral Interpretation: A Systematic Approach*; CRC Press: Boca Raton, 1999.

103.   Vaska, L., Reversible Activation of Covalent Molecules by Transition-Metal Complexes. The Role of the Covalent Molecule. *Acc. Chem. Res.* **1968**, *1*, 335-344.

104.   Huber, C. J.; Anglin, T. C.; Jones, B. H.; Muthu, N.; Cramer, C. J.; Massari, A. M., Vibrational Solvatochromism in Vaska's Complex Adducts. *J. Phys. Chem. A* **2012**, *116*, 9279-9286.

105.   Kubo, R., A Stochastic Theory of Lineshape. *Adv. Chem. Phys.* **1969**, *15*, 101-127.

106.   Hamm, P.; Hochstrasser, R. M., Structure and Dynamics of Proteins and Peptides: Femtosecond Two-Dimensional Infrared Spectroscopy. In *Ultrafast Infrared and Raman Spectroscopy*, Fayer, M. D., Ed. Marcel Dekker, Inc: New York, 2001; pp 273-348.

107.   Eckbreth, A. C., Boxcars - Crossed-Beam Phase-Matched Cars Generation in Gases. *Appl. Phys. Lett.* **1978**, *32*, 421-423.

108.   Khalil, M.; Demirdoven, N.; Tokmakoff, A., Coherent 2D IR Spectroscopy: Molecular Structure and Dynamics in Solution. *J. Phys. Chem. A* **2003**, *107*, 5258-5279.

109.   Asbury, J. B.; Steinel, T.; Kwak, K.; Corcelli, S. A.; Lawrence, C. P.; Skinner, J. L.; Fayer, M. D., Dynamics of Water Probed with Vibrational Echo Correlation Spectroscopy. *J. Chem. Phys.* **2004**, *121*, 12431-12446.

110.   Park, S.; Kwak, K.; Fayer, M. D., Ultrafast 2D-IR Vibrational Echo Spectroscopy: A Probe of Molecular Dynamics. *Laser Phys. Lett.* **2007**, *4*, 704-718.

111.   Jonas, D. M., Two-Dimensional Femtosecond Spectroscopy. *Annu. Rev. Phys. Chem.* **2003**, *54*, 425-463.

112.   Asbury, J. B.; Steinel, T.; Fayer, M. D., Vibrational Echo Correlation Spectroscopy Probes of Hydrogen Bond Dynamics in Water and Methanol. *J. Lumin.* **2004**, *107*, 271-286.

113.   Roy, S.; Pshenichnikov, M. S.; Jansen, T. L. C., Analysis of 2D CS Spectra for Systems with Non-Gaussian Dynamics. *J. Phys. Chem. B* **2011**, *115*, 5431-5440.

114.   Kwac, K.; Cho, M. H., Molecular Dynamics Simulation Study of N-Methylacetamide in Water. II. Two-Dimensional Infrared Pump-Probe Spectra. *J. Chem. Phys.* **2003**, *119*, 2256-2263.

115.   Lazonder, K.; Pshenichnikov, M. S.; Wiersma, D. A., Easy Interpretation of Optical Two-Dimensional Correlation Spectra. *Opt. Lett.* **2006**, *31*, 3354-3356.

116.   Kwak, K.; Rosenfeld, D. E.; Fayer, M. D., Taking Apart the Two-Dimensional Infrared Vibrational Echo Spectra: More Information and Elimination of Distortions. *J. Chem. Phys.* **2008**, *128*, 204505.

117.   Kwak, K.; Park, S.; Finkelstein, I. J.; Fayer, M. D., Frequency-Frequency Correlation Functions and Apodization in Two-Dimensional Infrared Vibrational Echo Spectroscopy: A New Approach. *J. Chem. Phys.* **2007**, *127*, 17.

118.   Tan, H. S.; Piletic, I. R.; Fayer, M. D., Polarization Selective Spectroscopy Experiments: Methodology and Pitfalls. *J. Opt. Soc. Am. B-Opt. Phys.* **2005**, *22*, 2009-2017.

119.   Castner, E. W.; Maroncelli, M., Solvent Dynamics Derived from Optical Kerr Effect, Dielectric Dispersion, and Time-Resolved Stokes Shift Measurements: An Empirical Comparison. *J. Mol. Liq.* **1998**, *77*, 1-36.

120.   Joo, T. H.; Jia, Y. W.; Yu, J. Y.; Lang, M. J.; Fleming, G. R., Third-Order Nonlinear Time Domain Probes of Solvation Dynamics. *J. Chem. Phys.* **1996**, *104*, 6089-6108.

121.   Kwon, O. H.; Yoo, T. H.; Othona, C. M.; Van Deventer, J. A.; Tirrell, D. A.; Zewail, A. H., Hydration Dynamics at Fluorinated Protein Surfaces. *Proc. Nat. Acad. Soc. USA* **2010**, *107*, 17101-17106.

122.   Stratt, R. M.; Maroncelli, M., Nonreactive Dynamics in Solution: The Emerging Molecular View of Solvation Dynamics and Vibrational Relaxation. *J. Phys. Chem.* **1996**, *100*, 12981-12996.

123.   Barbara, P. F.; Meyer, T. J.; Ratner, M. A., Contemporary Issues in Electron Transfer Research. *J. Phys. Chem.* **1996**, *100*, 13148-13168.

124.   Villa, J.; Warshel, A., Energetics and Dynamics of Enzymatic Reactions. *J. Phys. Chem. B* **2001**, *105*, 7887-7907.

125.   Tuckerman, M. E.; Marx, D.; Parrinello, M., The Nature and Transport Mechanism of Hydrated Hydroxide Ions in Aqueous Solution. *Nature* **2002**, *417*, 925-929.

126.   Castner, E. W.; Margulis, C. J.; Maroncelli, M.; Wishart, J. F.; Leone, S. R.; Cremer, P. S.; Groves, J. T.; Johnson, M. A., Ionic Liquids: Structure and Photochemical Reactions. *Annu. Rev. Phys. Chem.* **2011**, *62*, 85-105.

127.   Hu, Z. H.; Huang, X. H.; Annapureddy, H. V. R.; Margulis, C. J., Molecular Dynamics Study of the Temperature-Dependent Optical Kerr Effect Spectra and Intermolecular Dynamics of Room Temperature Ionic Liquid 1-Methoxyethylpyridinium Dicyanoamide. *J. Phys. Chem. B* **2008**, *112*, 7837-7849.

128.   Rothschild, W. G., Solvation by Benzene: Molecular Dynamics Simulation of Orientational Motion, Translational Diffusion, and Site-Site Radial Distributions of the Solutes Di- and Trichloromethane (Chloroform). *Mol. Phys.* **2007**, *105*, 1003-1011.

129.   Gnanakaran, S.; Hochstrasser, R. M., Vibrational Relaxation of HgI in Ethanol: Equilibrium Molecular Dynamics Simulations. *J. Chem. Phys.* **1996**, *105*, 3486-3496.

130.   Chang, Y. J.; Castner, E., Femtosecond Dynamics of Hydrogen-Bonding Solvents - Formamide and N-Methylformamide in Acetonitrile, DMF, and Water. *J. Chem. Phys.* **1993**, *99*, 113-125.

131.   Zhong, Q.; Fourkas, J., Optical Kerr Effect Spectroscopy of Simple Liquids. *J. Phys. Chem. B* **2008**, *112*, 15529-15539.

132.   Cang, H.; Li, J.; Fayer, M. D., Orientational Dynamics of the Ionic Organic Liquid 1-Ethyl-3-Methylimidazolium Nitrate. *J. Chem. Phys.* **2003**, *119*, 13017-13023.

133.   Cho, M. H.; Rosenthal, S. J.; Scherer, N. F.; Ziegler, L. D.; Fleming, G. R., Ultrafast Solvent Dynamics - Connection between Time Resolved Fluorescence and Optical Kerr Measurements. *J. Chem. Phys.* **1992**, *96*, 5033-5038.

134.   Deeg, F. W.; Stankus, J. J.; Greenfield, S. R.; Newell, V. J.; Fayer, M. D., Anisotropic Reorientational Relaxation of Biphenyl - Transient Grating Optical Kerr Effect Measurements. *J. Chem. Phys.* **1989**, *90*, 6893-6902.

135.   Giraud, G.; Gordon, C. M.; Dunkin, I. R.; Wynne, K., The Effects of Anion and Cation Substitution on the Ultrafast Solvent Dynamics of Ionic Liquids: A Time-Resolved Optical Kerr-Effect Spectroscopic Study. *J. Chem. Phys.* **2003**, *119*, 464-477.

136.   Smith, N. A.; Lin, S. J.; Meech, S. R.; Shirota, H.; Yoshihara, K., Ultrafast Dynamics of Liquid Anilines Studied by the Optical Kerr Effect. *J. Phys. Chem. A* **1997**, *101*, 9578-9586.

137.   Maroncelli, M., The Dynamics of Solvation in Polar Liquids. *J. Mol. Liq.* **1993**, *57*, 1-37.

138.   Underwood, D. F.; Blank, D. A., Ultrafast Solvation Dynamics: A View from the Solvent's Perspective Using a Novel Resonant-Pump, Nonresonant-Probe Technique. *J. Phys. Chem. A* **2003**, *107*, 956-961.

139.   de Boeij, W.; Pshenichnikov, M.; Wiersma, D., Ultrafast Solvation Dynamics Explored by Femtosecond Photon Echo Spectroscopies. *Annu. Rev. Phys. Chem.* **1998**, *49*, 99-123.

140.   Zimdars, D.; Tokmakoff, A.; Chen, S.; Greenfield, S. R.; Fayer, M. D.; Smith, T. I.; Schwettman, H. A., Picosecond Infrared Vibrational Echoes in a Liquid and Glass Using a Free Electron Laser. *Phys. Rev. Lett.* **1993**, *70*, 2718-2721.

141.   Mukamel, S., Multidimensional Femtosecond Correlation Spectroscopies of Electronic and Vibrational Excitations. *Annu. Rev. Phys. Chem.* **2000**, *51*, 691-729.

142.   Baiz, C. R.; McRobbie, P. L.; Anna, J. M.; Geva, E.; Kubarych, K. J., Two-Dimensional Infrared Spectroscopy of Metal Carbonyls. *Acc. Chem. Res.* **2009**, *42*, 1395-1404.

143.   Hamm, P.; Lim, M. H.; Hochstrasser, R. M., Structure of the Amide I Band of Peptides Measured by Femtosecond Nonlinear-Infrared Spectroscopy. *J. Phys. Chem. B* **1998**, *102*, 6123-6138.

144.   Khalil, M.; Tokmakoff, A., Signatures of Vibrational Interactions in Coherent Two-Dimensional Infrared Spectroscopy. *Chem. Phys.* **2001**, *266*, 213.

145.   Shim, S. H.; Strasfeld, D. B.; Ling, Y. L.; Zanni, M. T., Automated 2D IR Spectroscopy Using a Mid-IR Pulse Shaper and Application of This Technology to the Human Islet Amyloid Polypeptide. *Proc. Nat. Acad. Soc. USA* **2007**, *104*, 14197-14202.

146.   Eigner, A. A.; Jones, B. H.; Koprucki, B. W.; Massari, A. M., Static and Dynamic Structural Memory in Polyaniline Thin Films. *J. Phys. Chem. B* **2011**, *115*, 8686-8695.

147.   Eigner, A. A.; Jones, B. H.; Koprucki, B. W.; Massari, A. M., Ground-State Structural Dynamics in Doped and Undoped Polyaniline Films Probed by Two-

Dimensional Infrared Vibrational Echo Spectroscopy. *J. Phys. Chem. B* **2011**, *115*, 4583-4591.

148. Eigner, A. A.; Anglin, T. C.; Massari, A. M., 2D-IR Studies of Annealing-Induced Changes to Structural Dynamics in Organic Semiconductor Thin Films. *J. Phys. Chem. C* **2010**, *114*, 12308-12315.

149. Kolano, C.; Helbing, J.; Kozinski, M.; Sander, W.; Hamm, P., Watching Hydrogen-Bond Dynamics in a Beta-Turn by Transient Two-Dimensional Infrared Spectroscopy. *Nature* **2006**, *444*, 469-472.

150. Nydegger, M. W.; Dutta, S.; Cheatum, C. M., Two-Dimensional Infrared Study of 3-Azidopyridine as a Potential Spectroscopic Reporter of Protonation State. *J. Chem. Phys.* **2010**, *133*, 134506.

151. Stafford, A. J.; Ensign, D. L.; Webb, L. J., Vibrational Stark Effect Spectroscopy at the Interface of Ras and Rap1A Bound to the Ras Binding Domain of RalGDS Reveals an Electrostatic Mechanism for Protein-Protein Interaction. *J. Phys. Chem. B* **2010**, *114*, 15331-15344.

152. Suydam, I. T.; Boxer, S. G., Vibrational Stark Effects Calibrate the Sensitivity of Vibrational Probes for Electric Fields in Proteins. *Biochemistry* **2003**, *42*, 12050-12055.

153. Merchant, K. A.; Noid, W. G.; Akiyama, R.; Finkelstein, I. J.; Goun, A.; McClain, B. L.; Loring, R. F.; Fayer, M. D., Myoglobin-Co Substate Structures and Dynamics: Multidimensional Vibrational Echoes and Molecular Dynamics Simulations. *J. Am. Chem. Soc.* **2003**, *125*, 13804-13818.

154. Baiz, C. R.; Kubarych, K. J.; Geva, E., Molecular Theory and Simulation of Coherence Transfer in Metal Carbonyls and Its Signature on Multidimensional Infrared Spectra. *J. Phys. Chem. B* **2011**, *115*, 5322-5339.

155. Fecko, C. J.; Eaves, J. D.; Loparo, J. J.; Tokmakoff, A.; Geissler, P. L., Ultrafast Hydrogen-Bond Dynamics in the Infrared Spectroscopy of Water. *Science* **2003**, *301*, 1698-1702.

156. Vaska, L.; Chen, L.; Senoff, C., Oxygen-Carrying Iridium Complexes: Kinetics, Mechanism, and Thermodynamics. *Science* **1971**, *174*, 587-589.

157. Atwood, J., Organoiridium Complexes as Models for Homogeneously Catalyzed Reactions. *Coord. Chem. Rev.* **1988**, *83*, 93-114.

158. La Placa, S.; Ibers, J., Structure of $IrO_2Cl(CO)(P(C_6H_5)_3)_2$, the Oxygen Adduct of a Synthetic Reversible Molecular Oxygen Carrier. *J. Am. Chem. Soc.* **1965**, *87*, 2581-2586.

159. Geoffroy, G.; Hammond, G.; Gray, H., Photochemical Reductive Elimination of Oxygen, Hydrogen, and Hydrogen Chloride from Iridium Complexes. *J. Am. Chem. Soc.* **1975**, *97*, 3933-3936.

160. Grushin, V. V., Reductive Elimination of Hydrogen-Chloride from Chloro-Hydrido-Transition Metal-Complexes - an Efficient and Simple Method for Generation of Electron-Rich, Coordinatively Unsaturated, Reactive Intermediates. *Acc. Chem. Res.* **1993**, *26*, 279-286.

161. Schultz, R., Unusual Behavior in the 308 nm Flash Photolysis of Vaska's Complex. *J. Organomet. Chem.* **2003**, *688*, 1-4.

162. Wink, D. A.; Ford, P. C., Common Intermediates in the Flash-Photolysis of Vaskas Compound IrCl(CO)(PPh$_3$)$_2$ and Its Dihydride Adduct H$_2$IrCl(CO)(PPh$_3$)$_2$ - Implications with Regard to Reductive Elimination Mechanisms. *J. Am. Chem. Soc.* **1985**, *107*, 5566-5567.

163. Margl, P.; Ziegler, T.; Bloechl, P., Migratory CO Insertion and Aldehyde Formation in Carbonylation of Methane by the Rh (Ph$_3$) $_2$Cl Catalyst. A Dynamical Density Functional Study. *J. Am. Chem. Soc* **1996**, *118*, 5412-5419.

164. Margl, P.; Ziegler, T.; Bloechl, P., Reaction of Methane with Rh (Ph$_3$) $_2$Cl: A Dynamical Density Functional Study. *J. Am. Chem. Soc.* **1995**, *117*, 12625-12634.

165. Selke, M.; Foote, C., Reactions of Organometallic Complexes with Singlet Oxygen. Photooxidation of Vaska's Complex. *J. Am. Chem. Soc.* **1993**, *115*, 1166-1167.

166. Stang, P. J.; Schiavelli, M. D.; Keith Chenault, H., Kinetic Deuterium Isotope Effects in the Reaction of Vaska's Compound (Ph$_3$P) $_2$Ir (CO)Cl with CH$_3$I and CH$_3$OSO$_2$CF$_3$. *Organometallics* **1984**, *3*, 1133-1134.

167. Thompson, W.; Sears Jr, C., Kinetics of Oxidative Addition to Iridium (I) Complexes. *Inorg. Chem.* **1977**, *16*, 769-774.

168. Zahalka, H. A.; H., A., Homogeneous Decarbonylation of Formate Esters Catalyzed by Vaska's Compound. *Organometallics* **1986**, *5*, 2497-2499.

169. Fayer, M. D., Fast Protein Dynamics Probed with Infrared Vibrational Echo Experiments. *Ann. Rev. Phys. Chem.* **2001**, *52*, 315-356.

170. Massari, A. M.; Finkelstein, I. J.; McClain, B. L.; Goj, A.; Wen, X.; Bren, K. L.; Loring, R. F.; Fayer, M. D., The Influence of Aqueous vs. Glassy Solvents on Protein Dynamics: Vibrational Echo Experiments and Molecular Dynamics Simulations. *J. Am. Chem. Soc.* **2005**, *127*, 14279-14289.

171. Cotton, F. A., *Advanced Inorganic Chemistry*, 5th ed.; Wiley-Interscience, Inc.: New York, 1988.

172. Ray, G. B.; Li, X. Y.; Ibers, J. A.; Sessler, J. L.; Spiro, T. G., How Far Can Proteins Bend the Feco Unit - Distal Polar and Steric Effects in Heme-Proteins and Models. *J. Am. Chem. Soc.* **1994**, *116*, 162-176.

173. Cho, M., Vibrational Solvatochromism and Electrochromism: Coarse-Grained Models and Their Relationships. *J. Chem. Phys.* **2009**, *130*.

174. Mayer, U.; Gutmann, V.; Gerger, W., Acceptor Number - Quantitative Empirical Parameter for Electrophilic Properties of Solvents. *Mon. Chem.* **1975**, *106*, 1235-1257.

175. Pensack, R. D.; Banyas, K. M.; Asbury, J. B., Vibrational Solvatochromism in Organic Photovoltaic Materials: Method to Distinguish Molecules at Donor/Acceptor Interfaces. *PCCP* **2010**, *12*, 14144-14152.

176. Marcus, Y., The Properties of Organic Liquids That Are Relevant to Their Use as Solvating Solvents. *Chem. Soc. Rev.* **1993**, *22*, 409-416.

177. Chang, C. M., DFT-Based Linear Solvation Energy Relationships for the Infrared Spectral Shifts of Acetone in Polar and Nonpolar Organic Solvents. *J. Phys. Chem. A* **2008**, *112*, 2482-2488.

178. Engberts, J.; Famini, G. R.; Perjessy, A.; Wilson, L. Y., Solvent Effects on C = O Stretching Frequencies of Some 1-Substituted 2-Pyrrolidinones. *J. Phys. Org. Chem.* **1998**, *11*, 261-272.

179. Barwick, V. J., Strategies for Solvent Selection - a Literature Review. *TrAC-Trend. Anal. Chem.* **1997**, *16*, 293-309.

180. Snyder, L. R., Classification of Solvent Properties of Common Liquids. *J. Chromatogr. Sci.* **1978**, *16*, 223-234.

181. *CRC Handbook of Chemistry and Physics*, 91st ed.; CRC Press: Cleveland, 2011.

182. Dlott, D. D.; Fayer, M. D.; Hill, J. R.; Rella, C. W.; Suslick, K. S.; Ziegler, C. J., Vibrational Relaxation in Metalloporphyrin CO Complexes. *J. Am. Chem. Soc.* **1996**, *118*, 7853-7854.

183. Hill, J. R.; Dlott, D. D.; Fayer, M. D.; Peterson, K. A.; Rella, C. W.; Rosenblatt, M. M.; Suslick, K. S.; Ziegler, C. J., Vibrational-Relaxation of Carbon-Monoxide in Model Heme Compounds - 6-Coordinate Metalloporphyrins (M=Fe, Ru, Os). *Chem. Phys. Lett.* **1995**, *244*, 218-223.

184. Silverstein, R. M.; Bassler, G. C.; Morrill, T. C., *Spectrometric Identification of Organic Compounds*, Fourth ed.; John Wiley and Sons: New York, 1981.

185. Laurent, T.; Hennig, H.; Ernsting, N.; Kovalenko, S., The Ultrafast Optical Kerr Effect in Liquid Fluoroform: An Estimate of the Collision-Induced Contribution. *PCCP* **2000**, *2*, 2691-2697.

186. Loughnane, B. J.; Scodinu, A.; Farrer, R. A.; Fourkas, J. T.; Mohanty, U., Exponential Intermolecular Dynamics in Optical Kerr Effect Spectroscopy of Small-Molecule Liquids. *J. Chem. Phys.* **1999**, *111*, 2686-2694.

187. Rector, K. D.; Jiang, J. W.; Berg, M. A.; Fayer, M. D., Effects of Solvent Viscosity on Protein Dynamics: Infrared Vibrational Echo Experiments and Theory. *J. Phys. Chem. B* **2001**, *105*, 1081-1092.

188. Berg, M. A.; Hubble, H. W., A Viscoelastic Continuum Model of Non-Polar Solvation. II. Vibrational Dephasing in Moderate to High-Viscosity Liquids and Glasses. *Chem. Phys.* **1998**, *233*, 257-266.

189. Chang, Y. J.; Castner, E., Deuterium-Isotope Effects on the Ultrafast Solvent Relaxation of Formamide and N,N-Dimethylformamide. *J. Phys. Chem.* **1994**, *98*, 9712-9722.

190. Witt, R.; Sturz, L.; Doelle, A.; Mueller-Plathe, F., Molecular Dynamics of Benzene in Neat Liquid and a Solution Containing Polystyrene. [13]C Nuclear Magnetic Relaxation and Molecular Dynamics Simulation Results. *J. Phys. Chem. A* **2000**, *104*, 5716-5725.

191. Gaffney, K. J.; Ji, M.; Odelius, M.; Park, S.; Sun, Z., H-Bond Switching and Ligand Exchange Dynamics in Aqueous Ionic Solution. *Chem. Phys. Lett.* **2011**, *504*, 1-6.

192. Ji, M.; Gaffney, K. J., Orientational Relaxation Dynamics in Aqueous Ionic Solution: Polarization-Selective Two-Dimensional Infrared Study of Angular Jump-Exchange Dynamics in Aqueous 6M NaClO$_4$. *J. Chem. Phys.* **2011**, *134*.

193. Valentine, J. S., Dioxygen Ligand in Mononuclear Group VIII Transition Metal Complexes. *Chem. Rev.* **1973**, *73*, 235-245.

194. Jones, B. H.; Huber, C. J.; Massari, A. M., Solvation Dynamics of Vaska's Complex by 2D-IR Spectroscopy. *J. Phys. Chem. C* **2011**, *115*, 24813-24822.

195.   Mathew, N. A.; Rickard, M. A.; Kornau, K. M.; Pakoulev, A. V.; Block, S. B.; Yurs, L. A.; Wright, J. C., Coherent Multidimensional Vibrational Spectroscopy of Representative N-Alkanes. *J. Phys. Chem. A* **2009**, *113*, 9792-9803.

196.   Yurs, L. A.; Block, S. B.; Pakoulev, A. V.; Selinsky, R. S.; Jin, S.; Wright, J., Spectral Isolation and Measurement of Surface-Trapped State Multidimensional Nonlinear Susceptibility in Colloidal Quantum Dots. *J. Phys. Chem. C* **2012**, *116*, 5546-5553.

197.   Zhao, W.; Wright, J. C., Doubly Vibrationally Enhanced Four Wave Mixing: The Optical Analog to 2D NMR. *Phys. Rev. Lett.* **2000**, *84*, 1411-1414.

198.   Besemann, D. M.; Condon, N. J.; Murdoch, K. M.; Zhao, W.; Meyer, K. A.; Wright, J. C., Interference, Dephasing, and Vibrational Coupling Effects between Coherence Pathways in Doubly Vibrationally Enhanced Nonlinear Spectroscopies. *Chem. Phys.* **2001**, *266*, 177-195.

199.   Banno, M.; Ohta, K.; Yamaguchi, S.; Hirai, S.; Tominaga, K., Vibrational Dynamics of Hydrogen-Bonded Complexes in Solutions Studied with Ultrafast Infrared Pump-Probe Spectroscopy. *Acc. Chem. Res.* **2009**, *42*, 1259-1269.

200.   Leahy, D. E.; Morris, J. J.; Taylor, P. J.; Wait, A. R., Model Solvent Systems for QSAR .3. An LSER Analysis of the Critical Quartet - New Light on Hydrogen-Bond Strength and Directionality. *J. Chem. Soc.-Perkin Trans. 2* **1992**, 705-722.

201.   McLellan, A. L., *Tables of Experimental Dipole Moments*; W.H. Freeman: San Francisco, 1963; Vol. 1.

202.   Li, J.; Zhang, Y.; Carr, P. W., Novel Triangle Scheme for Classification of Gas Chromatographic Phases Based on Solvatochromic Linear Solvation Energy Relationships. *Anal. Chem.* **1992**, *64*, 210-218.

203.   Kenkre, V. M.; Tokmakoff, A.; Fayer, M. D., Theory of Vibrational-Relaxation of Polyatomic-Molecules in Liquids. *J. Chem. Phys.* **1994**, *101*, 10618-10629.

204.   Ohta, K.; Tominaga, K., Vibrational Population Relaxation of Hydrogen-Bonded Phenol Complexes in Solution: Investigation by Ultrafast Infrared Pump-Probe Spectroscopy. *Chem. Phys.* **2007**, *341*, 310-319.

205.   King, J.; Ross, M.; Kubarych, K., Water-Assisted Vibrational Relaxation of a Metal Carbonyl Complex Studied with Ultrafast 2D-IR. *J. Phys. Chem. B* **2012**, *116*, 3754-3759.

206.   Hamm, P.; Lim, M.; Hochstrasser, R. M., Vibrational Energy Relaxation of the Cyanide Ion in Water. *J. Chem. Phys.* **1997**, *107*, 10523-10531.

207.   Oxtoby, D. W., Vibrational Relaxation in Liquids. *Annu. Rev. Phys. Chem.* **1981**, *32*, 77-101.

208.   Schweizer, K. S.; Chandler, D., Vibrational Dephasing and Frequency-Shifts of Polyatomic-Molecules in Solution. *J. Chem. Phys.* **1982**, *76*, 2296-2314.

209.   Tan, H. S.; Piletic, I. R.; Fayer, M. D., Orientational Dynamics of Water Confined on a Nanometer Length Scale in Reverse Micelles. *J. Chem. Phys.* **2005**, *122*, 057405.

210.   Jones, B. H.; Huber, C. J.; Massari, A. M., Solvent-Mediated Vibrational Energy Relaxation from Vaska's Complex Adducts in Binary Solvent Mixtures. *J. Phys. Chem. A* **2013**, *117*, 6150-6157.

211.   Aagaard, O. M.; Meier, R. J.; Buda, F., Ruthenium-Catalyzed Olefin Metathesis: A Quantum Molecular Dynamics Study. *J. Am. Chem. Soc.* **1998**, *120*, 7174-7182.

212.   Bianco, R.; Hay, P. J.; Hynes, J. T., Theoretical Study of O-O Single Bond Formation in the Oxidation of Water by the Ruthenium Blue Dimer. *J. Phys. Chem. A* **2011**, *115*, 8003-8016.

213.   Caratzoulas, S.; Vlachos, D. G., Converting Fructose to 5-Hydroxymethylfurfural: A Quantum Mechanics/Molecular Mechanics Study of the Mechanism and Energetics. *Carbohydr. Res.* **2011**, *346*, 664-672.

214.   Ensing, B.; Meijer, E. J.; Blochl, P. E.; Baerends, E. J., Solvation Effects on the S_N2 Reaction between CH_3Cl and Cl^- in Water. *J. Phys. Chem. A* **2001**, *105*, 3300-3310.

215.   Grossman, M.; Born, B.; Heyden, M.; Tworowski, D.; Fields, G. B.; Sagi, I.; Havenith, M., Correlated Structural Kinetics and Retarded Solvent Dynamics at the Metalloprotease Active Site. *Nat. Struct. Mol. Biol.* **2011**, *18*, 1102-1108.

216.   Handgraaf, J. W.; Meijer, E. J., Realistic Modeling of Ruthenium-Catalyzed Transfer Hydrogenation. *J. Am. Chem. Soc.* **2007**, *129*, 3099-3103.

217.   Wang, L. P.; Wu, Q.; Van Voorhis, T., Acid-Base Mechanism for Ruthenium Water Oxidation Catalysts. *Inorg. Chem.* **2010**, *49*, 4543-4553.

218.   Faeder, S. M. G.; Jonas, D. M., Two-Dimensional Electronic Correlation and Relaxation Spectra: Theory and Model Calculations. *J. Phys. Chem. A* **1999**, *103*, 10489-10505.

219.   Benamotz, D.; Scott, T. W., Microscopic Frictional Forces on Molecular-Motion in Liquids - Picosecond Rotational Diffusion in Alkanes and Alcohols. *J. Chem. Phys.* **1987**, *87*, 3739-3748.

220.   Spears, K. G.; Cramer, L. E., Rotational Diffusion in Aprotic and Protic Solvents. *Chem. Phys.* **1978**, *30*, 1-8.

221.   Khalil, M.; Demirdoven, N.; Tokmakoff, A., Obtaining Absorptive Line Shapes in Two-Dimensional Infrared Vibrational Correlation Spectra. *Phys. Rev. Lett.* **2003**, *90*, 047401.

222.   Bakulin, A. A.; Liang, C.; Jansen, T. L.; Wiersma, D. A.; Bakker, H. J.; Pshenichnikov, M. S., Hydrophobic Solvation: A 2D IR Spectroscopic Inquest. *Acc. Chem. Res.* **2009**, *42*, 1229-1238.

223.   Ugo, R.; LaMonica, G.; Cenini, S.; Segre, A.; Conti, F., Zerovalent Platinum Chemistry. Part Vi. The Reactions of Bis- and Tris-Triphenylphosphineplatinum(0) with Hydrogen Sulfide, Hydrogen Selenide, Sulfur, and Related Molecules. *J. Chem. Soc. A* **1971**, 522-528.

224.   Vaska, L.; Chen, L. S., Reversible Oxygenation of Metal Complexes: Electronic and Steric Factors. *J. Chem. Soc. D-Chem. Comm.* **1971**, 1080-1081.

225.   Fenn, E.; Moilanen, D.; Levinger, N.; Fayer, M., Water Dynamics and Interactions in Water− Polyether Binary Mixtures. *J. Am. Chem. Soc.* **2009**, *131*, 5530-5539.

226.   Delacruz, C.; Sheppard, N., A Review of v_{CO} Bond-Stretching Wave-Numbers for CO Ligands in Metal Coordination-Compounds or Clusters with Emphasis on the Less Common Types of Metal/CO Bonding Patterns, and of the Relationship between v_{CO} and the Internuclear Distance, R(CO). *J. Mol. Struct.* **1990**, *224*, 141-161.

227. Vaska, L.; Patel, R. C.; Brady, R., Oxygenation of Metal-Complexes - Mechanistic Details of Initial Interaction. *Inorg. Chim. Acta* **1978**, *30*, 239-242.

228. Battino, R.; Rettich, T. R.; Tominaga, T., The Solubility of Oxygen and Ozone in Liquids. *J. Phys. Chem. Ref. Data* **1983**, *12*, 163-178.

229. Shirono, K.; Morimatsu, T.; Takemura, F., Gas Solubilities (CO_2, O_2, Ar, N_2, H_2, and He) in Liquid Chlorinated Methanes. *J. Chem. Eng. Data* **2008**, *53*, 1867-1871.

230. Plucinski, P. K.; Bavykin, D. V.; Kolaczkowski, S. T.; Lapkin, A. A., Liquid-Phase Oxidation of Organic Feedstock in a Compact Multichannel Reactor. *Ind. Eng. Chem. Res.* **2005**, *44*, 9683-9690.

231. Krichevsky, I. R., Thermodynamics of an Infinitely Dilute Solution in Mixed Solvents. I. The Henry's Coefficient in a Mixed Solvent Behaving as an Ideal Solvent. *Zh. fiz. khim.* **1937**, *9*, 41-47.

232. Shulgin, I.; Ruckenstein, E., Henry's Constant in Mixed Solvents from Binary Data. *Ind. Eng. Chem. Res.* **2002**, *41*, 1689-1694.

233. Corbett, J. F., Pseudo First-Order Kinetics. *J. Chem. Ed.* **1972**, *49*, 663.

234. Bosch, E.; Roses, M., Relationships between E_T Polarity and Composition in Binary Solvent Mixtures. *J. Chem. Soc.-Faraday Trans.* **1992**, *88*, 3541-3546.

235. Roses, M.; Rived, F.; Bosch, E., Dissociation Constants and Preferential Solvation in Some 2-Methylpropan-2-Ol Alcohol Mixtures. *J. Chem. Soc.-Faraday Trans.* **1993**, *89*, 1723-1728.